NASA TECHNICAL NOTE

NASA TN D-7150

NASA TN D-7150

INVESTIGATION OF FLOW FIELDS WITHIN LARGE-SCALE HYPERSONIC INLET MODELS

by

A. Vernon Gnos and Earl C. Watson
Ames Research Center
Moffett Field, Calif. 94035

and

William R. Seebaugh, Robert J. Sanator,
and Joseph P. DeCarlo
Fairchild Industries, Inc., Fairchild Republic Division
Farmingdale, Long Island, N.Y. 11735

NATIONAL AERONAUTICS AND SPACE ADMINISTRATION • WASHINGTON, D. C. • APRIL 1973

1. Report No. TN D–7150	2. Government Accession No.	3. Recipient's Catalog No.

4. Title and Subtitle INVESTIGATION OF FLOW FIELDS WITHIN LARGE-SCALE HYPERSONIC INLET MODELS	5. Report Date April 1973 6. Performing Organization Code
7. Author(s) A. Vernon Gnos, Earl C. Watson, William R. Seebaugh, Robert J. Sanator, and Joseph P. DeCarlo	8. Performing Organization Report No. A–4274
9. Performing Organization Name and Address NASA Ames Research Center Moffett Field, Calif. 94035 and Fairchild Industries, Inc., Fairchild Republic Division Farmingdale, Long Island, New York, 11735	10. Work Unit No. 11. Contract or Grant No. NAS 2-5052 NAS 2-5719
12. Sponsoring Agency Name and Address National Aeronautics and Space Administration Washington, D. C. 20546	13. Type of Report and Period Covered Technical Note 14. Sponsoring Agency Code

15. Supplementary Notes

16. Abstract

Analytical and experimental investigations were conducted to determine the internal flow characteristics in model passages representative of hypersonic inlets for use at Mach numbers to about 12. The passages were large enough to permit measurements to be made in both the core flow and boundary layers. The analytical techniques for designing the internal contours and predicting the internal flow-field development accounted for coupling between the boundary layers and inviscid flow fields by means of a displacement-thickness correction. Three large-scale inlet models, each having a different internal compression ratio, were designed to provide high internal performance with an approximately uniform static-pressure distribution at the throat station. The models were tested in the Ames 3.5-Foot Hypersonic Wind Tunnel at a nominal free-stream Mach number of 7.4 and a unit free-stream Reynolds number of 8.86×10^6 per meter.

The experimental results indicated that the static pressure was not uniform across the throat station. Total-pressure recovery at the throat (the ratio of the local total pressure to the mean total pressure at the cowl lip station) also was nonuniform. The pressure recovery in the core flow ranged from lows of about 0.25 to 0.54 on the cowl side, depending on the inlet compression ratio, to highs of about 0.88 to 0.96. The predicted pressure recoveries agreed in general with those measured and indicated that the nonuniformity was caused primarily by the cowl leading-edge bluntness. Because the analytical techniques do not adequately account for the various interactions between the viscid and inviscid components of the flow, the shock-wave patterns in the inlets were not predicted; consequently, the longitudinal distributions of surface pressure were not predicted well in regions influenced by shock-wave boundary-layer interactions. The analytical techniques were used successfully to design internal contours for inlets that provided high performance, but they require improvement to account for the shock-wave boundary-layer interactions, and the boundary layer that developed downstream of leading edges having small bluntness where the boundary layer may be subject to both transition and entropy layer effects.

17. Key Words (Suggested by Author(s)) Hypersonic inlets Internal flow fields Boundary layer Shock-wave boundary-layer interactions	18. Distribution Statement Unclassified – Unlimited

19. Security Classif. (of this report) Unclassified	20. Security Classif. (of this page) Unclassified	21. No. of Pages 175	22. Price* $3.00

---

* For sale by the National Technical Information Service, Springfield, Virginia 22151

TABLE OF CONTENTS

SYMBOLS

C	temperature–viscosity ratio, $\frac{\mu T_\infty}{\mu_\infty T}$
L_i	length over which the pressure rise occurs in a shock–wave boundary–layer interaction (fig. 9)
$\dot{m}$	mass flow rate
M	Mach number
p	static pressure
p_p	pitot pressure
p_t	total pressure
$\dot{q}$	heat–transfer rate
R	recovery factor, $\frac{T_{t_{\text{measured}}} - T_{\text{true}}}{T_{t_{\text{true}}} - T_{\text{true}}}$
Re	Reynolds number
T	temperature
T_t	total temperature
U	streamwise velocity component
X,Y,Z	spatial coordinates
α	angle of attack of wedge forebody
δ	boundary–layer thickness
δ^*	displacement thickness
ϵ	flow angle; surface angle
θ	momentum thickness
λ	cowl initial turning angle
μ	viscosity

ρ	density
τ	shear stress
$\bar{\chi}$	viscous–interaction parameter, $M^3 \sqrt{\frac{C}{Re_X}}$

Subscripts

$_{1,2}$	stations specified in figure 9
e	boundary–layer edge
o	station at which laminar boundary–layer calculations are initiated
s	geometric surface
w	wall
∞	tunnel free stream

Superscript

$'$	coordinate measured from the geometric surface

INVESTIGATION OF FLOW FIELDS WITHIN LARGE-SCALE HYPERSONIC INLET MODELS

A. Vernon Gnos and Earl C. Watson
Ames Research Center

and

William R. Seebaugh, Robert J. Sanator, and Joseph P. DeCarlo
Fairchild Industries, Inc., Fairchild Republic Division

SUMMARY

Analytical and experimental investigations were conducted to determine the internal flow characteristics in model passages representative of hypersonic inlets for use at Mach numbers to about 12. The passages were large enough to permit measurements to be made in both the core flow and boundary layers. The goal of the program was to obtain the analytical and experimental information needed to improve the current method of designing internal contours of hypersonic inlets. The experimental results were used in the evaluation of analytical techniques for computing the flow fields in internal passages.

Three large-scale inlet models, each having a different internal compression ratio, were designed to provide high performance and approximately uniform static-pressure distributions at the throat stations. A wedge forebody was used to simulate the flow-field conditions at the entrance of the internal passages, thus removing the actual vehicle forebody from consideration in the design of the wind-tunnel models. Tests were conducted in the Ames 3.5-Foot Hypersonic Wind Tunnel at a nominal test Mach number of 7.4 and free-stream unit Reynolds number of 8.86×10^6 per meter.

The entering inviscid and viscous flow conditions were determined from flow-field survey data at the inlet entrance. Profiles of flow properties were obtained near the centerlines of the internal passages to define the boundary-layer development on the internal surfaces and the internal shock-wave configuration. Flow-field properties were measured at several lateral locations across the throat stations to evaluate the overall performance of the internal passages.

The experimental results for each inlet showed a nonlinear distribution of total-pressure recovery in the core flow at the throat stations. For the inlet having the lowest compression ratio, the internal recovery (the ratio of the total pressure at the throat station to that at the inlet-entrance station) ranged from about 0.25 near the cowl to a maximum of about 0.96. For the inlet with the intermediate compression the range was from about 0.54 near the cowl to 0.88 near the centerbody. These ranges of recovery were in general agreement with those predicted, but the measured distributions differed from those predicted. The distribution of recovery for the inlet having the highest compression could not be determined accurately because of the uncertainty in the measurements of the flow-field static pressures. The analytical techniques for predicting the internal flow-field development, which utilized a displacement-thickness correction to account

for the coupling between the boundary layers and the inviscid flow fields, yielded integral boundary-layer properties that were in poor to good agreement with experimental results. The desired uniform static-pressure distributions at the throat stations were not obtained experimentally because of the presence of unpredicted shock waves within the internal passages.

It was found that improvement in the analytical methods is needed for predicting (1) the details of the boundary-layer development through and downstream of regions of boundary-layer transition; (2) the boundary-layer and inviscid flow-field development downstream of leading edges with small bluntness; and (3) the detailed characteristics of shock-wave boundary-layer interactions, including the flow fields downstream of the interaction regions. Because of the specific vehicle configuration under consideration, the design procedure could utilize two-dimensional inviscid flow analyses with corrections for boundary-layer displacement effects. Despite the shortcomings of the analytical methods for predicting details of the internal flow, the results show that this procedure was sufficient to design contours that provided high-pressure recovery in the core flow.

INTRODUCTION

The aerodynamic performance of the air-induction system is an important factor in establishing the viability of a hypersonic vehicle design. Since inlet performance is primarily a function of the internal contour design, the development and assessment of analytical techniques for the design of internal contours are items of primary concern, and they must be based on results of wind tunnel tests of scale models of representative hypersonic inlets. Previous experimental investigations (ref. 1, e.g.) have been performed with scale models of entire vehicle configurations, and because of the very small internal flow passages, measurements of the internal flow field properties were very difficult, or impossible, to obtain. Consequently, improvements in the methods used for designing and analyzing hypersonic air-induction systems depend in large measure on the development of techniques for testing relatively large-scale inlet models.

For this investigation a method was devised for testing a large-scale inlet model of one of the engine modules used with the hypersonic vehicle configuration shown in figure 1. This air-breathing vehicle, intended for flight at Mach numbers up to about 12, has a conical compression surface that forms the forebody and delivers air to the engine modules located circumferentially about the fuselage. Since the fuselage maximum diameter is large relative to the engine module height, the flow at the inlet entrance and within the internal passage is nearly two-dimensional. Thus, when the proper two-dimensional entrance flow is provided only the internal contours of the inlet need to be modeled. For this investigation, a wedge was used to provide an entrance Mach number of about 6.0, which corresponds to that on the vehicle for flight at $M \approx 12$. An approximately 1/3-scale, two-dimensional model (fig. 2) of the internal contours was used that provided throat heights of 2 to 6 cm.

The objective of the investigation was to obtain experimental and analytical results that can be used to improve the current methodology for designing the internal contours for hypersonic inlets. Both the analytical and empirical techniques used to design the internal contours are evaluated by comparing predictions for the flow field and boundary-layer properties, including shock-wave patterns, boundary-layer development, and overall performance, with the properties obtained experimentally. Only the most significant results are reported herein; complete results of the investigation are reported in references 2 and 3.

VEHICLE AND FLIGHT CONSIDERATIONS

Configurations for hypersonic vehicles with air-breathing engines vary with mission requirements. In particular, the amount of compression required of the inlet system depends on whether the mission is for cruise, such as with a manned vehicle, or for acceleration, such as with a missile. A possible configuration for a high-wing hypersonic vehicle, intended to cruise at Mach numbers of about 10 to 12, is presented in figure 1, which indicates the relationship of the inlets and engine modules to the aerodynamic surfaces of the vehicle. The vehicle design is discussed in detail in reference 1. A limitation imposed by vehicle considerations is that the length of the engine modules should be less than 15 percent of the length of the vehicle forebody, as shown. The inlet internal surfaces are part of the retractable engine modules located at the aft end of the vehicle forebody. Because of the large vehicle diameter, the modules have nearly rectangular cross sections, and the flow approaching the inlet entrance is approximately two-dimensional. Considerations of the bow shock strength, the internal volumetric efficiency, and the need for regeneratively cooled surfaces govern the geometric characteristics of the vehicle forebody. For cruise conditions, these considerations dictated that the blunted conical forebody should have an initial half-angle of 7°, followed by a compression surface providing 12° of isentropic turning, thus giving a final forebody angle of 19° at the cowl lip or inlet-entrance station.

Certain features of the vehicle, which must be carried over into the inlet model design, are determined by the flight conditions. Aerodynamic heating dictates that the cowl leading edge be blunt. Also, since the internal surfaces are regeneratively cooled, the ratio of wall temperature to free stream stagnation temperature must be low. Since boundary-layer bleed is considered impractical, the boundary-layer thickness – both at the inlet-entrance station and within the inlet – will be a significant portion of the internal passage.

The internal compression ratio (i.e., the ratio of the static pressure at the throat to that at the inlet entrance) provided by the inlet for the configuration considered herein depends on the mission requirements. For example, the internal compression required for a mission that consists primarily of high-altitude cruise is higher than that for a mission that consists completely of acceleration at low altitude. For this investigation, internal compression ratios representative of acceleration and cruise conditions were considered: these were 2 (acceleration), and 8 and 12 (cruise). Since the forebody provided an external compression ratio (ratio of static pressure at the inlet-entrance station to the free-stream static pressure) of about 30 for the flight conditions and engine locations considered, the overall compression from the free stream to the throat would range from 60 to 360. For cruise missions requiring high propulsive efficiency, considerations of vehicle thrust requirements indicate that the flow direction in the combustor section (in effect, the flow direction at the inlet throat) should be nearly parallel to the vehicle longitudinal axis. For accelerating missions not requiring high propulsive efficiency, this requirement for flow direction at the throat can be relaxed and the internal compression obtained with less internal turning.

MODEL DESIGN

Concept and Design Criteria

The model design (fig. 2) was based on hypersonic vehicle considerations and on wind tunnel testing requirements. A two-dimensional model of the internal flow passage of an inlet module was considered to be appropriate for simulating the internal flow in the vehicle. A wedge forebody was used to simulate the flow conditions at the inlet entrance. However, complete simulation of the entrance flow conditions could not be realized in the wind tunnel tests because of the high flight enthalpy. Thus, in this investigation, entrance conditions were approximated by matching the Mach number, and by providing an appropriately thick turbulent boundary layer, and about the same ratio of wall to total temperature. In general, the entrance Mach number will depend on the flight Mach number, vehicle angle of attack, and the circumferential location of the engine module. For the cruise conditions and for a module near the vertical plane of symmetry, the entrance Mach number was determined to be about 6.0. This Mach number could be obtained in the wind tunnel with a 7° effective wedge forebody in a free stream of Mach number 7.4. (There is no relationship between this 7° wedge and the 7° conical half angle of the vehicle forebody.)

Three sets of internal contours were designed for the model to provide the internal compression ratios of 2, 8, and 12 noted earlier, and the inlet models were designated accordingly as P2, P8 and P12. In addition, the following general criteria governed the inlet designs:

1. Each inlet should have the same high theoretical total-pressure recovery, which was accomplished through:
    a. A common surface contour in the region of the cowl leading edge (thereby maintaining the same cowl shock wave shape for each inlet)
    b. Cancellation of the reflected shock through surface turning at the point of impingement of the shock on the centerbody
    c. Internal surfaces that provide isentropic flow downstream of the cowl shock wave
2. For inlets P8 and P12, flow turning between the inlet entrance and throat region had to correspond with that required on the vehicle to make the flow direction nearly parallel with the vehicle longitudinal axis (a vehicle thrust requirement for cruise conditions). This criterion was not applied in the case of the low compression inlet P2.
3. The static pressure across the passage in the throat region should be approximately constant (a condition generally considered desirable at the combustor entrance).

Model Sizing

The primary consideration in sizing the model (fig. 2) was to obtain the maximum internal dimensions for the inlet that would permit the wind tunnel to start. A near optimum configuration, achieved with internal passage heights that were approximately 1/3 scale, was an overall model length of about 127 cm, a forebody length of 81.28 cm, an inlet height of 8.89 cm, and an internal passage width of 35.56 cm. Throat heights and locations are shown in figure 2. Note that the model internal angles and flow directions may be oriented with the vehicle frame of reference (fig. 2) by adding 12° to the model angles. For example, the flow directions at the inlet entrance relative to the X axis are 7° and 19° for the model and flight vehicle, respectively. A further consideration in sizing the model forebody and selecting the nominal test conditions, was that the centerbody boundary layer be turbulent at the inlet entrance and that the ratio of boundary-layer thickness to the height of the inlet opening should be between 0.1 and 0.2 to approximate that for the flight vehicle.

FLOW ANALYSIS AND CONTOUR DEVELOPMENT

Flow analyses were conducted during the model design phase (see Design Analysis section) to obtain surface contours, and after the test phase (see Final Analysis section) to obtain properties of the viscid and inviscid flows using more refined methods.

Design Analysis

Wedge forebody contour– The geometric contour of the wedge forebody (fig. 3) was obtained by subtracting the computed boundary-layer displacement thickness from the coordinates of the 7° effective wedge. The displacement thickness was calculated using the modified Reshotko–Tucker procedure, as described in reference 4, with the assumption that a turbulent boundary layer exists over the entire wedge forebody at the nominal test conditions ($M_\infty = 7.4$, $p_{t_\infty} = 4.14 \times 10^6$ N/m², $T_{t_\infty} = 811°$ K, and $T_W = 303°$ K). The effective and geometric contours from the leading edge ($X = 0$) to the inlet-entrance station ($X = 81.28$ cm) are shown in figure 3, and the geometric coordinates are given in table 1(a).

Cowl leading edge– Because the minimum practical leading-edge diameter for a Mach 12 cruise vehicle using regenerative cooling is approximately 0.318 cm (ref. 5), and since the model was approximately 1/3-scale, a leading-edge diameter of 0.114 cm was selected for the cowl. In addition to the cowl bluntness, another important design variable in the region of the cowl leading edge is the initial internal surface angle λ which is determined at the point of tangency of the internal surface and the blunt leading edge. Figures 4 and 5 show the variations in total-pressure recovery and the surface pressure distribution with the initial internal surface angle which were obtained from flow solutions using the method-of-characteristics. From the data in figures 4 and 5, an initial internal angle (λ) of 1.0° relative to the model axes was selected to provide a reasonable balance between the total-pressure recovery and the surface pressure. A high initial surface pressure reduces the gradients imposed on the boundary layer by the compression of the flow to the throat pressure, thus reducing the tendency of the boundary layer to separate.

Inviscid internal flow– The inviscid internal flow was analyzed using an inlet computer program (ref. 6) which is based on the method of characteristics and which incorporates results from a blunt-body solution (ref. 7) for the flow in the region of the cowl leading edge. Design of the effective internal contours required consideration of the flow in specific regions identified in figure 6. The flow field in each region depended upon the characteristics of the flow entering the region and the surface contour bounding the region. The P12 inlet had the highest compression ratio and presented the greatest design challenge. The procedure used for the design of this inlet is discussed in detail below and it is followed by a review of approaches applicable to the P8 and P2 inlets.

P12 inlet: The shock wave originating at the cowl leading edge intersects the effective wedge-forebody contour at X = 112.39 cm and defines the boundary between the forebody flow (region I) and the internal flow. (The shock wave originating at the forebody leading edge passes outside the cowl leading edge.) The effective cowl contour was designed with a surface angle of 1.0° to X = 87.00 cm for all inlets. A Mach wave from this station intersects the centerbody at X = 112.39 cm; therefore, any cowl surface turning downstream of X = 87.00 cm does not influence the cowl shock wave. The portion of region II upstream of the Mach wave was common to all inlets.

The cowl contour that bounds region II was considered first. Many solutions for the internal flow were analyzed before one was found that provided the design compression and flow turning within a minimum length over which the pressure gradient would not be large enough to separate the boundary layer. An inward flow turning angle of 15° was required to obtain the design compression ratio of 12 (p/p_∞ = 37.5) with a final flow direction nearly parallel to the vehicle axis. The criterion adopted for an unseparated boundary layer was that the wall shear remain positive for a laminar boundary layer solution (ref. 8). Thus, in region II the cowl contour was based on conservative considerations. The downstream boundary of region II is defined by the Mach wave originating at the point of intersection of the cowl shock on the centerbody. This Mach wave and its subsequent reflections form the boundaries for regions II, III, and IV as shown in figure 6.

The centerbody contour in region III was designed by considering the characteristics of the entering flow field from region II and the requirement for isentropic compression to the uniform static pressure and flow direction at the throat.

In a similar manner the cowl contour in region IV was designed, using the entering flow properties from region III, to maintain approximately the compression level reached at the end of region II, and to prevent shocks from forming in the flow. For this purpose, a slight outward turning of the cowl surface between X = 121.9 cm and 122.48 cm was required.

The predicted surface pressure distributions shown in figures 7 and 8 were obtained after many variations of the effective surface contours. In figure 7 the impingement of the cowl shock wave is indicated by the abrupt pressure rise at X = 112.39 cm. The centerbody surface pressure increases monotonically to the design compression ratio of 12 (p/p_∞ = 37.5) at about X = 126.7 cm, the throat station. Discontinuous N-shaped distributions, evident at X = 127 cm on the centerbody and at X = 121.9 cm on the cowl, indicate the impingement of very weak shock waves. These occur because the characteristics of the computer program, which require that reflected shock waves be present, prohibit the complete cancellation of the shock wave by surface turning. Consequently, the regions bounded by Mach waves in figure 6 are bounded by very weak shocks in the solution obtained by the computer program.

P8 inlet: Surface contours for the P8 inlet were derived by using the P12 inlet contours to the stations where the design compression ratio of 8 (p/p_∞ = 25) was obtained, X = 123.2 and 115.1 cm for the centerbody and cowl, respectively (figs. 7 and 8). The contours downstream of these stations were designed to provide uniform flow in the throat region and maintain the design pressure ratio.

P2 inlet: The design compression ratio of 2 (p/p_∞ = 6.25) is lower than the compression ratio provided by the forebody and cowl shocks. Therefore, the internal passage for the P2 inlet had to provide an expanding flow field, and the flow direction in the throat region is not the same as that for the P8 and P12 inlets. The contours were obtained by using the common cowl leading-edge section and designing the cowl and centerbody contours downstream of the Mach wave from cowl station X = 87.0 cm to provide a slight expansion of the flow field to the design compression ratio.

Boundary layer– Predictions of boundary-layer development in the internal flow passages were obtained from computer programs that used edge conditions of pressure and velocity from the method-of-characteristics solutions. Calculations of the centerbody boundary layer used the modified Reshotko-Tucker procedure described in reference 4 with the assumption that the boundary layer was turbulent from the leading edge.

The cowl boundary-layer development was computed with the method of Clutter and Smith (ref. 8), with the assumption that the boundary layer was laminar for the entire length of the cowl.

Geometric internal contours– In most regions, the geometric inlet contours were obtained by subtracting the boundary-layer displacement thickness predicted by the methods of references 4 and 8 from the effective inviscid contours. A special procedure was developed for the shock-wave cancellation region on the centerbody to account for the boundary-layer development across a shock-induced pressure rise.

The centerbody contours from the inlet-entrance station (X = 81.28 cm) to approximately X = 110.23 cm, where the cowl shock wave impinges upon the centerbody boundary layer, are extensions of the wedge-forebody contour and are identical for the three inlets. The procedure developed during the present investigation to design contours through shock-wave cancellation regions is illustrated in figure 9. Simple subtraction of the computed displacement thickness from the effective contour yields the basic contour line (labeled BCL) of figure 9(a) with a forward-facing step where the shock wave impinges upon the effective contour (X = 112.39 cm). Since a contour of this nature was unacceptable, the surface was modified as shown in figures 9(b) and 9(c).

To obtain the modified geometric contours in the interaction region a control volume analysis described by Kutschenreuter, et al., (ref. 9) was applied. From the analysis for the forebody, the flow-field and boundary-layer properties at station 1 (fig. 9(a)) were M_1 = 6.03, ϵ_1 = 7.00°, δ_1 = 1.275 cm, and $\delta_1{}^*$ = 0.719 cm. Calculations of the inviscid flow indicated that conditions at station 2 downstream of the shock wave (where the longitudinal location of station 2 is to be determined) were M_2 = 5.22 and ϵ_2 = 1.34°. The pressure ratio p_2/p_1 across the shock wave is 2.284. The control volume analysis indicates the following ratios of boundary-layer properties: $\delta_2/\delta_1 = 0.575$ and $\delta_2{}^*/\delta_1{}^* = 0.575$; therefore, $\delta_2 = 0.734$ cm and $\delta_2{}^* = 0.414$ cm. The interaction-region length over which the rise in surface pressure occurs was estimated to be equal to that given for flat plates by the correlations of Pinckney (ref. 10). In this case the interaction length was chosen to be $L_i \cong 2\delta_1 \cong 2.54$ cm. For each inlet, a straight line was constructed from the BCL line at X = 112.39 cm parallel to ϵ_2, as shown in figure 9(b). This line was terminated where it reached a vertical distance of 0.414 cm ($\delta_2{}^*$) from the effective contour downstream of the shock wave. The axial location of this termination point was defined as station 2. Station 3 was located 2.54 cm (L_i) upstream of station 2. A conic section was then faired between station 1 (X = 110.23 cm) and station 3. Another conic section was faired between station 2 and the downstream basic contour line as shown in figure 9(c). Since inlet P2 had an expanding flow field, station 2 could not be located with the above method used for inlets P8 and P12. Therefore, station 2 was defined as the throat station for inlet P2, and station 3 was located at the same position as for inlet P12.

The effective and geometric contours for the cowl and centerbody of the three inlets are shown in figure 10 and the geometric coordinates are given in table 1. Figure 10 shows that the displacement thickness corrections applied to the centerbody were significant whereas those for the cowl were minor. For example, for the centerbody of inlet P8 at X = 109.22 and 125.73 cm the corrections were 16 and 9 percent of the passage height, respectively. The corrections to the cowl contours at these same stations were 1 and 2 percent of the passage heights, respectively.

The centerbody boundary-layer characteristics for the three inlets were identical upstream of the shock wave impingement location, X = 112.39 cm. Displacement thickness was predicted to decrease significantly through the interaction region downstream of the shock impingement. At the throat station, displacement thickness decreased with increasing compression ratio.

Final Analysis

The final analysis after the tests were performed was an attempt to predict the experimental results better and to account for departures from the nominal experimental test conditions. Geometric model contours were used for the viscous analysis and predicted displacement thicknesses were added to these contours to form the effective contours for inviscid solutions. The final analysis accounted for (1) the nonuniformity of the free-stream flow field, (2) the viscous interaction at the leading edge of the forebody, (3) boundary-layer development with both laminar and turbulent regions on the forebody and cowl, and (4) streamwise variation of the entropy at the edge of the cowl boundary layer. In addition, a control volume method was used in an attempt to predict the experimental effects of the interaction of the cowl shock wave with the centerbody boundary layer.

A detailed description of the analysis of the forebody flow to the inlet entrance is presented in appendix A. The analysis of the internal flows from the entrance to the throat is discussed in detail in appendix B.

An attempt was made in the final analysis to improve the prediction of the shock-wave boundary-layer interaction on the centerbody by applying the control volume analysis described in reference 11. This analysis was modified to account for surface turning in the interaction region and a strong adverse pressure gradient downstream of the cowl shock wave impingement. (As shown in ref. 11 for conical impinging shock waves, the presence of a strong compression following the incident wave resulted in significant changes in boundary-layer properties in the interaction region.) Solutions for the inlet flow fields were attempted by means of an iterative procedure that coupled the interaction-region model with the method of characteristics for the external flow. Unfortunately, a completely self-consistent solution for the entire flow field was not realized. Although adequate predictions of the interaction-region length and the downstream boundary-layer properties were obtained, the surface pressure distribution was physically unrealistic. It appears doubtful that a control volume analysis is capable of predicting the detailed results of such a complex flow. Preliminary results (not included here) based on the "two-layer" method of Rose (ref. 12) indicate that such advanced methods may describe the flow characteristics. Because the interaction region analysis using the control volume method was unsuccessful, results of the final analysis are not presented for regions influenced by the interaction.

APPARATUS AND PROCEDURE

Wind-Tunnel Facility and Test Conditions

The experimental programs of the present investigation were conducted in the Ames 3.5-Foot Hypersonic Wind Tunnel. The facility, shown schematically in figure 11, is a blow-down tunnel with a run time of from 1 to 4 minutes at the nominal test conditions used in the investigation. For most tests, the conditions were:

Mach number	$M_\infty = 7.4$
Total pressure	$p_{t_\infty} = 4.14 \times 10^6$ N/m^2
Total temperature	$T_{t_\infty} = 811°$ K
Reynolds number	$Re_\infty = 8.86 \times 10^6$ m^{-1}

Several tests were conducted at total pressures as low as 1.38×10^6 N/m^2 to investigate the effects of Reynolds number on the internal flow-field development, and total pressures from 0.52×10^6 to 9.31×10^6 N/m^2 were used during a series of instrument calibration tests with flat plates to simulate inlet internal conditions. Acquisition of test data was accomplished through a 108-channel Beckman analog-to-digital system, and the data were recorded on magnetic tape and processed by an IBM 7094 digital computer.

Models

The inlet models are shown in figures 2 and 12; their most significant features are:

1. Wedge forebody, undercarriage, and sting support common to all internal passages
2. Remotely controlled rotating section having interchangeable internal passages
3. Glass inserts in side walls to permit schlieren observation of internal flows

For the typical wind-tunnel installation shown in figure 12, the wedge surface is alined at a nominal 6.5° angle to the flow. The wedge was constructed of solid aluminum 92.31 cm long, 45.72 wide, and approximately 2.5 cm thick. It was fitted with a water-cooled sharp leading-edge constructed of stainless steel. Because of the mass of the aluminum plate and the cooling near the leading edge, nearly isothermal wall conditions were maintained for the relatively short test runs.

The rotating internal passage section outlined in figure 2 is typical of the three interchangeable inlets used in the experimental investigation. Each internal passage comprised a centerbody block, a cowl block, and two side walls constructed of aluminum. The side walls were equipped with sharp stainless-steel leading edges. The cowl leading edges and the forward portion of the cowl blocks were water cooled; the combination of water cooling and the large masses of aluminum provided nearly isothermal wall conditions during the relatively short tunnel runs. Figure 2 gives the dimensions that were common to the internal passages for all three inlets: (1) the inlet entrance height above the wedge surface, 8.89 cm, and station, $X = 81.28$ cm; (2) the width of the internal passage, 35.56 cm; and (3) the diameter of the cowl leading edge, 0.114 cm.

The rotating internal passage section was remotely controlled and served several important functions. First, the contraction ratio of the inlet could be varied by rotating the inlet, thus ensuring starting of the internal passage. Second, it allowed the inlet cowl to close on the wedge so that the airflow was almost entirely diverted from the internal passage during the wind-tunnel starting process. Shielding of the internal passage from the tunnel flow was required to maintain uniformly low surface temperatures within the internal passage and prevent instrumentation damage during the tunnel start. Third, when the P8 and P12 internal passages were in the closed position, model blockage for the wind tunnel start was minimized. After stabilization of the tunnel flow, these internal passages were opened for data acquisition. For some tests, tunnel blockage problems made it necessary to start the tunnel with the P2 inlet in the open position. After data acquisition, the internal passages were closed prior to tunnel shutdown to again prevent instrumentation damage. In addition, the rotating section provided a sealed internal passage with fixed alignment of the surfaces, and eliminated the need for sliding side-wall seals.

Two flat-plate models with sharp leading edges were employed to test and calibrate surface and flow field instrumentation. Pertinent calibration results are presented in the next section.

Instrumentation

Free-stream parameters– The total pressure was sensed by a probe located within the settling chamber and measured by one of a series of transducers in the permanent tunnel installation. The pitot pressure was measured by a pitot tube located at the leading-edge station below the model. The Mach number was computed from the ratio of pitot pressure to total pressure, and also from the wind-tunnel calibrations using the total pressure and the heater temperature. The test section Mach number computed from pitot pressure varied between 7.35 and 7.45, whereas the tunnel calibrations yielded a value of 7.40 ±0.01 at the wedge-forebody tip location ($X = 0$). The total temperature was measured with a triply shielded thermocouple probe (Rosemount Engineering Model 103H) located below the leading edge of the model. Temperatures were also measured in the heater section of the wind tunnel. The shielded probe was considered a more accurate sensor of the total temperature within the test section, and the reference temperature for each data point was taken as the temperature measured by the shielded probe at the same time during the run.

Surface pressure and temperature– Surface pressures on the calibration plates, on the wedge forebody, and within the internal passages of the inlet models were sensed by 0.159 cm diameter orifices connected to Statham absolute strain-gage pressure transducers. The maximum response time for a measurement was determined during the calibration tests to be about 5 seconds. Surface temperatures were measured using thermocouple junctions of 30-gage chromel-alumel wire imbedded in the plate surfaces. Each junction was formed by passing the wires through a 0.102 cm diameter hole in the plate and by forcing a conical pin, constructed of the plate material and flattened on one side, into the hole in the plate surface until electrical continuity between the thermocouple wires was established. The excess pin material was then removed, the surface polished, and the wires cemented to the undersurface of the plate. The locations of the pressure orifices and thermocouples are given in table 2.

Surface heat-transfer rate– To obtain heat-transfer data within the P2 and P8 inlet models, heat-transfer gages (Hy-Cal models C-1170-A-05-060 (range 0–5.67×10^4 W/m^2) and C-1301-A-15-072 (range 0–17.02×10^4 W/m^2)) were installed at one cowl station in each internal passage. Calibration curves supplied by the manufacturer were used to obtain heat-transfer rates from the output voltages.

Wall shear stress– Wall shear stress measurements were made at the inlet-entrance station on the wedge forebody (X = 81.28 cm) using a Kistler model 322M102 skin-friction gage. The gage was calibrated before and after each series of runs, and the results were used in the data-reduction procedure to obtain wall shear stress.

Pitot-pressure probes– Pitot pressure measurements were obtained using 0.102 cm diameter stainless steel tubes. For the boundary layer surveys the tips were flattened to 0.051 cm height. Calibration tests showed that the time lag for pitot pressures was essentially zero and that the readings were unaffected by flow inclination through a range of angles of attack of at least 12°. Readings were obtained using Statham absolute strain-gage pressure transducers.

Total-temperature probes– The design for an aspirating total-temperature probe with a single shield and two vent holes is shown in figure 13(a). This particular assembly combined the total-temperature probe with a pitot-pressure probe. The temperature sensing element was comprised of a chromel-alumel thermocouple with magnesium-oxide insulation. The shield was formed of gold-plated stainless-steel tubing. Calibration data for the singly shielded probe are presented in figure 14(a) in terms of the probe recovery-factor variation with the parameter $p_p/(T_t)^{7/4}$. This parameter was derived by Winkler (ref. 13) and relates the local heat-transfer coefficient at the probe tip and the thermal resistance of the wire. As shown in figure 14(a), this type of probe required rather large corrections for a portion of the range of the parameter $p_p/(T_t)^{7/4}$ obtained during the inlet model tests. This undesirable characteristic, together with the requirement for an individual calibration of each probe, provided the impetus for the development of a more versatile total-temperature probe.

The design of an exposed thermocouple probe used in the present investigation is shown in figure 13(b). Support for the exposed thermocouple element was provided by two 0.102-cm diameter stainless-steel tubes, held by a plate brazed to a vertical wedge-shaped strut. The chromel-alumel thermocouple junction was formed by passing one wire through each tube, removing the insulation from the ends of the wires, inserting a ceramic insulator over each wire, and spot-welding the junction at the midpoint between the tips of the support tubes. Thermocouple wires with diameters of 0.014 cm were used in the inlet test program. The exposed thermocouple probes responded rapidly to temperature changes and could be assembled and repaired much more easily than the shielded probes. Figure 14(b) indicates the recovery factors that were obtained in the calibration of several probes. A constant value of recovery factor of 0.95 was used in the data reduction. The probes from the first design (not shown) and final design (fig. 13(b)) differed only in the support structure and not in the tips.

Static-pressure probes– Two types of static-pressure probes were used for flow field surveys. A small-diameter (0.051 cm), direct-reading probe with measuring orifices located on the probe shaft is shown in figure 15(a). This probe senses the stream pressure directly and requires a single pressure transducer since all orifices are interconnected. Calibration tests revealed a response time of approximately 10 seconds. The second static-pressure probe design (fig. 15(b)), was comprised of a 0.238-cm diameter shaft with a 30°-conical tip (included angle). Two pressures are sensed with this probe, allowing measurements of stream angle as well as static pressure when the appropriate calibrations are employed. The techniques presented in reference 14 were used during probe calibration tests and for reduction of measured data during inlet model tests. The response time of this probe was about 5 seconds.

Procedure

Vertical surveys of pitot pressure, static pressure, and total temperature were made (1) at several lateral locations across the inlet-entrance station, (2) at many longitudinal stations along the internal passages for P2 and P8 inlet models, and (3) at several lateral locations across the throat stations for all inlet models. Individual probes as well as rakes comprising several probes were used in the surveys.

Inlet-entrance flow-field surveys– At the inlet-entrance station, X = 81.28 cm, flow-field data were obtained at the nine lateral locations shown in figure 16. The survey data were acquired with only the wedge forebody part of the model (fig. 2) installed in the tunnel. Two rakes, one with pitot-pressure and total-temperature probes, and the other with static-pressure probes, were installed separately using sliding supports that were manually set and locked into position for each run. Singly shielded total-temperature probes (fig. 13(a)) were used in this part of the experimental investigation since exposed thermocouple probes were not developed until after the inlet-entrance flow-field tests. Static-pressure measurements were made with the small diameter, direct-reading probes (fig. 15(a)). The data were recorded once each second for 20 seconds.

Internal-passage surveys– Profiles of flow properties at desired X stations in the inlets were obtained with probe assemblies (fig. 13(b) is typical) traversed vertically during a run. The probe assemblies projected from interchangeable inserts, which maintained the cowl contours in the vicinity of the probes. A single probe assembly with an exposed thermocouple probe and a flattened pitot probe was employed with the P8 inlet. For the P2 inlet, two attached assemblies with a fixed vertical spacing between probes were traversed across the passage. The conical probe of figure 15(b) was used in inlets P2 and P8 to measure static pressure in the flow. An automatic probe-drive mechanism with 25 preset stop locations was used to advance the probe assemblies to make flow measurements at about 0.064-cm intervals. Six measurements were taken at each position to ensure that equilibrium conditions had been reached. Data were obtained at from 6 to 13 height positions per run; thus 3 to 9 tunnel runs were required at each X station to make a complete survey from the surface of the centerbody to the cowl. A slight mismatch of the pitot pressures at the junction of a few profile segments was observed in the data.

Surface properties at the survey stations were also measured during each run for use in data reduction. Both cowl and centerbody surface pressures were recorded when the probe assembly was at its maximum distance from the respective surface. Surface temperatures were recorded when the probe was at its minimum distance from the surface. This procedure minimized the effects of probe interference on surface pressure readings and it simultaneously afforded the best possible matching of surface and probe-measured temperature data.

Inlet-throat flow-field surveys– Two sets of fixed rakes, one with pitot-pressure and shielded total-temperature probes (fig. 13(a)), and the other with direct-reading static-pressure probes (shown mounted in the inlet throat in fig. 17) were used to obtain flow-field data for all inlets at the lateral stations given in figure 16. As with the entrance-station surveys, the rakes were manually set and locked into position for each run. Throat-station profile data were also obtained using traversing probes for the P2 and P8 inlet models.

Experimental error– Estimated maximum uncertainties in the measurements of the investigation are:

Measurement	Maximum uncertainty
p_{t_∞}	±0.3 percent
T_{t_∞}	±2.0 percent
T_w	±1.0 percent
$\dot{q}_w$	±3 percent
τ_w	±3 percent
p_p	±2 percent
T_t	±3 percent
p	±3 percent
Y'	±0.01 cm
α	±0.2°
ϵ	±0.5°

To ensure the accuracy of pressure measurements, the transducers were calibrated periodically in the range of the measurements. In addition to the possible instrument errors there were several tunnel entries and some variations in tunnel stagnation conditions. Variations that were significant are discussed in the section on results.

Data reduction– All data of this report are presented in the form of pressure and temperature ratios using free-stream total pressure, total temperature, and static pressure as normalizing quantities. Whereas free-stream total temperature, pitot pressure and total pressure were measured, free-stream static pressure was calculated from pitot and total pressures assuming isentropic flow and using real gas corrections based on the total temperature as given in reference 15.

For the model flow field, Mach numbers were calculated from the ratio of pitot pressure to surface pressure, or to flow field static pressure where it was available. Interpolated values of static pressure were used when measurements were not taken at the exact heights of the pitot-pressure data. Total-pressure recovery was computed from the Mach number and static pressure using the ideal-gas equations and the corrections for real gas effects given in reference 15. Corrected total temperatures were obtained from the measurements by applying the calibrations of figure 14. Density and velocity were calculated from Mach number and corrected total temperature using ideal-gas equations. Displacement thickness, momentum thickness, and mass flow were obtained by integrating the profile data from the surface to the selected boundary-layer edge.

Boundary-layer thicknesses were determined from the data in the following ways. The forebody boundary-layer thickness at the inlet-entrance station was determined from pitot pressure profiles. A straight line was drawn through the data in the region of varying pitot pressure near the edge of the boundary layer. A second straight line was drawn through the data in the inviscid region where pitot pressure was constant. The point of intersection of these two lines was defined as the boundary-layer edge.

For the flow fields in the internal passages, the edges of the boundary layers were selected from total-temperature profiles. Generally the height at which a maximum total temperature was reached was defined as δ. For profiles in which an overshoot in temperature was present a height just outside of the overshoot was chosen as δ.

RESULTS AND DISCUSSION

Experimental results are presented to show surface pressure and temperature distributions, and flow-field properties at many stations from the inlet entrance to the throat of the inlet models. Comparisons are made with results obtained from both the design and final analyses. While results of the design analysis are presented for the complete inlets, results of the final analysis are shown only for the portions of the flow field which were unaffected by the shock-wave boundary-layer interactions (regions I and II of fig. 6). Predicted profiles of flow-field properties are terminated at the edges of the boundary layers. In addition, internal inlet performance (expressed in terms of total-pressure recovery) obtained from the analyses is compared with the experimental performance calculated from the measured flow properties at the inlet entrance and the throat.

Forebody Flow

Surface properties— Predicted and measured distributions of surface pressure along the centerline of the wedge forebody are compared in figure 18(a). Results from the design analysis indicate a constant surface pressure. The final analysis indicates that viscous interaction effects are present both near the leading edge and near the center of the forebody where the turbulent boundary-layer growth is initially rapid. Experimental evidence for the occurrence of a viscous interaction near the leading edge is shown by the initially high surface pressure and by the shock-wave curvature observed in schlieren photographs (not shown). The experimental pressure distribution exhibits a slight increase between $X = 35$ and 46 cm where boundary-layer transition is occurring. Further evidence for this transition location is presented later.

Both the lateral distributions of surface pressure for the wedge forebody (fig. 18(b)) and the oil-flow pattern (fig. 19) for a flat plate model of approximately the same size and configuration as the forebody indicate the presence of symmetrical outflow toward the edges. In figure 19 the pertinent stations of the wedge forebody have been superimposed upon the flat plate model. For the flat plate model, surface flow angles at the lateral station of the inlet side walls ($Z = \pm 17.78$ cm) are about 7° at the inlet-entrance station ($X = 81.28$ cm), and about 6° at the side-wall and centerbody intersection ($X = 93.98$ cm). It is believed that similar flow angles are present at the surface of the wedge forebody since the configurations are similar. This outflow near the forebody surface is thought to be partially responsible for the corner effects in the inlets, which are discussed later.

Typical surface temperature data obtained near the centerline of the wedge forebody are shown in figure 20. The leading edge section and the plate to about $X = 25$ cm were water cooled, and the influence of the cooling is shown in the temperature distribution. The experimental distribution reaches the design level ($T_W = 303°$ K) near the inlet-entrance station ($X = 81.28$ cm), and at this station it did not vary laterally.

Profiles at the inlet-entrance station– Centerline profiles of pitot pressure at $X = 81.28$ cm are shown in figure 21. The measured pitot pressures increase with normal distance within the boundary layer to about $Y' = 5.3$ cm, decrease gradually between this height and the wedge-forebody shock wave, and then decrease discontinuously to the free-stream value above the shock wave. Both the data and the final analysis show that the flow is expanding normal to the surface between about $Y' = 5.3$ cm and the shock wave. Since there is qualitative agreement between the experimental results and the results obtained from the final analysis, it appears that effects of the viscid/inviscid interaction at the leading edge, and of the nonuniform tunnel flow are reasonably well accounted for in the analysis. The lack of precise agreement between the predicted and measured pitot pressures in the region between the boundary-layer edge and about $Y' = 5.3$ cm may be due to a strong viscous interaction in the immediate vicinity of the leading edge. However, no strong interaction calculations were performed during the present investigation.

The measured local static pressures and the corresponding analytical predictions for the centerline of the wedge forebody are also shown in figure 21. These pressures were obtained only between the boundary layer and the shock wave. The measured values are higher than both the surface value and the predictions over the entire flow field. An expanding flow field over the region between $Y' = 5.3$ cm and the shock wave is again evident. While the shape of the measured static-pressure distribution is in qualitative agreement with that for the final analysis, the level appears to be too high. The high levels may have been caused by viscous-interaction and boundary-layer effects on the probes. The measured static pressures were corrected by a factor that would make the measured values nearest the surface agree with the surface value. This method yielded a correction factor of 0.92. The resulting static-pressure distribution is shown by the square symbols.

Mach number distributions are compared to analytical predictions in figure 22. The design analysis predicts a Mach number of 6.03 over the entire flow field, whereas the final analysis predicts a variation in Mach number from 5.95 at the edge of the boundary layer to 6.11 at $Y' = 8.89$ cm (cowl leading-edge height). Both predicted distributions exceed the experimental distributions, and the best agreement is with the corrected experimental results.

Distributions of total-pressure recovery calculated from the Mach number distributions are also shown in figure 22. The final analysis indicates a substantial recovery loss relative to the design level just outside of the boundary layer and a slight decrease over the entire flow field. The experimental recovery levels obtained using both surface and local static pressures fall well below the results for both analyses. Also shown in figure 22 are estimates of the maximum variation of each flow property computed by combining the maximum error given in the instrumentation section for each measured quantity. The results of the final analysis generally fall within these error bands for the centerline data at the inlet-entrance station.

As a further comparison between experiment and analysis, the computed and experimentally observed locations of the forebody shock wave are shown in figure 23. The location of the experimental shock wave is quite well predicted by the final analysis.

Envelopes of the experimental flow field properties for all lateral stations are shown in figure 24. The centerline distributions are given by the solid lines, while the dashed lines bracket both the scatter and the trends of the data in the central region between $Z = -8.10$ and 6.25 cm. The pitot pressure variation for the central region is small (fig. 24(a)) with the largest changes occurring near the edge of the boundary layer. Although not shown in the figure, the trend of decreasing pitot pressure with increasing lateral distance from the centerline is symmetric about $Z = 0$. The envelopes of static-pressure distributions include corrections to account for differences between wall and free-stream pressures as previously described for the centerline profile. The envelopes of Mach number and total-pressure recovery for Z between -8.10 and $+6.25$ cm, shown in figure 24(b), are about the same as the error bands shown in figure 22.

Total-pressure recovery at the inlet entrance station is used later as a reference for evaluation of the internal performance. For this purpose, the recovery in the central region ($Z = -8.10$ to $+6.25$ cm) of the inlet-entrance station is taken to be 0.8. This value is based on the results of figure 22 and was obtained by averaging the predicted and experimental recoveries. To arrive at this average, it was assumed that the values 0.85 and 0.75 represent the predicted and experimental recoveries, respectively. It was also considered that for the experimental recovery, the centerline data (fig. 24(b)) are representative of the results in the central region.

Boundary layer– As noted previously, it was required that the boundary layer be turbulent on the wedge forebody at the entrance station. From the data of reference 16 it was determined that transition should occur ahead of $X = 64$ cm. It was confirmed in this investigation by means of a fluorine sublimation technique that the end of transition occurred at about $X = 35$ cm. As shown in figure 25, this location is in fair agreement with other unpublished results.[1]

The turbulent nature of the boundary layer at the entrance station was verified by shear-stress data, obtained by a skin-friction gage, and by velocity profiles. The shear stress obtained

---

[1] Private communication with Mr. Thomas Polek of Ames Research Center, April 1970.

from the gage measurement was τ_W = 63.7 N/m^2; a value 20 percent lower than that calculated by means of turbulent boundary-layer theory of Sasman and Cresci (ref. 17). The dimensionless velocity profile near the centerline is shown in figure 26, together with the envelope for the profiles at the other lateral stations, and the profiles predicted by the design and final analyses. The experimental profiles indicate fully developed turbulent flow, and the profile obtained by the final analysis is in better agreement with the data than that obtained from the design analysis.

The boundary-layer integral properties at the inlet entrance are shown in figure 27. The final analytical predictions are in good agreement with the centerline values of boundary-layer thickness and displacement thickness, since the experimental displacement thickness was purposely matched in the final analysis (appendix A). The agreement is not as good for momentum thickness. This lack of agreement may be a result of experimental inaccuracies in computing momentum thickness from relatively few profile points, the use of the turbulent skin-friction relations of references 4 and 12, and the assumed discontinuous process for boundary-layer transition.

Internal Passage Flow Fields

Cowl shock location– The cowl shock-wave location near the leading edge was determined from a schlieren photograph, since no survey data were obtained in this region. Both the experimental and analytical locations shown in figure 28 apply to all inlets. The experimental shock wave is located closer to the cowl surface than predicted by either the design or final analysis, and the shock-wave location from the final analysis is in somewhat better agreement with the experimental results. From these shock location results, it appears that the Mach number at the cowl leading edge may be higher than that used in either analysis. Thus, it is concluded that the local Mach number at the inlet entrance station may be higher than that indicated by the experimental results (fig. 22).

Shock-wave patterns, surface properties, and flow profiles– Representative data have been selected to show (1) shock-wave patterns, (2) distributions of surface pressure and temperature, and (3) profiles of pitot pressure, static pressure, total temperature, Mach number and total-pressure recovery in the internal passages of the inlets. With inlets P2 and P8, data were obtained from probe surveys at the longitudinal stations shown in figures 29 and 30. Data were taken at each station for the region indicated by the bar. With the P12 inlet, data were taken only at the throat station.

P2 inlet model: The shock-wave pattern and boundary layers can be observed in the schlieren photograph of figure 31, and in the profiles of figures 32 and 33, which summarize the pitot-pressure and total-temperature surveys, respectively, by showing the profiles superimposed upon the inlet contours. The shock-wave pattern (fig. 31) consists of an impinging cowl shock wave and a reflected shock wave. The impinging shock wave lies between the locations predicted by the design and final analysis. The reflected shock wave was not predicted by either analysis. After crossing the internal passage, the impinging wave enters the boundary layer on the centerbody at about X = 109 cm. (In fig. 32 the shock-wave location at a particular station must be determined by projecting the discontinuity in pressure associated with the shock wave to the vertical axis for that station. Note also that the shock waves do not affect the temperature measurements (fig. 33).) Within the interaction region where the shock wave is immersed in the boundary layer, neither the impinging wave nor the edge of the boundary layer is clearly defined in the pitot profiles (fig. 32). In the schlieren photograph (fig. 31), however, the impinging wave is well defined as it penetrates far into the boundary layer with only slight curvature. The reflected shock wave cannot be clearly located in the pitot profiles or the schlieren photograph until it emerges from the boundary layer at about the throat station, $X = 119.38$ cm, where the reflected shock wave can be seen in both sets of data. Thus, the reflected shock wave was not canceled by surface turning, and one of the design criteria was not satisfied.

From observations of the schlieren photograph and the pitot-pressure profiles, it appears that the length of the shock-wave boundary-layer interaction (defined here as the distance between the stations where the impinging wave enters, and the reflected wave leaves the boundary layer) is approximately 10.2 cm. Note that this definition of the experimental interaction length differs from the interaction-region length L_i, defined for use in the design analysis; L_i will generally be shorter except for separated interactions.

The boundary-layer region on the centerbody and the apparent boundary-layer region on the cowl are also evident in the data. For the centerbody the viscous region of variable total temperature (fig. 33) is in general agreement with the boundary layer region indicated by the schlieren photograph (fig. 31) and the pitot pressure profile (fig. 32). For the cowl, however, the viscous region of variable total temperature is considerably thinner than the apparent boundary-layer thickness indicated by the schlieren photograph and the pitot-pressure data. In the latter case, density gradients associated with the cowl boundary layer and the leading edge entropy layer are indicated by the schlieren photograph and pitot profiles.

The measured surface pressures on the centerbody and cowl are compared to predictions in figure 31. For the centerbody the pressure decrease between $X = 110.2$ and 113.0 cm is a result of surface turning which generates an expanding flow field. The pressure rise beginning at $X = 113.0$ cm is associated with the shock-wave boundary-layer interaction. In this interaction region, the continuous experimental pressure rise to nearly the design level at the throat station is unlike the prediction of a discontinuous pressure rise followed by a pressure decrease. A similar continuous pressure rise was observed by Seebaugh and Childs (ref. 11) for the interaction of a conical shock wave with a turbulent boundary layer when the overall pressure increase was insufficient to cause separation within the interaction region. For the centerbody, the final prediction is terminated at the intersection of the impinging shock wave and the edge of the boundary layer, since the analysis does not account for the effects of the shock-wave boundary-layer interaction. For the cowl surface and for the centerbody surface upstream of the interaction region, the predicted results are generally in good agreement with the measured pressure distributions.

The lateral distributions of surface pressure at the throat station are shown in figure 34. Both distributions are nearly constant in the regions critical to the internal flow-field surveys between $Z = -7.62$ and $+7.62$ cm; however, there is some evidence of corner effects farther out particularly for the centerbody surface. The lateral position of the flow field surveys, $Z = -5.32$ cm, is within this region of essentially constant pressure. Oil-flow patterns obtained on the centerbody surface confirmed that the corner effects were confined to regions near the side walls.

Typical surface temperature distributions for the internal passage are shown in figure 35. Unflagged symbols indicate the distribution at the beginning of a data sequence, and flagged symbols give the final temperatures after a run time of 20 seconds. The cowl surface temperature was maintained nearly uniform and constant by the water cooling. For the centerbody, which was uncooled, the temperature level was somewhat higher, and a small temperature increase occurred during the run. The entire range of surface temperatures shown is not large enough to significantly affect flow calculations based on a constant surface temperature of 303° K. Lateral variations in surface temperature were found to be negligible.

In figure 36 the experimental distributions of pitot pressure and total temperature, from which the summaries of figures 32 and 33 were constructed, are shown. These detailed distributions indicate features of the flow at the ten survey stations. In figures 36(a), (b), (c), and (d) the location of the impinging shock wave is clearly identified by the abrupt increase in pitot pressure. As the shock wave penetrates the centerbody boundary layer, just downstream of $X = 109.22$ cm, the wave location becomes more difficult to identify. Where abrupt pressure rises are not evident in the boundary-layer region, the wave location can be identified from changes in slope or small discontinuities in the profiles (figs. 36(e) to 36(i)). At the throat station (fig. 36(j)), the abrupt change in pitot pressure at about $Y' = 1.0$ cm indicates a location of the reflected wave consistent with that observed in the schlieren photograph of figure 31. Also, at this station, but for Y' between 1.0 and 2.5 cm, the low pitot pressures define an expansion region upstream of the reflected wave.

Additional data obtained at the centerline of the throat station with a fixed rake during a different tunnel entry are shown by the triangle symbols. The centerline data are in good agreement with results from the traversing probe except for the two points near $Y' = 1.2$ cm. A slight change in shock-wave location between tunnel entries is indicated.

The pitot-pressure distributions also indicate a rather thick region of variable flow properties near the cowl surface. As noted previously this region consists of a boundary layer and an entropy layer produced by the blunt leading edge of the cowl. In this region, the edge of the boundary layer could not be distinguished in the pitot-pressure profiles. Therefore, temperature data were used to determine the boundary-layer thickness. The total-temperature distributions of figure 36 were used to select the boundary-layer edges shown on the pitot-pressure profiles. Uncorrected total temperatures are shown because in most of the inviscid flow regions the Mach number is unknown; thus, the corrections from indicated to true temperature through the recovery factor cannot be made. However, in places where the Mach number could be determined, the correction increased the temperature ratio (T_t/T_{t_∞}) to about 1.0. (Corrected temperatures for the boundary-layer regions are presented in the boundary layer discussion.)

Analytical predictions are compared to experimental data in figures 36(b), (i), and (j), corresponding to $X = 101.60$, 116.85, and 119.38 cm, respectively. At $X = 101.6$ cm, the measured pitot pressures are lower than the design predictions over nearly the entire height of the internal passage, and the experimental shock wave is closer to the cowl. The final analysis shows somewhat better agreement with the experimental results. The design pitot-pressure distribution at $X = 116.84$ cm is nearly uniform over the lower half of the internal passage and exceeds the measured level. The final prediction is in qualitative agreement with experiment over the upper half of the passage; however, the predicted pitot-pressure level near $Y' = 2.54$ cm remains slightly higher than that obtained experimentally. At the throat, $X = 119.38$ cm, the design analysis predicts a flow field with no reflected wave, whereas an expansion and a reflected shock wave between $Y' = 1.0$ and 2.5 cm are delineated by the experimental distribution. The pitot pressure level predicted by the design analysis is again higher than the measured level across the central region at the throat station. The final predictions are generally in better agreement with experiment for Y' greater than approximately 2.54 cm.

Local static pressures and flow angles in the flow field are presented in figure 37. The expansion region immediately upstream of the reflected shock wave (noted previously in the discussion of the pitot profiles) is evident in the local static pressures and flow angles obtained from experimental data: the upper boundary of this region appears to be about $Y' = 2.0, 2.5$, and 3.0 cm at $X = 113.03$, 116.84, and 119.38 cm, respectively. While most of the static-pressure data were obtained with the conical probe, some static pressures acquired during a different tunnel entry, were also obtained at the throat station with the direct-reading probe (fig. 37(d)). It is evident that the pressures obtained by the two methods do not agree, but it is not apparent that one should be considered more correct than the other. For probe heights near the edge of the boundary layer, the reading of either probe could be affected by the proximity of the reflected shock. Part of the difference may also be attributed to lateral variations in the flow-field properties and to slight variations in flow conditions that might have existed during the different tunnel entries. Assessment of the results obtained with the conical probe can best be made by comparing the experimental and analytical results presented in figures 37(a) to (c). While any assessment is made difficult by the disagreement between the design and final predictions, it appears that the cone probe does a better job in measuring stream angle than static pressure since the stream-angle gradients appear to have the correct trends in the expansion region. Note however, that the measured angles in the central portion of the passage exceed those obtained in the final analysis by as much as 1°.

Mach number distributions at $X = 101.16$, 116.84, and 119.38 cm are shown in figure 38. Only one experimental distribution, computed using the surface pressure, is shown in figure 38(a) since no local static pressures were obtained at this station. The experimental and predicted Mach number distributions are nearly uniform in the inviscid flow regions above and below the shock wave, and the agreement between both predictions and experiment is good. At $X = 116.84$ and 119.38 cm the experimental and analytical results are also in good agreement for the inviscid flow regions above $Y' = 2.0$ and 3.0 cm, respectively. In the expansion region above the shock wave (between about $Y' = 0.9$ to 1.8 cm for $X = 116.84$ cm, and 1.0 to 3.0 cm for $X = 119.38$ cm) the Mach numbers calculated from the two static probes are different; each profile indicates a different trend and none of the Mach numbers in these regions is believed to be correct.

Distributions of total-pressure recovery corresponding to the Mach number distributions discussed above are presented in figure 39. At $X = 101.6$ (fig. 39(a)) the shape of the experimental profile obtained using the surface pressure is in general agreement with the predicted shapes in the region between the shock wave and cowl. The difference between the final analysis and experiment near the centerbody is similar in magnitude to that observed at the inlet-entrance station (fig. 22).

At $X = 116.84$ cm (fig. 39(b)) considerable scatter in the two experimental distributions is evident. Recoveries obtained with data from the conical probe at $Y' = 1.07$ and 1.35 cm have been omitted because the computed values were greater than 1.0. The recoveries shown for the conical probe are considered unreliable because of the uncertainties in the static pressure, but they illustrate the extreme sensitivity of total-pressure recovery to the static pressure. Consequently, the recovery obtained using the surface pressure must be considered the most reliable, but it is generally lower than would be expected from theoretical considerations. The recovery using surface pressure is not presented in the expansion region between the edge of the centerbody boundary layer and $Y' = 2.0$ cm. From the results obtained with the conical probe its usefulness appears limited to the detection of flow angularity and the presence of gradients in the flow.

At the throat station (fig. 39(c)) the experimental results obtained with the direct-reading probe, on centerline, are in general agreement with the levels obtained from the traversing probes, off centerline, using the surface pressure. The predicted recovery levels are lower than the experimental results above $Y' \simeq 4.0$ cm and exceed them below this height. Experimental results are not presented in the expansion region above the edge of the centerbody boundary layer. Because experimental recoveries at $Y' = 1.73$ and 2.49 cm exceeded 1.0 when local static pressure was used, the static-pressure measurements in this region (fig. 37(d)) are considered too low.

A complete tabulation of the traversing probe data, including pitot pressure, total temperature, static pressure, Mach number and velocity, is given in reference 18.

P8 inlet: The shock-wave pattern in the internal passage of the P8 inlet can be seen in the schlieren photograph of figure 40 and in the pitot-pressure profiles summarized in figure 41. This pattern differs somewhat from that observed in the P2 inlet. Although the impinging cowl shock wave, which enters the centerbody boundary layer at about $X = 109$ cm, is the same as that for the P2 inlet, the complex reflected shock-wave system (waves A and B) is unlike the single reflected wave observed in the P2 inlet. In addition, with the P8 inlet there is an interaction between the reflected wave system and the cowl boundary layer at about $X = 124$ cm followed by another reflected wave (C).

The most upstream reflected wave (A) exists only near the side walls. This was concluded after examination of the probe survey data, which did not indicate a wave near the centerline at the location shown in the schlieren photograph. In addition, surface oil flow patterns (not presented) showed that the shock reflection line on the surface was farther upstream near the side walls than in the central region of the passage. Near the side walls, the patterns showed the extent of the corner effects and the presence of a weak shock wave that propagated from the intersection of the leading edge of the side walls and the centerbody.

Shock wave B exists in the central portion of the passage and was detected by the probe survey (fig. 41). The presence of this reflected wave indicates that the design criterion of shock-wave cancellation by surface turning was also not satisfied for the P8 inlet. In the schlieren photograph (fig. 40) wave B initially consists of two shock waves near the centerbody that coalesce into a single wave as the shock propagates toward the cowl. Dual-shock, reflected wave patterns have previously been observed for the interactions of shock waves with turbulent boundary layers on flat plates and compression surfaces (refs. 5 and 19).

The shock-wave pattern, excluding wave A, can be seen in the pitot-pressure surveys (fig. 41) except in the regions of shock-wave boundary-layer interactions where the shock wave is immersed in the boundary layer. In these regions, discontinuities associated with a shock are obscured by the local gradients in the boundary layer. At the throat station ($X = 125.73$ cm) the profile clearly shows the location of wave C. Consideration of the schlieren photograph and profiles shows that the length of the interaction region on the centerbody is about 7.6 cm, somewhat less than the 10.2 cm observed for the P2 inlet.

The measured surface pressures on the centerbody and cowl are compared with predictions in figure 40. For the centerbody the measured pressures differ considerably from the results obtained by the design analysis. Upstream of $X = 109$ cm, the surface pressure is the same as that for the P2 inlet, and the predictions from the final analysis, not evident in figure 40 because of the pressure scale, are also the same. In the region of surface curvature ($110.2 < X < 112.1$ cm) the pressure decreases only slightly. Further downstream the pressure increases to exceed the predicted pressure at $X = 114.9$ cm, then it continues to increase and reaches a nearly constant value of about 90 percent of the design throat pressures between $X = 120.6$ and 125.7 cm. A comparison of figures 31 and 40 shows that the additional compression provided by the cowl curvature of the P8 inlet produces an overall pressure rise through the interaction region for this inlet that is higher than that for the P2 inlet. Consequently, the interaction has a larger upstream influence, and the surface pressure rise for inlet P8 begins about 1 cm upstream of that for inlet P2. A qualitatively similar increase in upstream influence with an increase in pressure rise across an interaction was observed by Seebaugh and Childs (ref. 11) for conical impinging shock waves and by Watson (ref. 19) for plane waves impinging upon flat plates and compression surfaces.

The experimental cowl pressures fall below the predictions obtained from both the design and final analyses upstream of approximately $X = 123.9$ cm, where the reflected shock wave impinges on the cowl surface. Downstream of this station, the experimental pressure jumps to a level exceeding the design value. On the basis of exploratory analytical techniques, not reported here, it is believed that the decrease in the experimental cowl pressure between $X = 119.4$ and 123.2 cm is due primarily to the effect of an expansion that is formed as the cowl shock wave enters the centerbody boundary layer near $X = 109$ cm, and secondarily to the effect of the expansion associated with the region of centerbody surface curvature that begins at $X = 110.2$ cm. The existence of an expansion region in the vicinity of a shock-wave boundary-layer interaction has been noted previously (refs. 12 and 19).

Lateral surface pressure distributions on the cowl and centerbody at the throat are presented in figure 42. Both distributions exhibit corner effects in the regions farthest from the passage centerline, but the position of the flow field surveys, $Z = -5.32$ cm, is within the region of nearly constant surface pressures. Oil-flow patterns (not shown) indicated that the flow near both surfaces was essentially parallel to the model centerline for $-7.6 < Z < +7.6$ cm between $X = 104.1$ cm and the throat, the region in which survey data were taken.

Surface temperatures measured in the internal passages are given in figure 43. At $X = 124.46$ cm, near the throat station, the cowl and centerbody surface temperatures increased by about 15 percent during the 20-second period. Smaller increases in temperature are evident upstream of the shock-wave reflection on the centerbody ($X < 115$ cm) and in the cooled region of the cowl. Lateral variations in surface temperature were small.

Results of the pitot-pressure and total-temperature surveys for the P8 inlet are presented in figure 44. Generally the character of the inviscid flow field is different than for the P2 inlet. Significant normal gradients in pitot pressure are shown in all of the profiles of figure 44; whereas small gradients were shown for the P2 inlet, except at the throat station. For the P8 inlet the gradients above the impinging shock wave (figs. 44(a) to (d)) result from cowl compression. Downstream of the shock-wave boundary-layer interaction (figs. 44(f) to (m)) the gradients are a result of the combined effects of cowl compression and the expansion region from the centerbody shock interaction.

The pitot-pressure profiles indicate a rather thick region of variable flow properties near the cowl similar to that noted for the P2 inlet. As for the P2 inlet, the boundary-layer edges could not be identified from pitot pressures because of the gradients introduced by the entropy layer generated by the blunt leading edge. Consequently, the temperature profiles of figure 44 were used to select the boundary-layer edges which are shown on the pitot profiles. Note that the entropy layer is still thicker than the boundary layer at the throat station (X = 125.73 cm).

Design analysis predictions of the pitot pressure are shown at X = 104.1, 116.84, 119.38, 124.46, and 125.73 cm. Predictions from the final analysis are shown only at X = 104.1 and 116.84 cm because the effects of the expansion from the centerbody shock interaction are felt at the next downstream station (X = 119.38 cm). The predicted pitot pressures are generally higher than the measured values. The differences between predicted and measured pitot pressures are moderate at the upstream station (fig. 44(a)) and large at the downstream stations (figs. 44(h), (i), (l), and (m)) where there is little resemblance between the profiles. At X = 104.14 cm the results of the final analysis provide the best agreement with both the measured pitot pressure and the shock-wave location. Shock waves are not predicted at the downstream stations. At the throat station (fig. 44(m)), the difference in level exhibited by the two sets of experimental data between about Y' = 0.8 and 1.6 cm is attributed to variations in model and tunnel conditions for the different tunnel entries and lateral variations in flow properties.

Experimental local static pressures and flow angles are compared with predicted values in figure 45. At X = 114.3 and 116.84 cm, data were obtained with the conical probe (fig. 15(b)), and at the throat station (X = 125.73 cm) data were obtained with direct-reading probes during another tunnel entry (figs. 15(a) and 17). At X = 114.3 and 116.84 cm (figs. 45(a) and (b)), the static-pressure data indicate a trend of increasing compression with height above the reflected shock wave ($Y' \approx 0.53$ cm). The flow angles from experimental data show the influence of the expansion region above the reflected wave. Both theories show a static pressure variation similar to that measured, but the trends in stream angle differ from those measured. Both experimental distributions were obtained with a relatively large probe in a region of shock-wave boundary-layer interaction. Therefore, the measurements may be inaccurate. At the throat station (fig. 45(c)), the measurements indicate a slight decrease in static pressure between the centerbody and Y' = 1.5 cm. The compression region above Y' = 1.7 cm is a result of the reflected shock wave.

Experimental and predicted Mach number profiles for several stations are compared in figure 46. Experimental Mach numbers calculated from surface pressure are shown at all stations. In addition, results obtained from local static pressure, whenever available, are shown. At X = 116.84 cm, the experimental results indicate the difference introduced by assuming a constant surface pressure in the region above the reflected shock wave. At X = 125.73 cm, the two sets of experimental results are in fairly good agreement since, as shown in figure 45(c), the local static pressure is nearly equal to the surface pressure.

Only limited agreement between experimental and predicted Mach numbers was found. Figure 46(a) illustrates the portion of the upstream flow field where the agreement was good. Experimental results are not shown for most of the flow field above the shock wave at Y' = 2.9 cm because the Mach numbers calculated from cowl surface pressure were unrealistically low, and the analyses predicted a static-pressure gradient in this region. The agreement shown at X = 124.46 and 125.73 cm is probably fortuitous since the experimental pitot pressures shown in figures 44(l) and (m) do not agree with predictions. Generally the use of surface pressures to calculate experimental Mach numbers in the inviscid flow field downstream of the cowl shock wave provides incorrect results. However, it is believed that the predicted Mach numbers are also incorrect in regions influenced by the shock-wave boundary-layer interaction since the expansion region from the interaction is not predicted.

Distributions of total-pressure recovery calculated from the Mach number and pitot-pressure data are compared with predictions in figure 47. The analyses generally overpredict the experimental recovery, probably because of the effects of reflected shock waves and expansion regions that are not included in the analyses. On the basis of the two-layer analysis for interactions reported in reference 12, a reduction in total-pressure recovery below that indicated by the design analysis would be expected. The apparently low values of experimental recovery result from the use of surface pressure in the calculation of Mach number and recovery.

Experimental results for the throat station (X = 125.73 cm) are considered to be the most reliable since static pressure gradients were small below the reflected shock wave and local static pressure was nearly equal to the surface pressure. Three experimental distributions are shown in figure 47(e) to illustrate the sensitivity of pressure recovery to variations in static and pitot pressure. The sensitivity to the small differences between the surface and local static pressures, such as those shown in figure 45(c), can be seen by comparing the profiles for the open and filled symbols at lateral station Z = -5.32 cm. The effects of a lateral variation of pitot pressure (fig. 44(m)) can be seen by comparing the pressure recovery distribution at Z = 0 (triangular symbols) with that at Z = -5.32 cm (filled symbols). For the throat station it is believed that the experimental results obtained from local static pressure provide the best measure of the total-pressure recovery.

P12 inlet: The shock-wave pattern and surface pressure distributions in the internal passage of the P12 inlet are shown in figure 48. Since the centerbody contours of the P8 and P12 inlets are nearly identical upstream of X = 121.9 cm, and since the cowl contours are also the same upstream of X = 114.3 cm, the general discussion concerning the characteristics of the shock-wave pattern for the P8 inlet also applies to the P12 inlet. Because of the additional compressive turning of the cowl surface of the P12 inlet downstream of X = 114.3 cm, the second reflection occurs farther upstream on the cowl surface than it did for the P8 inlet and the down-running shock wave enters the centerbody boundary layer near the throat station, X = 126.75 cm.

The data for the cowl surface show a reduction in pressure similar to that observed in the P8 inlet immediately upstream of the shock-wave impingement location. The cowl pressure for the P12 inlet exceeds the design level at X = 124.5 cm and decreases sharply to the design level at the throat station, X = 127.2 cm. The good agreement between the design analysis predictions and the experimental results at the throat station may be fortuitous since the local gradient in the experimental distribution immediately upstream of the throat station is very large. The pressure distribution downstream of the throat station was not measured so that it could not be determined if the gradient continued.

Lateral distributions in surface pressure at throat are shown in figure 49. The cowl distribution is quite uniform and, unlike that for the P8 inlet, exhibits little corner influence. This result is attributed to the relatively large distance between the secondary reflected shock wave and the cowl surface in the throat region. The corresponding lateral distribution for the centerbody indicates extreme corner effects. Over a series of runs the centerbody pressures at the throat station varied between runs and fluctuated during the runs over the range shown in figure 49(b). It can be seen that the lateral distribution is nearly symmetric about the model centerline. The pressure fluctuations may have occurred because of the shock-wave boundary-layer interaction on the centerbody immediately downstream of the throat station (fig. 48). Because of the fluctuating surface pressures and large corner effects, flow field surveys were made only at the throat station and not at other longitudinal stations. Results of the throat surveys are presented later.

The characteristics of the surface temperature distributions shown in figure 50 are similar to those for the P8 inlet (fig. 43).

Pressure distributions on the forward cowl surfaces and cowl boundary-layer transition– Pressure distributions for the complete cowl surface could not be shown in the composite form of figures 31, 40, and 48; the distributions for the forward regions are shown in figure 51. For the P2 inlet, the pressure obtained from the design analysis decreases continuously to the throat value, whereas the distribution for the final analysis exhibits several inflection points. The experimental results, which were obtained at $Z = -2.54$ and -8.10 cm, indicate that a decrease in pressure of about 5 percent occurred between these lateral locations. Both predictions fall between the experimental levels upstream of $X = 106$ cm and slightly above the experimental results downstream of this station. The pressure distributions for the P8 and P12 inlets should be the same to about $X = 114$ cm, but it can be seen in figures 51(b) and (c) that the surface pressure for the P8 inlet is slightly lower than that for the P12 inlet downstream of $X = 106$ cm. The design analysis provides a slightly better prediction of surface pressure for the forward regions of the cowls.

From all the pressure distribution results for the P8 and P12 inlets (i.e., figs. 40, 48, and 51) it is evident that further refinements are needed in the way viscid and inviscid solutions are coupled to obtain predictions of surface pressure distribution. Neither of the techniques employed in the design and final analysis is adequate for the entire cowl surface. Furthermore, exploratory solutions (not reported here) have indicated that a better prediction of inlet entrance conditions, as well as the effects of the shock-wave boundary-layer interaction on the centerbody, is required to obtain better agreement with measured cowl pressure.

The cowl boundary layers for the P2 and P8 inlets were investigated to determine if transition from laminar to turbulent flow occurred. Because of the difference in pressure distributions shown in figures 31, 40, and 51 for these inlets, the likelihood of transition should be different. Both experimental and analytical results were used to assess the boundary-layer condition. The experimental results include local heat-transfer rate, wall-shear stress, surface pitot pressure, schlieren photographs, and velocity profiles. Table 3 shows the heat-transfer and wall-shear stress data obtained analytically and experimentally for each inlet.

For the P2 inlet, analytical results were obtained with the assumption that the boundary layer was either laminar or turbulent over the full length of the cowl. The method of Lubard and Schetz (ref. 20) was used to predict the laminar characteristics, whereas the method of Sasman and Cresci (ref. 17) was used to predict the turbulent characteristics. The measured heat transfer and shear stress are of the same order as the analytical results for laminar flow, but are substantially smaller than the predicted values for turbulent flow. Therefore, it is concluded that the boundary layer was laminar at the throat station ($X = 119.38$ cm).

For the P8 inlet, the distribution of measured surface pitot pressure (fig. 52) indicates that transition occurred between $X = 103$ and 112 cm. From the characteristics of the shock-wave boundary-layer interaction on the cowl, shown in the schlieren photograph of figure 40, it was concluded that the boundary layer was turbulent at the interaction location ($X \simeq 124$ cm).

experimental velocity profile. At X = 119.38 cm, both the temperature and velocity profiles are in fairly good agreement with experimental results. Between X = 104.14 and 111.76 cm, both the temperature and velocity profiles obtained experimentally show significant shape changes. The data indicate that the boundary layer is initially laminar and then transitional. The location of the end of transition has previously been shown (fig. 52) to be at about X = 111.76 cm on the basis of pitot-pressure measurements. Downstream of X = 111.76 cm, the profiles remain full, change only slightly, and indicate that the flow is turbulent. Thus, the profile data support the previous discussion concerning transition on the cowl. Some of the scatter in the profile shape downstream of X = 111.76 cm may result from the fact that the edge velocity gradient, caused by leading-edge bluntness, is not the same at each station.

Streamwise variations of other boundary layer parameters are shown in figure 64. Experimental parameters ($\delta^*, \theta, M_e, \dot{m}_{BL}$) at stations X = 123.19 and 124.46 cm (flagged symbols) were obtained in a region of high normal pressure gradient, because of the shock-wave boundary-layer interaction on the cowl; they are questionable, therefore, since surface pressure was used in the data reduction. The experimental boundary-layer thickness (fig. 64(a)) is nearly constant from X = 104.14 to 114.3 cm, which is a region subjected to both adverse pressure gradient (fig. 40) and transition (fig. 52). A rapid increase in thickness occurs between X = 114.3 and 121.92 cm. In this region the surface pressure is nearly constant to X = 119.4 cm and then the pressure gradient is favorable downstream to X = 123.2 cm. A decrease in thickness is evident in the shock-wave boundary-layer interaction region, X = 122 to 125 cm. Displacement thickness (fig. 64(b)) decreases significantly and momentum thickness (fig. 64(c)) decreases moderately from X = 104.14 to 114.3 cm; then both increase in the region between X = 114.3 and 121.92 cm. All thickness parameters decrease across the shock-wave boundary-layer interaction. Boundary-layer mass flow (fig. 64(e)) increases along the surface, especially across the interaction. As for the P2 inlet, the results from the design analysis do not predict the observed boundary-layer growth; in particular, they do not account for the interaction. The predictions from the final analysis are better. The need for improvement is obvious, however, indicating that more advanced analytical methods may have to be used to match the edge velocity gradient with that in the inviscid flow, and provide for transition.

P12 inlet: No experimental results for the longitudinal development of the boundary layer, other than the schlieren photograph in figure 48, were obtained for the P12 inlet. Since the P8 and P12 inlets had essentially the same contours to about X = 121.92 cm for the centerbody, and X = 114.3 cm for the cowl, the boundary-layer development for these inlets should differ only downstream of these stations. However, at the throat station several measurements were obtained with the fixed rakes in the centerbody boundary layer. The boundary-layer and displacement thicknesses obtained from those measurements are:

Parameter	δ, cm	δ^*, cm
Experiment	0.406	0.213
Design prediction	0.432	0.173

Inlet Performance

Inlet performance is discussed in terms of throat-station measurements of pitot pressure, static pressure, and total temperature made at the lateral locations indicated in figure 16. Also considered are the distributions of Mach number and total-pressure recovery derived from these measurements, and the internal pressure recovery that accounts for the losses in total pressure between the throat and entrance (or cowl lip) stations.

P2 inlet– Experimental flow-field properties at the throat station are presented in figure 65. The pitot-pressure ratios (fig. 65(a)) fall within a range of about ±4 percent from the centerline value for the central region bounded by $-8.10 < Z < 0.0$ cm and $2.5 < Y' < 5.1$ cm (dashed lines). The pitot-pressure level is generally lower in the region outboard of $Z = -8.10$ cm, especially in the centerbody boundary layer.

Measured static-pressure ratios in the region above $Y' = 2.5$ cm range between 5.0 and 6.0 (fig. 65(b)). Since the pressure ratio at the inlet entrance was about 3.1, the internal passage compression ratio varied from about 1.6 to 2.0 (the design value) above the shock wave and had a slightly higher value near the centerbody. Static pressure could not be measured accurately near the shock wave and in the expansion region $1.0 < Y' < 2.5$ cm.

Mach number profiles (fig. 65(c)) show that the variation in Mach number is small in the central region ($-8.13 < Z < 0.0$ cm) for $2.5 < Y' < 5.1$ cm, and it increases within the boundary-layer regions. Mach numbers outboard of $Z = -8.10$ cm are generally lower than the values at stations closer to the centerline.

Experimental total-pressure recovery is presented in figure 65(d). A double scale is provided to show the recovery from the free stream total pressure (p_t/p_{t_∞}) as well as the recovery of the internal passage, $p_t/p_{t_{\text{entrance}}}$. The latter was obtained by dividing the ratio p_t/p_{t_∞} by the recovery at the entrance station which was determined to be 0.8 on the basis of surveys and predictions. This value of recovery at the entrance station was also used with the other inlets to determine their internal recovery. Since the flow above the reflected shock wave traverses only the cowl shock wave between the entrance and throat stations, the internal recovery should be the same as the recovery across the cowl shock. The data appear to indicate general agreement between the maximum value of 0.96 for the predicted recovery across the cowl shock (obtained by combining the results from figs. 22 and 39(c)) and the experimental internal recovery shown in figure 65(d) for regions near the centerline.

The experimental pressure recovery varies considerably both in the lateral direction and in the vertical direction across the height of the duct. The regions outboard of $Z = -8.13$ cm have the lowest recoveries. The vertical distribution of recovery is nonlinear, with the lowest values near the cowl boundary layer and the highest values near the center of the duct. The nonlinear distribution reflects the losses in total pressure associated with the shock wave from the blunt leading edge of the cowl. In the inviscid core flow region the internal recovery at the centerline ranges from a low value of about 0.25 at $Y' = 5.75$ cm (the edge of the cowl boundary layer as identified in fig. 39(c)) to a high value of about 0.96 near the center of the duct. However, most of the core flow region has high internal recovery.

P8 inlet– Experimental flow-field properties at the throat station are presented in figure 66. The pitot-pressure profiles (fig. 66(a)) show the large variations across the throat height that result from the reflected shock wave. Also, the lateral variations from the centerline profile are large above $Y' = 1.0$ cm.

The static pressures (fig. 66(b)) show that there are relatively small lateral variations in the central region below the shock wave, which increase at lateral stations outboard of $Z = -8.13$ cm. The compression ratio relative to that at the inlet entrance, where the pressure ratio is about 3.1, decreases across the passage from about 7.4 on the centerbody side to about 6.9 near $Y' = 1.5$ cm, and then increases to about 12.4 at the cowl surface. Thus, the internal compression ratio for the region of this inlet below the shock wave appears to be approximately 7, about 12 percent below the design value.

The Mach number profiles presented in figure 66(c) show that the Mach number varies from about 3.9 to 4.25 in the inviscid flow region below the shock wave.

Experimental total-pressure recovery is shown in figure 66(d). The experimental recovery varies considerably both in the lateral and vertical directions. The nonlinear vertical distribution shows losses in total pressure through the reflected shock waves in addition to the losses through the cowl shock wave. For the centerline curve, the internal recovery in the inviscid core flow region varies from about 0.54 at $Y' = 1.98$ (the edge of the cowl boundary layer as identified in fig. 47(e)) to about 0.88 near the edge of the boundary layer on the centerbody side. Thus it appears that the P8 inlet has a lower maximum recovery and a smaller variation across the core flow than the P2 inlet.

The data for the P2 and P8 inlets can be used to estimate the strength of the reflected wave that occurred for the P8 inlet since most of the flow in this inlet crossed two shocks ahead of the throat while the flow in the P2 inlet crossed one shock. From the difference between the high values of internal recoveries (0.96 and 0.88) in each inlet, it appears that the loss in internal total-pressure ratio was about 0.08.

P12 inlet– Experimental flow-field properties at the throat station of the P12 inlet are shown in figure 67. The pitot-pressure measurements (fig. 67(a)) indicate that large variations were present in both the vertical and the lateral directions, especially below the shock wave ($0 < Y' < 0.65$ cm). (The centerline data and design predictions are included in fig. 67 for comparison.) The reflected shock wave, which did not exist in the design analysis, lies close to the edge of the centerbody boundary layer at the throat station. Although the shock location is not obvious in the pitot-pressure profile, it is evident in the static-pressure profile of figure 67(b) and in the schlieren photograph of figure 48.

The measured static pressures (fig. 67(b)) indicate that the lateral variation is large both below and above the reflected shock wave. Above the shock wave the trend of the data is approximated by the results of the design analysis.

Consideration of the experimental static pressure results for the three inlets shows that there is a trend of increasing flow nonuniformity laterally across the duct, with increasing internal compression ratio. When coupled inlet-combustor flows are considered this trend is important because an additional pressure rise, due to combustion and heat addition, would occur immediately downstream of the throat. The limiting internal pressure rise for inlet-flow instability was not determined, but the results indicate that it may be incipient for internal compression ratios near 12.

The Mach number profiles (fig. 67(c)) show large variations both vertically and laterally, and the predicted distribution does not agree with experimental results.

The experimental total-pressure recovery for the P12 inlet is compared with the prediction from the design analysis in figure 67(d). Both the experimental and predicted recoveries have a very nonlinear vertical distribution. The experimental results show large lateral variations from the centerline data. The centerline recovery is higher than expected in the region above the shock wave. It should be no higher than that for the P8 inlet, and in fact should be lower because of the presence of the additional reflected shock (making a total of three shock waves in the P12 inlet). It is believed that the total-pressure recovery is high because the measured static pressures are too low. Static pressure estimates from the measured pitot pressure in the P12 inlet and the recovery of the P8 inlet indicate that the static-pressure ratio should be about 42 or greater, depending on losses assumed for the third shock in the P12 inlet. On the basis of this type of analysis and the measured wall pressure, a reduction in static pressure from the shock wave to the cowl would be expected. The measured static pressure near the center of the duct (fig. 67(b)) indicate such a gradient, but the level of pressure is low.

Off-Design Operation

Data were obtained at off-design conditions for the P2 and P8 inlets by changing the angle of attack of the wedge forebody to 4.5° and 8.5°, which provided entrance Mach numbers of 6.3 and 5.7, respectively, representing those that would occur when the inlet was operated at over and under speed conditions, respectively. Distributions of surface pressure for the design and off design conditions are shown in figures 68 and 69.

Internal-flow characteristics of both inlets changed at off-design conditions, With increasing angle of attack, the surface pressures increased both on the cowl and the centerbody, and the impingement point of the cowl shock wave on the centerbody moved upstream. Schlieren photographs (not shown) also indicated that the shock-wave pattern moved upstream with increasing angle of attack. For the centerbody of both inlets and the cowl of the P2 inlet the changes in surface pressure at the throat stations were proportional to the changes at the inlet entrance station. Thus, internal compression ratio ($p_{\text{throat}}/p_{\text{entrance}}$) was changed little with increasing angle of attack. However, for the cowl of the P8 inlet, internal compression ratio varied considerably as the reflected shock wave moved upstream with increasing angle of attack. A large increase in surface pressure at the throat station is shown in figure 69(a) as α increased from 4.5° to 6.5°. A much smaller increase in pressure occurred as α increased from 6.5° to 8.5°.

The difference between the pressure ratios on the cowl and centerbody, $(p/p_\infty)_{\text{cowl}} - (p/p_\infty)_{\text{centerbody}}$, at the throat is a measure of the flow distortion across the duct. This parameter is shown in figure 70 for both inlets. For the P2 inlet the variation of the distortion with angle of attack is small compared with that for the P8 inlet. The large pressure differential for the P8 inlet results from the movement and strength of the shock-wave boundary-layer interaction on the cowl.

CONCLUDING REMARKS

This experimental and analytical investigation of the internal flow characteristics and performance of hypersonic inlets consisted of (1) a design phase, (2) a test phase, and (3) a final analysis phase. The design of the two-dimensional inlets used in the experimental investigation was based on the modular engine concept of a specific hypersonic vehicle configuration intended for flight at Mach numbers of about 12. Three large-scale inlets which modeled only the contours of the internal flow passages were tested at a free-stream Mach number of 7.4. For these models and test conditions, the inlet entrance Mach number for the models simulated that for the vehicle. These inlets provided internal compression ratios (ratio of static pressure at the throat to that at the inlet-entrance station) of 2, 8, and 12 and, accordingly, are designated as inlets P2, P8, and P12. A significant body of internal flow data was acquired in the experimental investigation. The major results, as well as an assessment of the analytical techniques used to design the inlet contours and predict the internal-flow characteristics, are summarized here.

In each inlet, a reflected shock wave originated in the interaction region where the cowl leading-edge shock wave impinged on the centerbody boundary layer. The reflected wave pattern was experimentally observed to vary among the inlets; the waves generally moved upstream and steepened as the internal compression ratio of the inlet increased. Analytical techniques that assumed the local surface turning of the centerbody was sufficient to cancel the cowl shock wave, or that applied a control volume analysis (one that accounted for both surface turning and compression effects from the cowl) in the interaction region were unsuccessful in predicting the wave pattern and flow characteristics in the interaction region.

Longitudinal distributions of surface pressure were predicted reasonably well in regions unaffected by shock-wave boundary-layer interactions. However, for all inlets the pressure distribution on the centerbody was not predicted well in the region downstream of the location of the impingement of the cowl shock wave on the centerbody. The cowl of the P2 inlet was not subject to the effects of shock-wave boundary-layer interactions; the cowls of the P8 and P12 inlets were, however, and for them a considerable unpredicted reduction in surface pressure was observed in the region immediately upstream of the location of the interaction between the reflected cowl shock and the cowl boundary layer. This reduction in pressure appeared to be caused primarily by the interaction associated with the penetration of the cowl shock wave into the thick boundary layer on the centerbody.

A nonuniform distribution of static pressure was observed across the height of the throat station of each inlet, a further effect of the reflected cowl shock wave. The design analysis predicted a nearly uniform distribution of static pressure across the throat.

The turbulent centerbody boundary layer was significantly affected by the interaction with the cowl shock wave. Experimental results indicated that velocity and temperature profiles were altered, the boundary-layer thickness and displacement thickness were reduced, and the mass flow in the boundary layer was increased by the shock interaction. The theory used in the design analysis provided a good prediction of the boundary-layer development downstream of the interaction region. However, the agreement may have been fortuitous since the boundary-layer development was not predicted in the interaction region and the predicted pressure distribution used in the analysis did not agree with experimental results.

The cowl boundary layer for all inlets was subject to an interaction with the inviscid entropy layer from the blunt leading edge. For the P8 and P12 inlets its development was further subject to streamwise pressure gradients as well as an interaction with the reflected cowl shock wave downstream of the transition region. For the P2 inlet the boundary layer remained laminar. Thus, with the increased compression provided by the P8 and P12 inlets (i.e., higher local Reynolds number), natural transition occurred earlier. Predictions of the cowl boundary layer properties were fair for the P2 inlet and poor for the P8 inlet.

Internal total–pressure recovery ($p_{t_{throat}}/p_{t_{entrance}}$) in the core flow varied nonlinearly across the height of the inlets: from about 0.25 near the cowl to a maximum of 0.96 for the P2 inlet, and from about 0.54 to 0.88 for the P8 inlet. For both inlets much of the core flow had high recovery. Thus no serious degradation of core flow performance occurred from the additional shock wave as the internal compression ratio was increased from 2 to 8. No assessment can be made of the effect of increasing the compression ratio from 8 to 12 because of the uncertainty in determining the throat static pressure for the P12 inlet. In general, the experimental results at the throat show that with increasing compression ratio, the size of the core flow decreases and the importance of viscous effects increases. Predicted pressure recoveries were in general agreement with the experimental results and indicated that the nonlinear distribution was caused primarily by the bluntness of the cowl leading edge.

For the P12 inlet fluctuations of centerbody surface pressures and extensive corner effects were observed near the throat. This result suggests that the onset of inlet flow instability may be incipient for internal compression ratios near 12.

The results show that the design techniques, which were based on inviscid flow calculations with corrections for boundary–layer displacement thickness, were successfully used to design the inlet contours that provided high performance despite the complexity of the flow and the failure of the analytical methods to account for all of the flow details.

Ames Research Center
National Aeronautics and Space Administration
Moffett Field, Calif. 94035, October 10, 1972

APPENDIX A

WEDGE-FOREBODY FLOW-FIELD ANALYSIS

The calculation procedures used in the final analysis for predicting the flow over the wedge forebody accounted for (1) nonuniform free-stream flow, (2) the effects of a viscous interaction near the leading edge, and (3) boundary-layer development with both laminar and turbulent regions. An iterative procedure was employed to couple the solutions for the viscid and inviscid flows at an effective surface, which was obtained by adding a displacement thickness correction to the geometric contours (table 1).

Experimental results showed that the free stream ahead of the wedge-forebody shock wave was nonuniform, and that the Mach number varied from 7.4 at $X = 0.0$ (leading edge) to 7.58 at $X = 81.28$ cm (inlet entrance). The free-stream flow direction also varied slightly. Since flow-angle distributions were only available for tunnel-empty conditions, a map of flow-angle distribution based on measured pitot pressures, with the model in the tunnel, and Prandtl-Meyer turning was prepared. Zero angularity was assumed at the tunnel centerline, and the angle varied from -0.40° at the leading edge (below the centerline) to +0.44° ahead of the forebody shock at the inlet-entrance station (above the centerline). These variations in free-stream flow properties are large enough to affect the flow field over the wedge forebody at the inlet-entrance station.

Viscous interaction effects near the leading edge must be accounted for to obtain predictions for the forebody flow that correctly describe both the boundary-layer development and the inviscid flow field, including the location of the leading edge shock wave. In accounting for the interaction effects, one objective is to determine a starting station, and initial input quantities that are required by the method of characteristics solution for the inviscid flow. This entails the determination of an effective initial wedge angle derived from considerations of the displacement thickness growth near the leading edge (see sketch (a)).

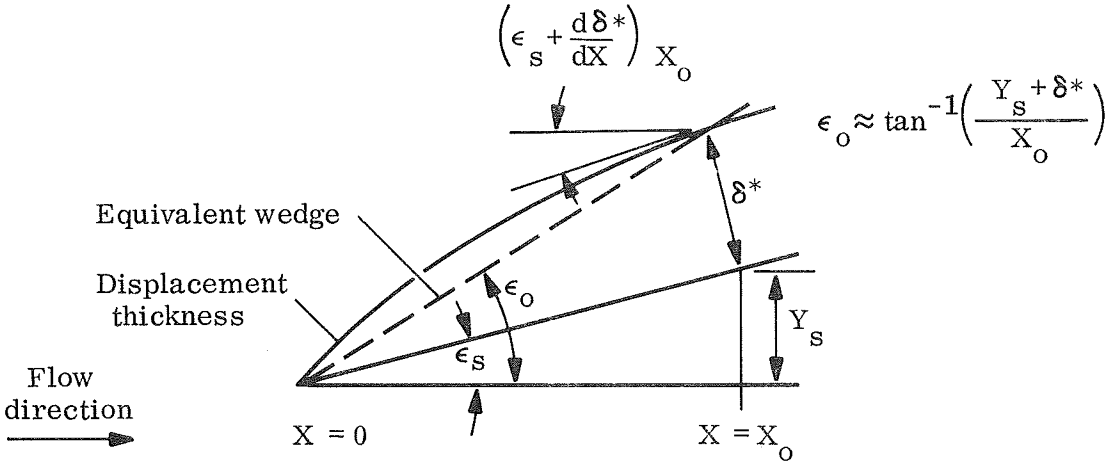

Sketch (a).– Equivalent wedge angle.

The viscous interaction method of reference 21 was used to obtain the displacement thickness. A weak interaction analysis was assumed because, as indicated in reference 21, weak interaction effects should appear on flat plates with sharp leading edges at low angles of attack for high Mach numbers and Reynolds numbers. The length used in determining the hypersonic similarity parameter $\bar{\chi}$ was 0.25 cm, which, together with other required quantities ($p_{t_\infty} = 4.14 \times 10^6$ N/m², $M_\infty = 7.4$, $T_{t_\infty} = 811°$ K, $T_W = 303°$ K) gave a value for $\bar{\chi}$ of 2.94. This value is close to that for the upper limit for second-order weak interactions. The resulting displacement-thickness distribution is shown in figure 71(a) for $X = 0.25$ cm to the approximate transition location, $X = 35.56$ cm. With the starting station X_O and the displacement thickness specified, the equivalent wedge angle, ϵ_O (sketch (a)) used to determine the initial conditions for the method of characteristics, was determined to be 9.81°. The effective inviscid surface used in the solution for the inviscid flow was obtained by adding the displacement thickness determined from the interaction analysis to the geometric coordinates of the wedge forebody. Perfect matching of all properties on the starting line could not be obtained because of the slight difference between the angles ϵ_O and $(\epsilon_S + d\delta^*/dX)_{X_O}$.

Results obtained from inviscid flow field calculations were then used as edge conditions in the laminar boundary layer programs of Clutter and Smith (ref. 8) and Lubard and Schetz (ref. 20). Initial conditions were also needed: the initial displacement thickness was assumed to be the same as that given by the interaction analysis, the velocity profile shape was obtained from similar solutions of reference 22, and the boundary-layer thickness was derived from the velocity profile and initial displacement thickness. Figure 71(a) shows that distributions of displacement thickness predicted by the various methods agree reasonably well.

Turbulent boundary-layer development was calculated using the method of Sasman and Cresci (ref. 17) with edge conditions from inviscid analyses. In the first solution tried, the boundary-layer calculations were started at $X = 35.56$ cm with an initial displacement thickness equal to the predicted laminar value. At the inlet entrance station ($X = 81.28$ cm), the predicted displacement thickness from this solution was considerably greater than that obtained from experimental results. To provide agreement with the experimental displacement thickness, the boundary-layer calculations were started at $X = 45.72$ cm. The resulting distribution of displacement thickness was graphically faired to the laminar distribution between $X = 35.56$ and 45.72 cm (similar to fig. 71(b)). Then the distribution of displacement thicknesses for the entire forebody was added to the geometric coordinates to define an effective surface contour, and the method of characteristics, with nonuniform free-stream properties, was employed to calculate a new set of boundary-layer edge conditions. Several iterations between the inviscid solution and the boundary-layer solution were required to obtain a self-consistent coupled solution for the entire flow-field upstream of the inlet entrance. The resulting distribution of displacement thickness is shown in figure 71(b). This coupled solution provided the final analytical prediction of surface pressure, boundary-layer development, and flow-field properties at the inlet entrance.

APPENDIX B

BLUNT COWL FLOW FIELD ANALYSIS

The final analysis for the internal flow downstream of the blunt cowl leading edge used an iterative procedure to couple the solutions for the viscid and inviscid flows. The analysis accounted for a prescribed variation of entropy at the edge of the boundary layer, which had both laminar and turbulent regions. The analysis was conducted with the inlet entrance flow conditions predicted by appendix A and the geometric cowl contours (table 1).

The boundary conditions imposed on the inviscid solution in the final analysis differed from those of the design analysis, in which the entropy at a wall point was equated to the entropy at the nearest upstream flow-field point. This technique allowed the wall entropy to decrease with axial distance, thereby approximating the effect of entropy swallowing in which the entropy at the boundary-layer edge downstream of a blunt leading edge decreases with axial distance until the entropy layer is entrained in the boundary layer. One inconsistency of this approximate technique is that the entropy variation at the wall in the inviscid solution is not related to the entrainment of the entropy layer into the boundary layer. This inconsistency was corrected in the final analysis by prescribing a variation of wall entropy consistent with the boundary-layer mass flow and the entropy distribution downstream of the cowl shock wave. The following procedure was used in the final analysis:

1. A blunt-body solution, including the variation of entropy downstream of the cowl shock wave with mass flow crossing the shock wave, was obtained using the method of reference 7 for a Mach number of 6.11 at the cowl lip.

2. The inviscid flow field and the variation of entropy downstream of the cowl shock wave with mass flow were computed for the remainder of the flow field over the design effective surface using the method of characteristics. The approximate technique discussed above for calculating the entropy was used in this step.

3. The laminar boundary-layer development from the input line in the characteristic mesh to the tangent point of the circular leading edge and the straight portion of the effective cowl contour (at $\lambda = +1.0^\circ$) was computed for the edge conditions determined in steps 1 and 2 by the method of Clutter and Smith (ref. 8). The computed velocity profile at the tangent point was used as the initial profile for subsequent boundary-layer calculations.

4. The laminar boundary-layer development over the remainder of the cowl surface for the P2 inlet or to the approximate transition location, $X = 106.68$ cm, was computed using the analysis of Lubard and Schetz (ref. 20) for the edge conditions determined in steps 1 and 2. Downstream of this station the turbulent boundary-layer development for the P8 and P12 inlets was computed with the method of Sasman and Cresci (ref. 17).

5. A new effective surface (the interface between the solutions for the inviscid and viscid flows) was obtained by adding the displacement thickness of step 4 to the geometric cowl coordinates.

6. The entropy at the inviscid–viscid interface to be prescribed for the next inviscid solution was determined in different ways, depending on the region of the cowl surface. Between the input line and the tangent point, the approximate technique noted above was used, since experience showed that this was the only technique that eliminated discontinuities in the surface–pressure distribution. Downstream of the tangent point the distributions of entropy and mass flow along the cowl shock wave were matched from steps 1 and 2, and the boundary layer mass flow from step 4.

Steps 4 to 6 were repeated until successive iterations yielded unchanging solutions for both the inviscid and viscid flows. This coupled solution was used for the final analytical predictions for the surface pressure distribution, the flow–field properties, and the boundary–layer development on the cowl for the portion of the internal flow that was not affected by the interaction of the cowl shock wave with the centerbody boundary layer.

REFERENCES

1. Sanator, Robert J.; DeCarlo, Joseph P.; Boccio, John L.; and Shannon, John A.: Development and Evaluation of an Inlet for Scramjet-Powered Hypersonic Cruise Vehicles. AFFDL-TR-68-48, vols. I and III, April 1968.

2. DeCarlo, Joseph P.; Shamsins, Dan.; Seebaugh, William R.; and Doran, Robert: Investigation of Hypersonic Flows in Large-Scale Model Internal Passages. Final Report. Contract NAS2-5052, Fairchild Hiller Rep. FHR 3834, Nov. 1969.

3. Seebaugh, W. R.; Doran, R. W.; and DeCarlo, J. P.: Detailed Investigation of Flow Fields Within Large-Scale Hypersonic Inlet Models Final Report, Contract NAS2-5719, NASA CR 114305, 1971.

4. Torrillo, D. T.; and Savage, S. B.: A Brief Review of Compressible Laminar and Turbulent Boundary-Layer Separation. Republic Aviation Rep. RAC-2325, April 1964.

5. Sanator, Robert J.; Boccio, John L.; and Shamshins, Dan: Effect of Bluntness on Hypersonic Two-Dimensional Inlet Type Flows. NASA CR-1145, 1968.

6. Sorenson, Virginia L.: Computer Program for Calculating Flow Fields in Supersonic Inlets. NASA TN D-2897, July 1965.

7. Lomax, Harvard; and Inouye, Mamoru: Numerical Analysis of Flow Properties About Blunt Bodies Moving at Supersonic Speeds in an Equilibrium Gas. NASA TR R-204, 1964.

8. Clutter, Darwin; and Smith, A. M. O.: Solution of the General Boundary Layer Equations for Compressible Laminar Flow, Including Transverse Curvature. Douglas Aircraft Rep. LB 31009, Feb. 1963.

9. Kutschenreuter, Paul H., Jr.; Brown, David L.; Hoelmer, Werner: Investigation of Hypersonic Inlet Shock-Wave Boundary-Layer Interaction, General Electric Co., AFFDL-TR-65-36, part II, April 1966.

10. Pinckney, S. Z.: Semiempirical Method for Predicting Effects of Incident-Reflecting Shocks on the Turbulent Boundary Layer. NASA TN D-3029, October 1965.

11. Seebaugh, William R.; and Childs, Morris E.: Influence of Suction on Shock Wave-Turbulent Boundary Layer Interactions for Two-Dimensional and Axially Symmetric Flows. NASA CR-1639, 1970.

12. Rose, William C.: A Method for Analyzing the Interaction of an Oblique Shock Wave With a Boundary Layer. NASA TN D-6083, 1970.

13. Winkler, Eva M.: Stagnation Temperature Probes for Use at High Supersonic Speeds and Elevated Temperatures. NAVORD Rep. 3834, Oct. 1954.

14. Vahl, Walter A.; and Weirich, Robert L.: Calibration of a 30° Included-Angle Cone for Determining Local Flow Conditions in Mach Number Range of 1.51 to 3.51. NASA TN D-4679, 1968.

15. Ames Research Staff: Equations, Tables, and Charts for Compressible Flow. NACA Rep. 1135, 1953.

16. Polek, Thomas E.; and Mateer, George G.: Measurement of Turbulent Heat Transfer on Cones and Swept Plates at Angle of Attack. NASA SP 216, 1969, Paper 17.

17. Sasman, Philip K.; and Cresci, Robert J.: Compressible Turbulent Boundary Layer with Pressure Gradient and Heat Transfer. AIAA J. vol. 4, no. 1, Jan. 1966, pp. 19-25.

18. Seebaugh, William R.: Summary of Profile Data Obtained Within Large-Scale Hypersonic Inlet Models. Fairchild Hiller Rep. FHR 4000-1, April 1971. Contract NAS2-5719.

19. Watson, Earl C.; Murphy, John D.; and Rose, William C.: Investigation of Laminar and Turbulent Boundary Layers Interacting with Externally Generated Shock Waves. NASA TN D-5512, 1969.

20. Lubard, Stephen C.; and Schetz, Joseph A.: The Numerical Solution of Boundary Layer Problems. Proc. 1968 Heat Transfer and Fluid Mechanics Institute, Stanford Univ. Press, June 1968, pp. 137-150.

21. Hayes, Wallace D.; and Probstein, Ronald F.: Hypersonic Flow Theory, Academic Press, N. Y., 1959, pp. 333-353.

22. Van Driest, E. R.: Investigation of Laminar Boundary Layer in Compressible Fluids Using the Crocco Method, NACA TN 2597, 1952.

TABLE 1.– GEOMETRIC COORDINATES FOR WEDGE FOREBODY AND INTERNAL PASSAGES

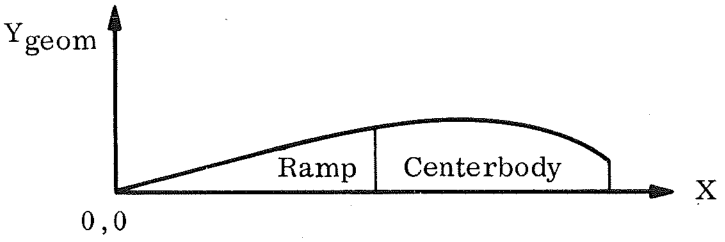

(a) Wedge forebody

X, cm	Y_{geom}, cm	dY/dX
0	0	0.11305
1.27	.144	↓
2.54	.287	↓
3.81	.431	↓
5.08	.574	↓
6.50	.735	↓
10.67	1.206	.11367
21.34	2.436	.11563
32.00	3.673	.11614
42.67	4.914	.11650
53.34	6.158	.11675
64.01	7.405	.11694
74.68	8.654	.11712
81.28	9.428	.11725
85.34	9.904	.11733
92.31	10.722	.11738

(b) P2 inlet centerbody

X, cm	Y_{geom}, cm	dY/dX
92.31	10.722	0.11738
110.23	12.825	.11742
113.72	13.110	.023392
121.74	13.313	.023392
123.14	13.338	---
124.35	13.338	---
125.63	13.318	---
126.91	13.249	---
128.17	13.165	---
129.54	13.008	---

TABLE 1.– GEOMETRIC COORDINATES FOR WEDGE FOREBODY AND INTERNAL PASSAGES – Continued

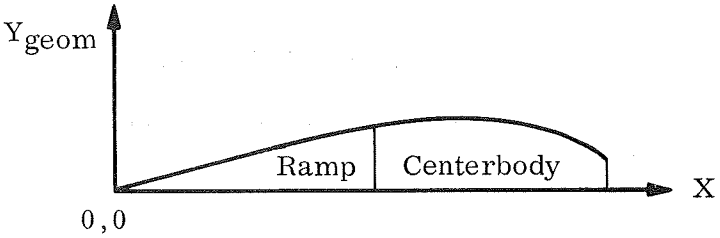

(c) P8 inlet centerbody

X, cm	Y_{geom}, cm	dY/dX
92.31	10.722	0.11738
110.23	12.825	.11742
113.66	13.103	.023392
116.20	13.163	.023392
120.71	12.887	---
122.29	12.646	---
123.23	12.483	---
124.51	12.256	---
125.78	12.027	---
127.06	11.799	---
128.27	11.574	---
129.54	11.323	---
130.81	11.052	---
132.08	10.761	---
133.35	10.446	---
134.62	10.106	---
136.20	9.648	---

TABLE 1.– GEOMETRIC COORDINATES FOR WEDGE FOREBODY AND INTERNAL PASSAGES – Continued

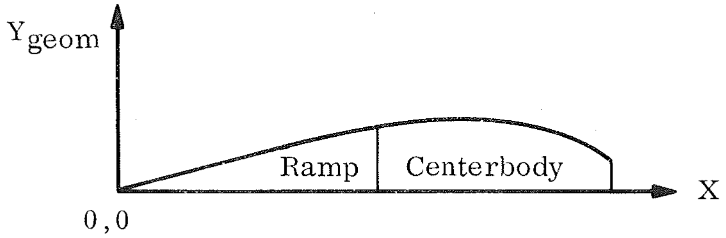

(d) P12 inlet centerbody

X, cm	Y_{geom}, cm	dY/dX
92.31	10.722	0.11738
110.23	12.825	.11742
113.73	13.110	.023392
116.27	13.169	.023392
120.71	12.885	---
122.30	12.645	---
124.51	12.226	---
125.16	12.093	---
125.75	11.968	---
126.10	11.888	---
126.63	11.754	---
127.16	11.622	---
128.52	11.279	---
129.54	11.017	---
130.81	10.677	---
132.08	10.227	---
133.35	9.937	---
134.62	9.519	---
136.20	8.944	---

TABLE 1.– GEOMETRIC COORDINATES FOR WEDGE FOREBODY AND INTERNAL PASSAGES – Continued

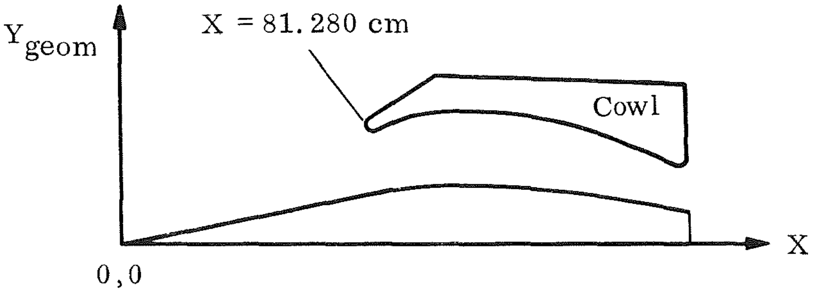

(e) P2 inlet cowl

X, cm	Y_{geom}, cm	X, cm	Y_{geom}, cm
81.280	18.330	84.325	18.344
81.308	18.281	85.439	18.367
81.312	18.279	86.545	18.390
81.315	18.278	89.773	18.458
81.320	18.276	91.718	18.503
81.328	18.274	94.106	18.563
81.342	18.274	97.098	18.644
81.439	18.276	99.148	18.702
81.471	18.277	101.803	18.788
81.534	18.279	104.368	18.876
81.601	18.281	107.403	18.984
81.674	18.283	109.707	19.070
81.748	18.285	112.252	19.164
81.831	18.287	114.417	19.243
81.951	18.290	117.109	19.340
82.100	18.294	117.956	19.368
82.134	18.295	119.134	19.411
82.497	18.303	120.313	19.454
83.215	18.320	129.540	20.091
83.307	18.322		

TABLE 1.– GEOMETRIC COORDINATES FOR WEDGE FOREBODY AND INTERNAL PASSAGES – Continued

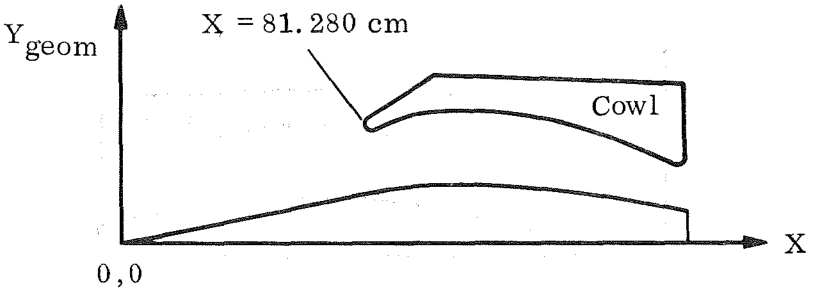

(f) P8 inlet cowl

X, cm	Y_{geom}, cm	X, cm	Y_{geom}, cm
81.280	18.330	87.620	18.410
81.308	18.281	89.705	18.425
81.312	18.279	91.520	18.415
81.315	18.278	94.520	18.351
81.320	18.276	97.320	18.238
81.328	18.274	99.593	18.110
81.342	18.274	101.806	17.953
81.439	18.276	104.461	17.723
81.471	18.277	107.078	17.452
81.534	18.279	109.325	17.180
81.601	18.281	112.168	16.781
81.674	18.283	114.718	16.365
81.748	18.285	116.080	16.124
81.831	18.287	117.373	15.897
81.951	18.290	118.546	15.690
82.100	18.294	119.635	15.498
82.134	18.295	120.600	15.328
82.497	18.303	122.534	14.988
83.215	18.320	123.262	14.861
83.307	18.322	124.635	14.618
84.325	18.344	125.740	14.413
85.439	18.367	136.200	12.979
86.545	18.390		

TABLE 1.– GEOMETRIC COORDINATES FOR WEDGE FOREBODY AND INTERNAL PASSAGES – Concluded

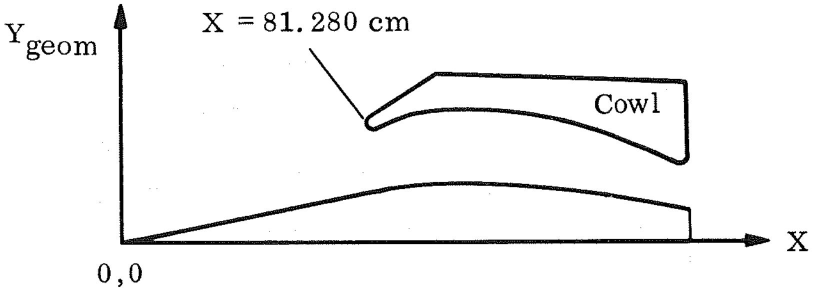

(g) P12 inlet cowl

X, cm	Y_{geom}, cm	X, cm	Y_{geom}, cm
81.280	18.330	87.620	18.410
81.308	18.281	89.705	18.425
81.312	18.279	91.520	18.415
81.315	18.278	94.520	18.351
81.320	18.276	97.320	18.238
81.328	18.274	99.593	18.110
81.342	18.274	101.806	17.953
81.439	18.276	104.461	17.723
81.471	18.277	107.078	17.452
81.534	18.279	109.935	17.180
81.601	18.281	112.168	16.781
81.674	18.283	114.718	16.366
81.748	18.285	117.351	15.872
81.831	18.287	119.714	15.355
81.951	18.290	120.777	15.097
82.100	18.294	121.845	14.828
82.134	18.295	122.202	14.737
82.497	18.303	123.181	14.495
83.215	18.320	124.525	14.165
83.307	18.322	125.895	13.829
84.325	18.344	126.854	13.594
85.439	18.367	127.523	13.427
86.545	18.390	136.200	12.014

TABLE 2.– SURFACE INSTRUMENTATION LOCATIONS FOR INLET MODELS

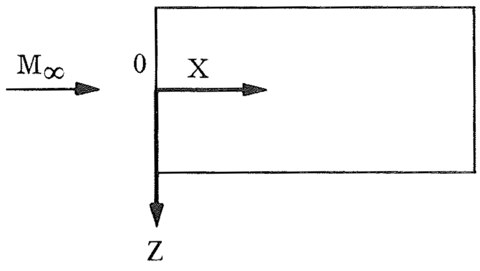

(a) Wedge forebody

(28) Pressure orifices

X, cm	Z, cm
81.28	14.12
81.92	13.66
80.64	9.96
81.92	9.96
80.64	6.25
81.92	6.25
80.64	2.54
81.92	2.54
3.81	0
10.16	↓
15.24	↓
20.32	↓
25.40	↓
35.56	↓
45.72	↓
55.88	↓
63.50	↓
71.12	↓
80.64	↓
81.92	↓
80.64	-2.54
81.92	-2.54
80.64	-8.10
81.92	-8.10
80.64	-11.81
81.92	-11.81
81.92	-13.66
81.28	-14.12

(14) Thermocouples

X, cm	Z, cm
81.28	13.66
81.28	2.54
7.62	-1.27
12.70	↓
17.78	↓
22.86	↓
30.48	↓
40.64	↓
50.80	↓
60.96	↓
76.20	↓
81.28	↓
81.28	-8.10
81.28	-13.66

TABLE 2.– SURFACE INSTRUMENTATION LOCATIONS FOR INLET MODELS – Continued

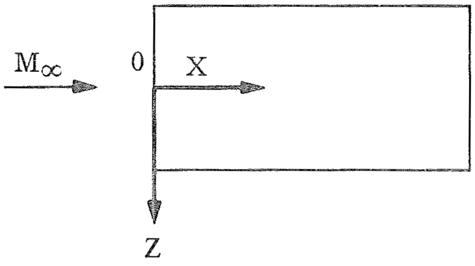

(b) P2 inlet centerbody

(53) Pressure orifices				(14) Thermocouples	
X, cm	Z, cm	X, cm	Z, cm	X, cm	Z, cm
116.59	13.66	96.52	-5.32	118.06	13.66
119.38	13.66	99.06	↓	↓	9.96
99.06	13.36	101.60	↓	↓	6.25
109.22	13.36	104.14	↓	96.52	0
109.22	9.96	106.68	↓	101.60	↓
116.59	9.96	107.95	↓	106.68	↓
119.38	9.96	109.60	↓	110.24	↓
109.22	6.25	110.34	↓	112.90	↓
109.96	↓	111.07	↓	114.38	↓
110.69	↓	111.81	↓	115.85	↓
111.43	↓	112.55	↓	118.06	-2.54
112.17	↓	115.57	↓	↓	-8.10
112.90	↓	118.11	↓	↓	-11.81
116.59	↓	109.22	-8.10	↓	-13.66
119.38	↓	110.49	↓		
113.64	2.54	113.03	↓		
115.11	↓	116.59	↓		
116.59	↓	119.38	↓		
118.06	↓	109.22	-11.81		
119.38	↓	116.59	↓		
94.23	0	119.38	↓		
118.06	↓	99.06	-13.36		
119.38	↓	109.22	-13.36		
113.28	-2.54	116.59	-13.66		
114.38	↓	119.38	-13.66		
115.85	↓				
116.84	↓				
119.38	↓				

TABLE 2.– SURFACE INSTRUMENTATION LOCATIONS FOR INLET MODELS – Continued

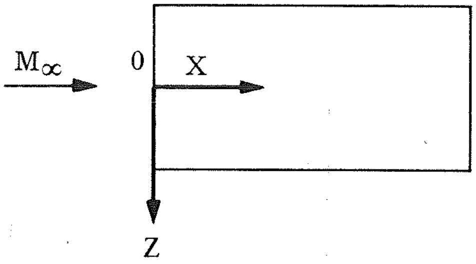

(c) P8 inlet centerbody

(60) Pressure orifices				(14) Thermocouples	
X, cm	*Z*, cm	*X*, cm	*Z*, cm	*X*, cm	*Z*, cm
109.22	13.66	113.67	-2.54	124.46	13.66
121.92	↓	114.94	↓	↓	9.96
125.73	↓	116.20	↓	↓	6.25
99.06	13.36	118.11	↓	96.52	0
109.22	9.96	120.65	↓	101.60	↓
121.92	↓	123.19	↓	106.68	↓
125.73	↓	125.73	↓	111.76	↓
105.41	6.25	96.52	-5.32	115.57	↓
106.68	↓	99.06	↓	118.11	↓
107.95	↓	101.60	↓	120.65	↓
109.22	↓	106.04	↓	124.46	-2.54
110.49	↓	107.32	↓	↓	-8.10
111.76	↓	108.58	↓	↓	-11.81
121.92	↓	109.86	↓	↓	-13.66
125.73	↓	111.12	↓		
113.03	2.54	112.40	↓		
114.30	↓	106.68	-8.10		
115.57	↓	107.95	↓		
116.84	↓	109.22	↓		
119.38	↓	110.49	↓		
121.92	↓	111.76	↓		
124.46	↓	113.03	↓		
125.73	↓	114.30	↓		
94.28	0	115.57	↓		
124.46	↓	116.84	↓		
125.73	↓	121.92	↓		
		125.73	↓		
		109.22	-11.81		
		121.92	↓		
		125.73	↓		
		99.06	-13.36		
		110.79	-13.66		
		121.92	↓		
		125.73	↓		

TABLE 2.– SURFACE INSTRUMENTATION LOCATIONS FOR INLET MODELS – Continued

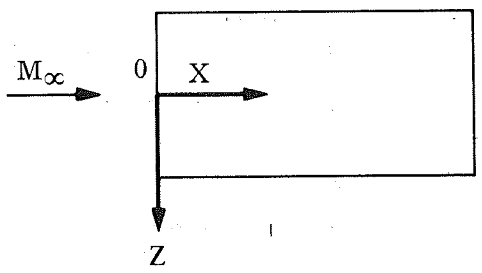

(d) P12 inlet centerbody

(48) Pressure orifices				(14) Thermocouples	
X, cm	*Z*, cm	*X*, cm	*Z*, cm	*X*, cm	*Z*, cm
109.22	13.66	113.67	–2.54	124.46	13.66
121.92	↓	114.94	↓	↓	9.96
126.75	↓	116.20	↓	↓	6.25
99.06	13.36	118.11	↓	96.52	0
109.22	9.96	120.65	↓	101.60	↓
121.92	↓	123.19	↓	106.68	↓
126.75	↓	126.75	↓	111.76	↓
105.41	6.25	106.04	–5.32	115.57	↓
106.68	↓	107.32	↓	118.11	↓
107.95	↓	108.58	↓	120.65	↓
109.22	↓	109.86	↓	124.46	–2.54
110.49	↓	111.12	↓	↓	–8.10
111.76	↓	112.40	↓	↓	–11.81
121.92	↓	121.92	–8.10	↓	–13.66
126.75	↓	126.75	–8.10		
113.03	2.54	109.22	–11.81		
114.30	↓	121.92	↓		
115.57	↓	126.75	↓		
116.84	↓	99.06	–13.36		
119.38	↓	110.79	–13.66		
121.92	↓	121.92	↓		
124.46	↓	126.75	↓		
126.75	↓				
94.28	0				
124.46	↓				
126.75	↓				

TABLE 2.– SURFACE INSTRUMENTATION LOCATIONS FOR INLET MODELS – Continued

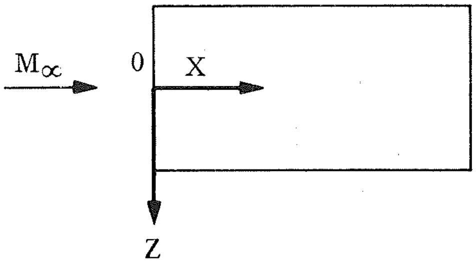

(e) P2 inlet cowl

(66) Pressure orifices				(16) Thermocouples	
X, cm	*Z*, cm	*X*, cm	*Z*, cm	*X*, cm	*Z*, cm
87.32	13.66	91.92	-2.54	90.63	13.66
115.32	↓	94.03	↓	118.06	13.66
119.48	↓	94.08	↓	98.65	13.36
96.16	13.36	96.52	↓	106.81	13.36
104.78	13.36	99.06	↓	118.06	9.96
87.32	9.96	100.43	↓	118.06	6.25
96.16	↓	101.60	↓	91.95	0
104.78	↓	102.54	↓	95.00	↓
115.32	↓	104.14	↓	98.60	↓
119.48	↓	106.68	↓	102.44	↓
87.32	6.25	115.57	↓	106.81	↓
96.16	↓	87.32	-8.10	113.64	↓
104.78	↓	96.16	↓	118.06	-2.54
115.32	↓	104.78	↓	↓	-8.10
119.48	↓	107.95	↓	↓	-11.81
87.32	2.54	109.23	↓	↓	-13.66
90.63	↓	110.49	↓		
96.16	↓	111.76	↓		
98.65	↓	113.03	↓		
104.78	↓	114.30	↓		
106.81	↓	115.32	↓		
112.27	↓	119.48	↓		
115.32	↓	118.11	-8.61		
118.06	↓	87.32	-11.81		
119.48	↓	96.16	↓		
85.55	0	104.78	↓		
118.06	↓	115.32	↓		
119.48	↓	119.48	↓		
83.31	-2.54	96.16	-13.36		
83.57	↓	104.78	-13.36		
85.65	↓	87.32	-13.66		
88.65	↓	115.32	↓		
91.44	↓	119.48	↓		

TABLE 2.– SURFACE INSTRUMENTATION LOCATIONS FOR INLET MODELS – Continued

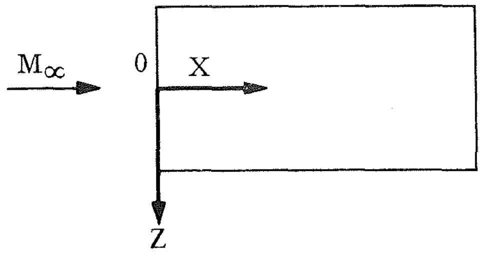

(f) P8 inlet cowl

(69) Pressure orifices				(16) Thermocouples	
X, cm	Z, cm	X, cm	Z, cm	X, cm	Z, cm
90.93	13.66	104.14	-2.54	91.44	13.66
111.76	↓	106.68	↓	116.84	↓
121.92	↓	110.62	↓	124.46	↓
126.14	↓	113.16	↓	101.60	13.36
99.06	13.36	114.30	↓	124.46	9.96
90.93	9.96	116.84	↓	124.46	6.25
99.06	↓	119.38	↓	92.25	0
109.22	↓	123.19	↓	96.52	↓
121.92	↓	126.14	↓	101.60	↓
126.14	↓	90.93	-8.10	106.68	↓
90.93	6.25	99.06	↓	111.76	↓
99.06	↓	101.60	↓	116.84	↓
109.22	↓	104.14	↓	124.46	-2.54
121.92	↓	106.68	↓	↓	-8.10
126.14	↓	110.49	↓	↓	-11.81
90.93	2.54	111.76	↓	↓	-13.66
95.12	↓	113.03	↓		
99.06	↓	115.57	↓		
101.60	↓	118.11	↓		
105.46	↓	120.65	↓		
109.22	↓	121.92	↓		
111.76	↓	125.73	↓		
115.57	↓	126.14	↓		
118.11	↓	124.46	-8.61		
120.65	↓	90.93	-11.81		
121.92	↓	99.06	↓		
124.46	↓	104.14	↓		
126.14	↓	121.92	↓		
85.09	0	126.14	↓		
125.73	↓	99.06	-13.36		
126.14	↓	90.93	-13.66		
83.18	-2.54	105.71	↓		
93.98	↓	121.92	↓		
96.52	↓	126.14	↓		
100.58	↓				

TABLE 2.– SURFACE INSTRUMENTATION LOCATIONS FOR INLET MODELS – Concluded

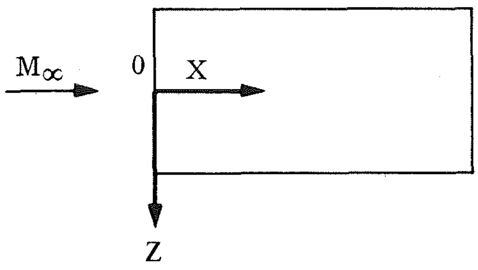

(g) P12 inlet cowl

(59) Pressure orifices				(16) Thermocouples	
X, cm	Z, cm	X, cm	Z, cm	X, cm	Z, cm
90.93	13.66	83.18	-2.54	91.44	13.66
111.76	↓	93.98	↓	116.84	↓
121.92	↓	96.52	↓	124.46	↓
127.20	↓	100.58	↓	101.60	13.36
99.06	13.36	104.14	↓	124.46	9.96
90.93	9.96	106.68	↓	124.46	6.25
99.06	↓	110.62	↓	92.25	0
109.22	↓	113.16	↓	96.52	↓
121.92	↓	114.30	↓	101.60	↓
127.20	↓	116.84	↓	106.68	↓
90.93	6.25	119.38	↓	111.76	↓
99.06	↓	123.19	↓	116.84	↓
109.22	↓	127.20	↓	124.46	-2.54
121.92	↓	90.93	-8.10	↓	-8.10
127.20	↓	99.06	↓	↓	-11.81
90.93	2.54	104.14	↓	↓	-13.66
95.12	↓	121.92	↓		
99.06	↓	127.20	↓		
101.60	↓	90.93	-11.81		
105.46	↓	99.06	↓		
109.22	↓	104.14	↓		
111.76	↓	121.92	↓		
115.57	↓	127.20	↓		
118.11	↓	99.06	-13.36		
120.65	↓	90.93	-13.66		
121.92	↓	110.79	↓		
124.46	↓	121.92	↓		
127.20	↓	127.20	↓		
85.09	0				
125.73	↓				
127.20	↓				

TABLE 3.– HEAT-TRANSFER AND WALL-SHEAR DATA

P2 inlet model cowl; station X = 119.38 cm

	τ_w, N/m^2	$\dot{q}$, W/m^2×10^{-4}
Analysis: Laminar	15.3	0.41
Turbulent	138.4	6.58
Experiment	21.5–23.9	0.83–0.86

P8 inlet model cowl; station X = 120.02 cm

	τ_w, N/m^2	$\dot{q}$, W/m^2×10^{-4}
Analysis: Laminar	15.3	0.94
Turbulent	456.8	22.81
Experiment	221.2	10.55

TABLE 4.– INDEX TO FIGURES

TABLE 4.– INDEX TO FIGURES – Continued

TABLE 4.– INDEX TO FIGURES – Continued

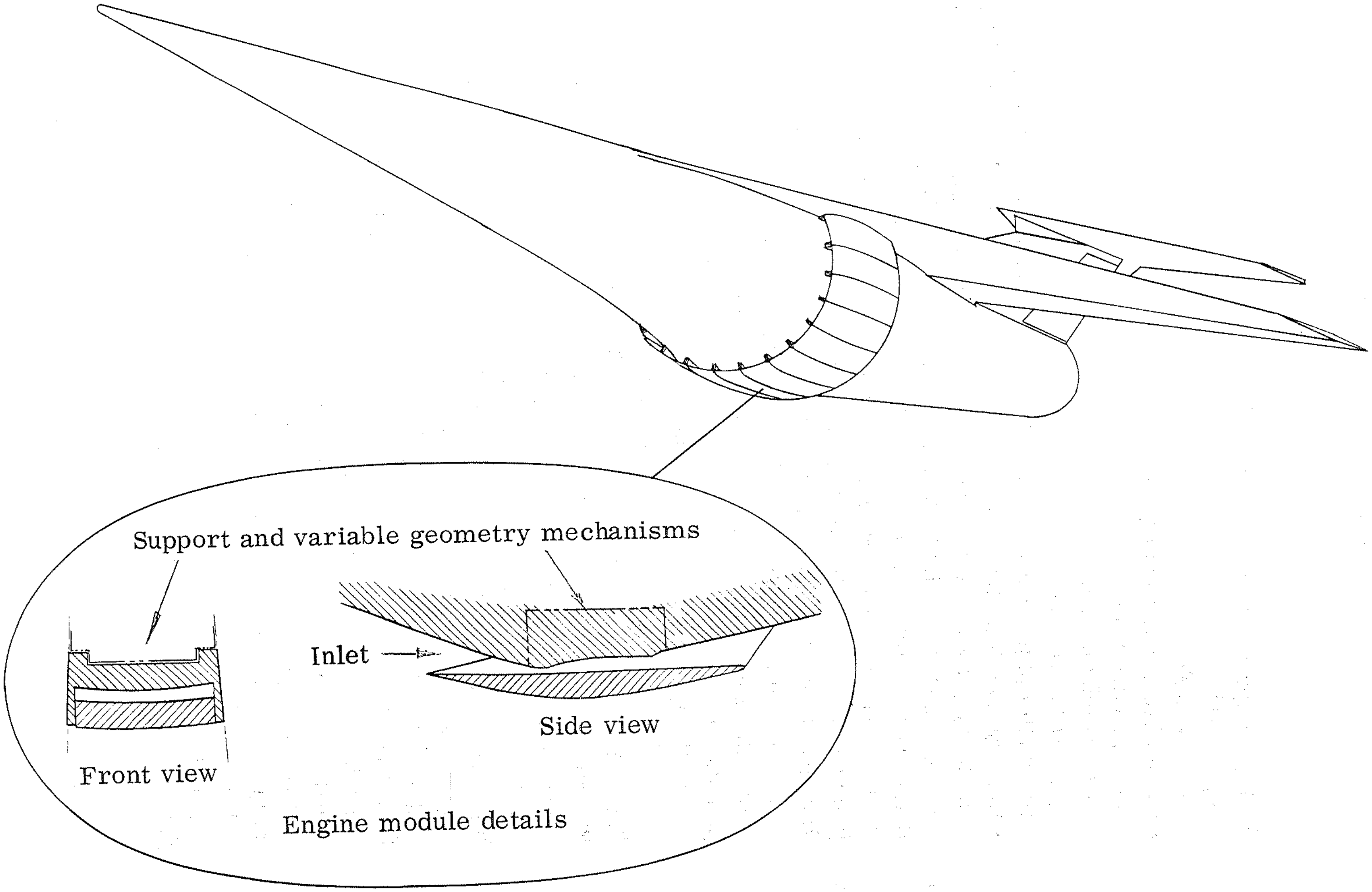

Figure 1.– Hypersonic cruise vehicle for Mach number 10 to 12.

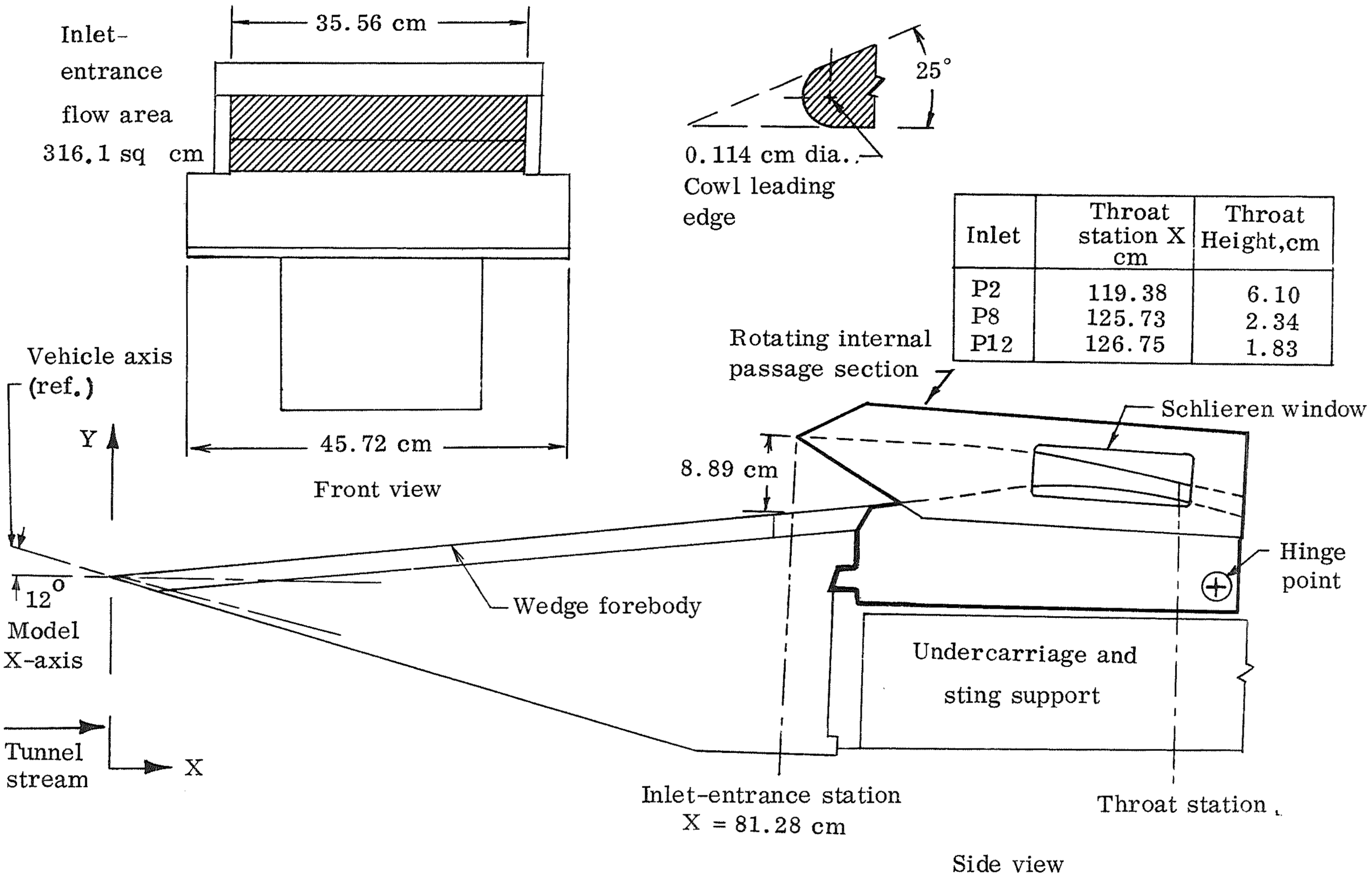

Inlet	Throat station X cm	Throat Height,cm
P2	119.38	6.10
P8	125.73	2.34
P12	126.75	1.83

Figure 2.– Schematic representation of inlet model.

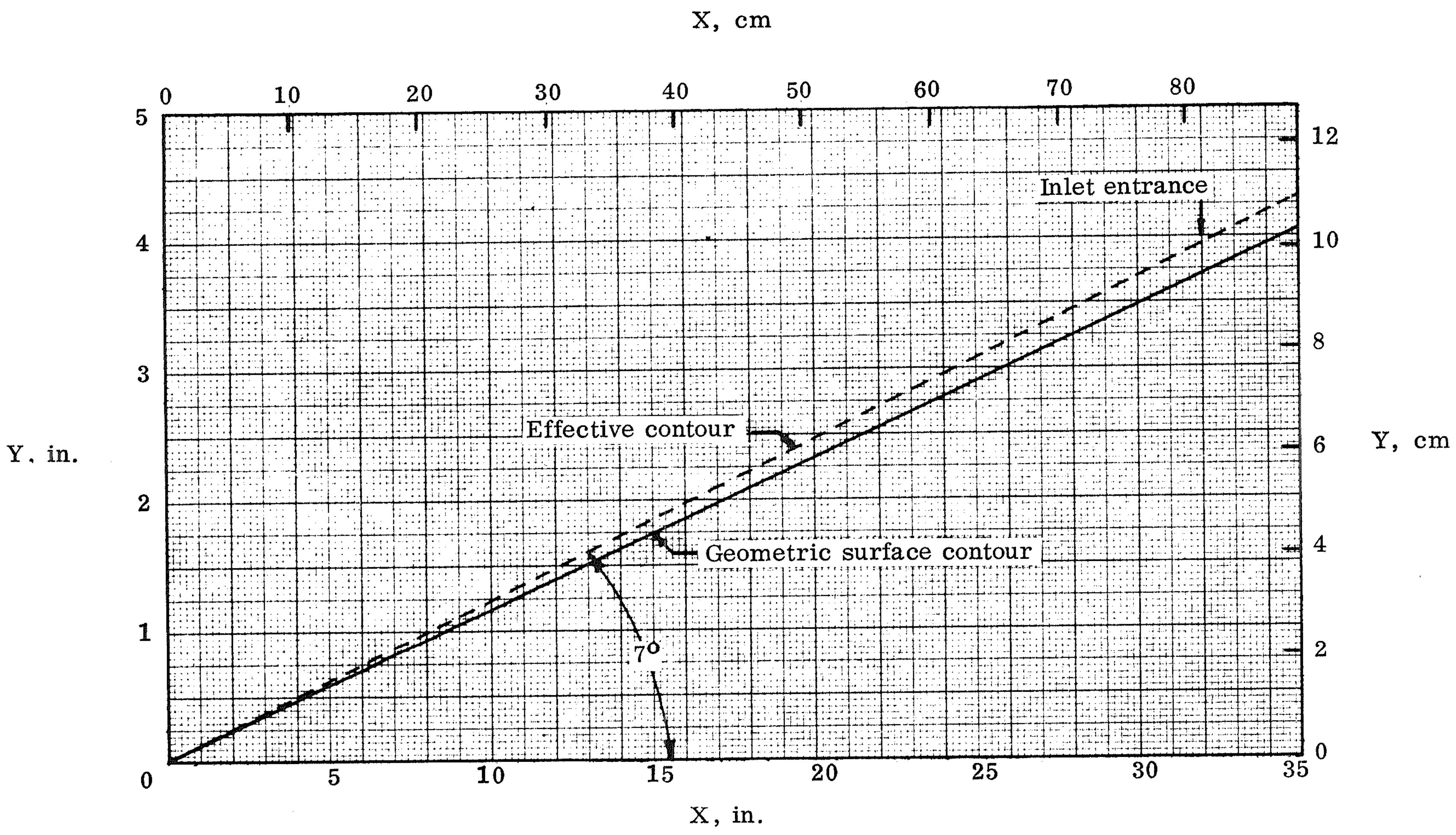

Figure 3.– Effective and geometric coordinates for wedge forebody.

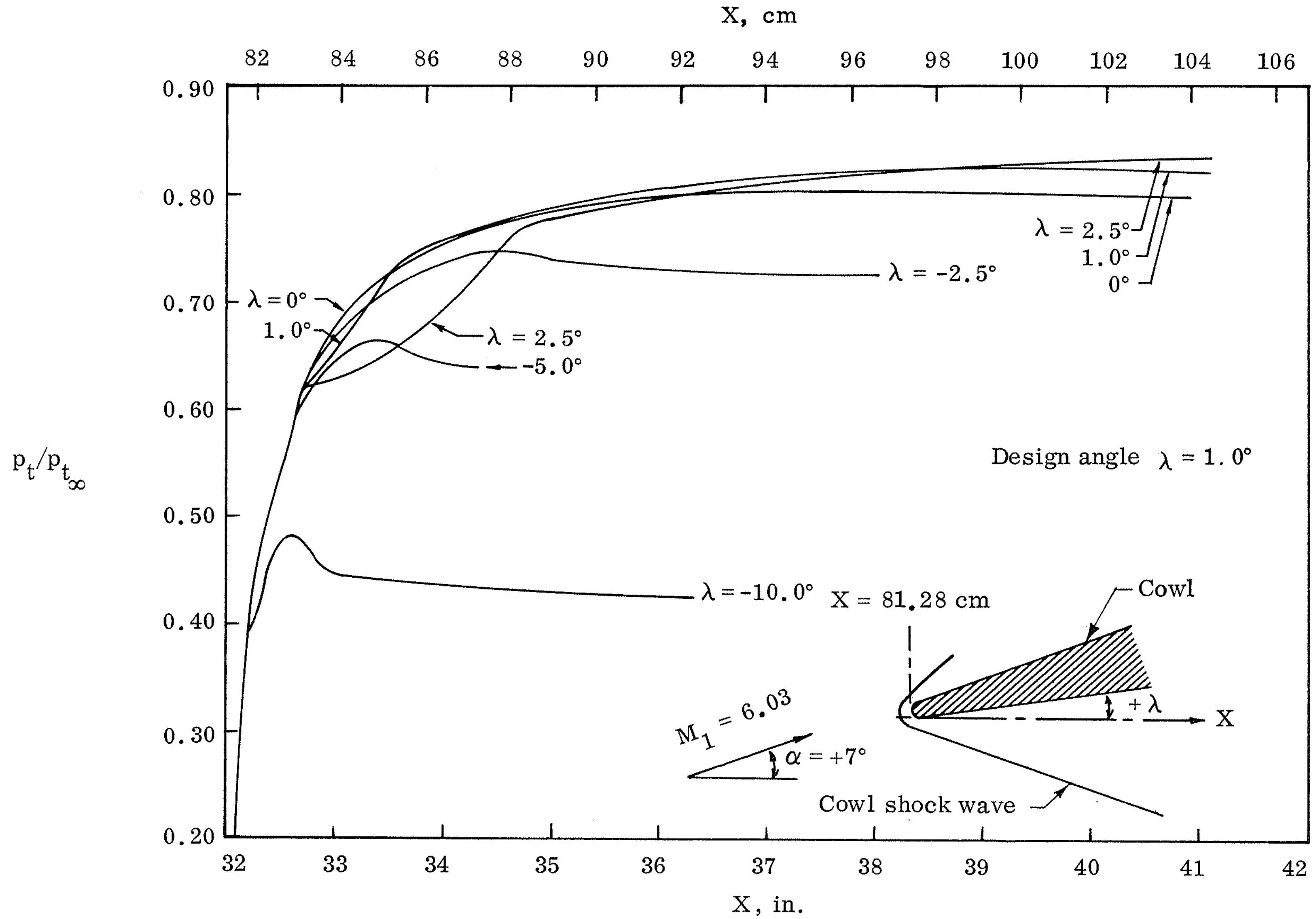

Figure 4.– Total-pressure recovery across shock waves from wedge forebody and cowl leading edge.

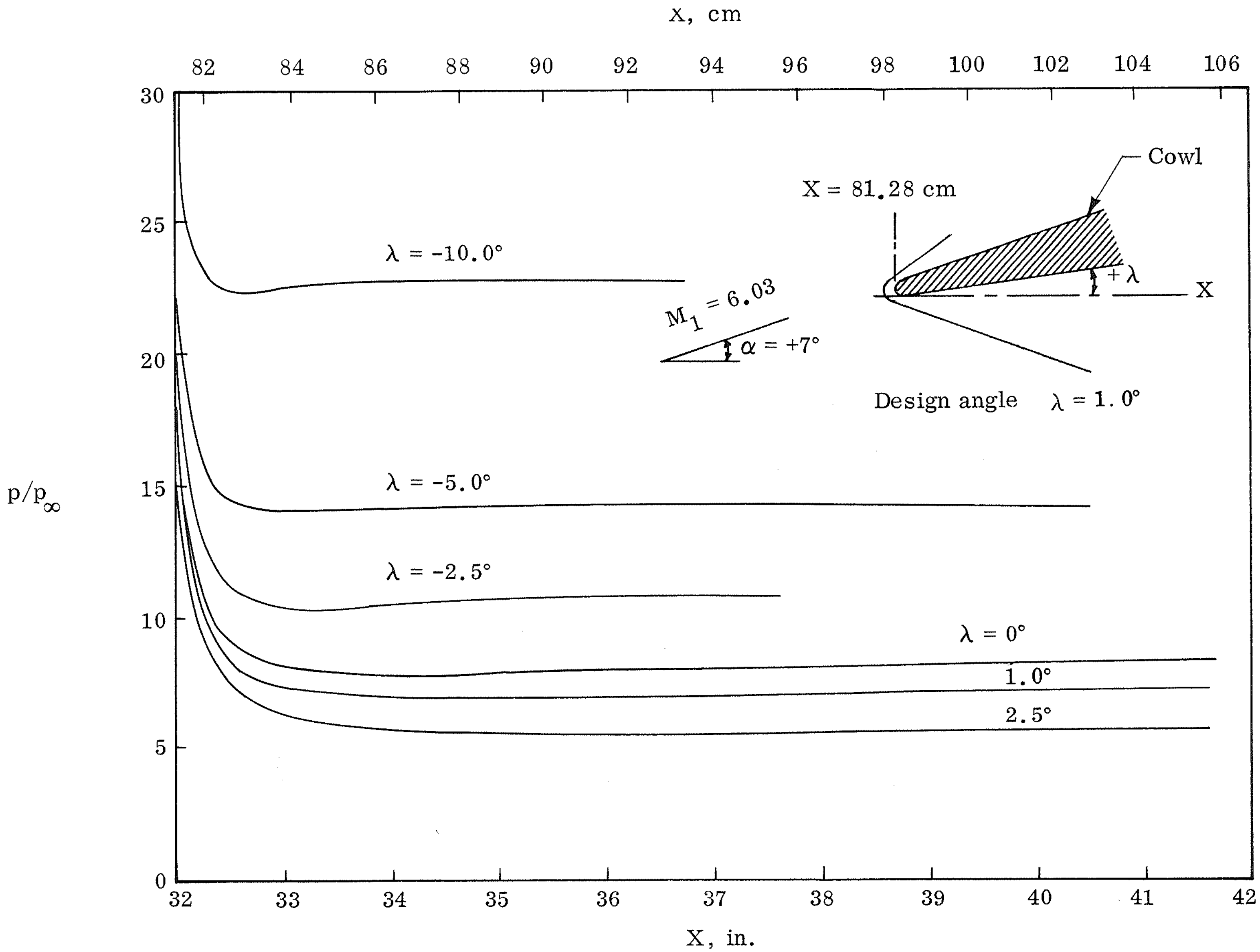

Figure 5.– Surface pressure distributions for blunt cowl leading edge.

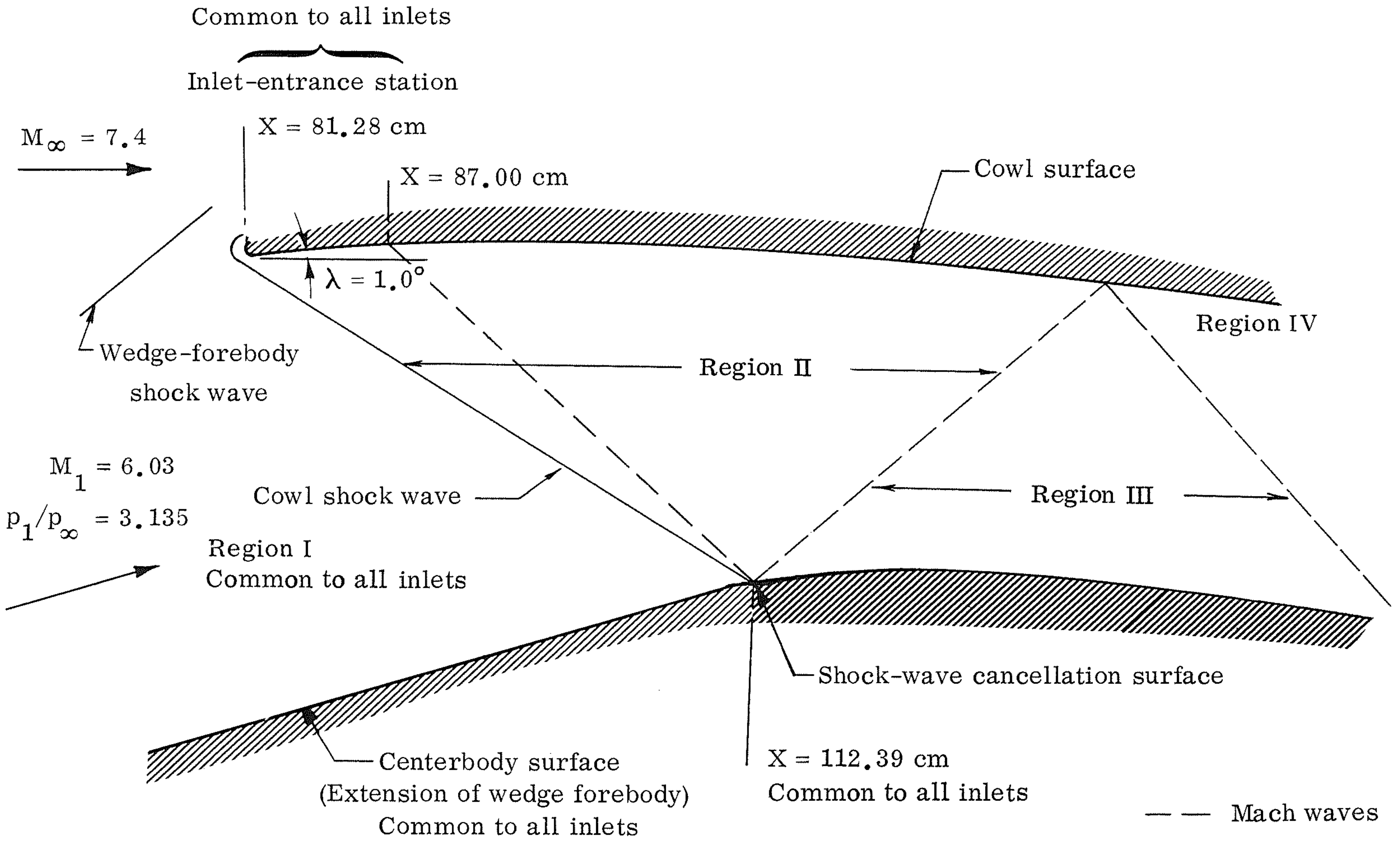

Figure 6.– Region specification for internal contour design.

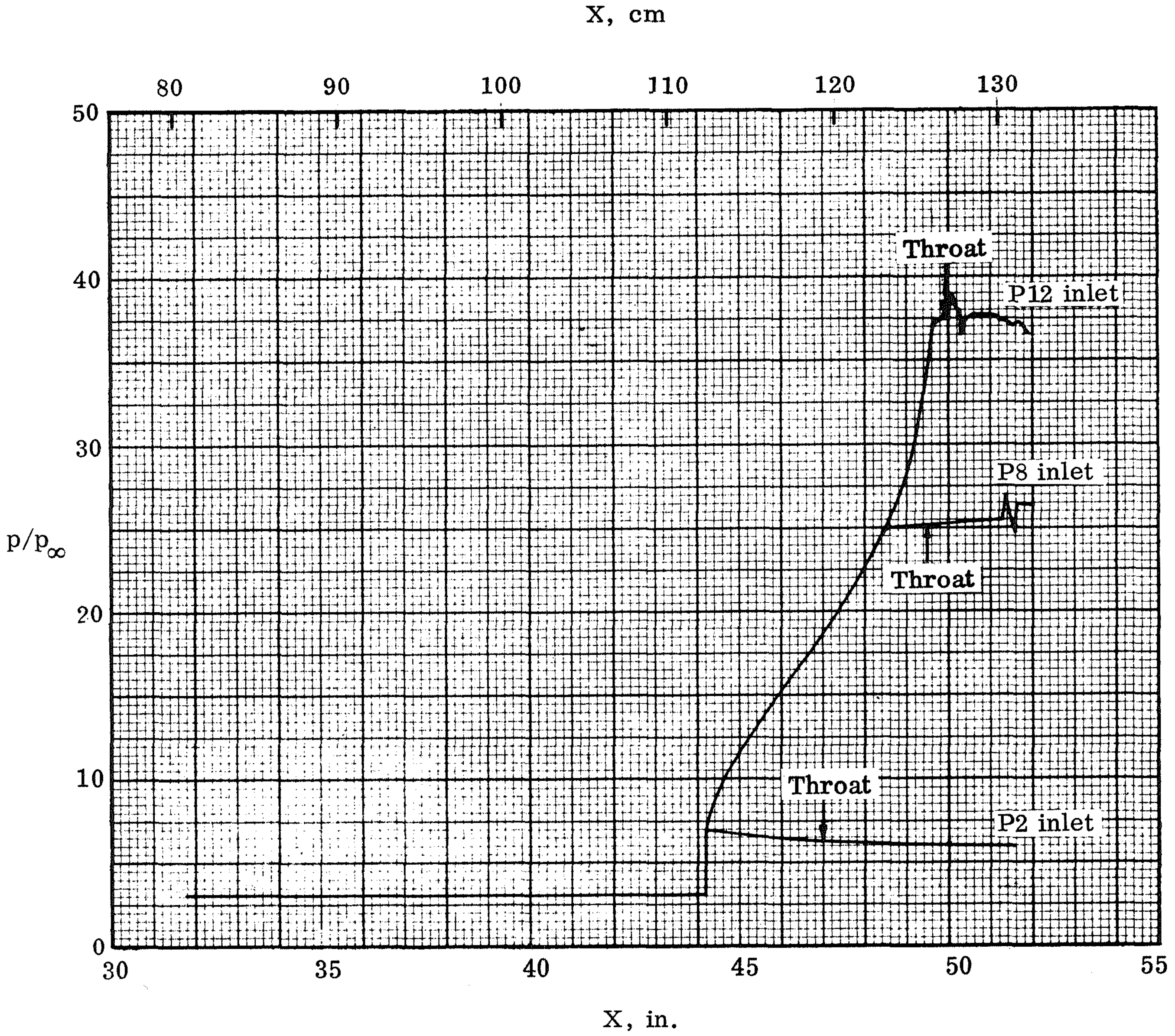

Figure 7.– Predicted surface pressure distributions; inlet centerbodies.

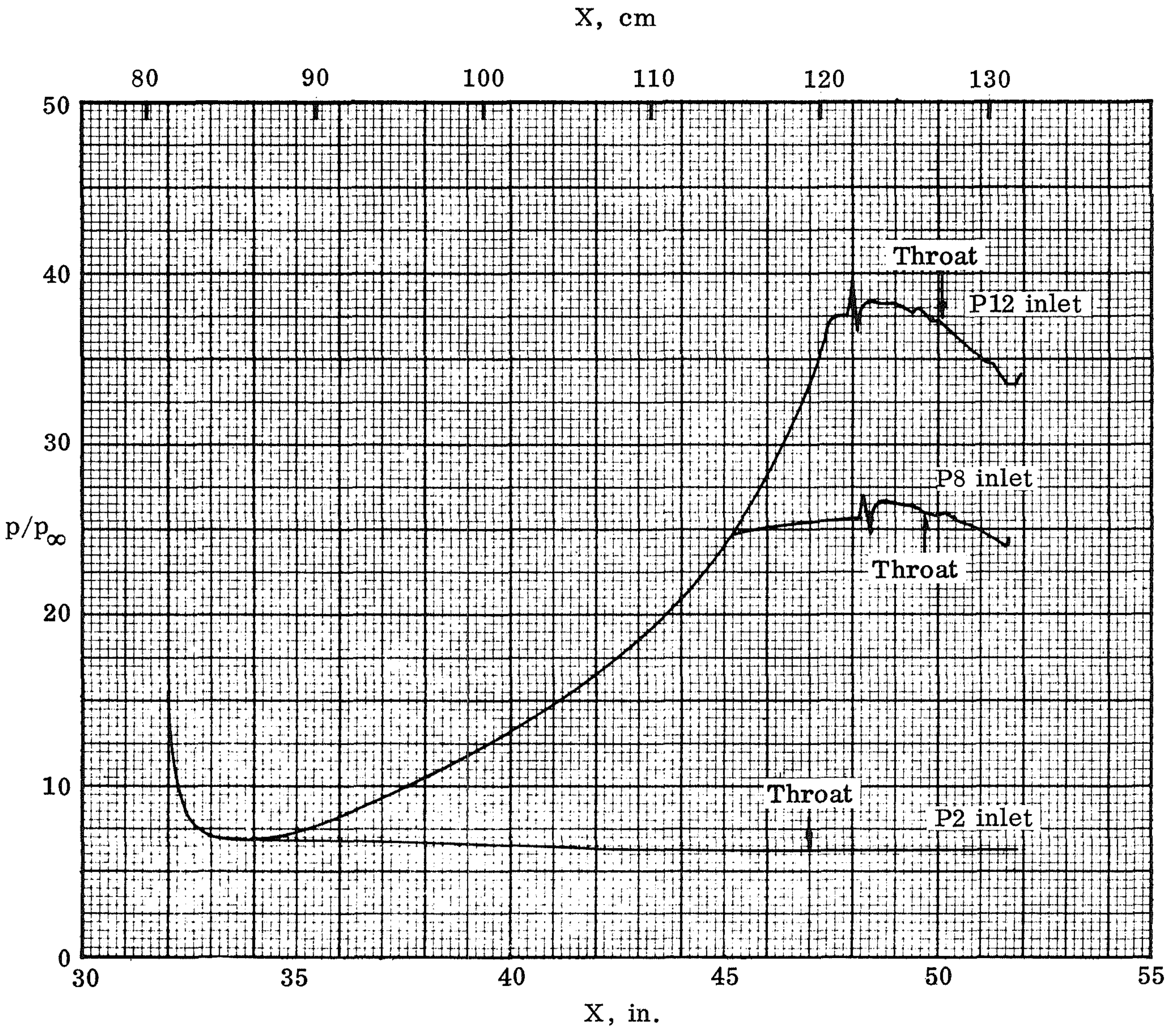

Figure 8.– Predicted surface pressure distributions; inlet cowls.

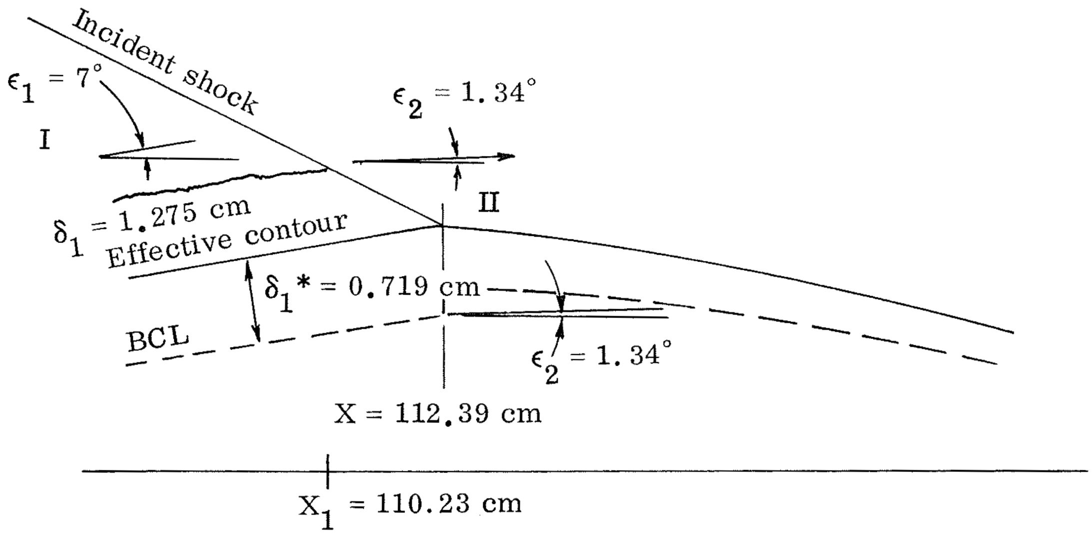

(a) Definition of basic contour line and angle ϵ_2.

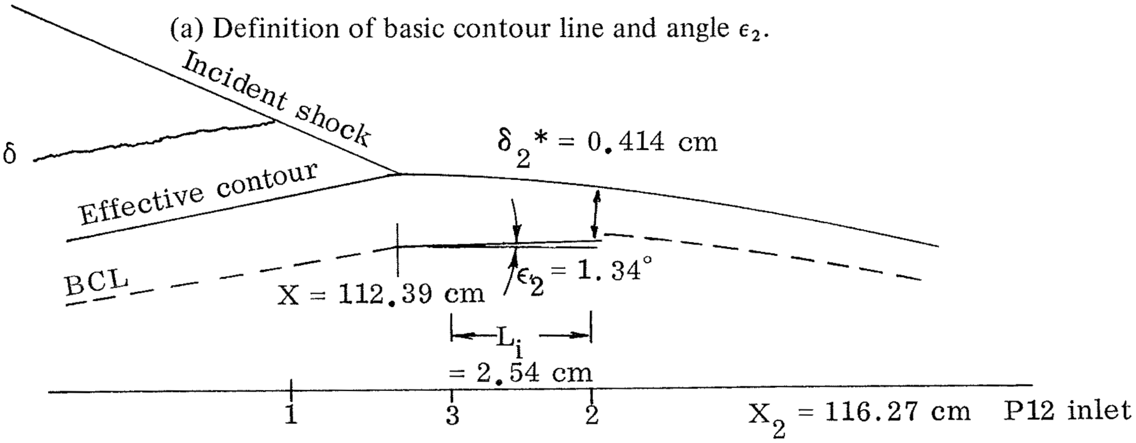

(b) Location of stations 2 and 3.

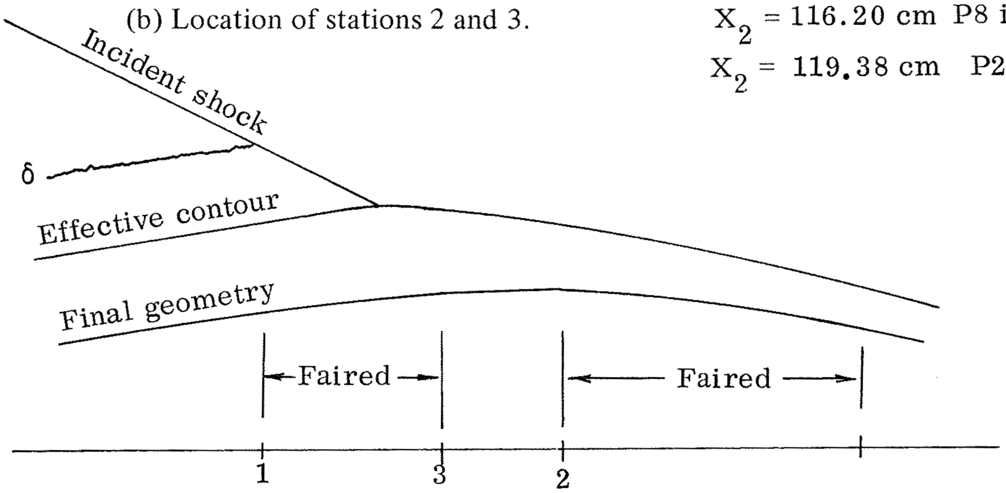

(c) Definition of final geometric contour.

Figure 9.– Centerbody contour design through shock-wave cancellation region.

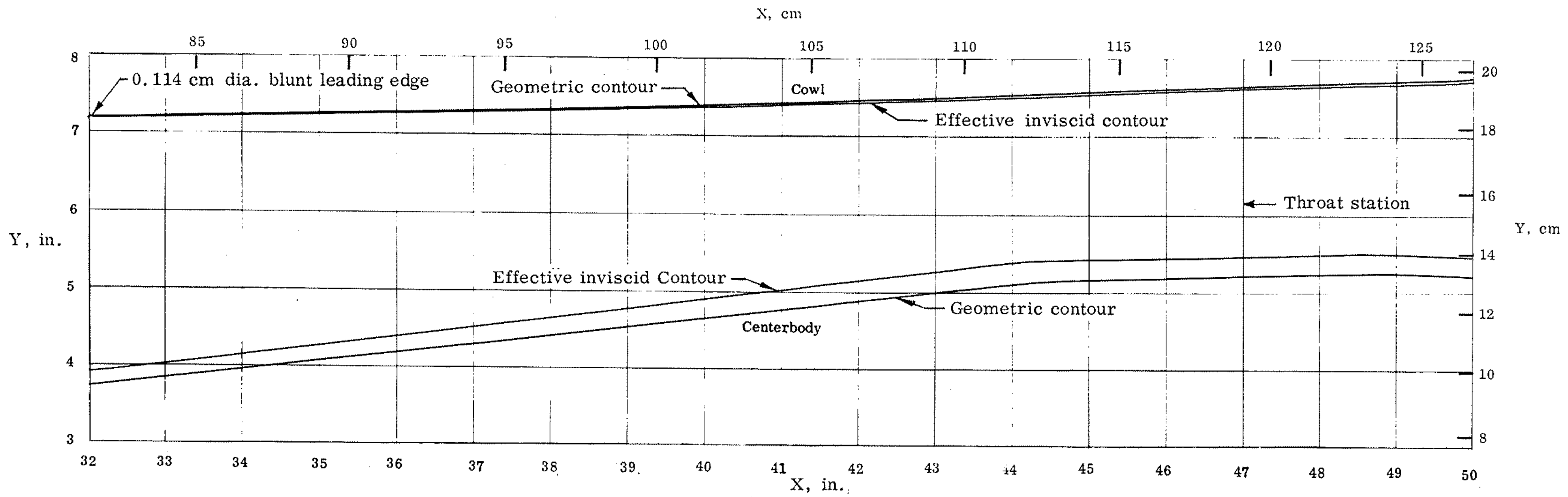

(a) P2 inlet.

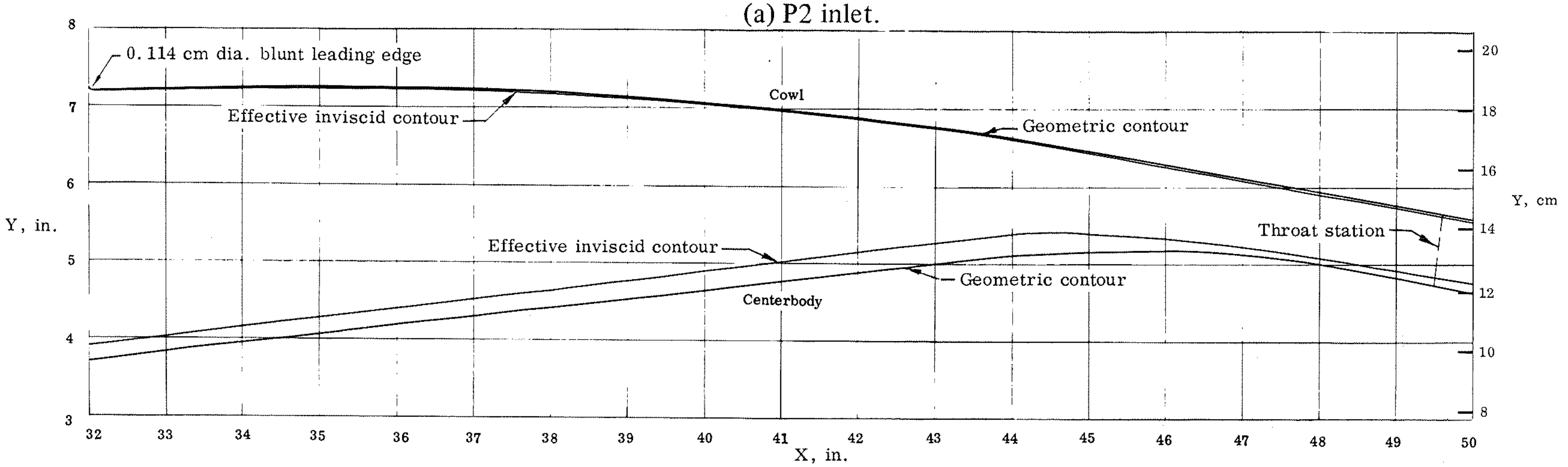

(b) P8 inlet.

Figure 10.– Effective and geometric coordinates for internal passages.

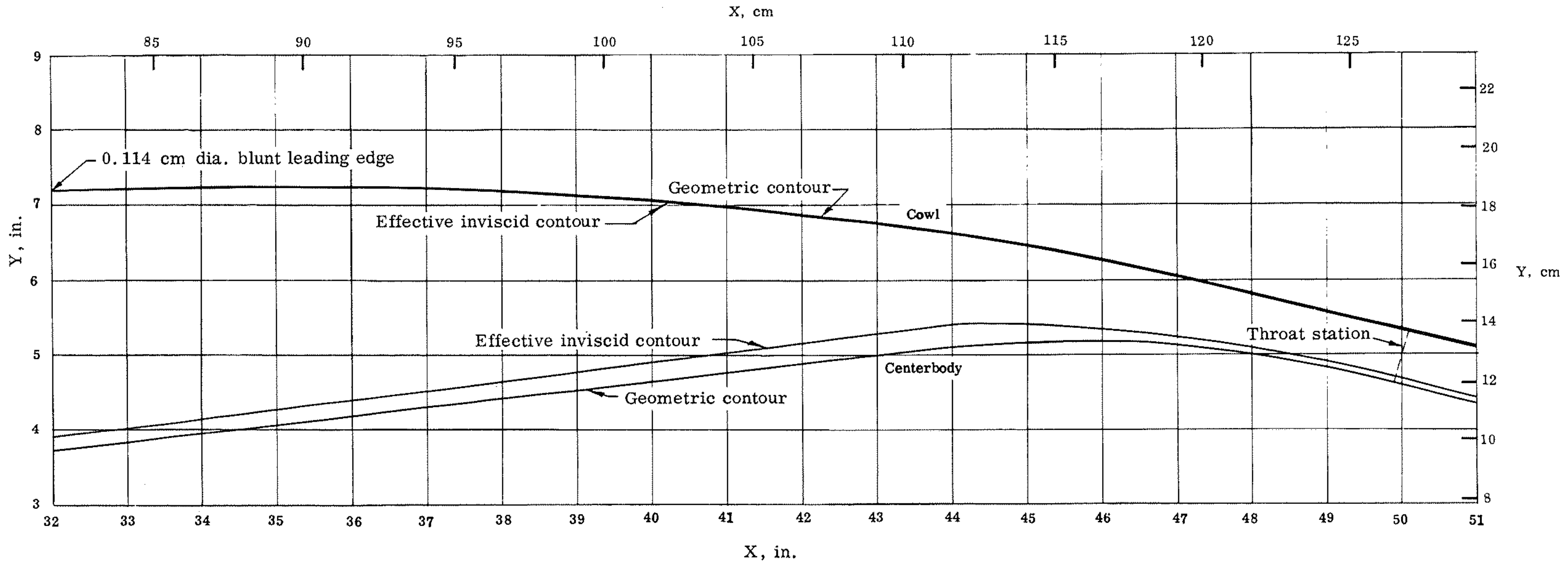

(c) P12 inlet.

Figure 10.– Concluded.

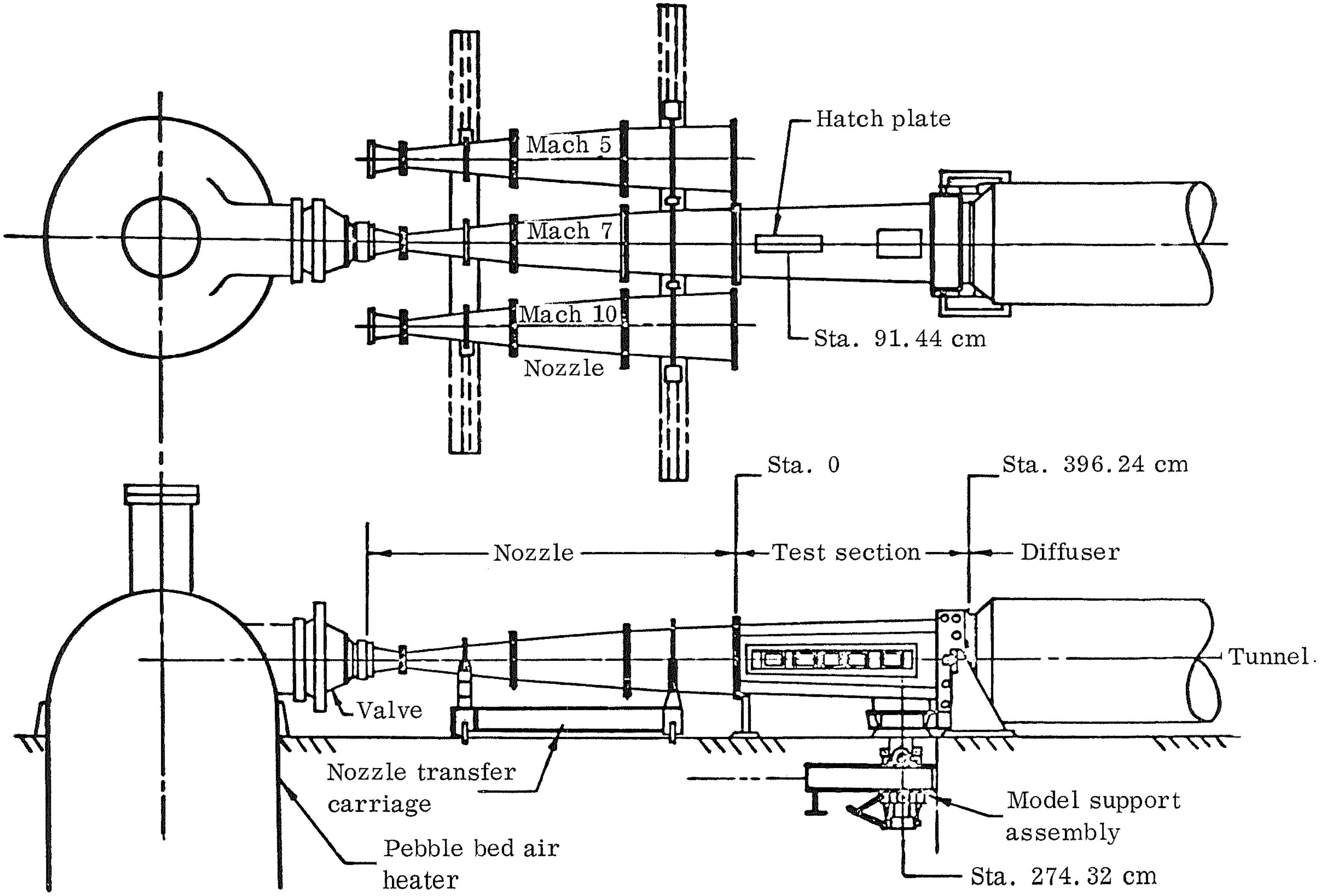

Figure 11.– Schematic representation of Ames 3.5 foot hypersonic wind tunnel.

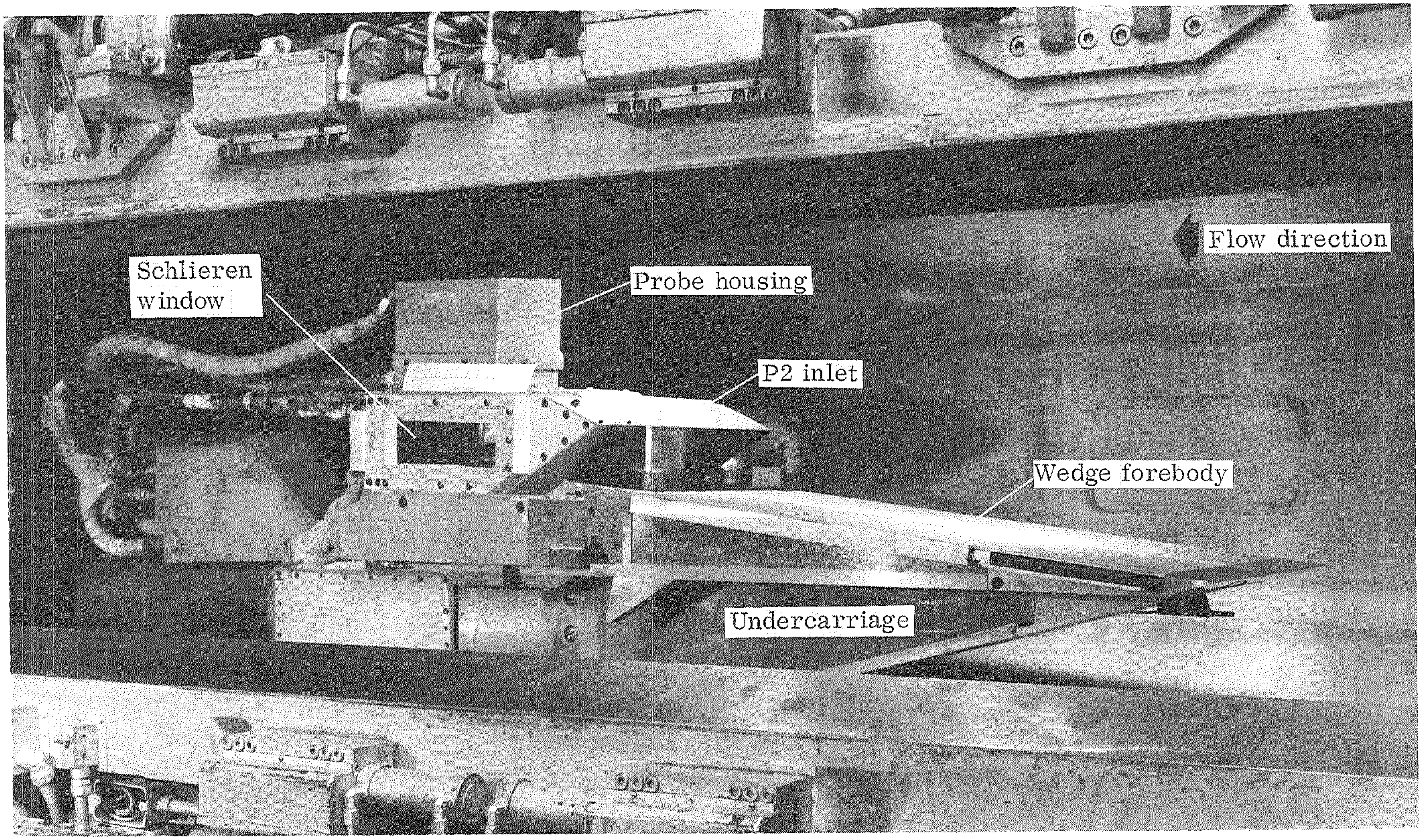

Figure 12.– Wedge forebody and P2 inlet model mounted in 3.5 foot hypersonic wind tunnel.

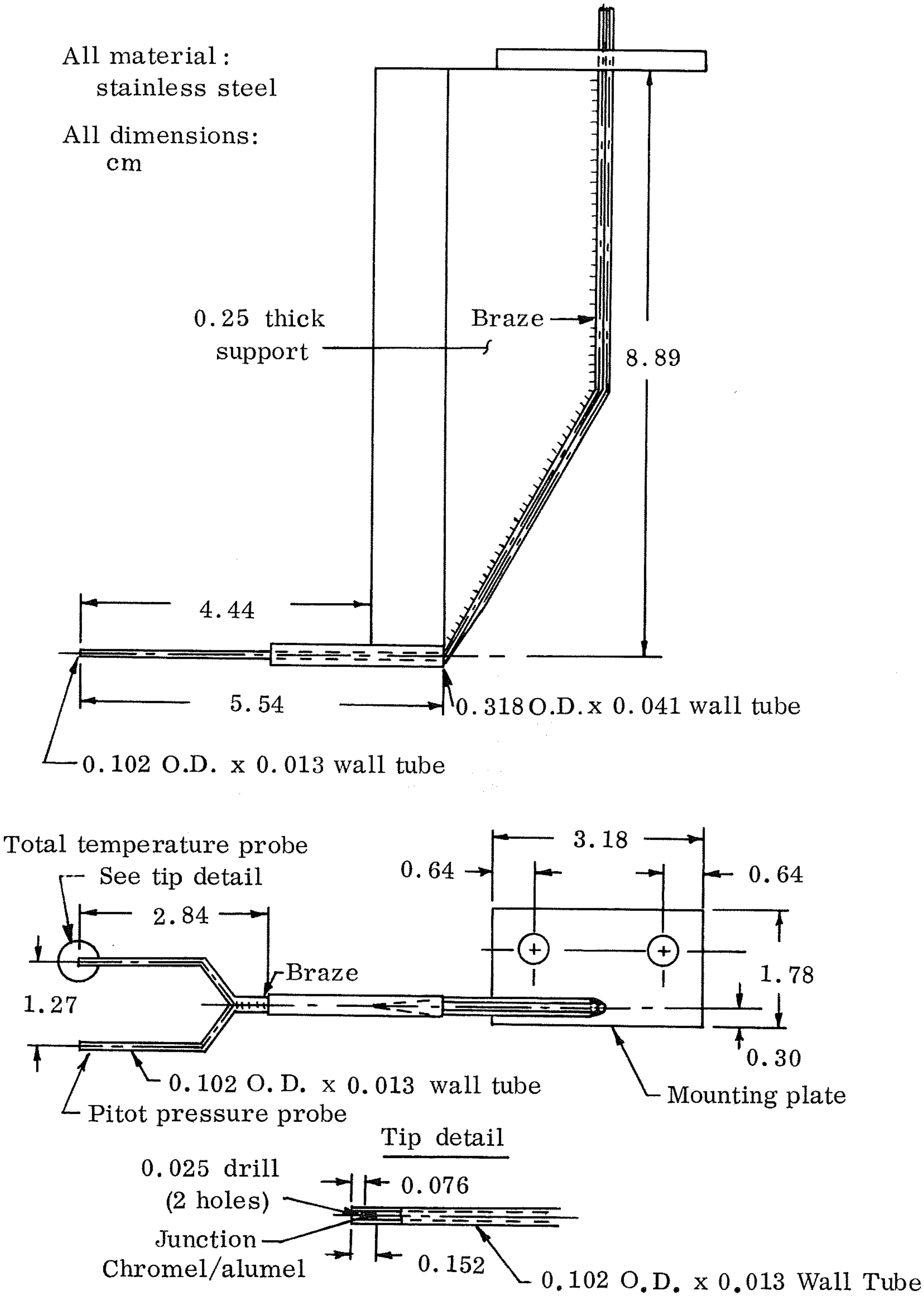

(a) Singly shielded thermocouple probe.

Figure 13.– Singly shielded and exposed thermocouple probes.

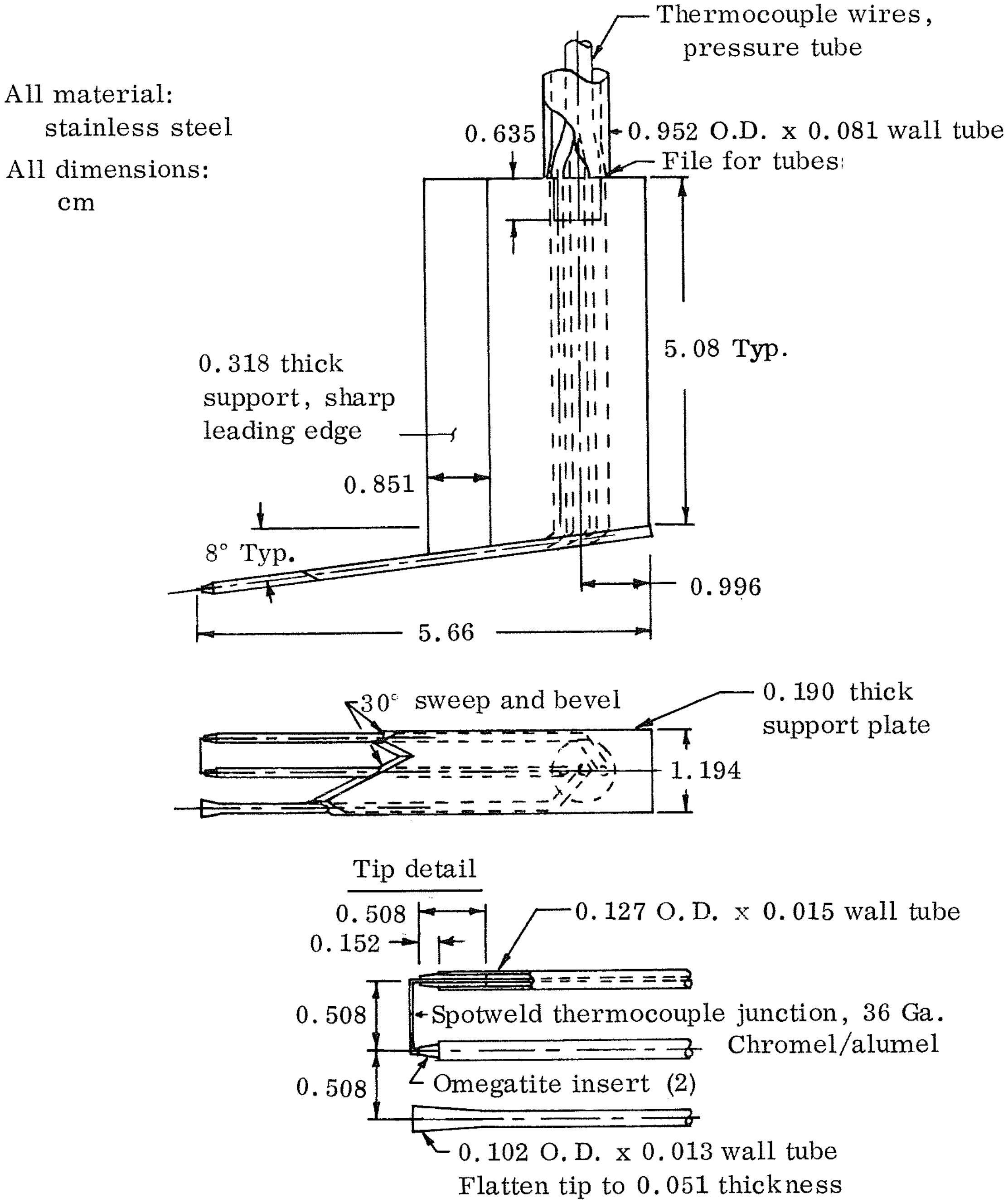

(b) Exposed thermocouple probe.

Figure 13.– Concluded.

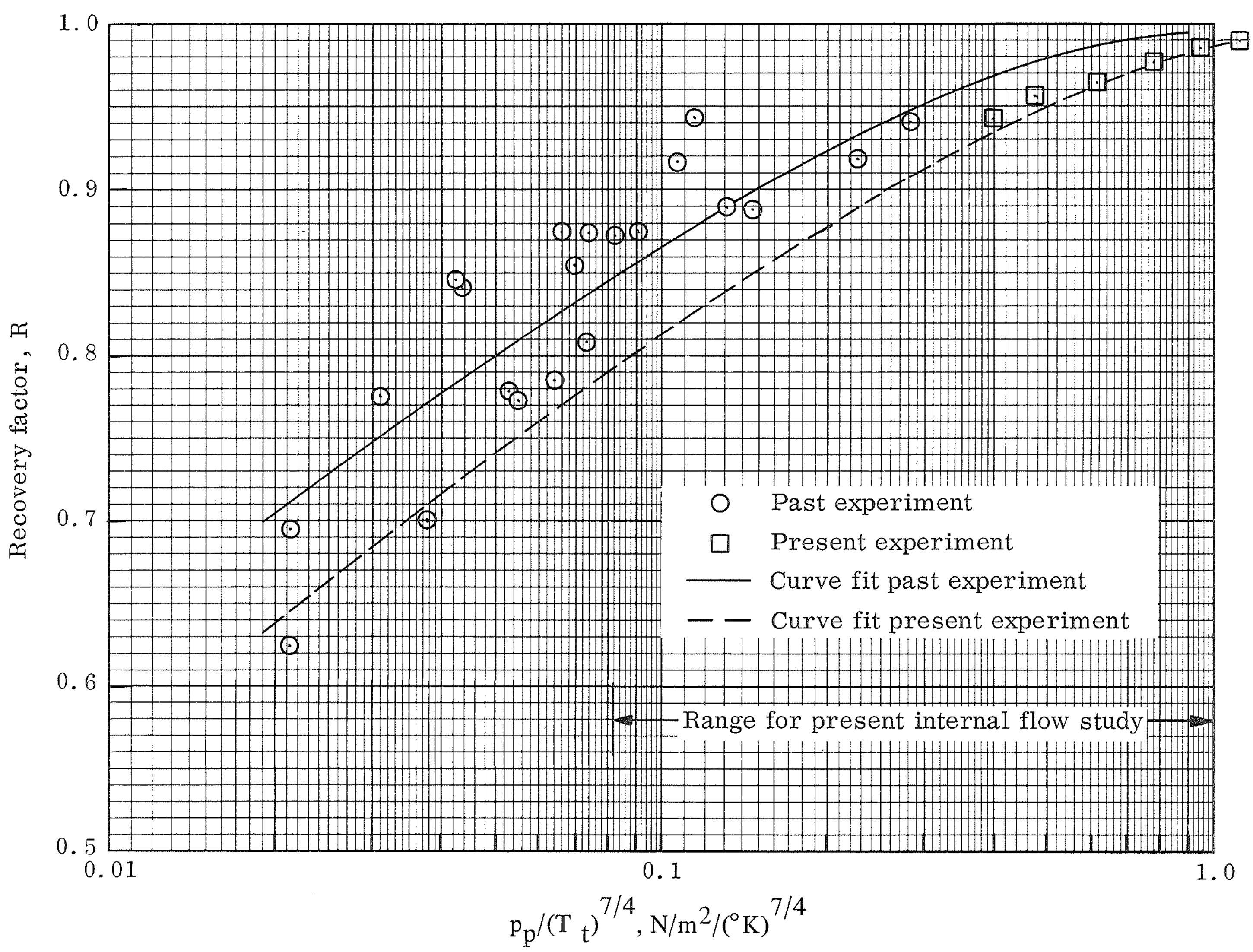

(a) Singly shielded thermocouple probe.

Figure 14.– Recovery factors for singly shielded and exposed thermocouple probes.

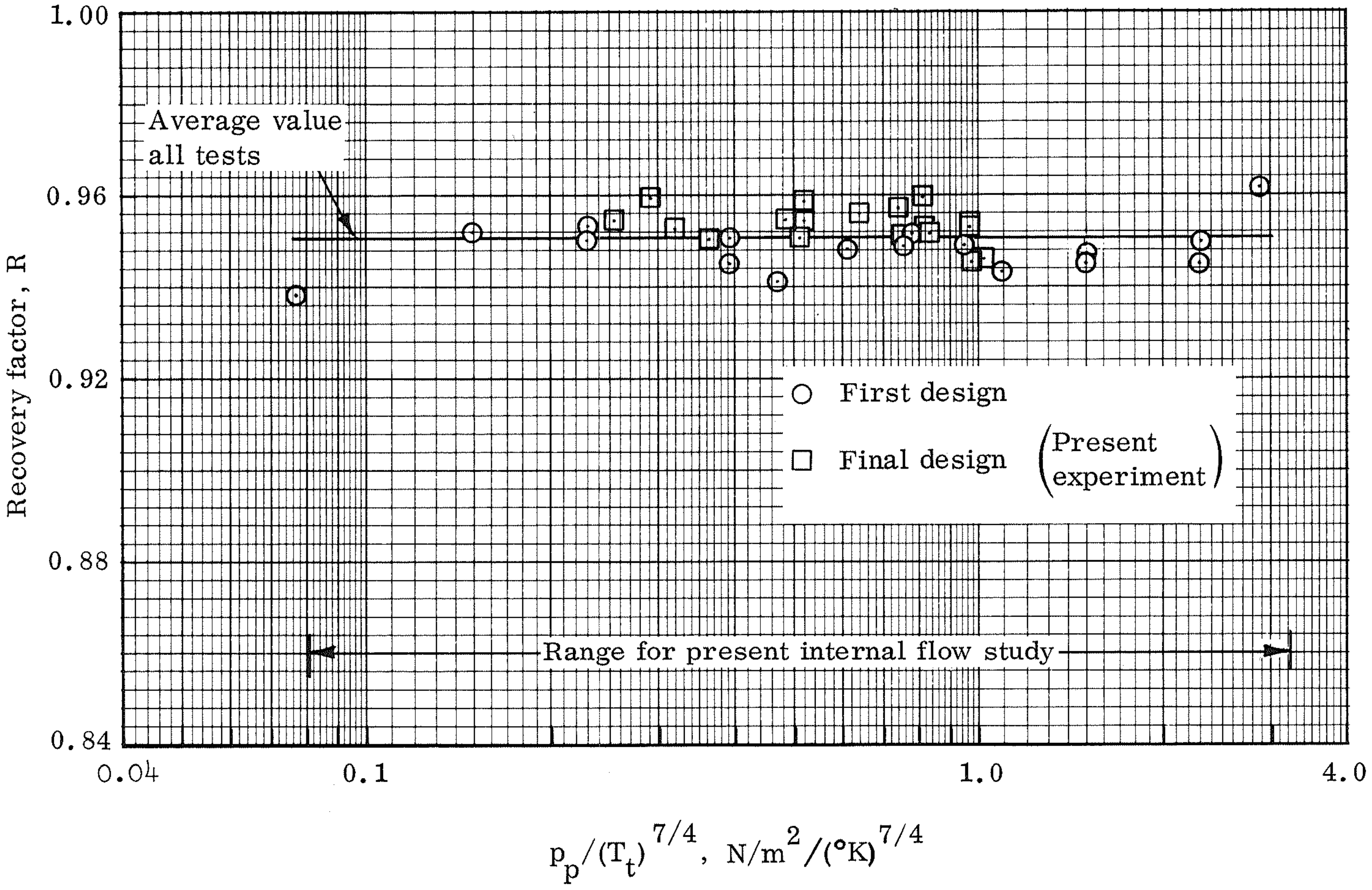

(b) Exposed thermocouple probe.

Figure 14.– Concluded.

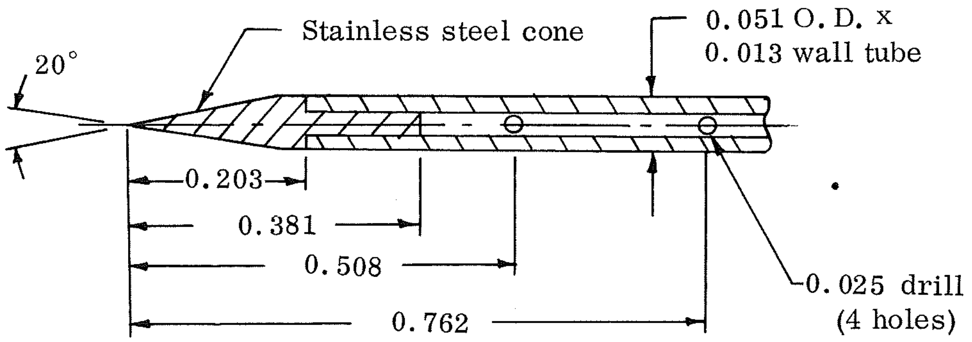

(a) Direct reading.

All dimensions:
cm

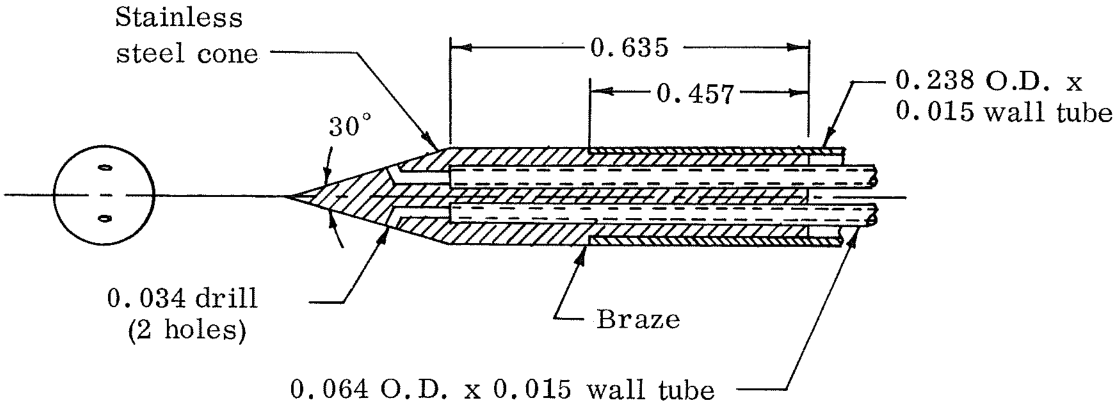

(b) Conical (flow-direction sensitive).

Figure 15.– Static-pressure probes.

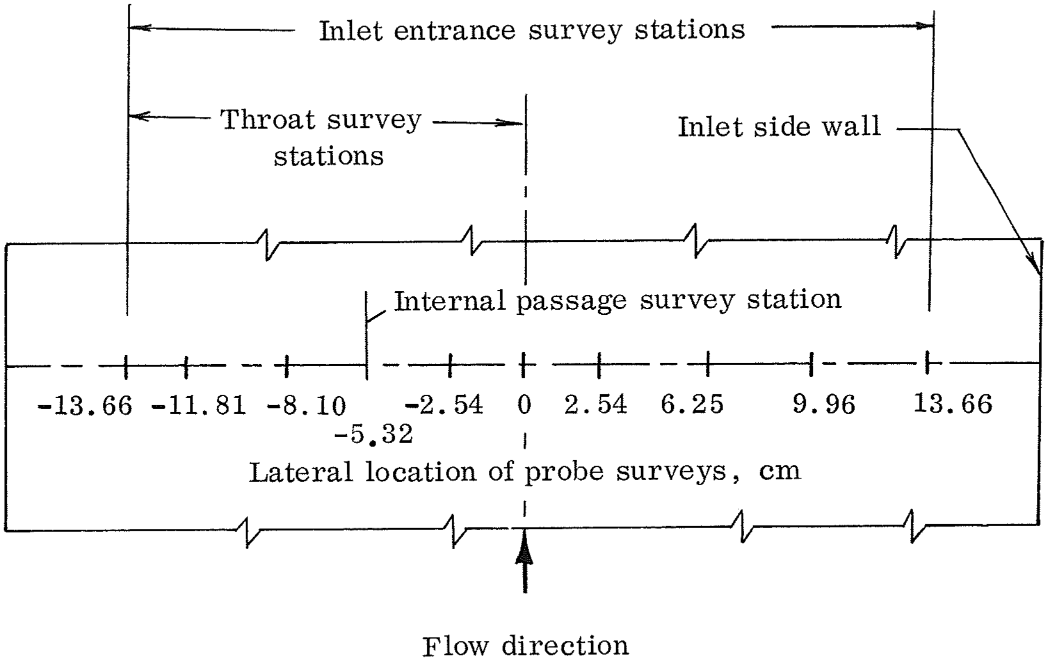

(a) Probe locations – plan view.

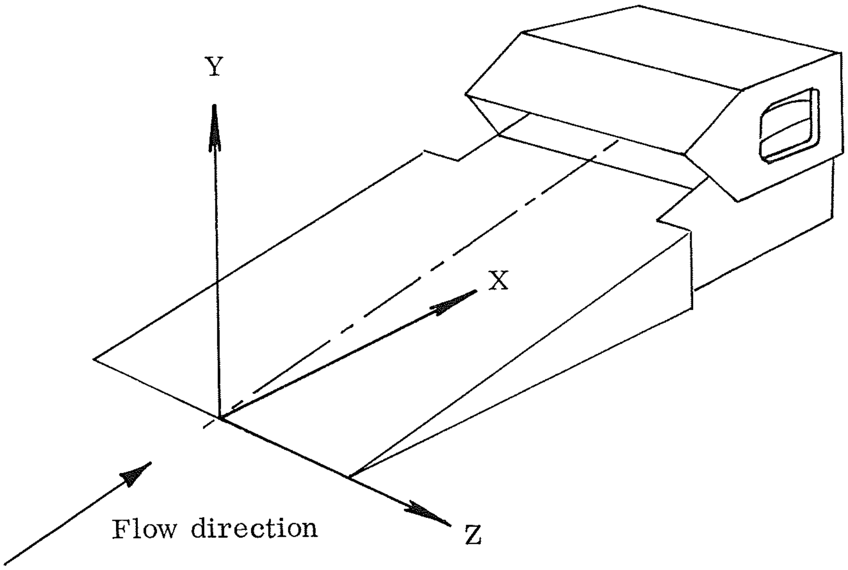

(b) Coordinate system.

Figure 16.– Lateral survey stations and coordinate axes.

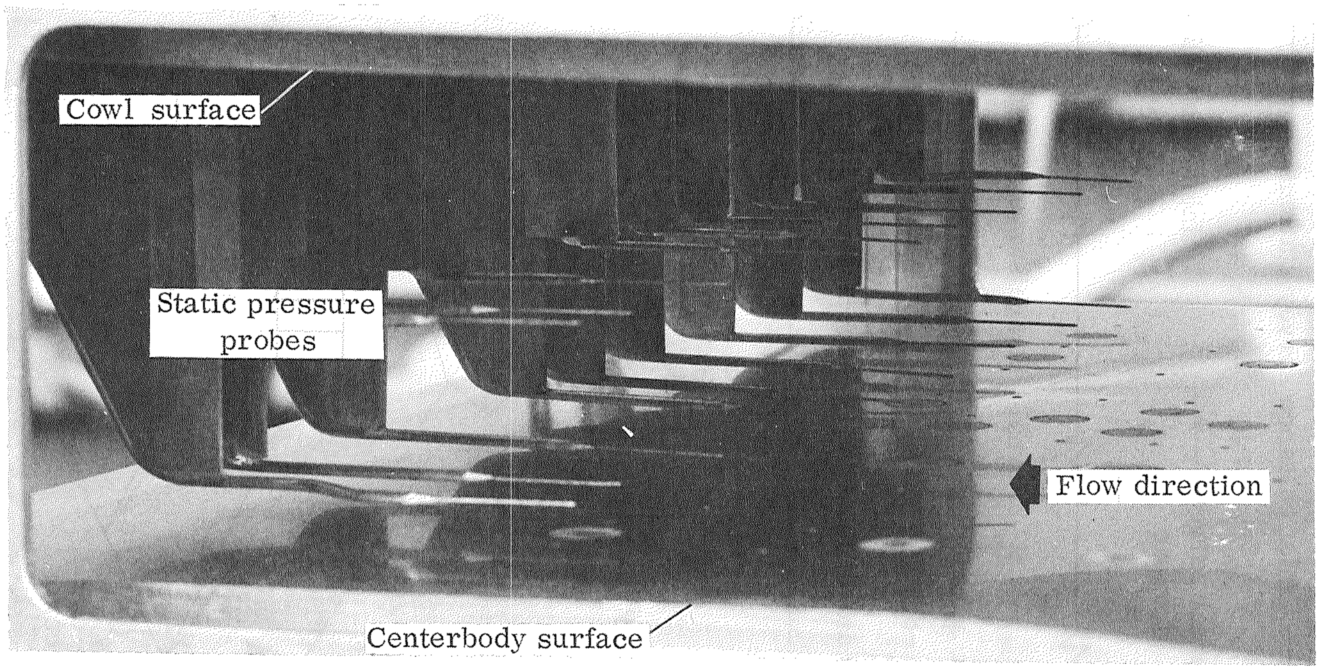

Figure 17.– Static–pressure probes installed at throat station of P2 inlet model.

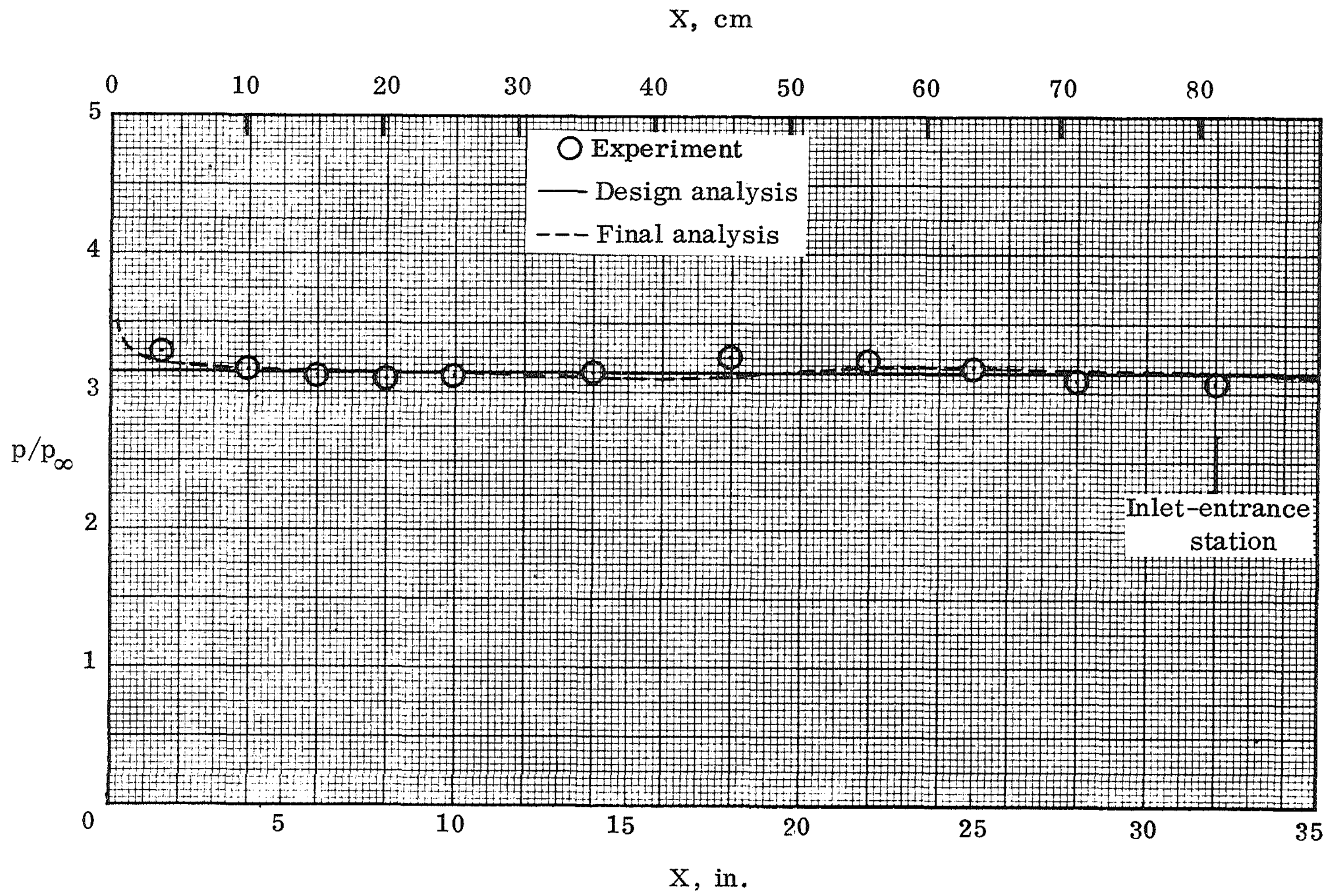

(a) Axial distributions on centerline.

Figure 18.– Surface pressure distributions; wedge forebody.

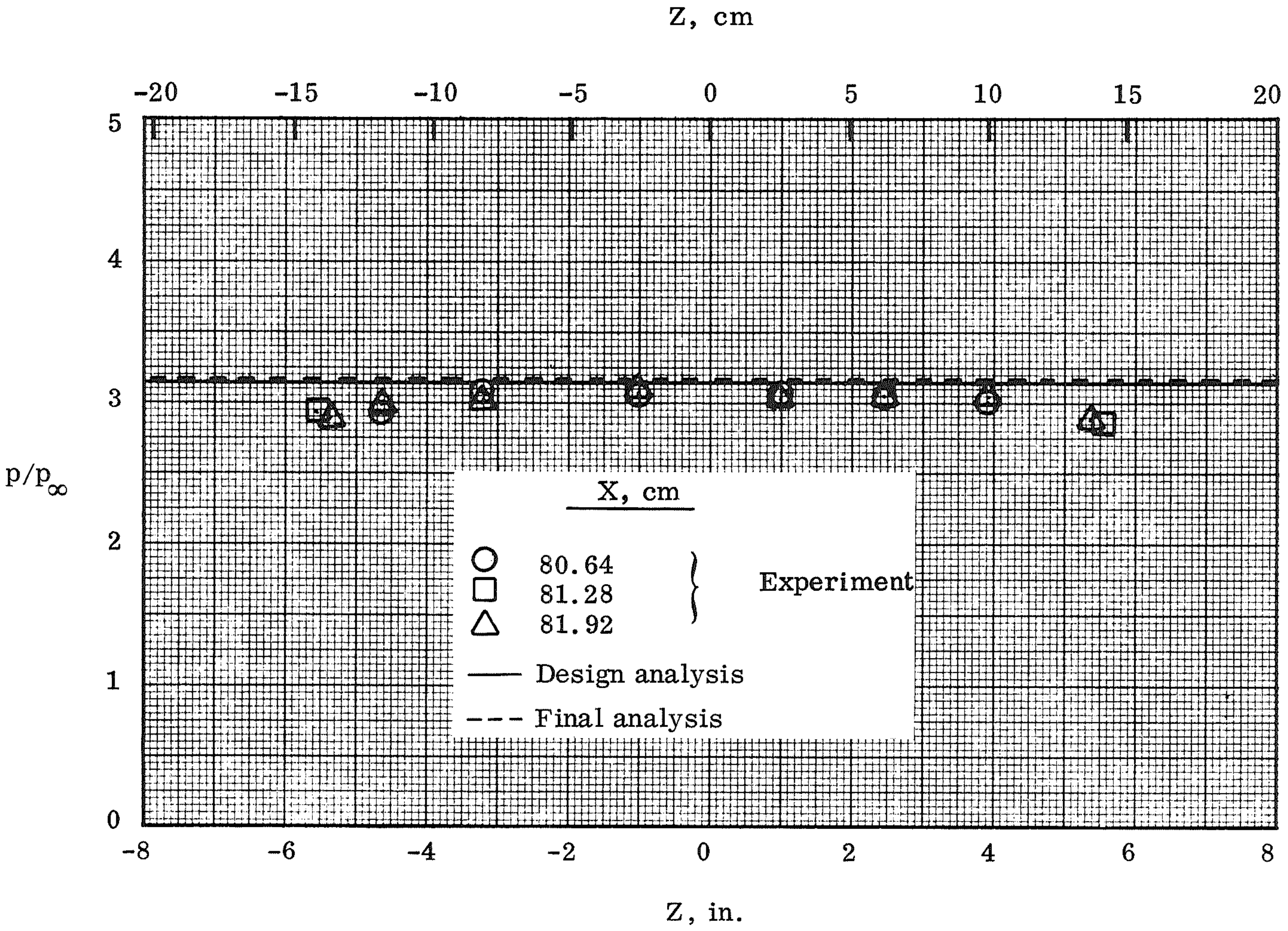

(b) Lateral distributions.

Figure 18.– Concluded.

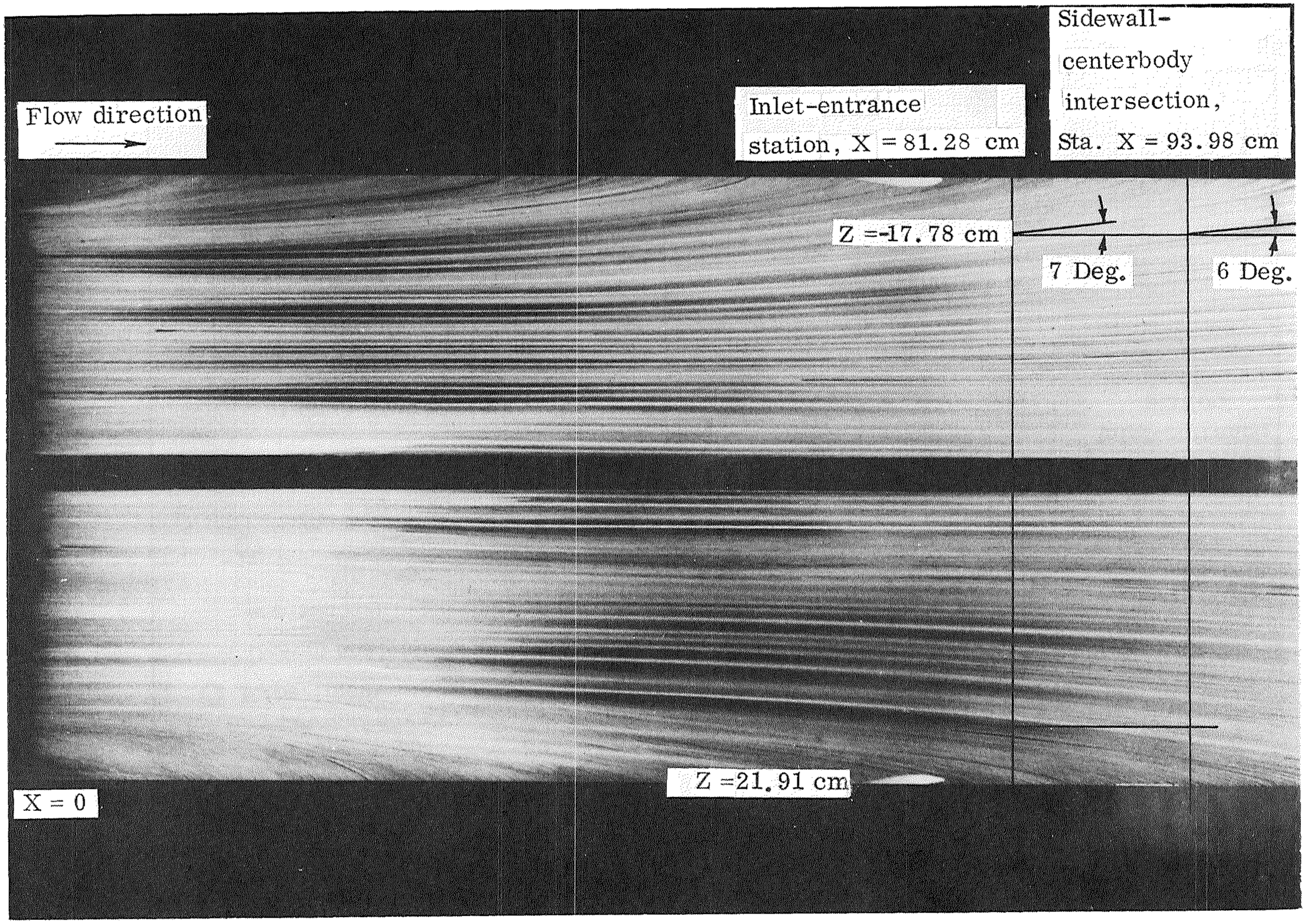

Figure 19.– Surface oil–flow pattern; flat plate at $\alpha = 6.4°$.

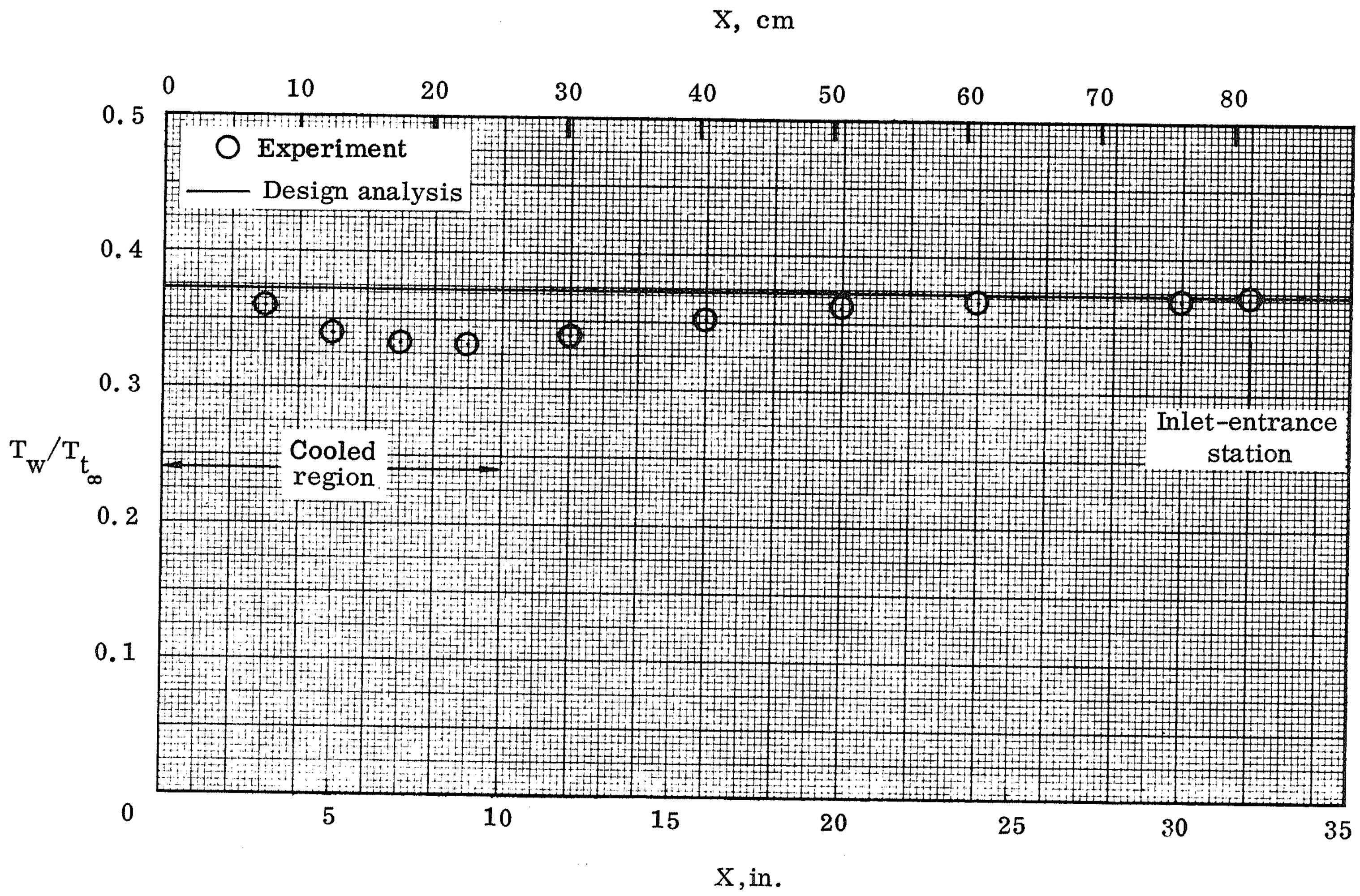

Figure 20.– Surface temperature distribution; $Z = -1.27$ cm, wedge forebody.

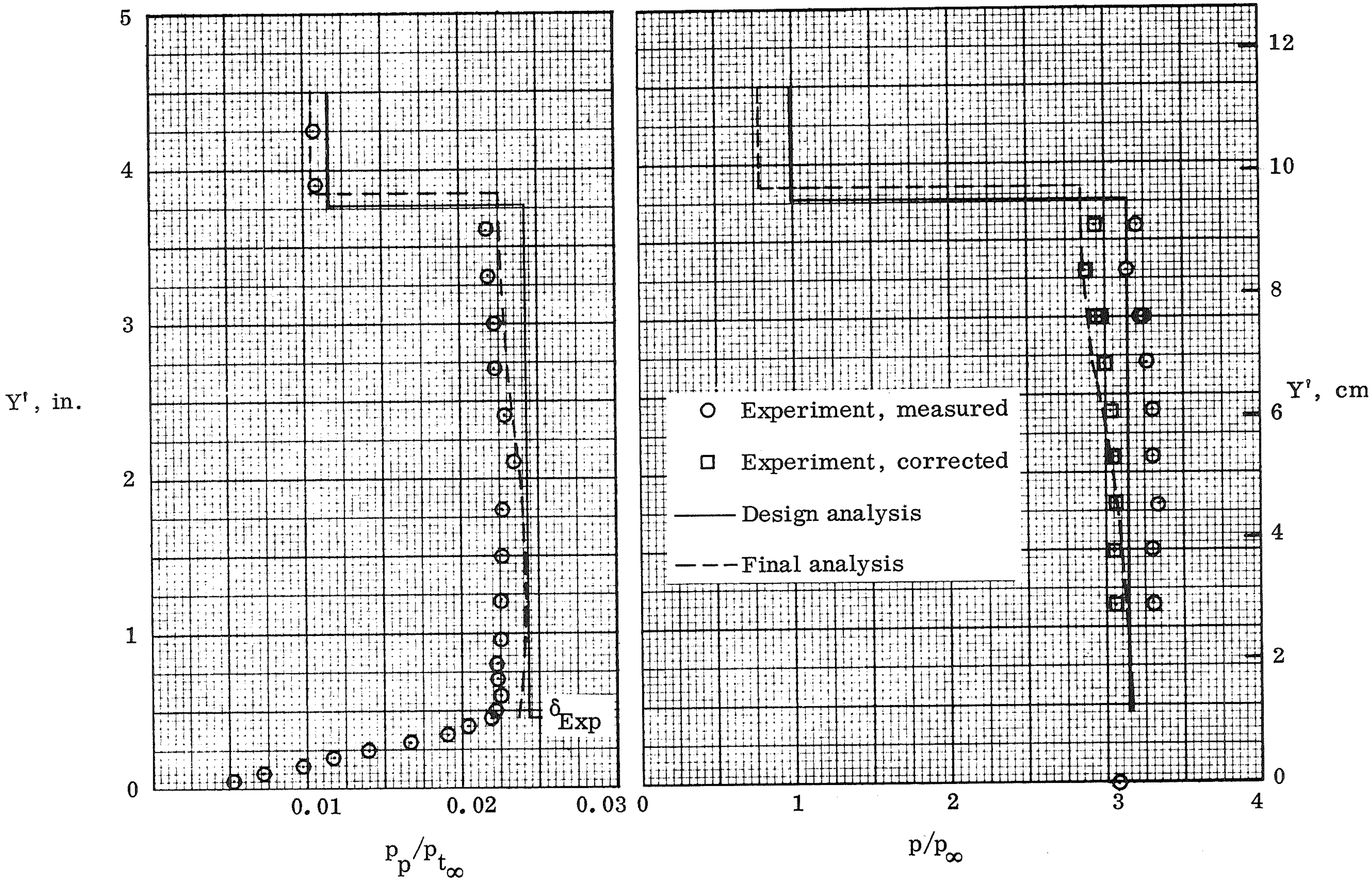

Figure 21.– Pitot and static-pressure distributions at inlet–entrance station; X = 81.28 cm, model centerline.

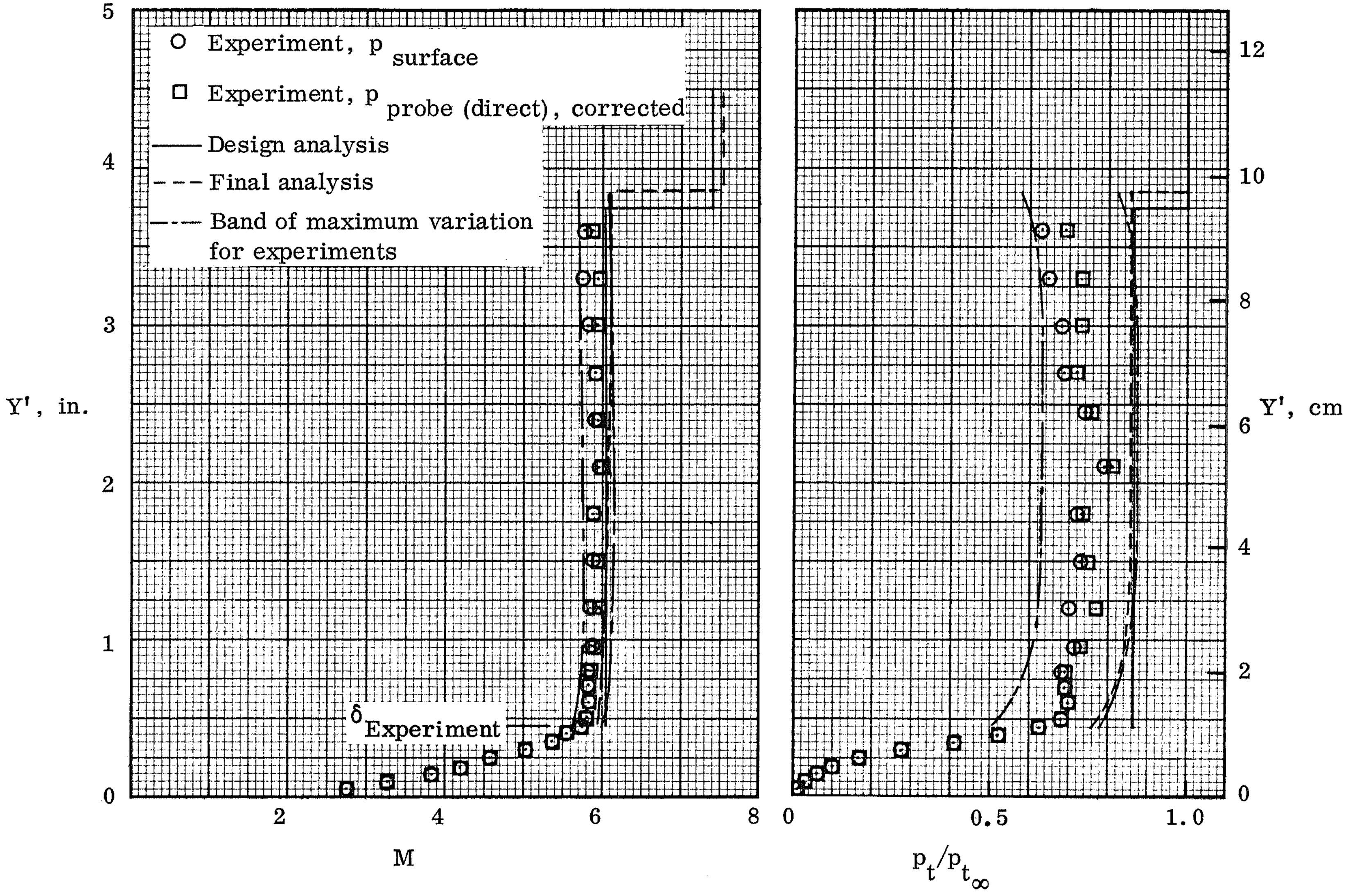

Figure 22.– Mach number and total-pressure recovery distributions at inlet-entrance station; *X* = 81.28 cm, model centerline.

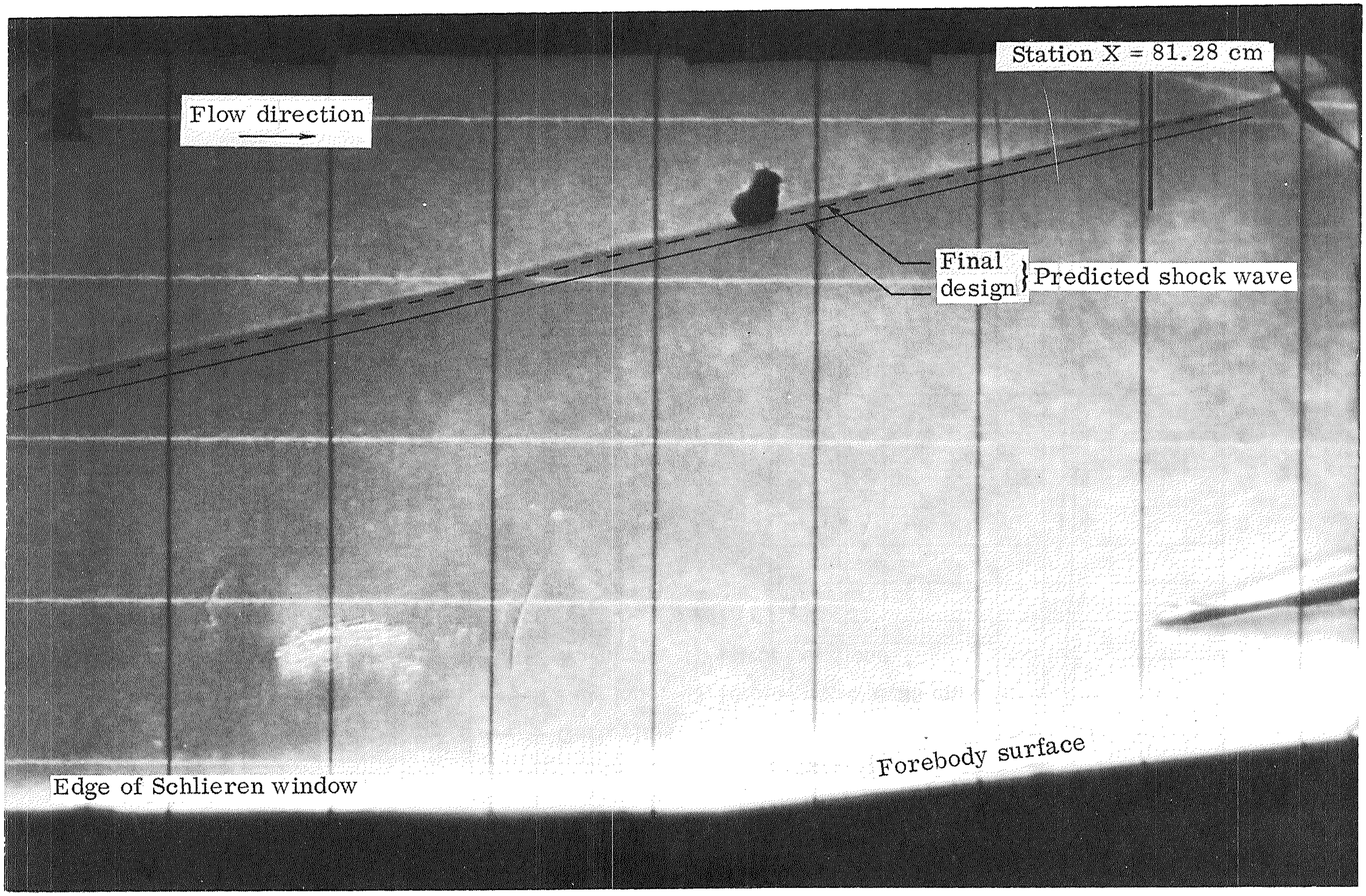

Figure 23.– Wedge-forebody shock wave at inlet-entrance station, $X = 81.28$ cm.

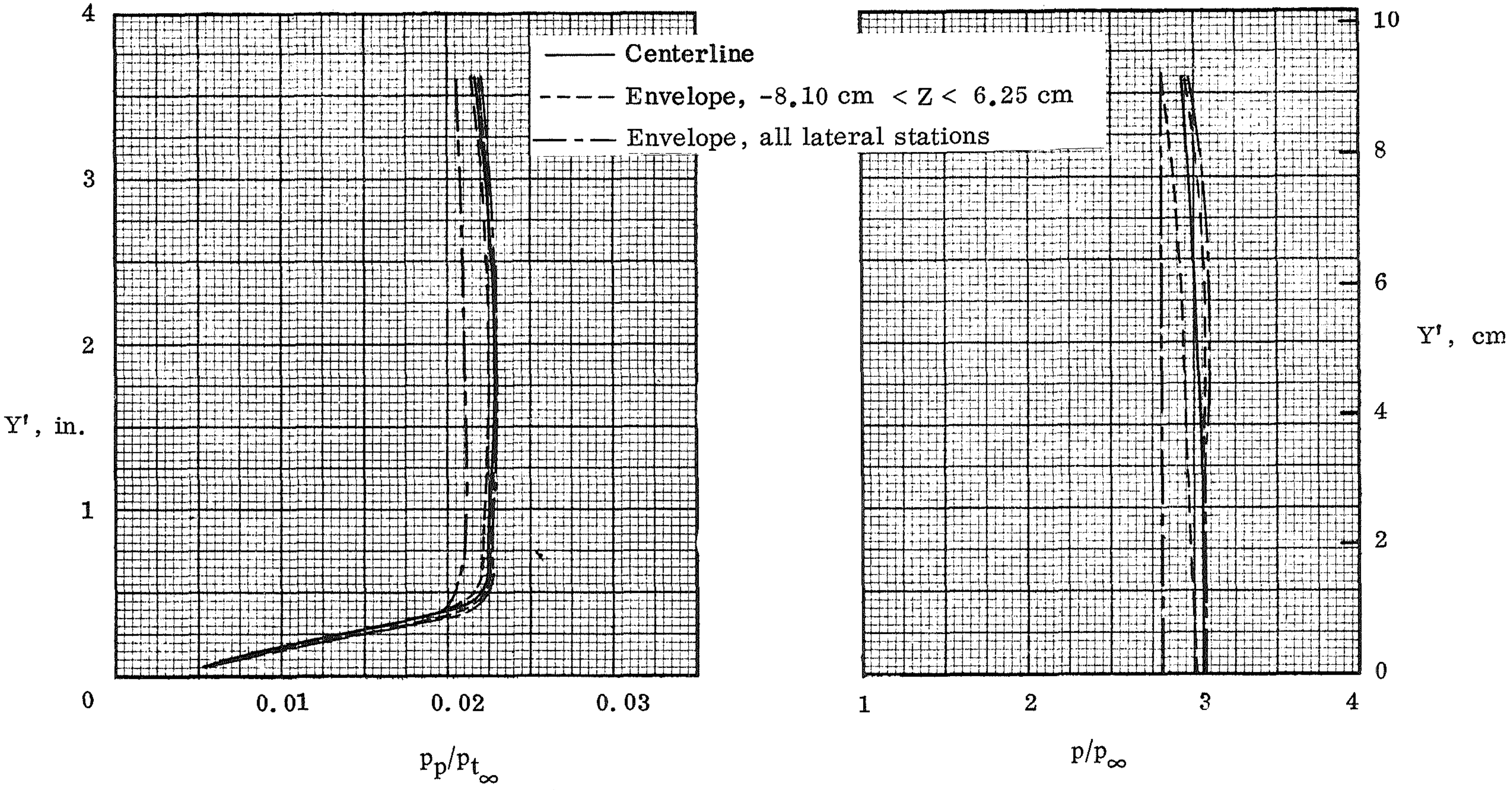

(a) Pitot and static pressure.

Figure 24.– Experimental flow-field properties at inlet-entrance station, X = 81.28 cm; all lateral stations.

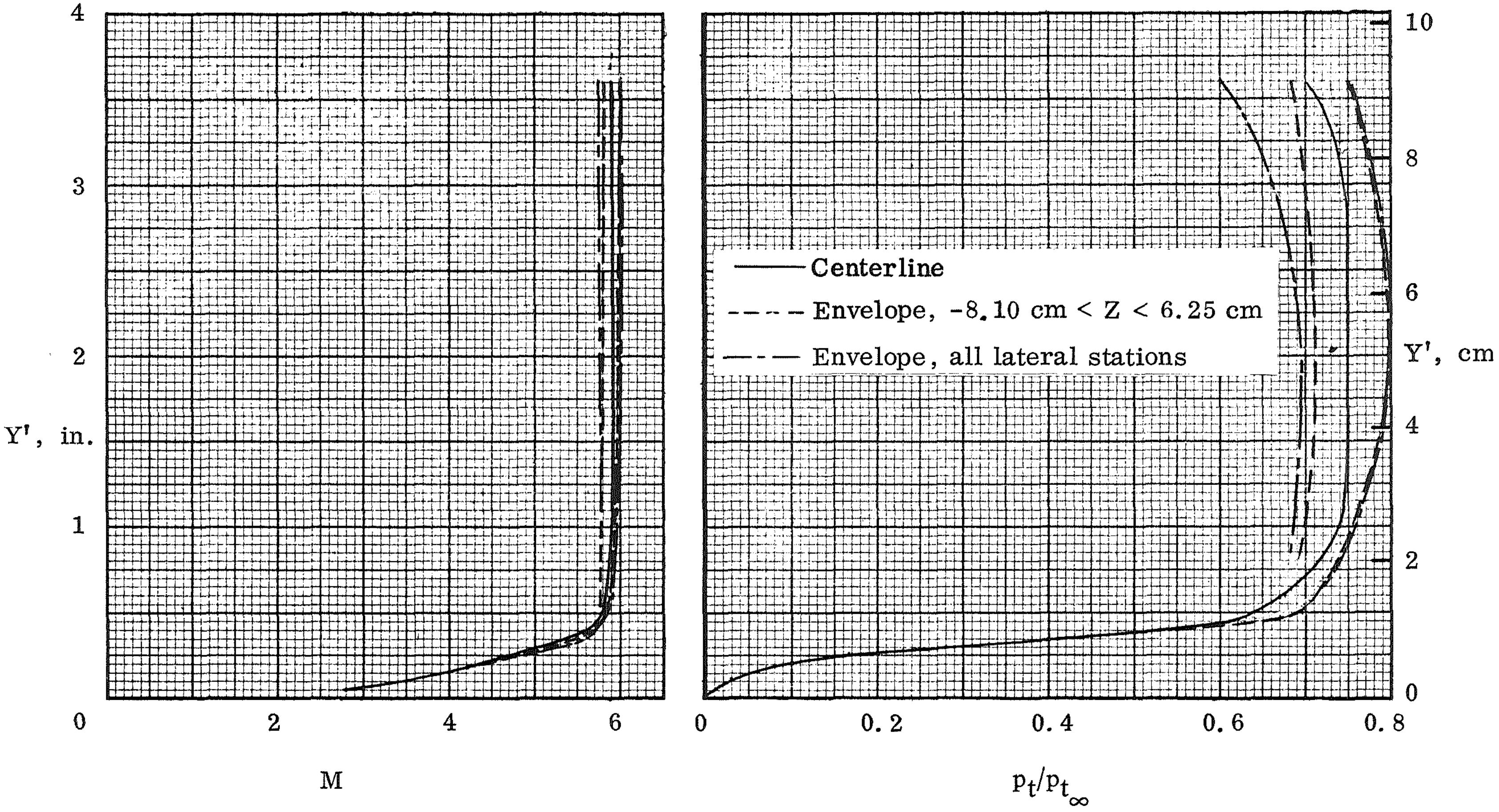

(b) Mach number and total-pressure recovery.

Figure 24.– Concluded.

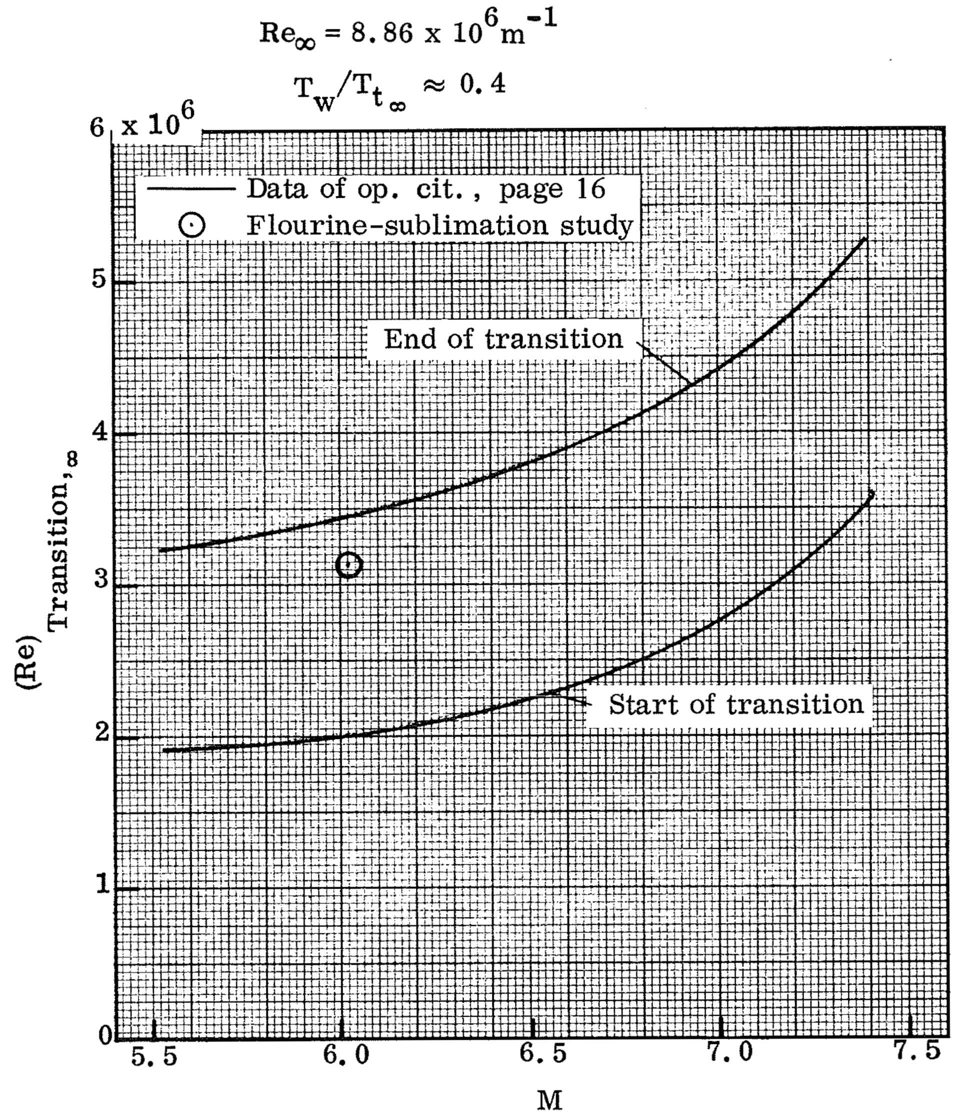

Figure 25.– Comparison of boundary-layer transition data for flat plates.

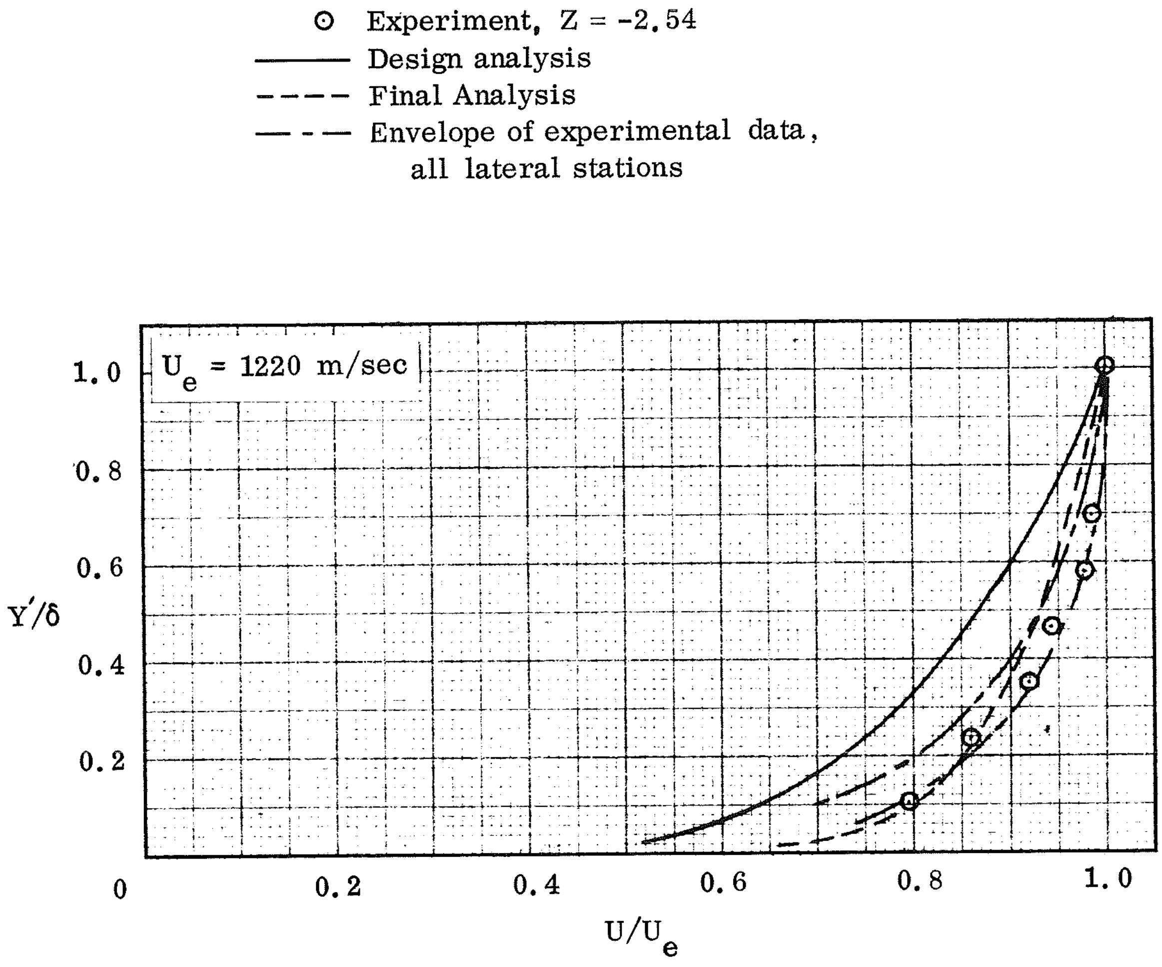

Figure 26.– Boundary-layer velocity profiles at inlet-entrance station; X = 81.28 cm, all lateral stations.

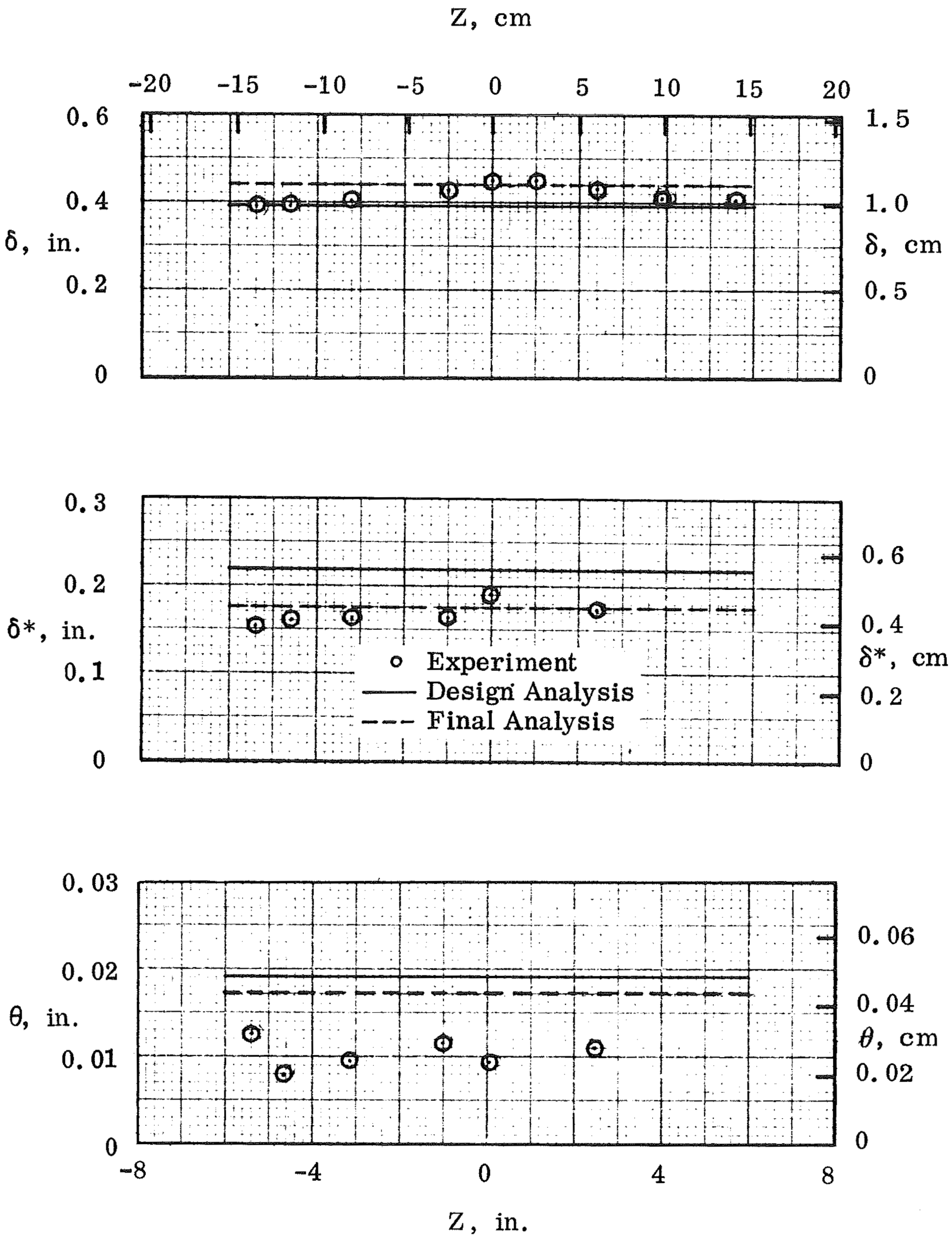

Figure 27.– Boundary-layer integral properties at inlet-entrance station; $X = 81.28$ cm.

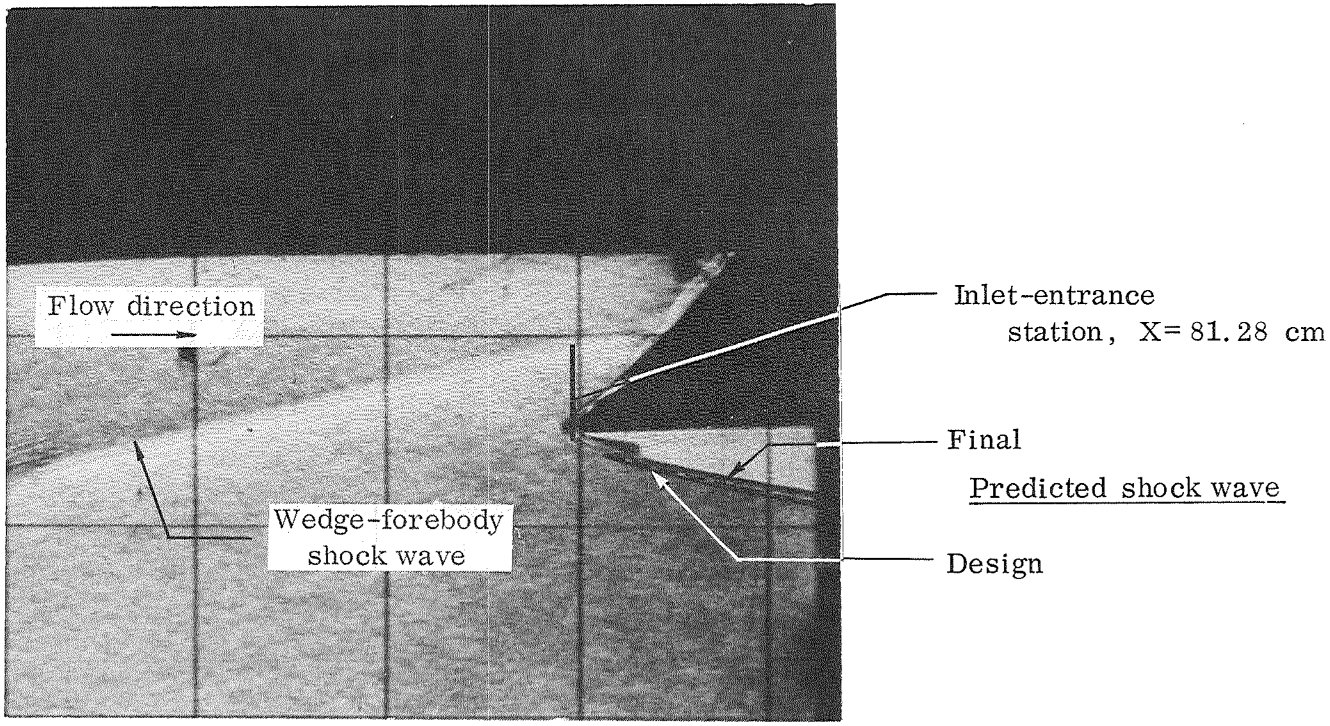

Figure 28.– Cowl shock wave in region of cowl leading edge.

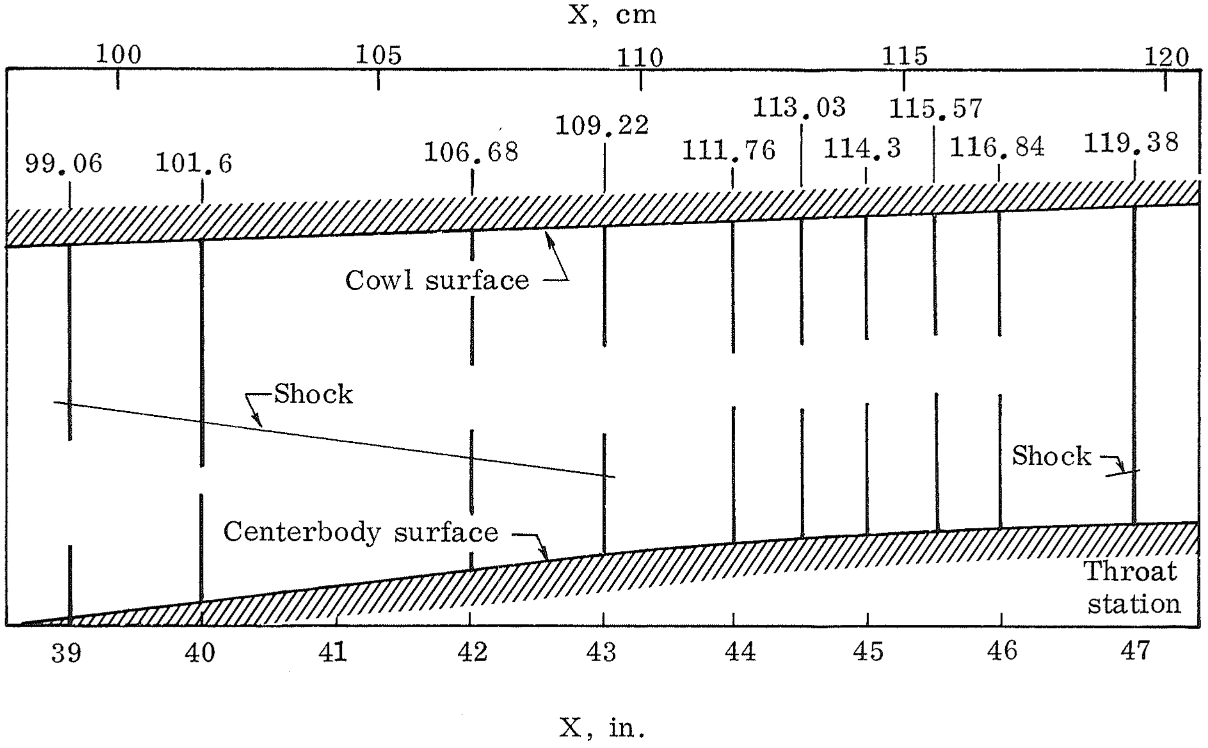

Figure 29.– Probe survey locations; $Z = -5.32$ cm, P2 inlet model.

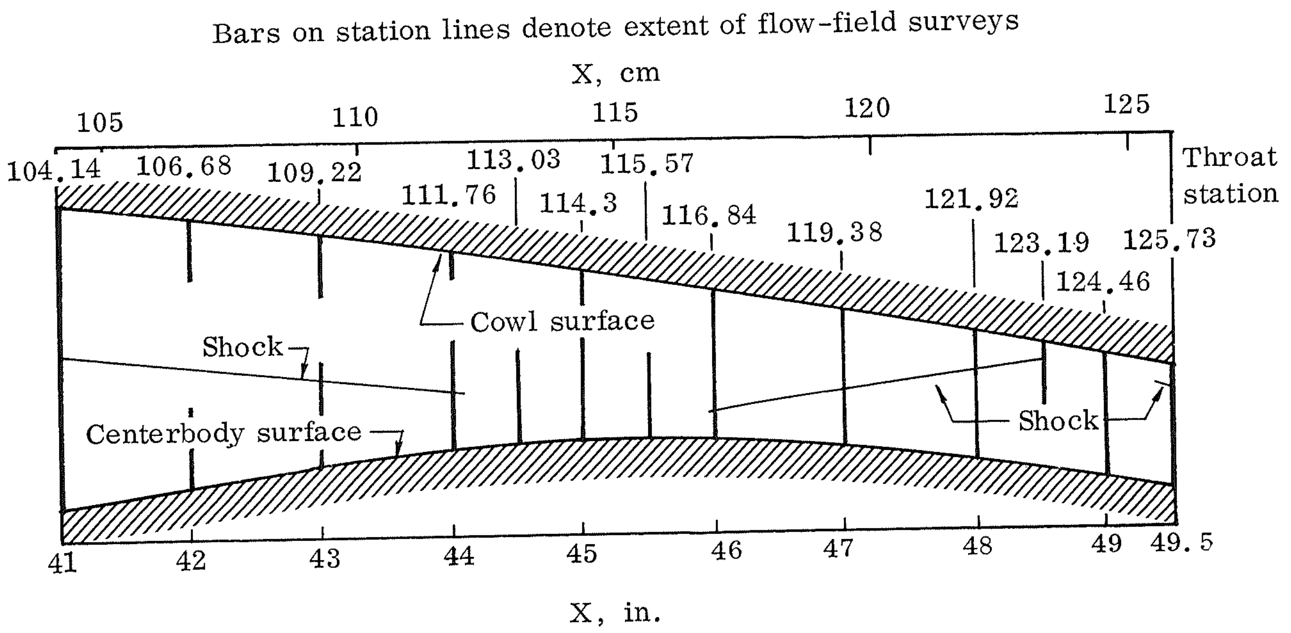
Bars on station lines denote extent of flow-field surveys

Figure 30.– Probe survey locations; Z = -5.32 cm, P8 inlet model.

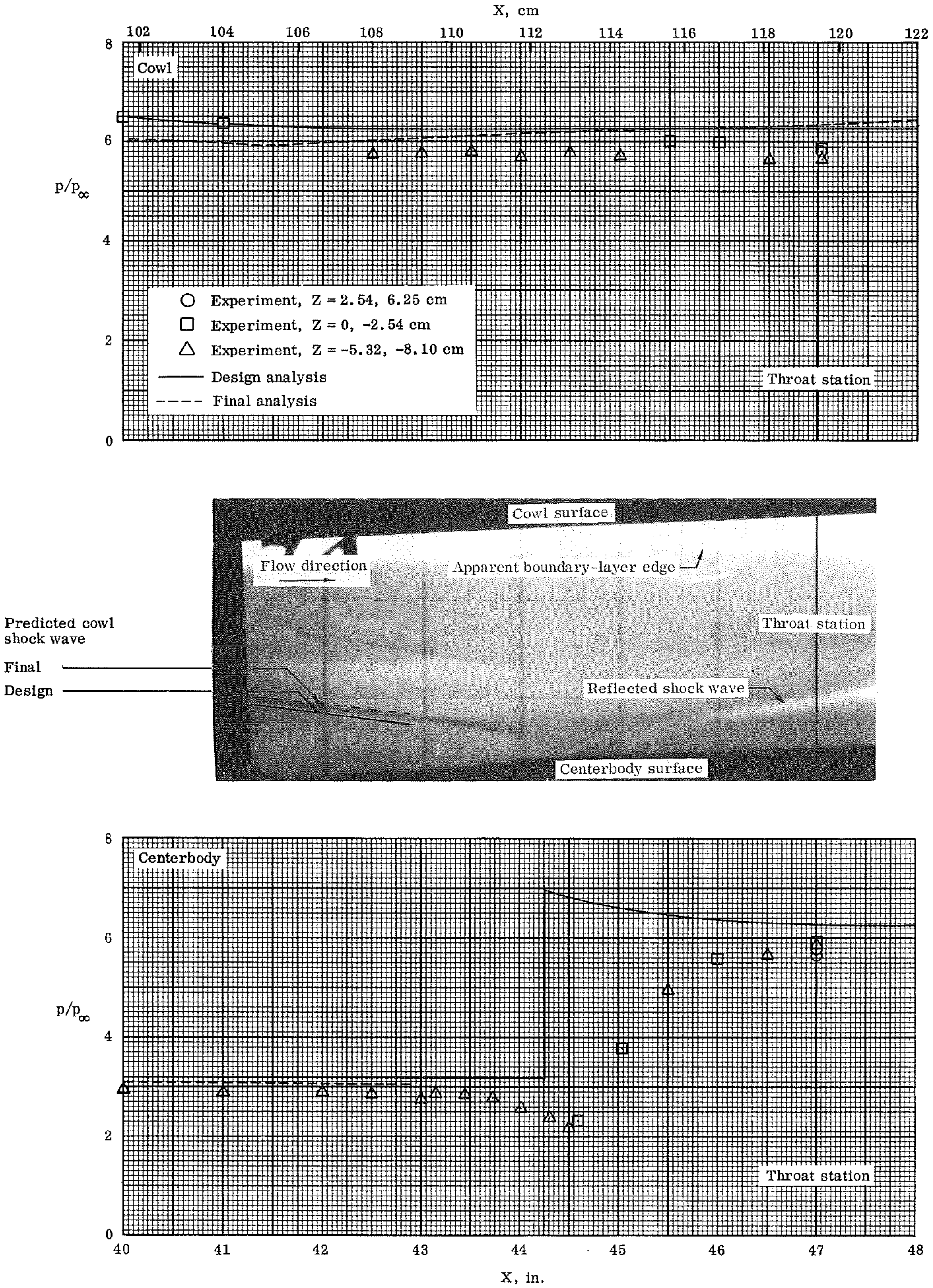

Figure 31.— Surface pressure distributions and shock-wave pattern; P2 inlet model.

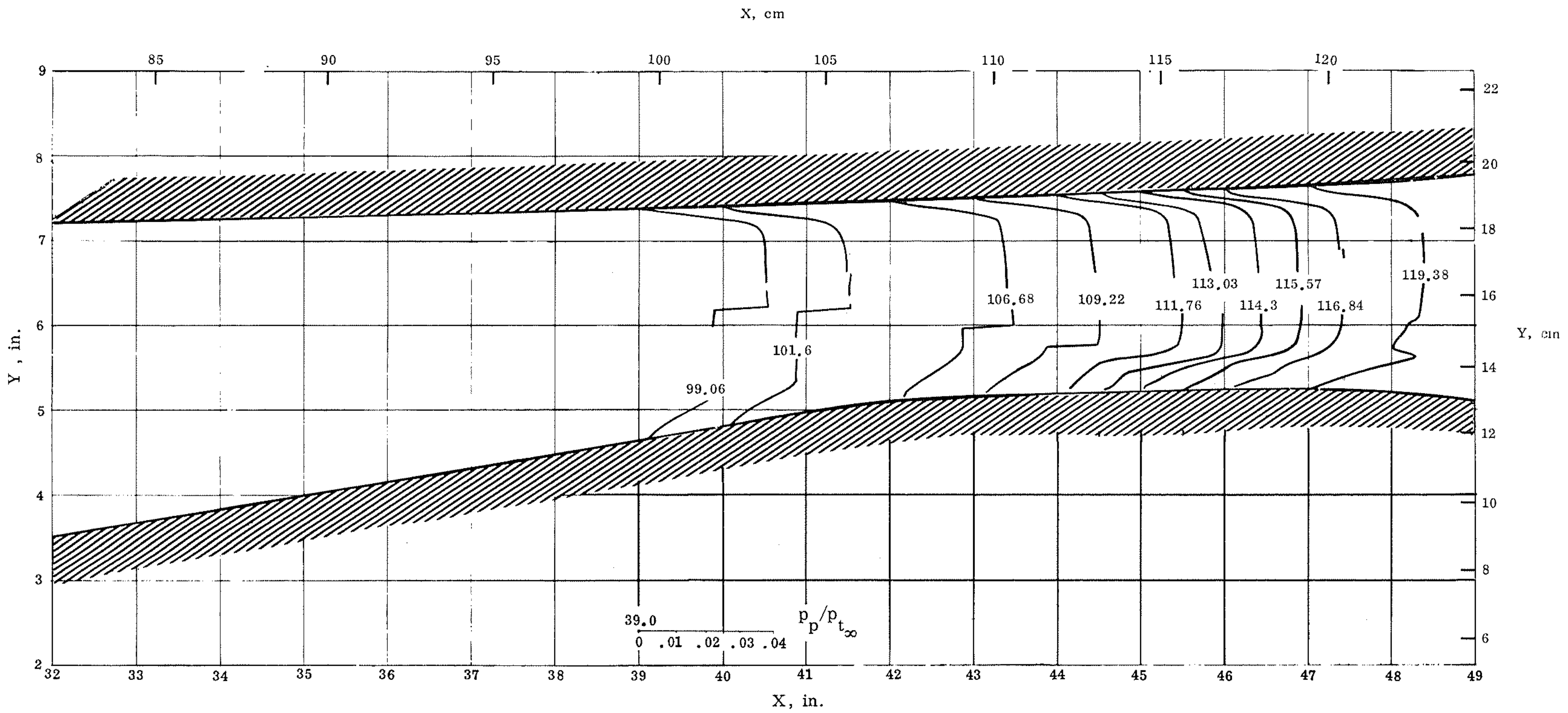

Figure 32.– Summary of experimental pitot-pressure distributions; $Z = -5.32$ cm, P2 inlet model.

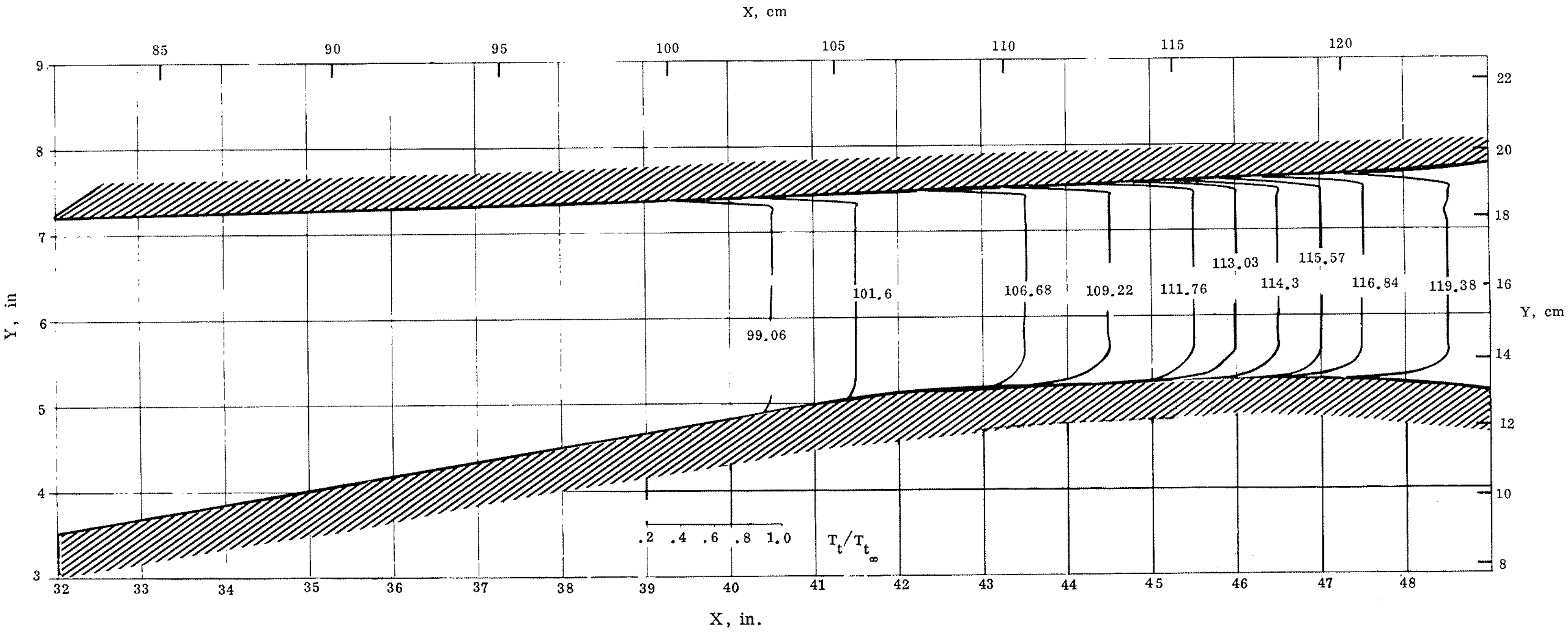

Figure 33.– Summary of experimental total-temperature distributions; $Z = -5.32$ cm, P2 inlet model.

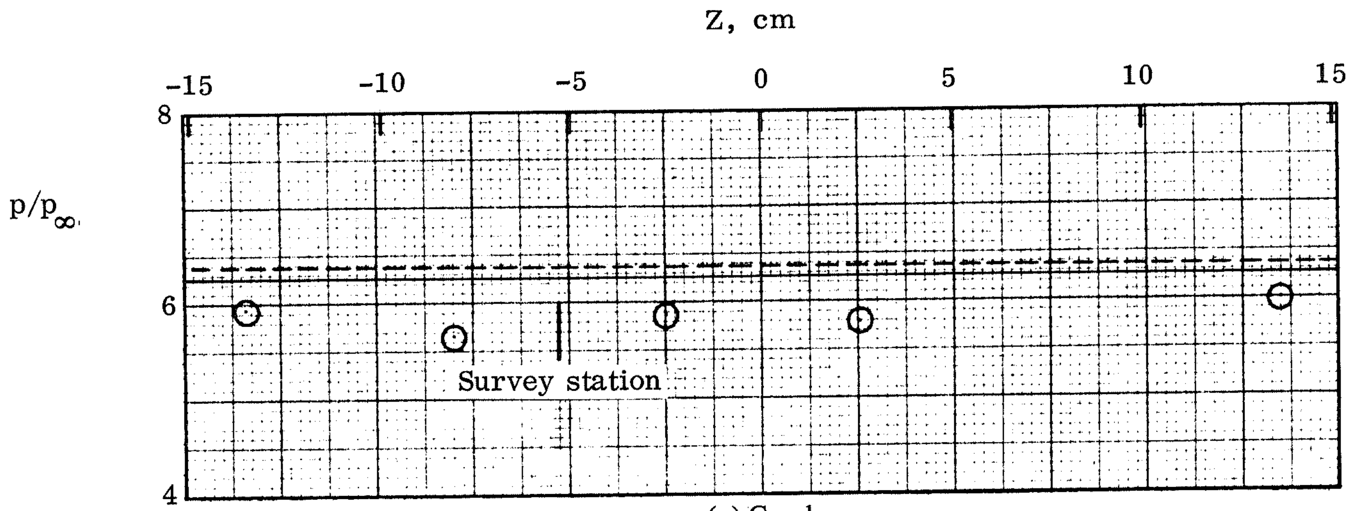

(a) Cowl.

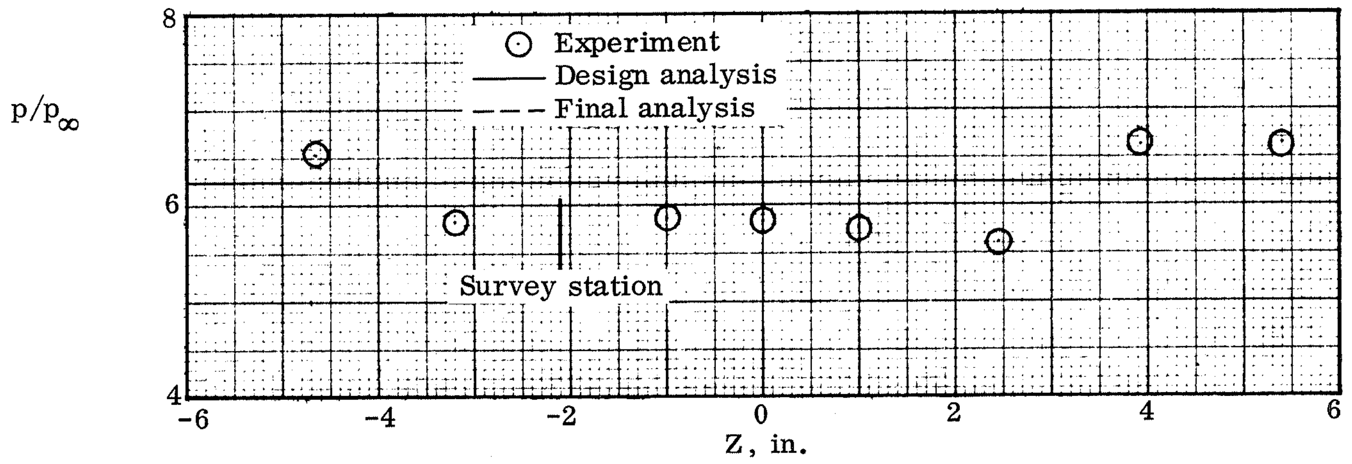

(b) Centerbody.

Figure 34.– Lateral distributions of surface pressure at throat station; X = 119.38 cm, P2 inlet model.

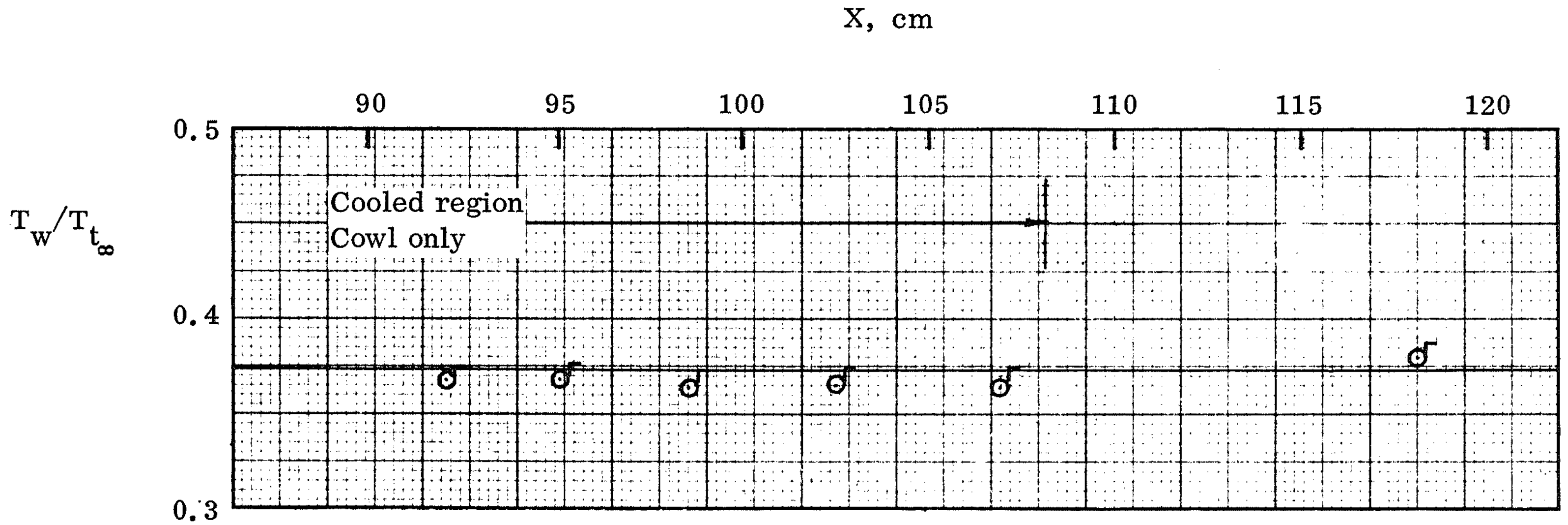

(a) Cowl.

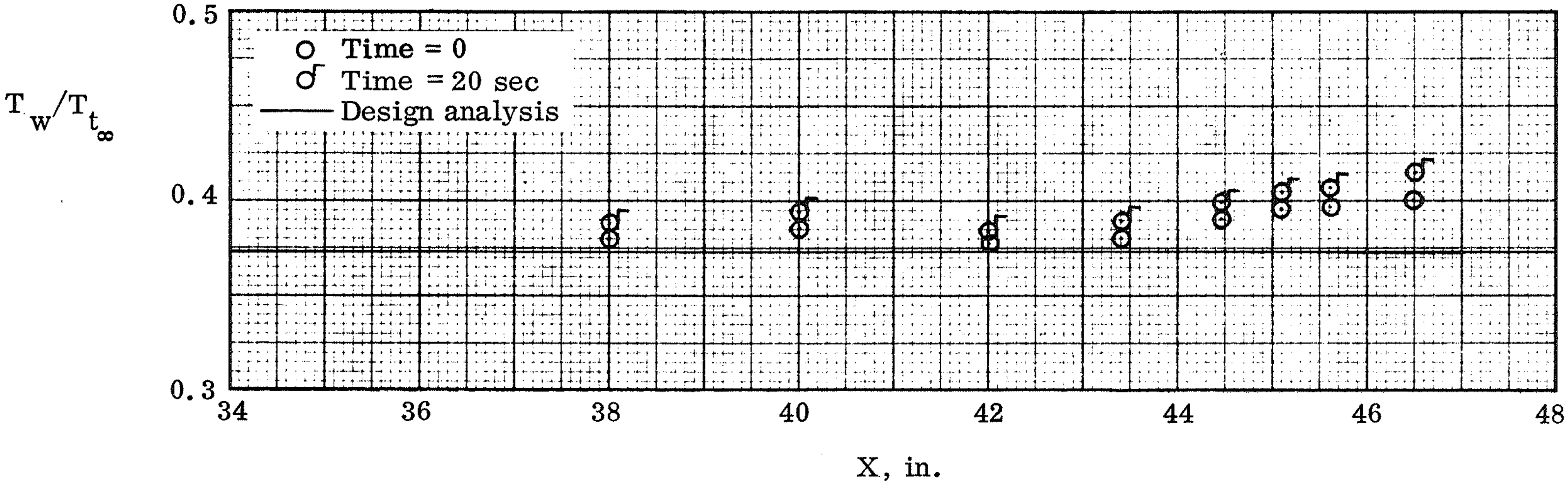

(b) Centerbody.

Figure 35.– Surface temperature distributions; P2 inlet model.

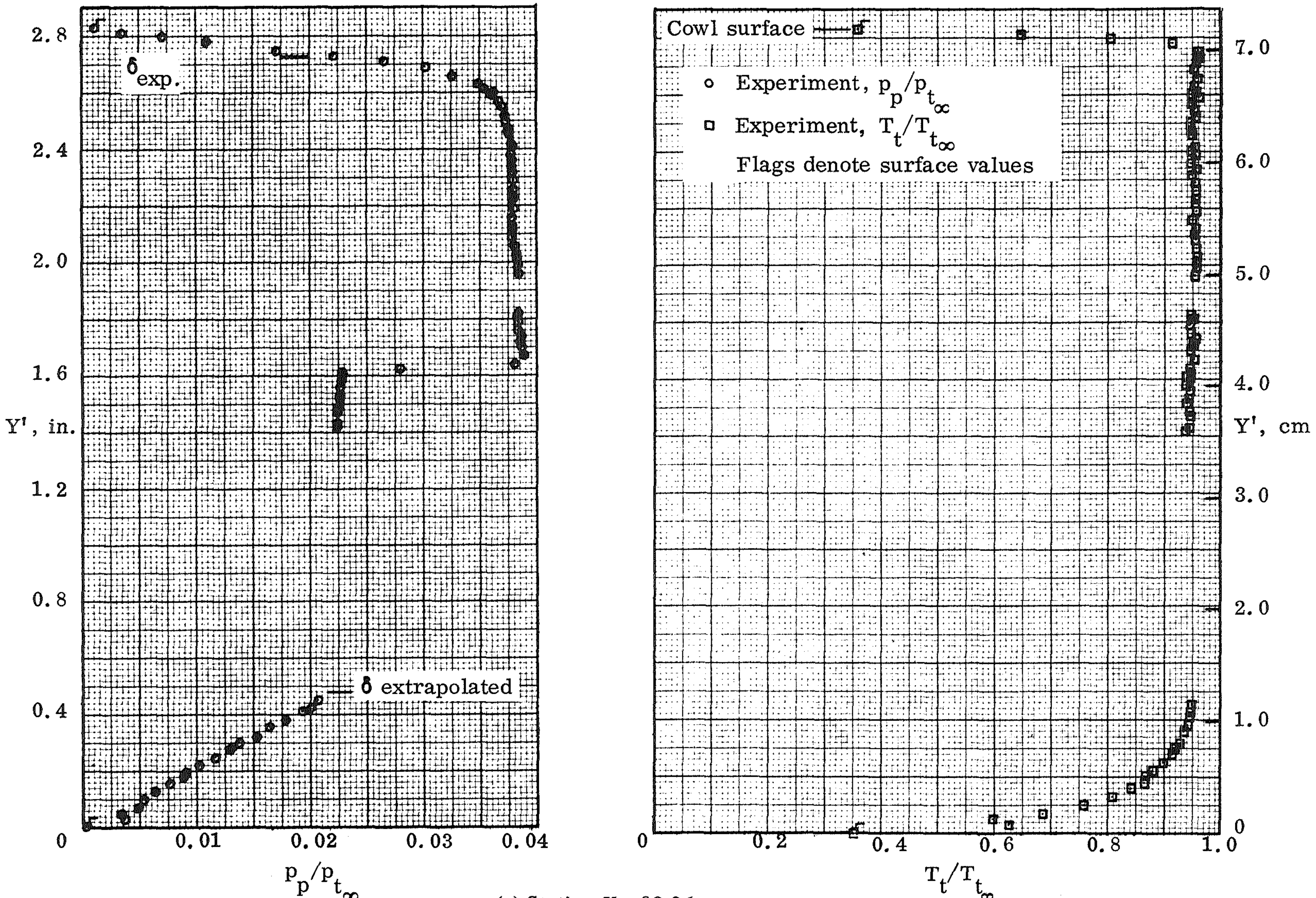

(a) Station $X = 99.06$ cm.

Figure 36.– Pitot pressure and total-temperature distributions; $Z = -5.32$ cm, P2 inlet model.

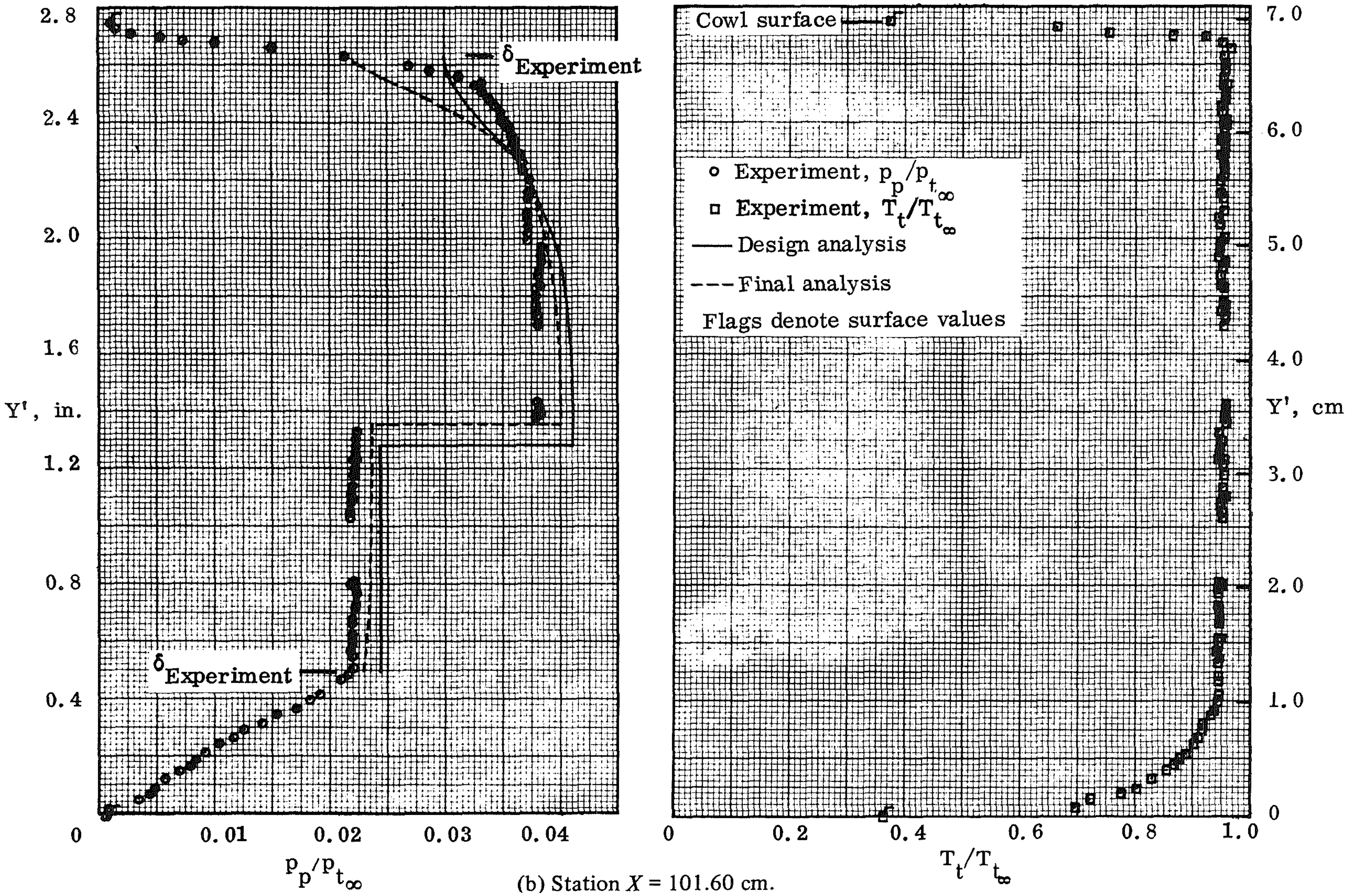

(b) Station $X = 101.60$ cm.

Figure 36.– Continued.

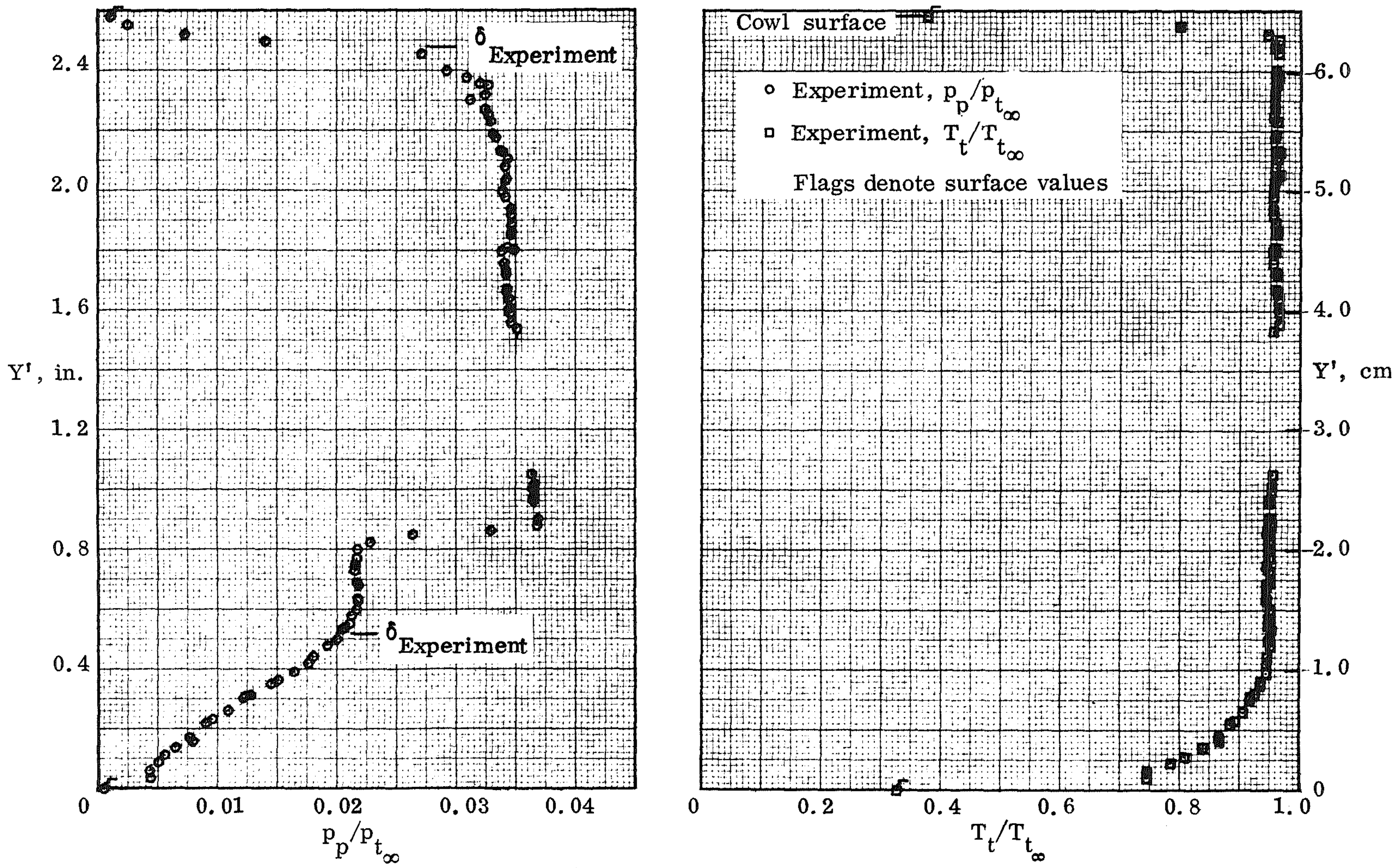

(c) Station X = 106.68 cm.

Figure 36.– Continued.

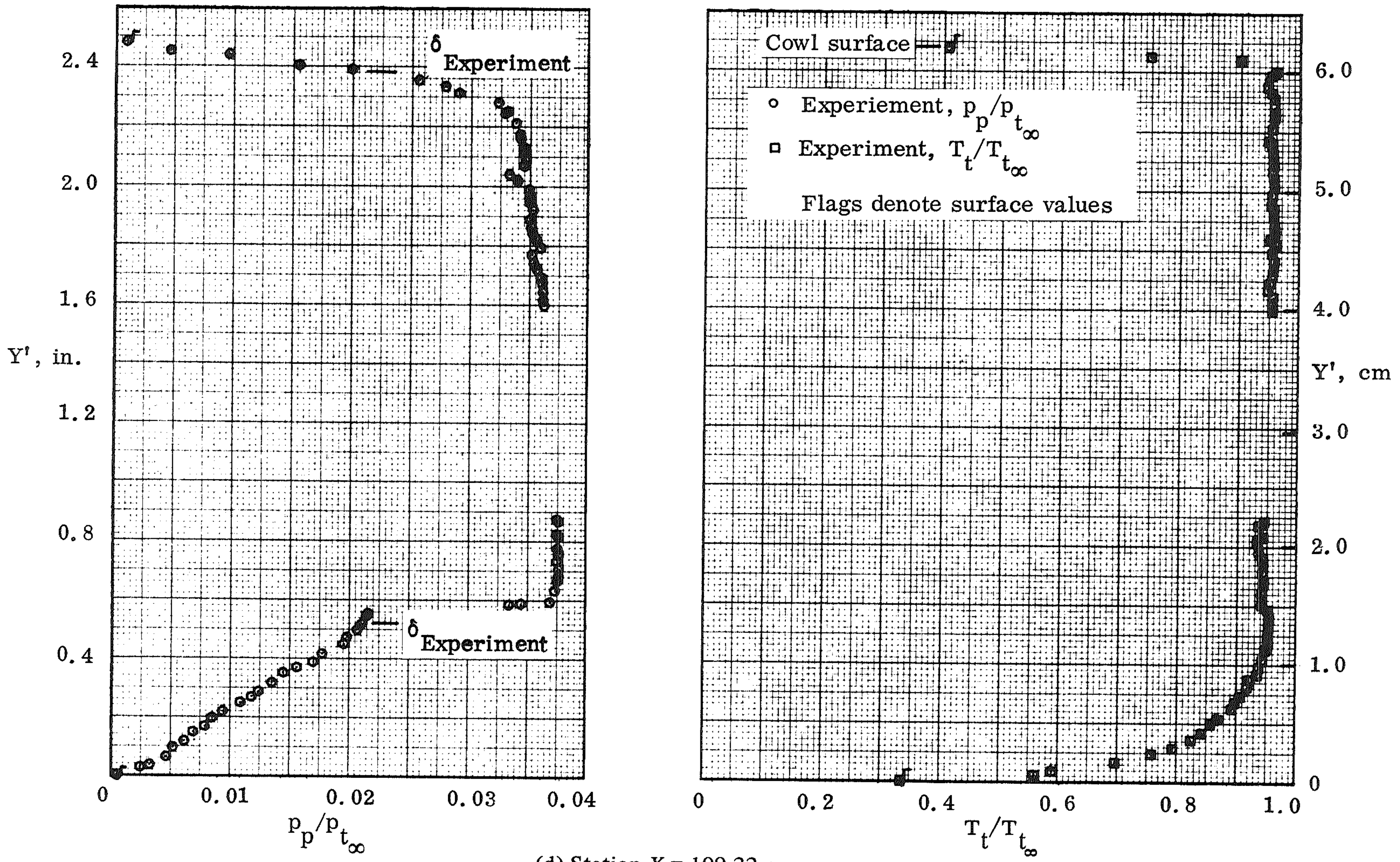

(d) Station X = 109.22 cm.

Figure 36.– Continued.

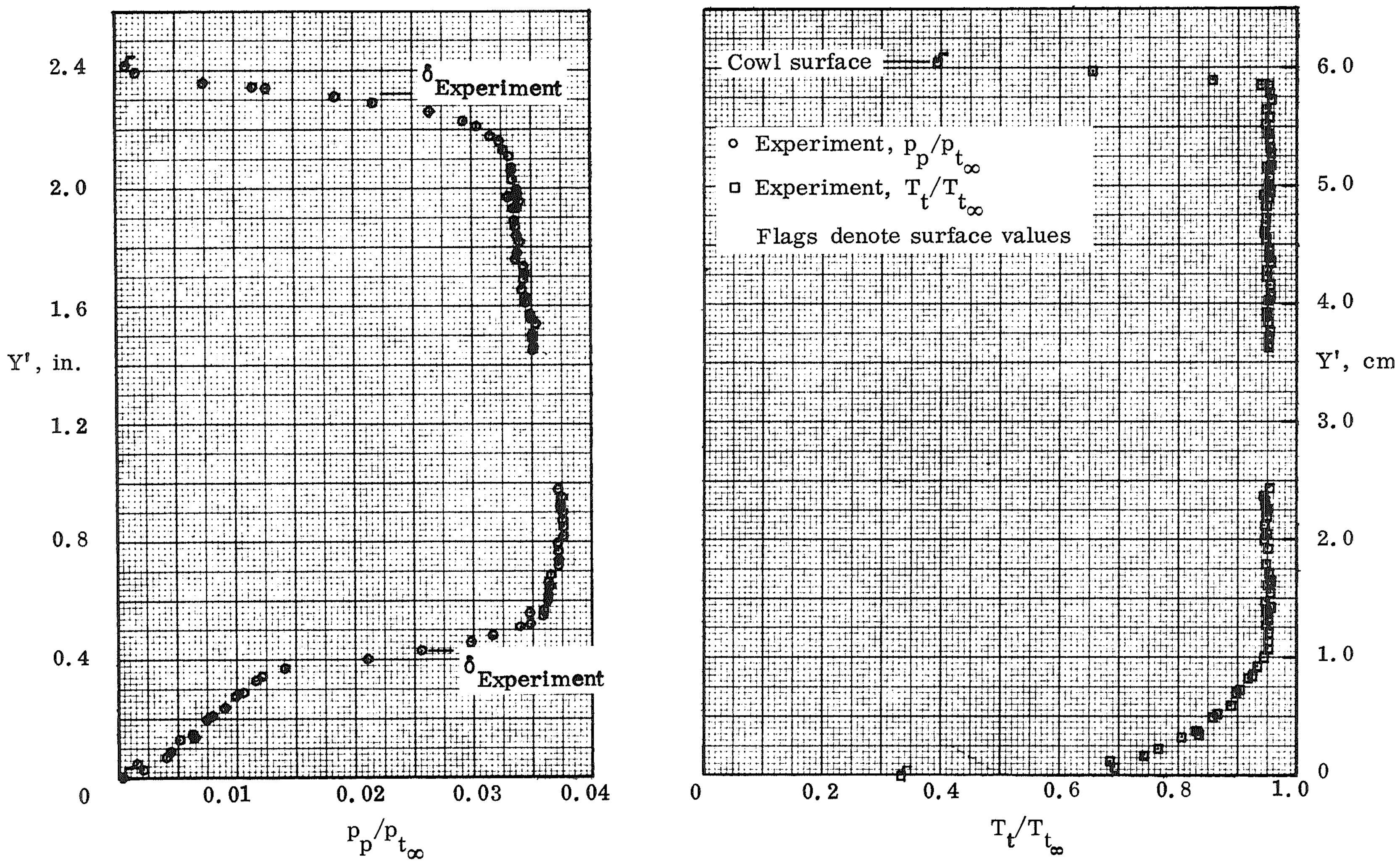

(e) Station $X = 111.76$ cm.

Figure 36.– Continued.

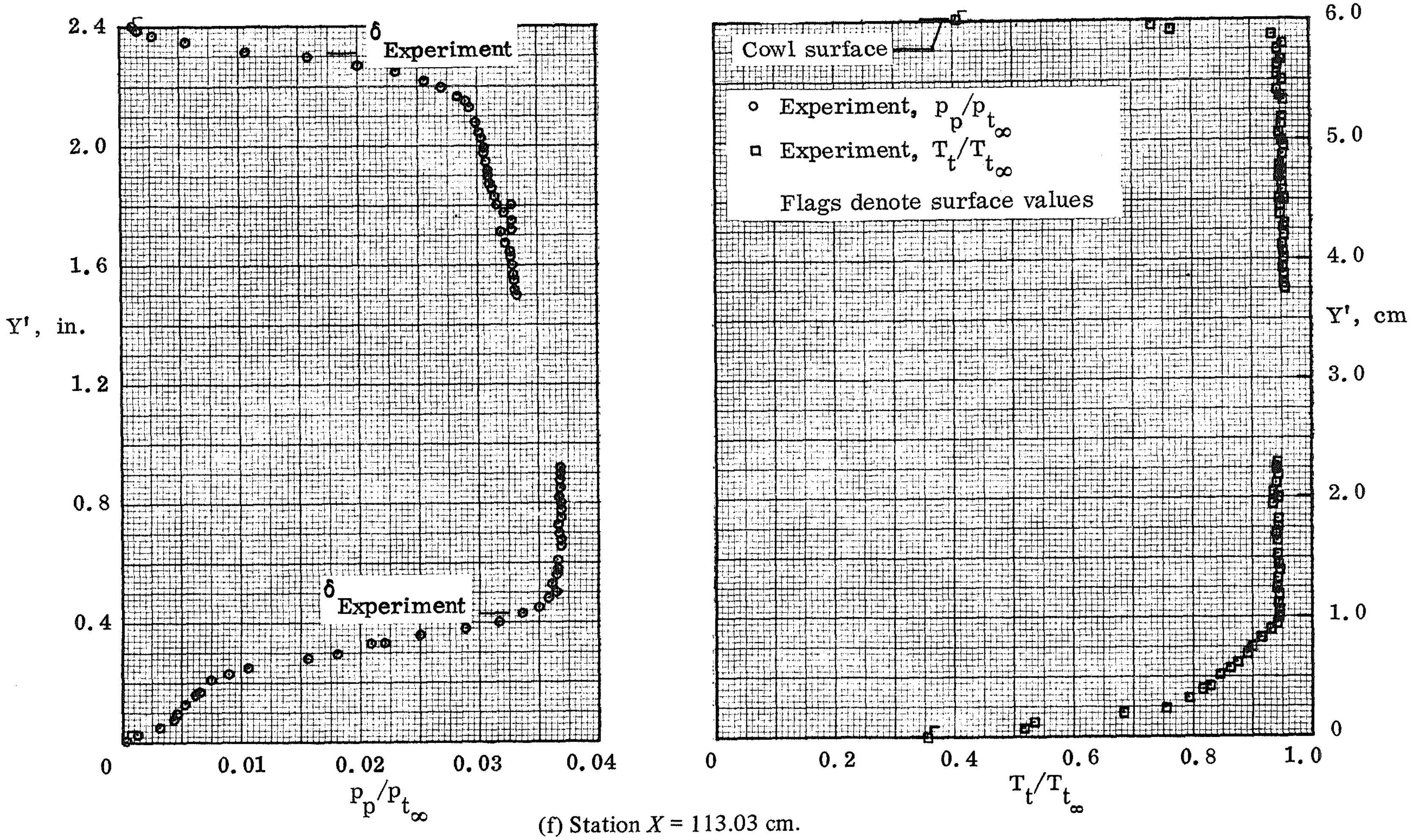

(f) Station X = 113.03 cm.

Figure 36.– Continued.

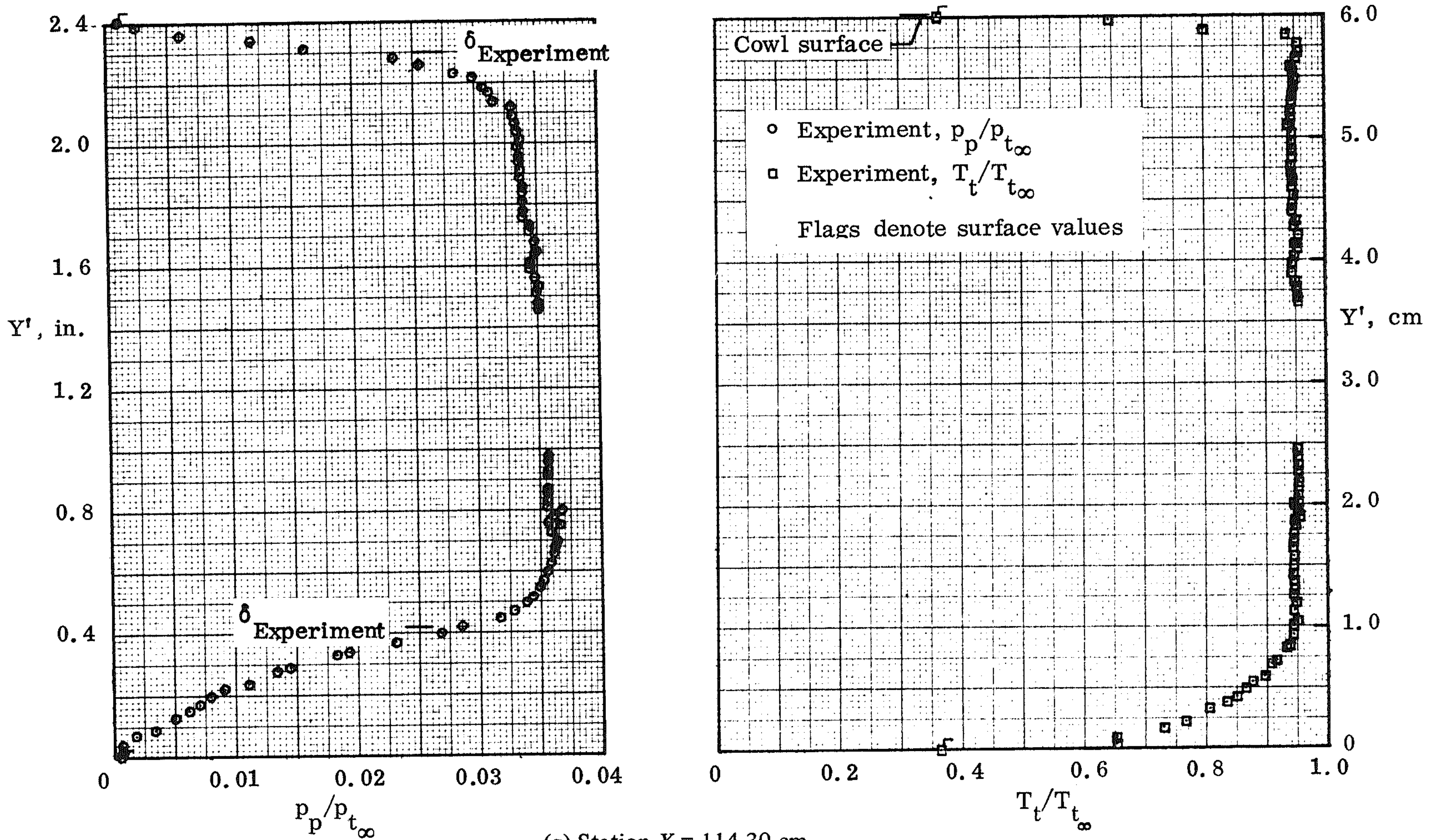

(g) Station X = 114.30 cm.

Figure 36.– Continued.

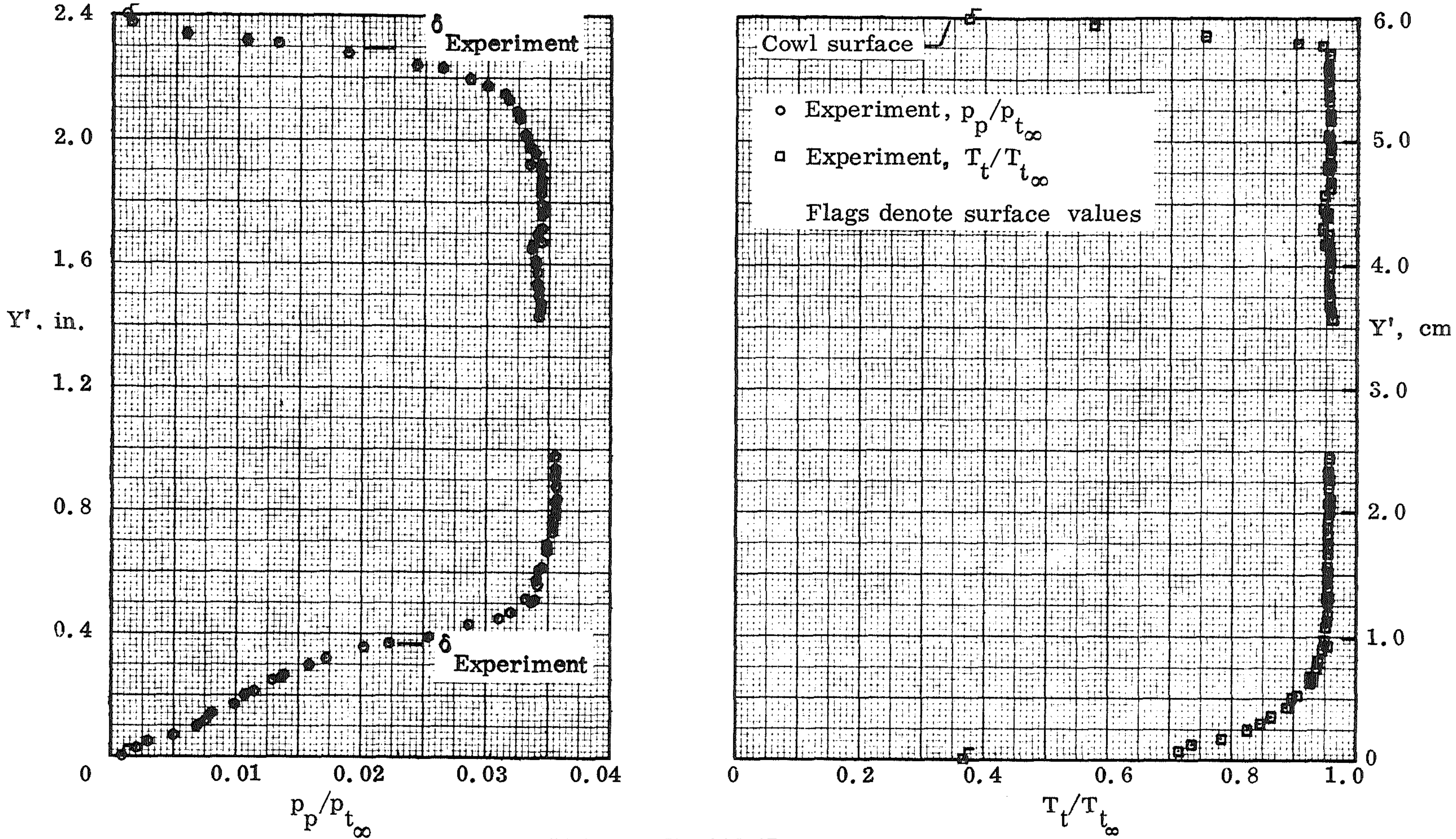

(h) Station X = 115.57 cm.

Figure 36.– Continued.

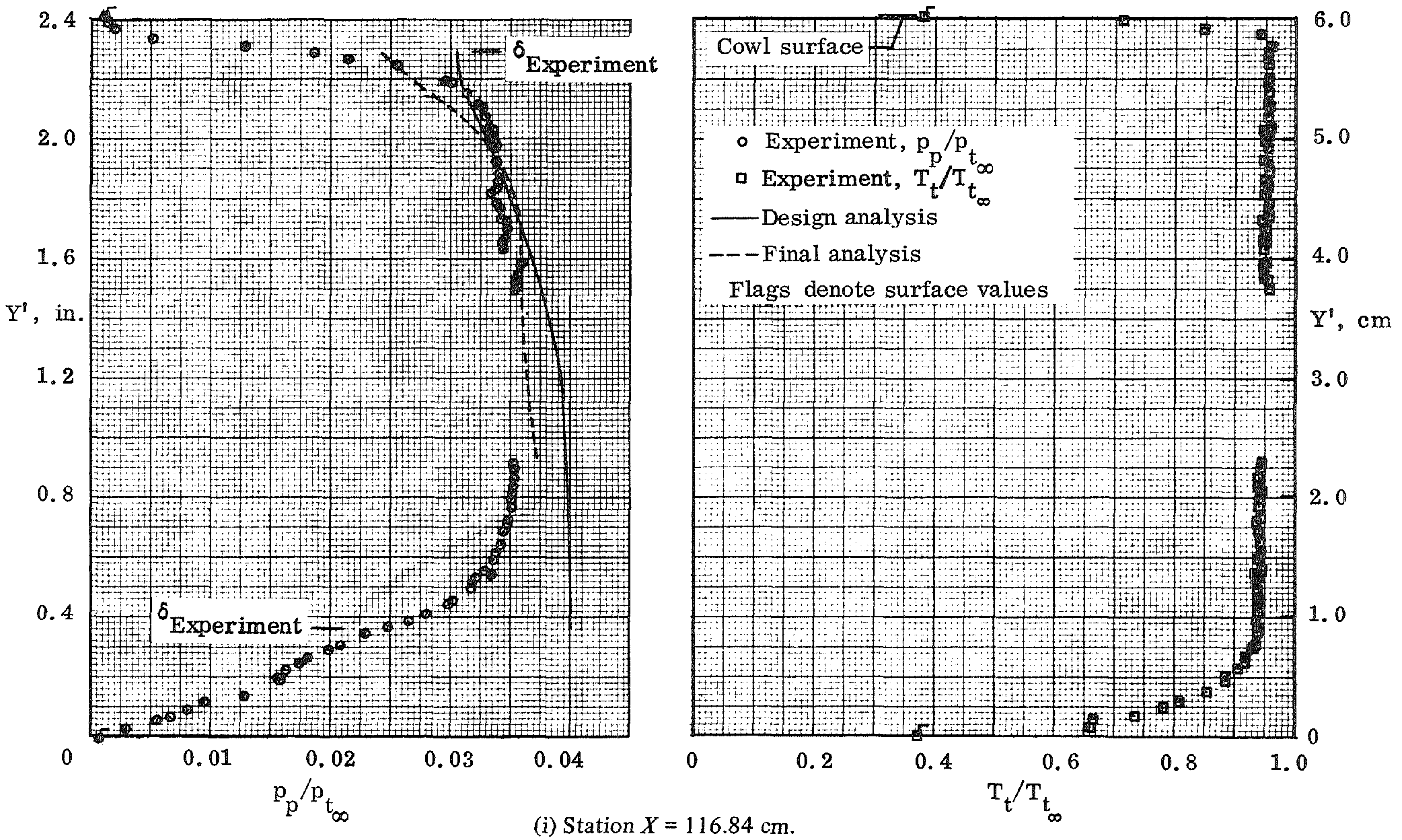

(i) Station $X = 116.84$ cm.

Figure 36.– Continued.

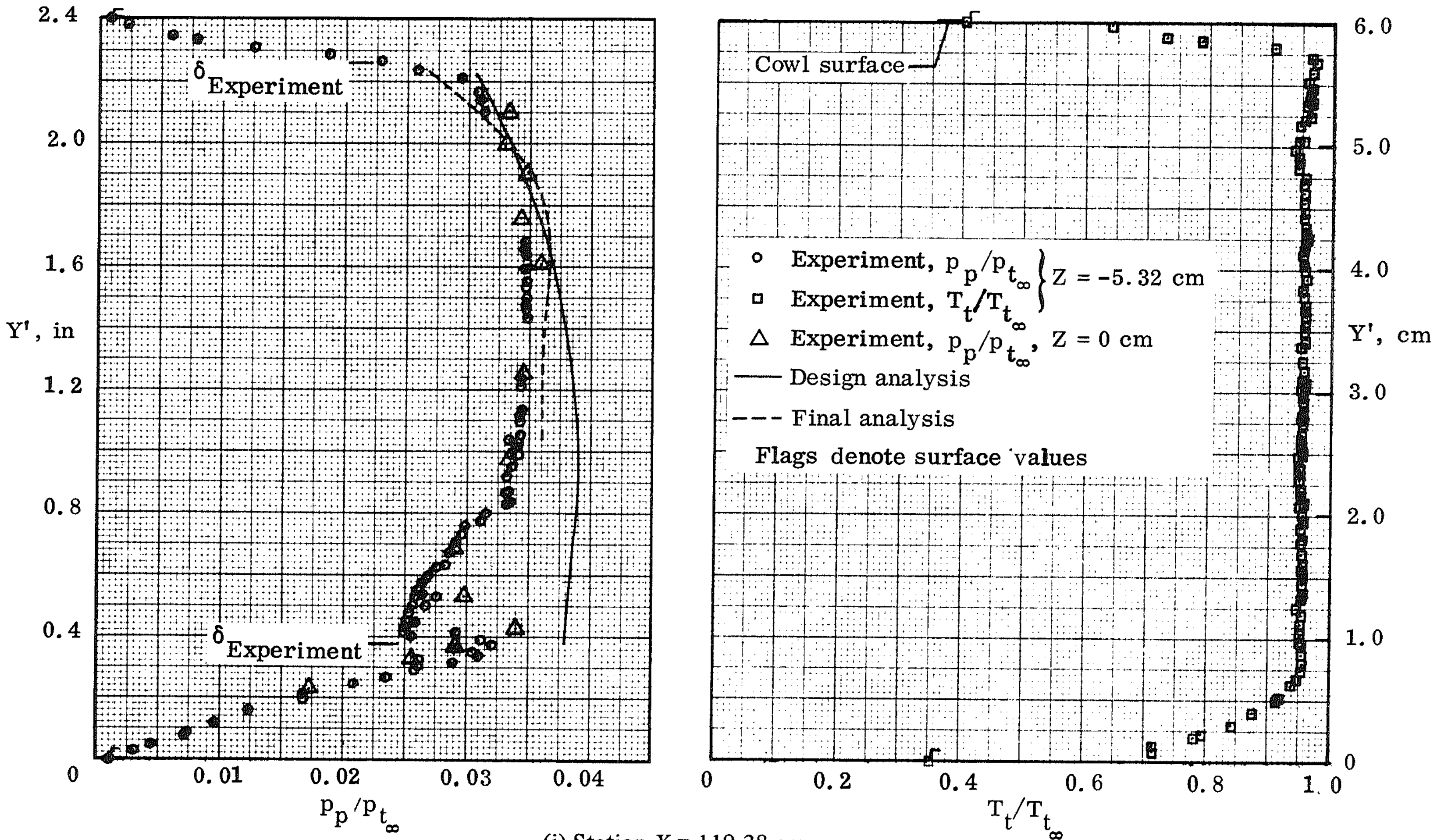

(j) Station $X = 119.38$ cm.

Figure 36.– Concluded.

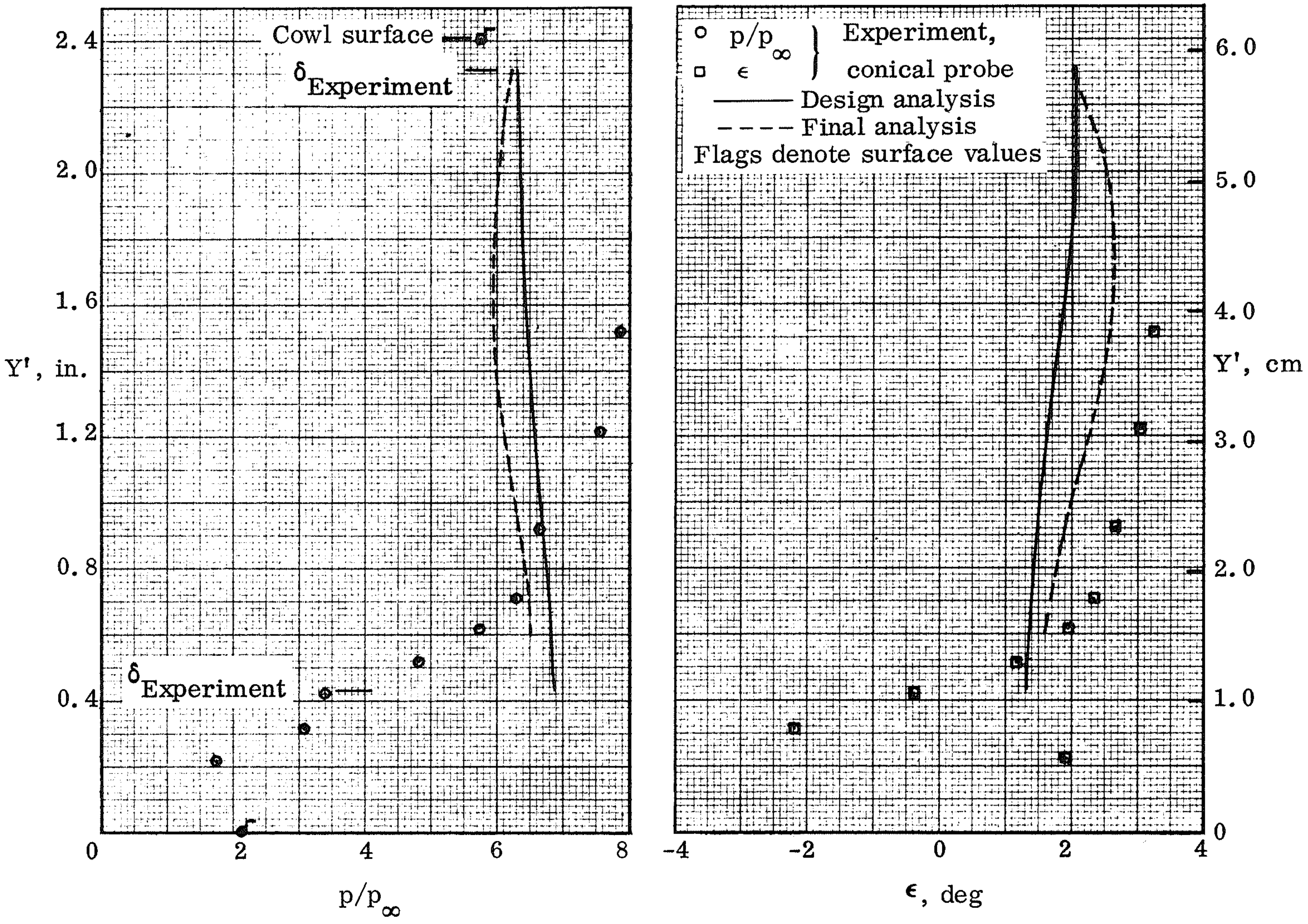

(a) Station X = 113.03 cm.

Figure 37.– Static pressure and flow angle distributions; Z = –5.32 cm, P2 inlet model.

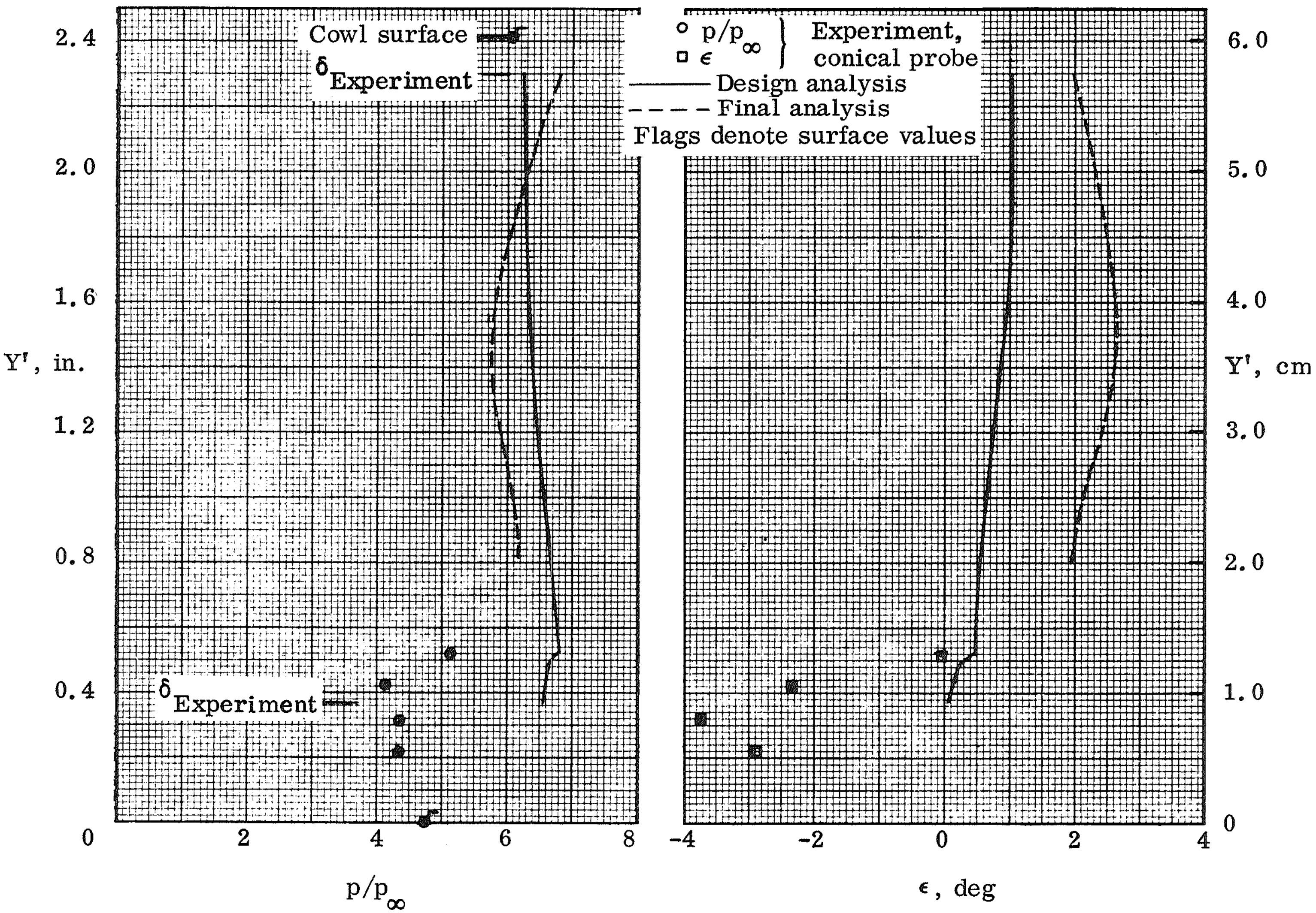

(b) Station X = 115.57 cm.

Figure 37.– Continued.

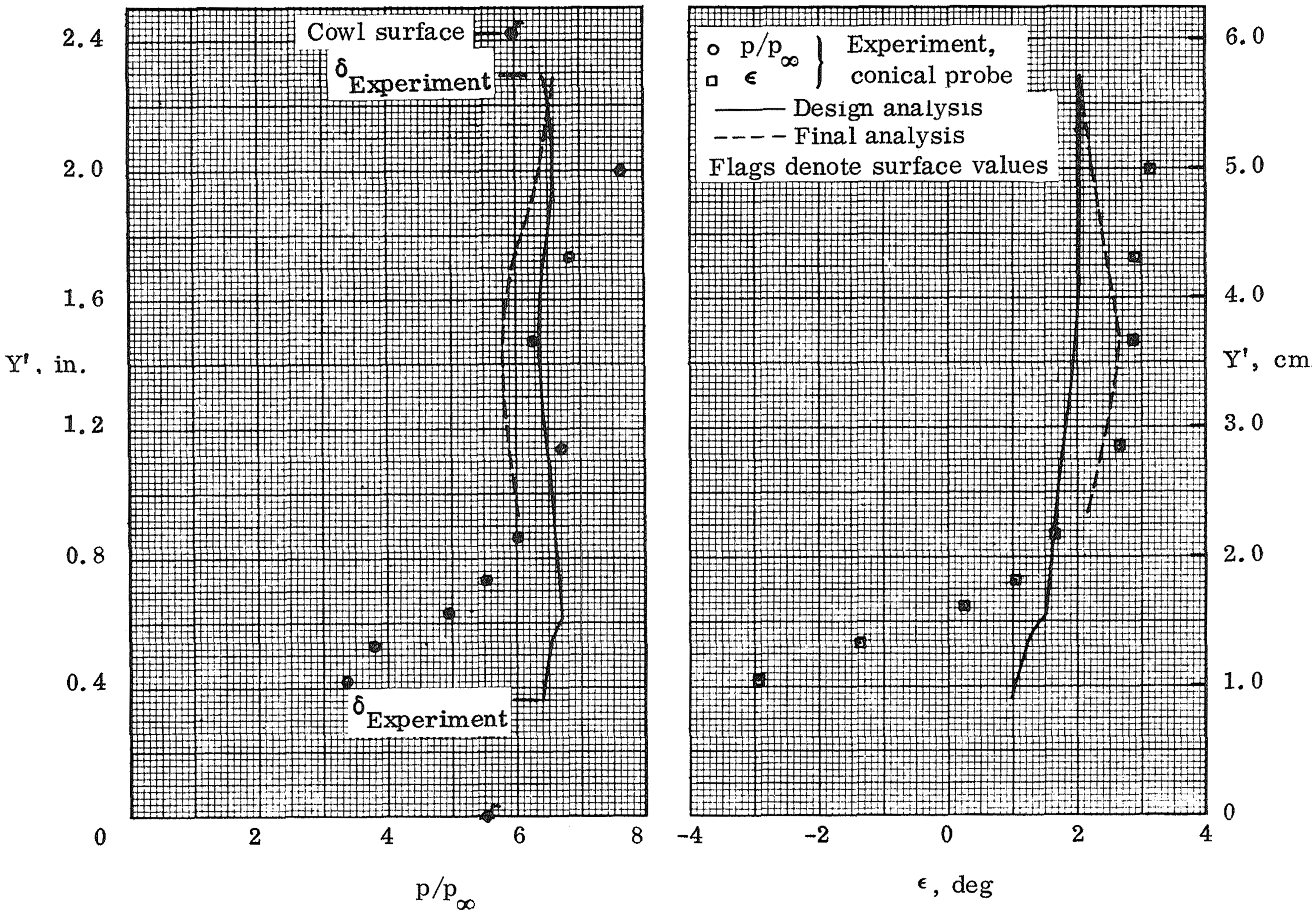

(c) Station $X = 116.84$ cm.

Figure 37.– Continued.

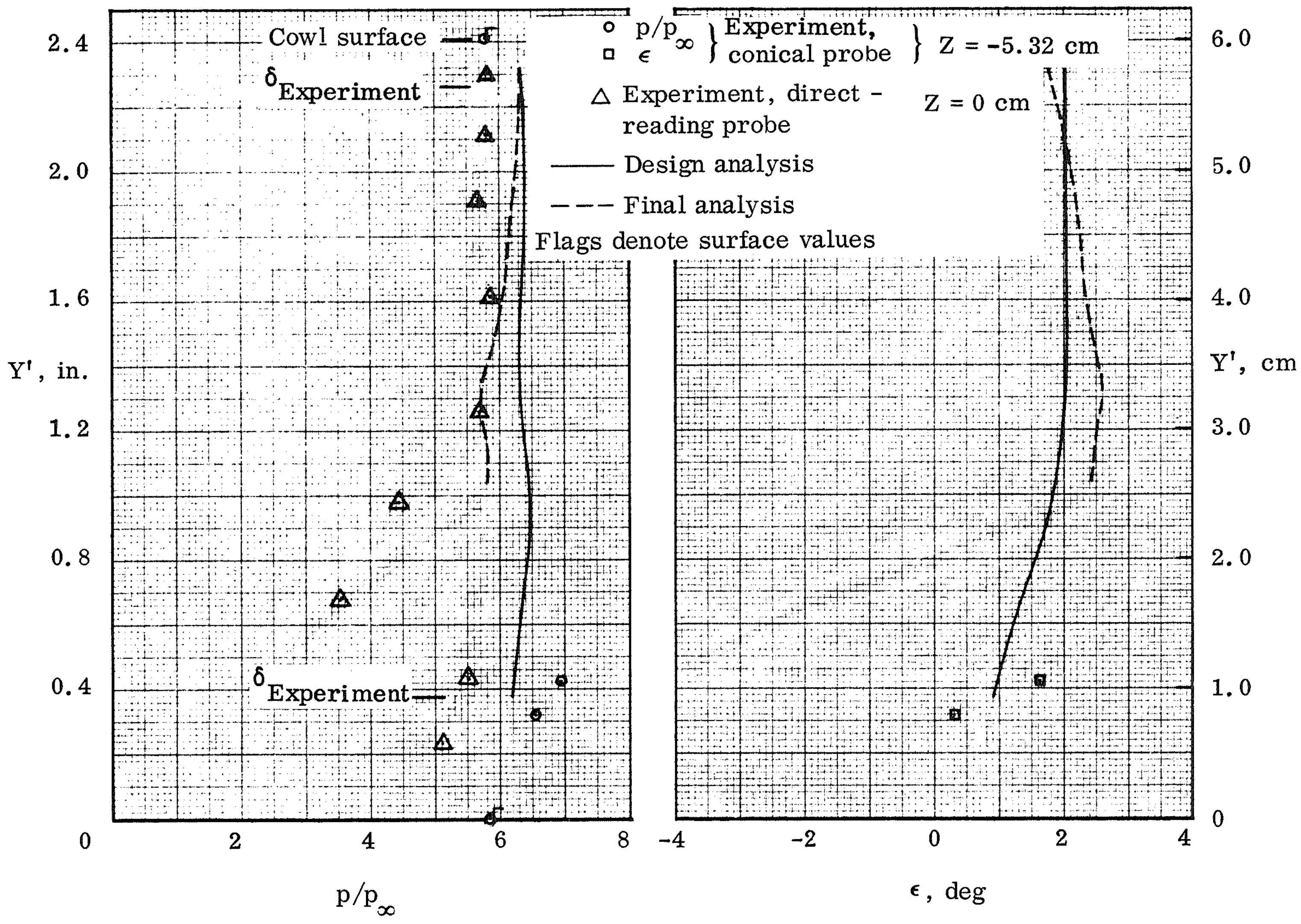

(d) Station $X = 119.38$ cm.

Figure 37.– Concluded.

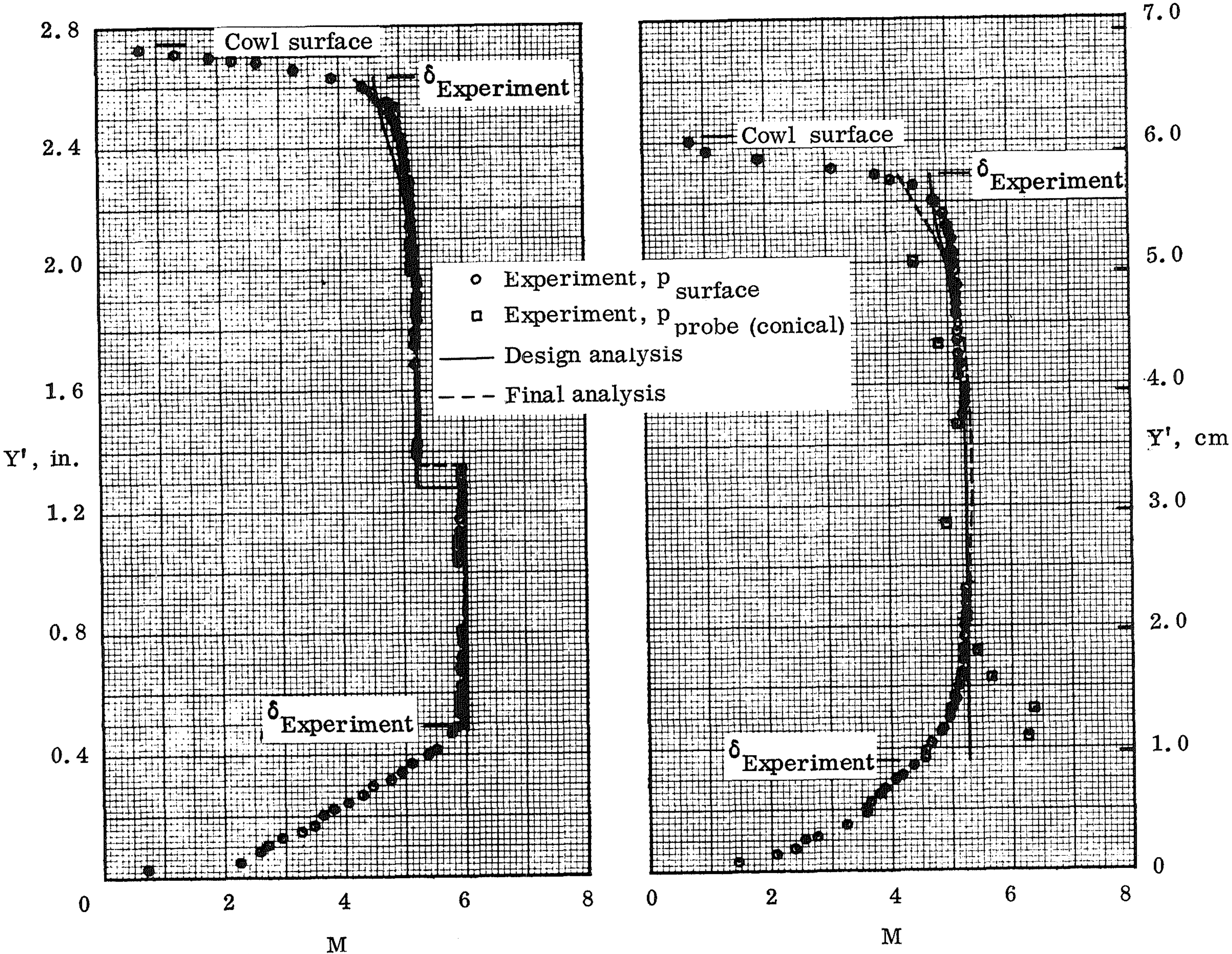

(a) Station X = 101.60 cm.

(b) Station X = 116.84 cm.

Figure 38.– Mach number distributions; Z = –5.32 cm, P2 inlet model.

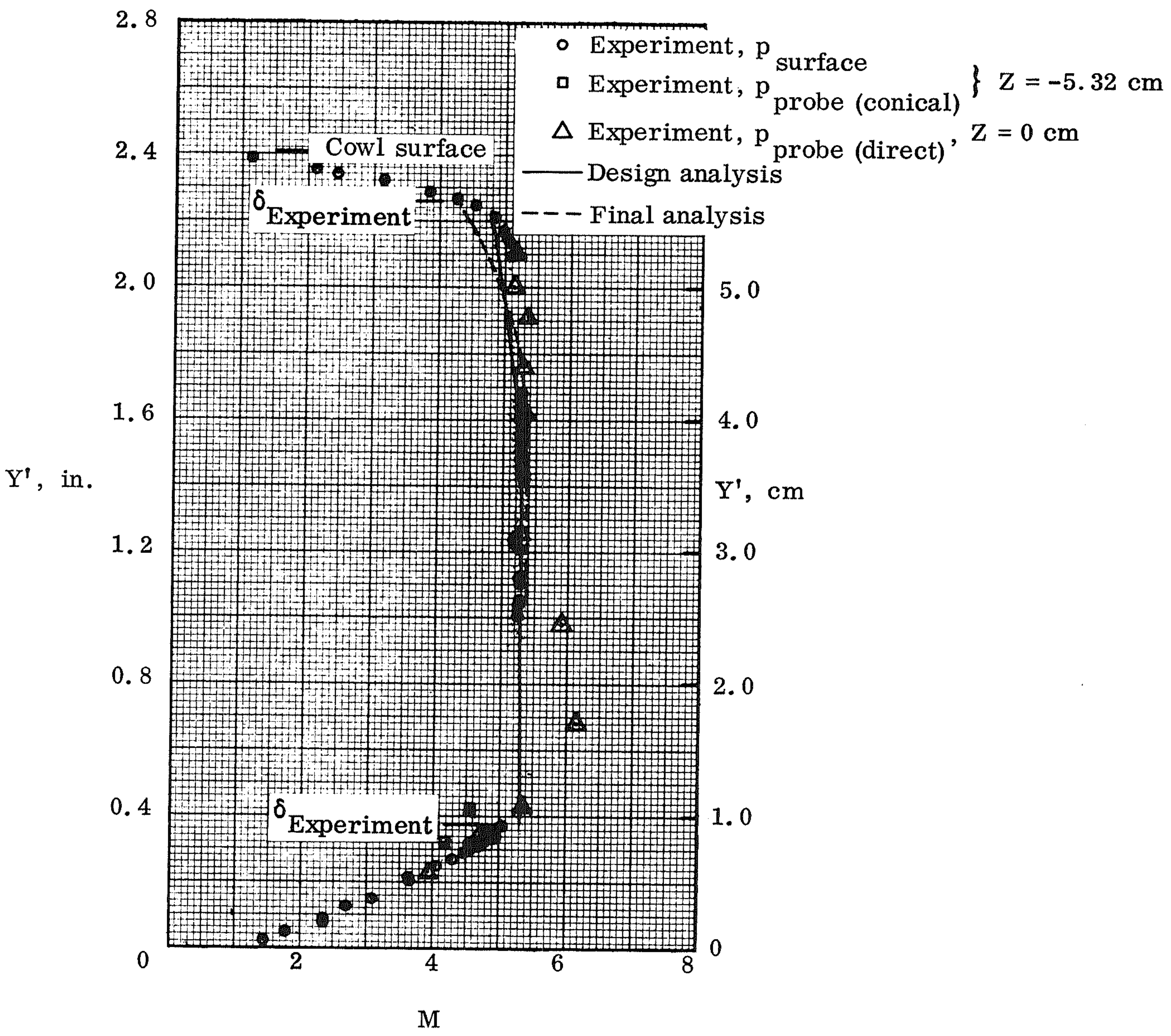

(c) Station X = 119.38 cm.

Figure 38.— Concluded.

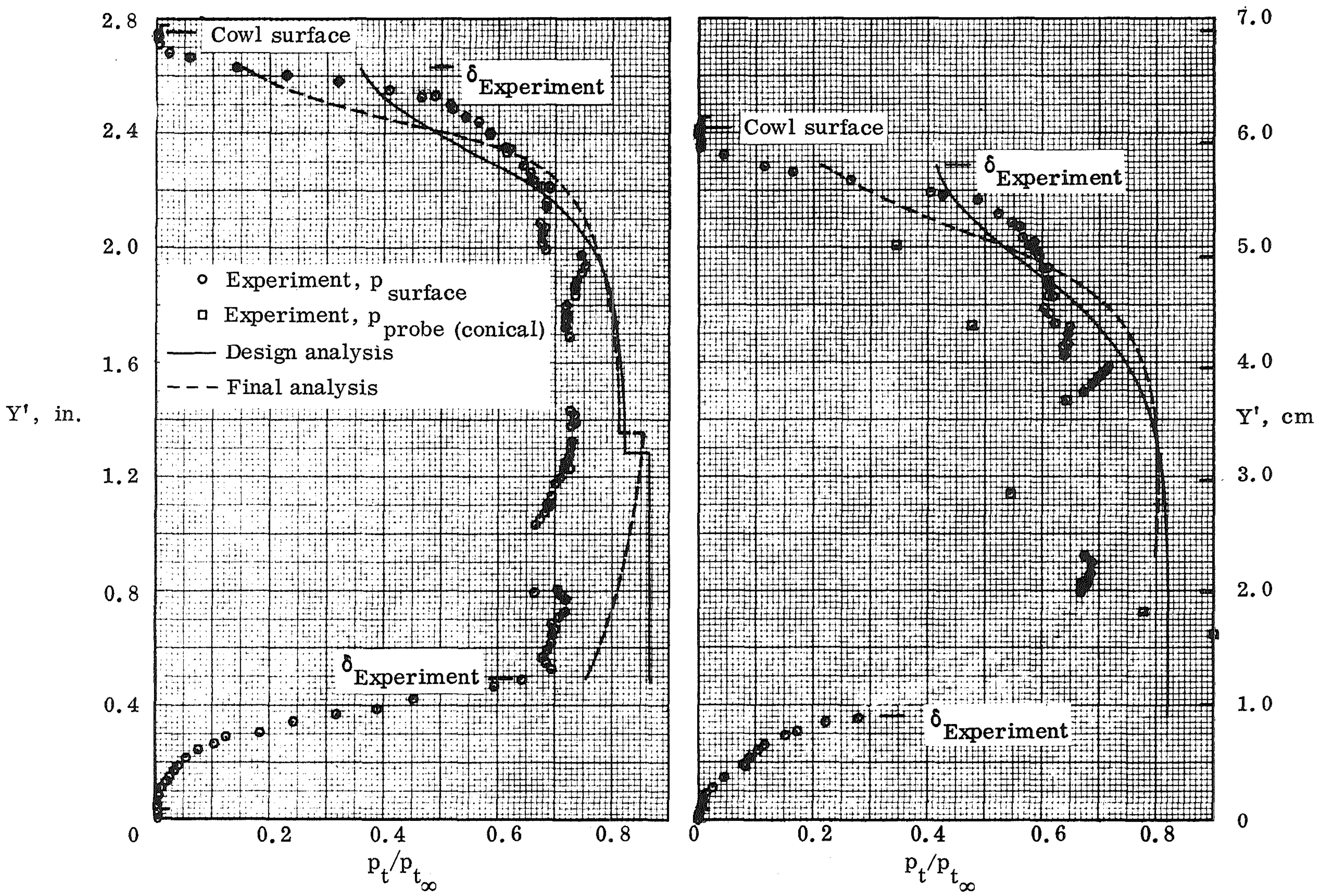

(a) Station X = 101.60 cm.

(b) Station X = 116.84 cm.

Figure 39.– Total-pressure recovery distributions; Z = –5.32 cm, P2 inlet model

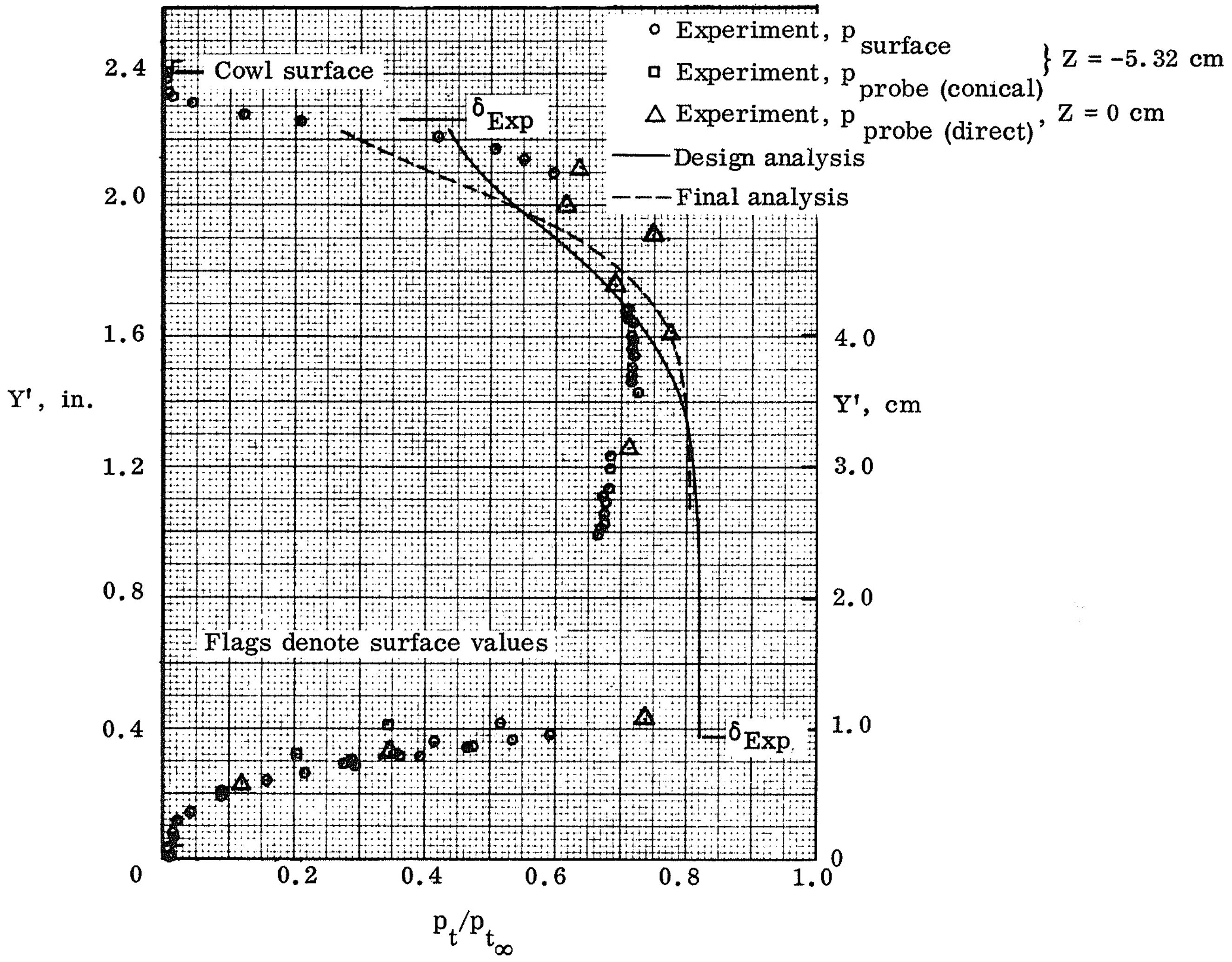

(c) Station X = 119.38 cm.

Figure 39.– Concluded.

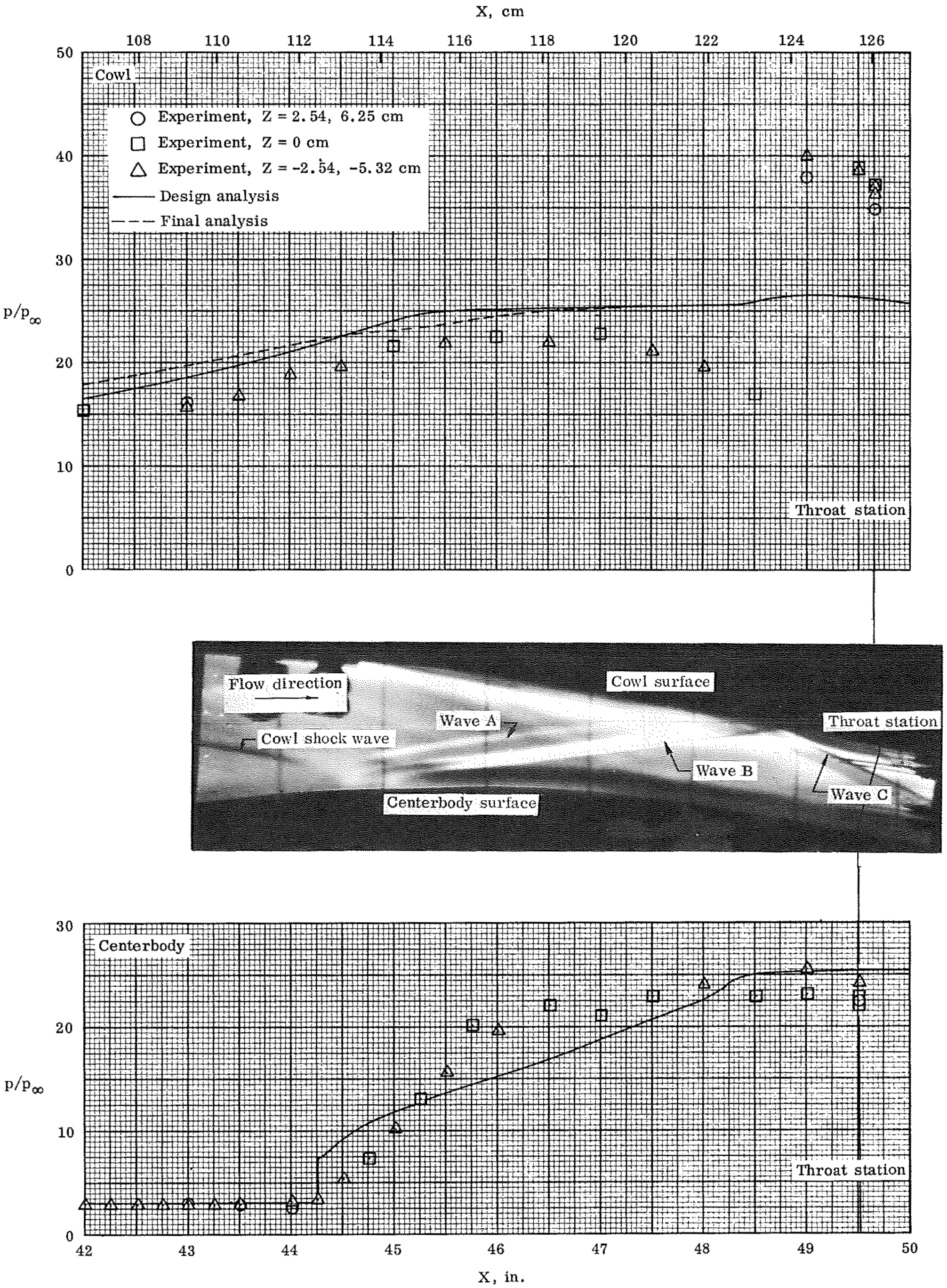

Figure 40.– Surface pressure distributions and shock-wave pattern; P8 inlet model.

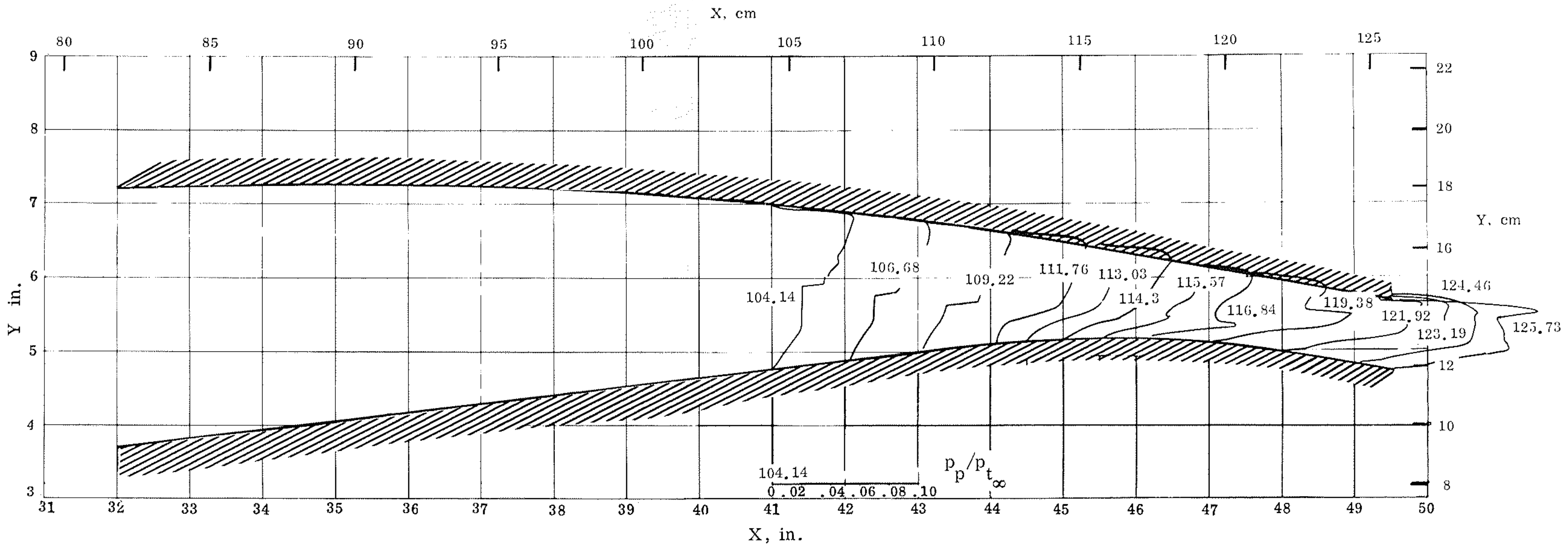

Figure 41.– Summary of experimental pitot-pressure distributions; Z = –5.32 cm, P8 inlet model.

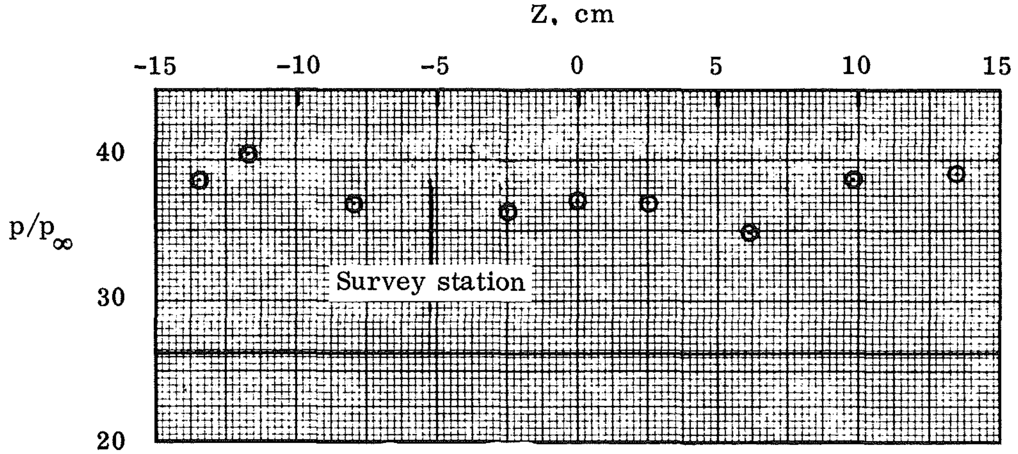

(a) Cowl, X = 126.14 cm.

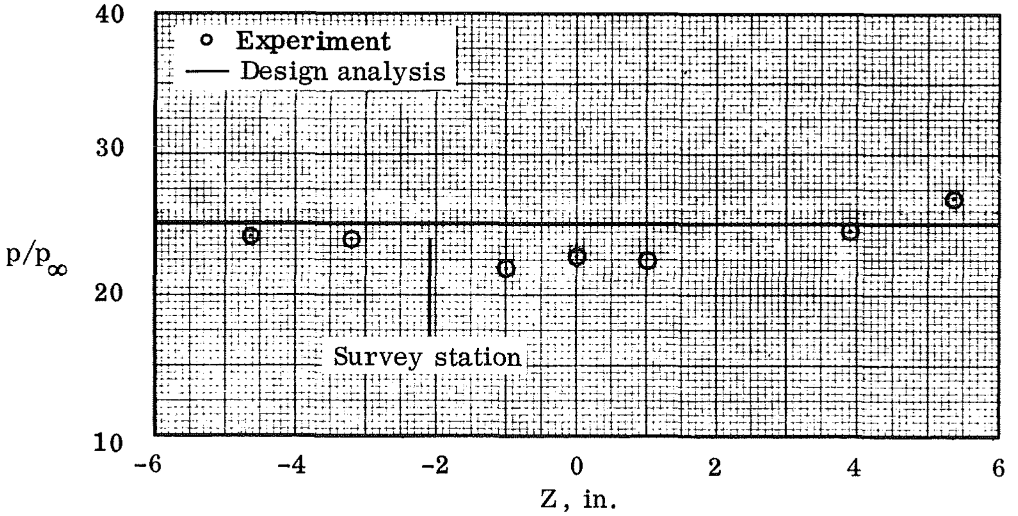

(b) Centerbody, X = 125.73 cm.

Figure 42.– Lateral distributions of surface pressure at throat station; P8 inlet model.

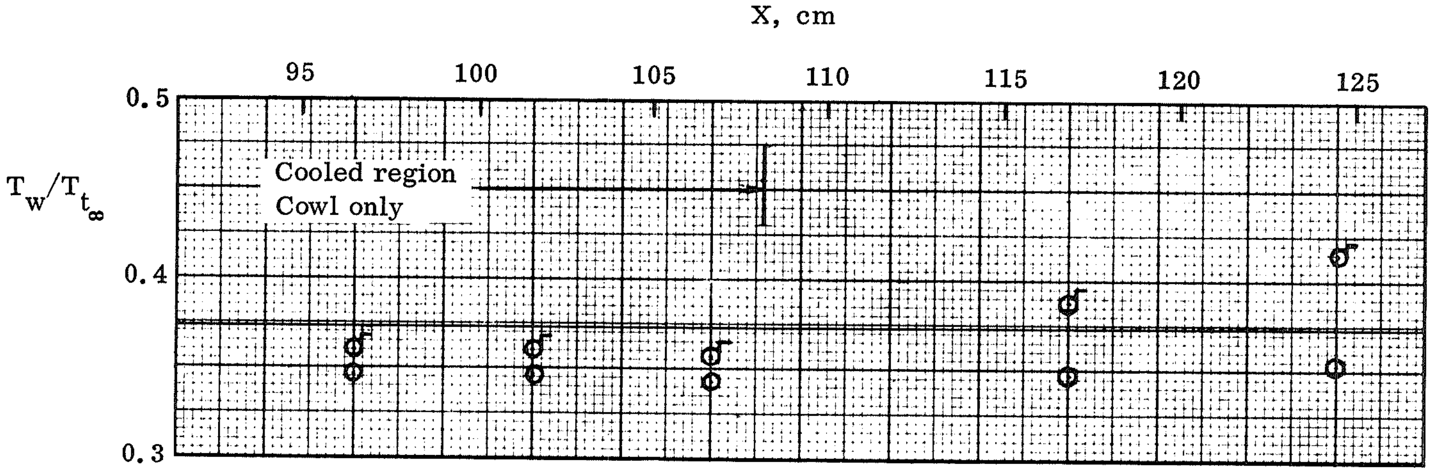

(a) Cowl.

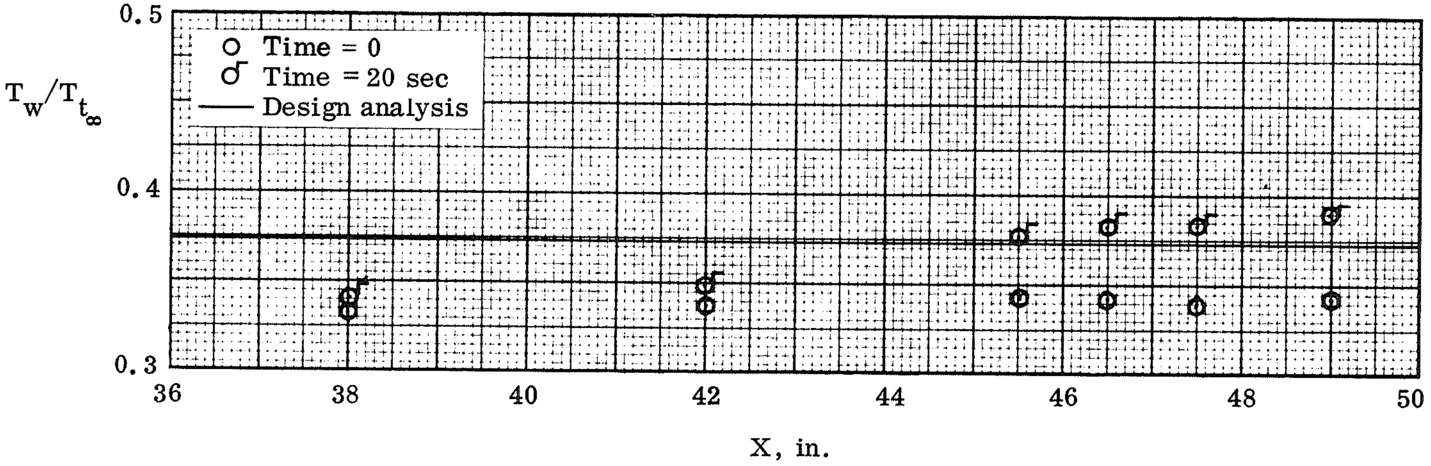

(b) Centerbody.

Figure 43.– Surface temperature distributions; P8 inlet model.

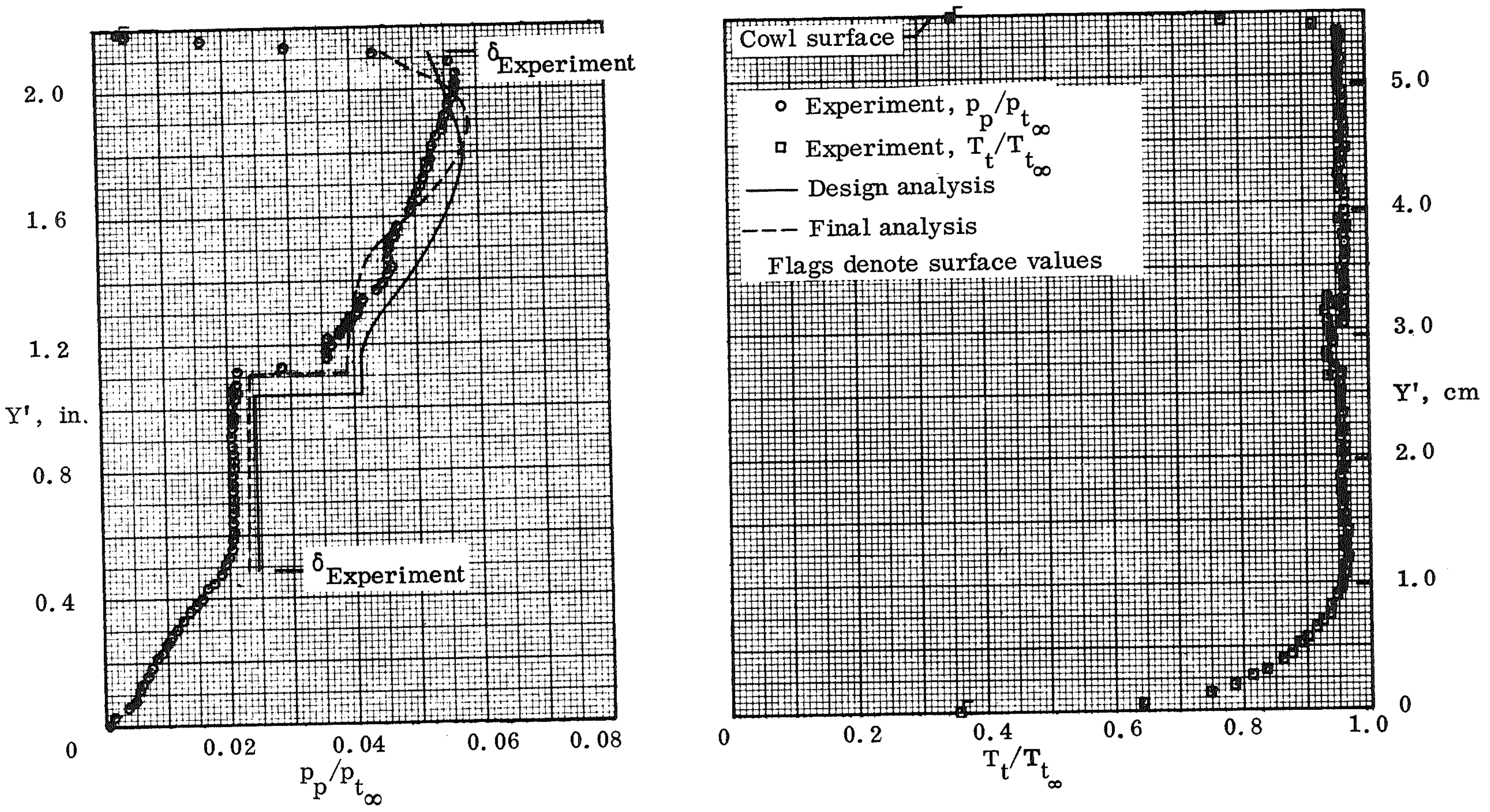

(a) Station X = 104.14 cm.

Figure 44.– Pitot pressure and total-temperature distributions; Z = –5.32 cm, P8 inlet model.

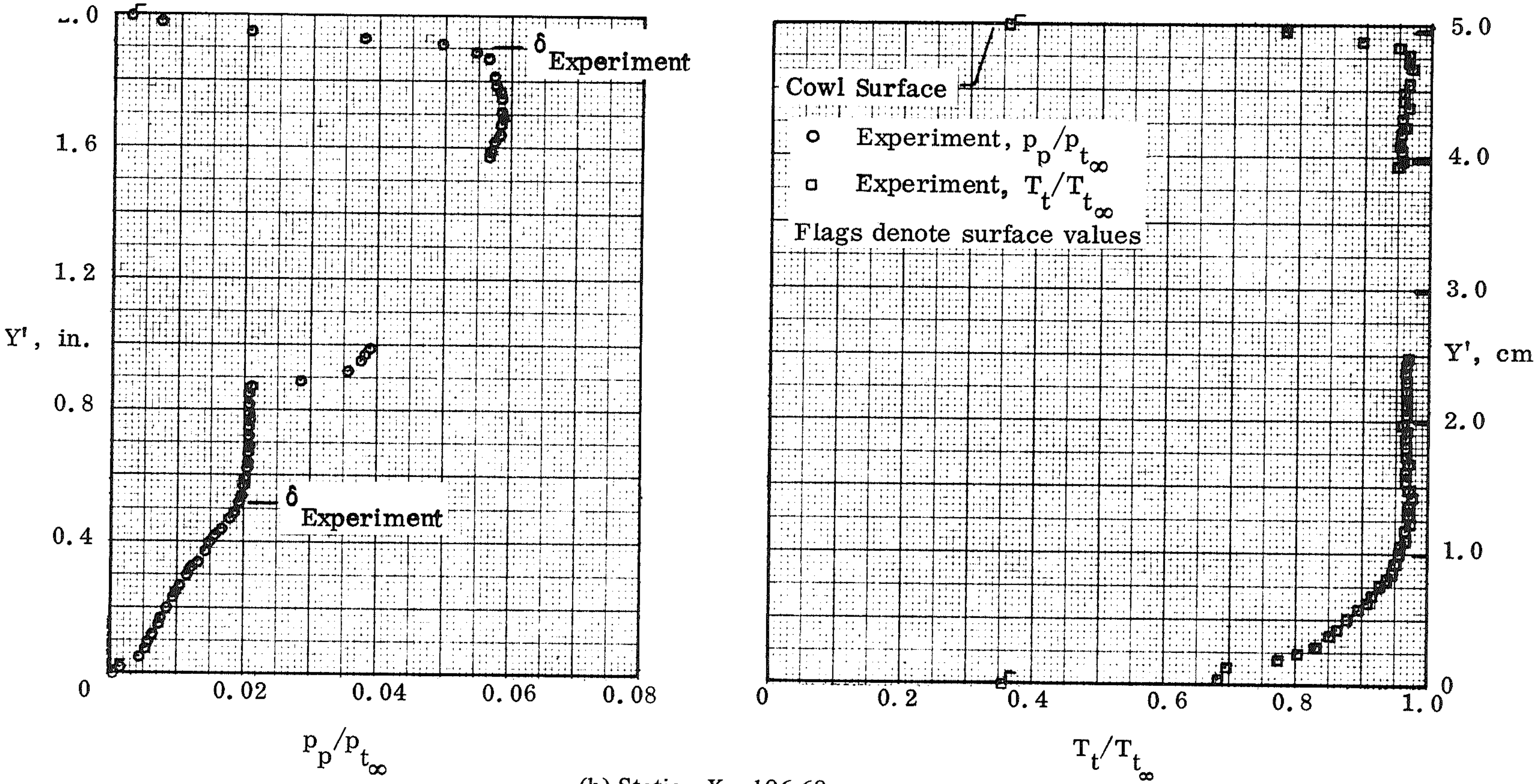

(b) Station X = 106.68 cm.

Figure 44.– Continued.

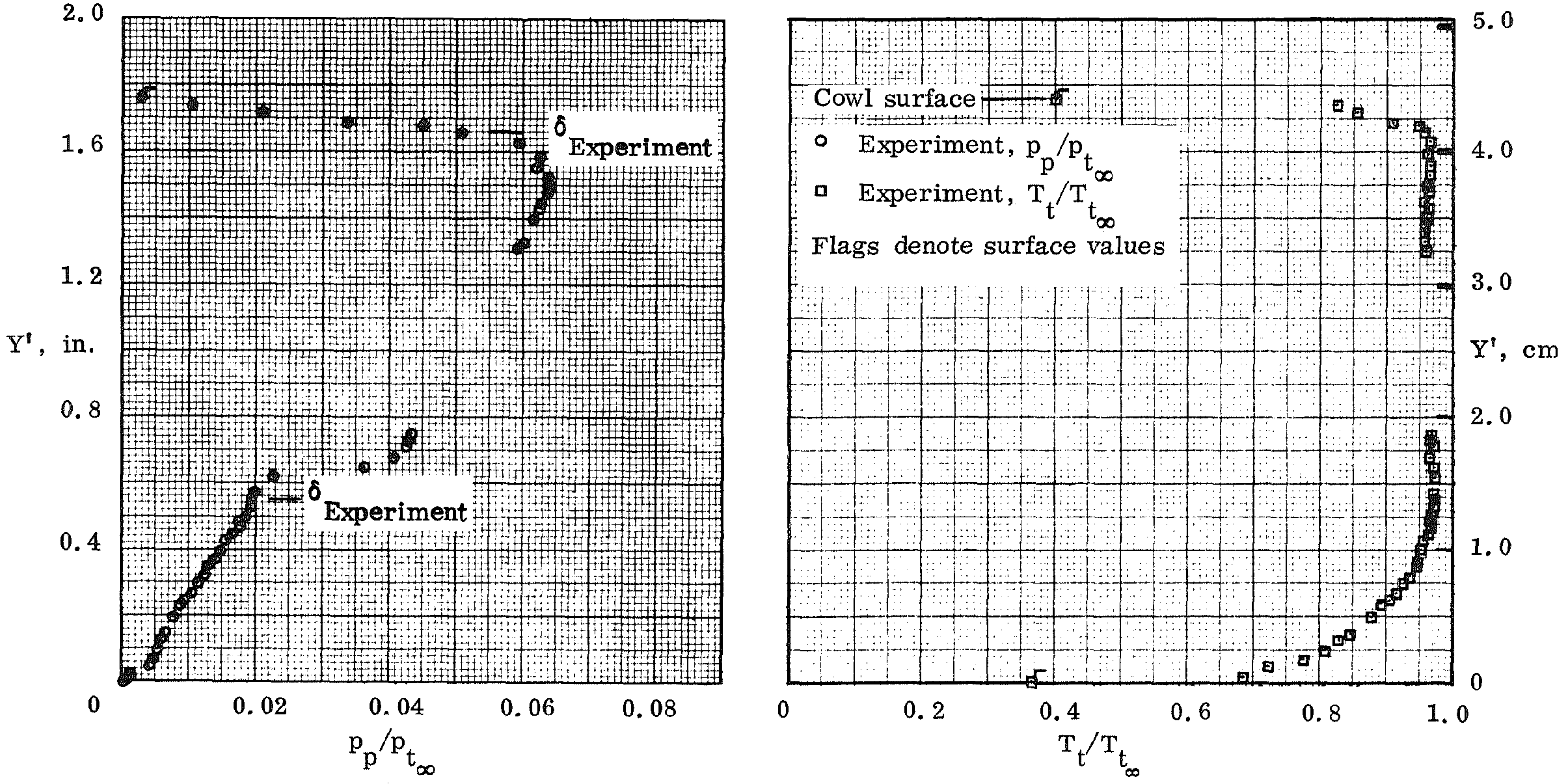

(c) Station X = 109.22 cm.

Figure 44.– Continued.

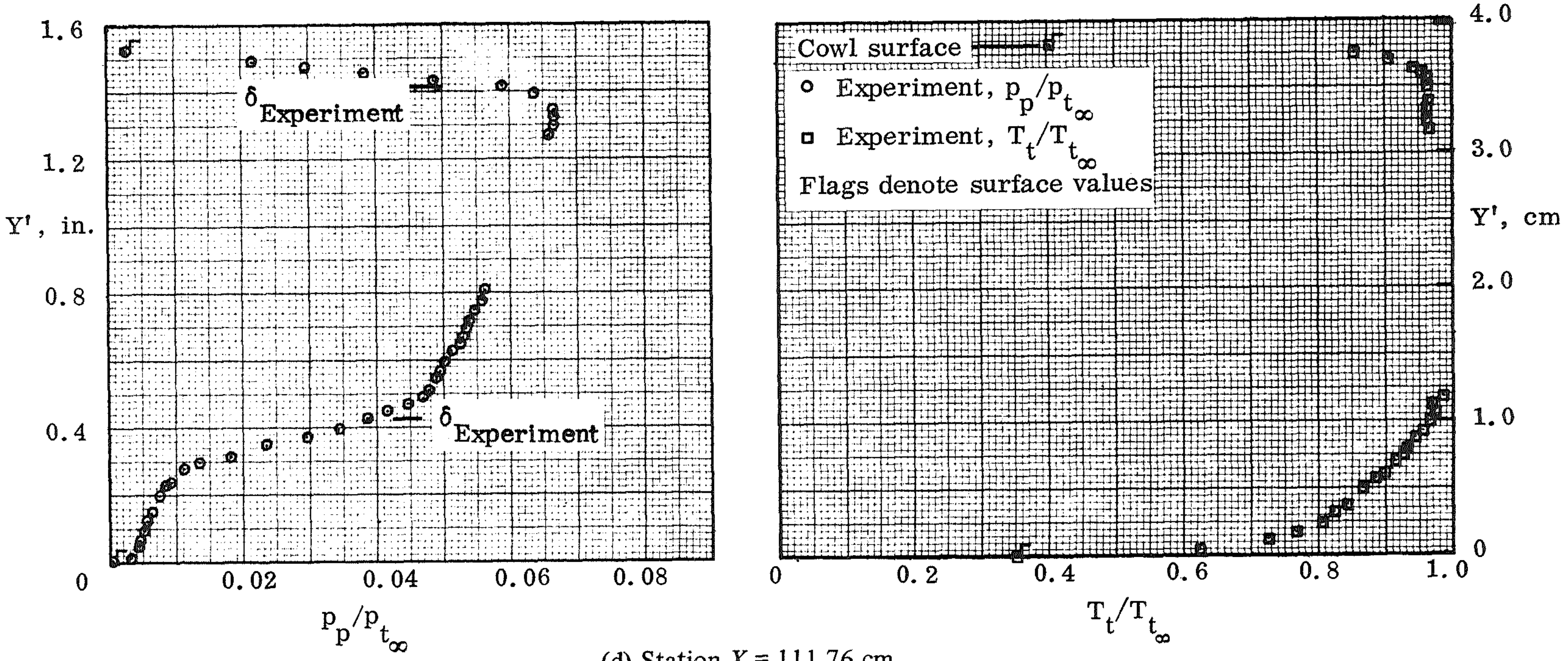

(d) Station X = 111.76 cm.

Figure 44.– Continued.

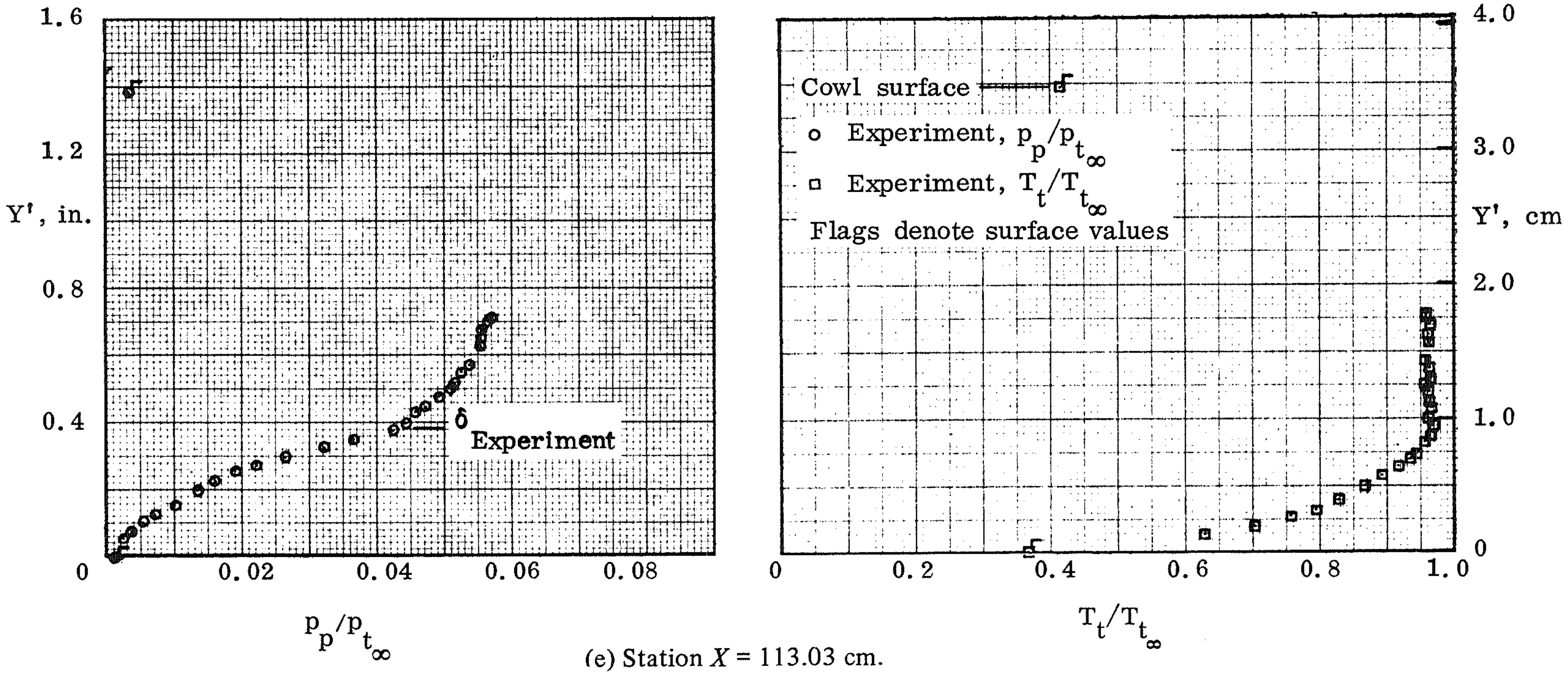

(e) Station X = 113.03 cm.

Figure 44.– Continued.

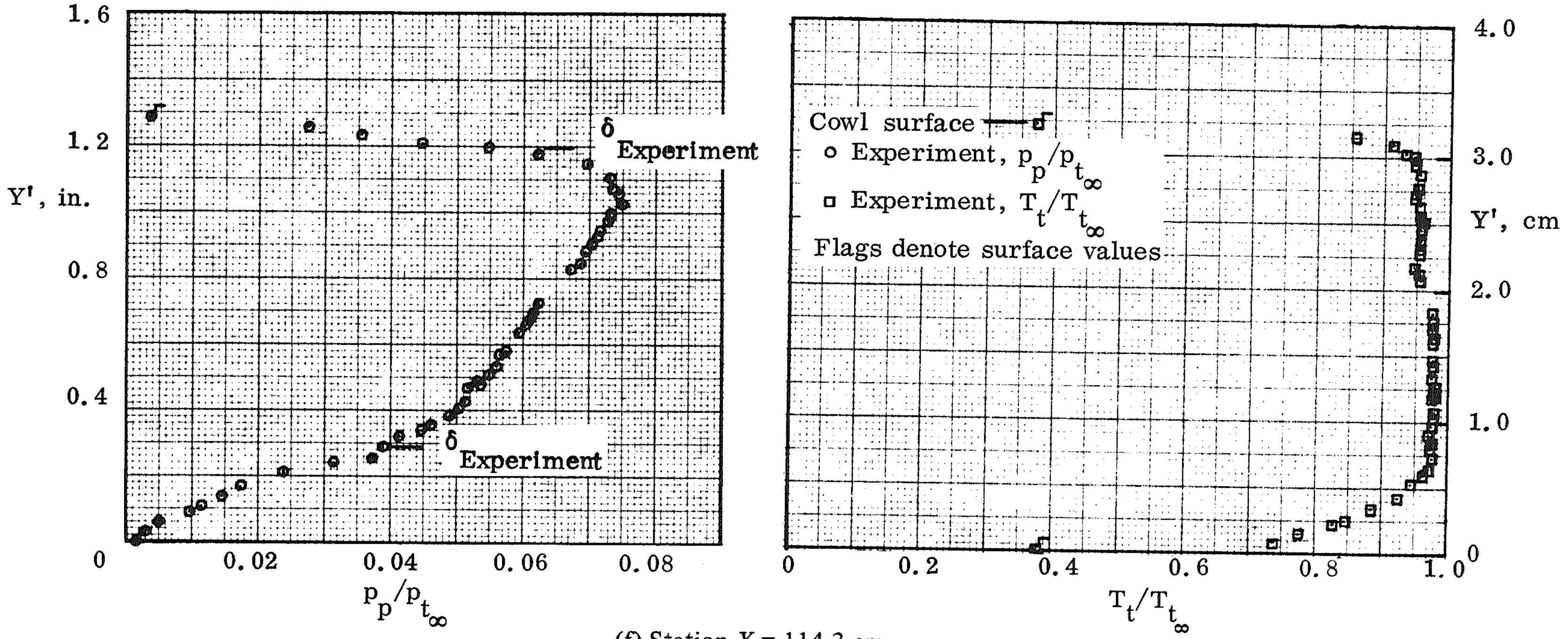

(f) Station X = 114.3 cm.

Figure 44.– Continued.

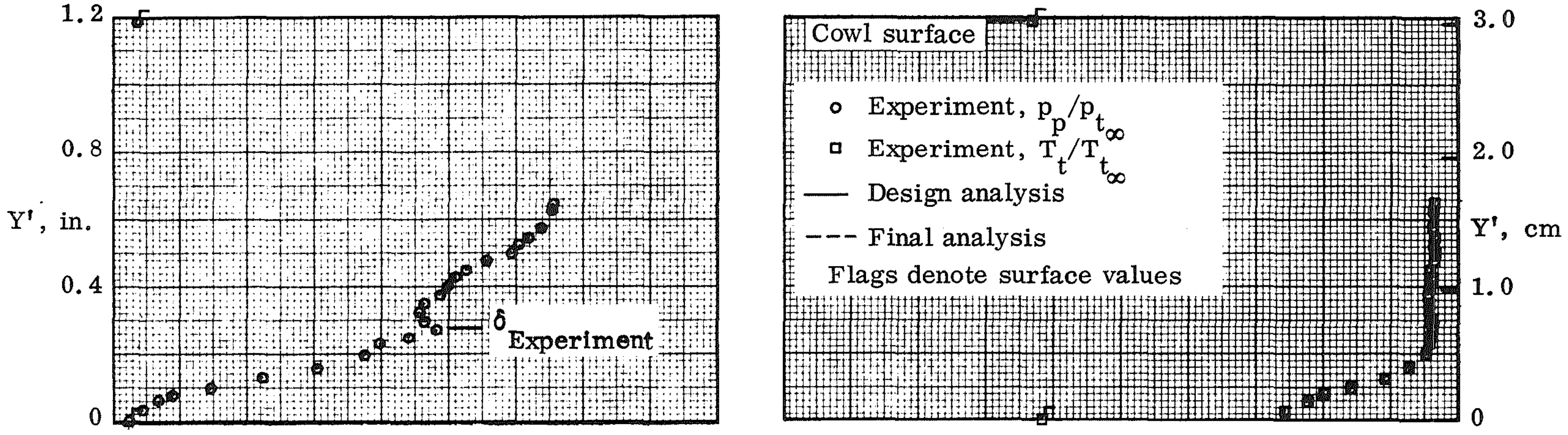

(g) Station X = 115.57 cm.

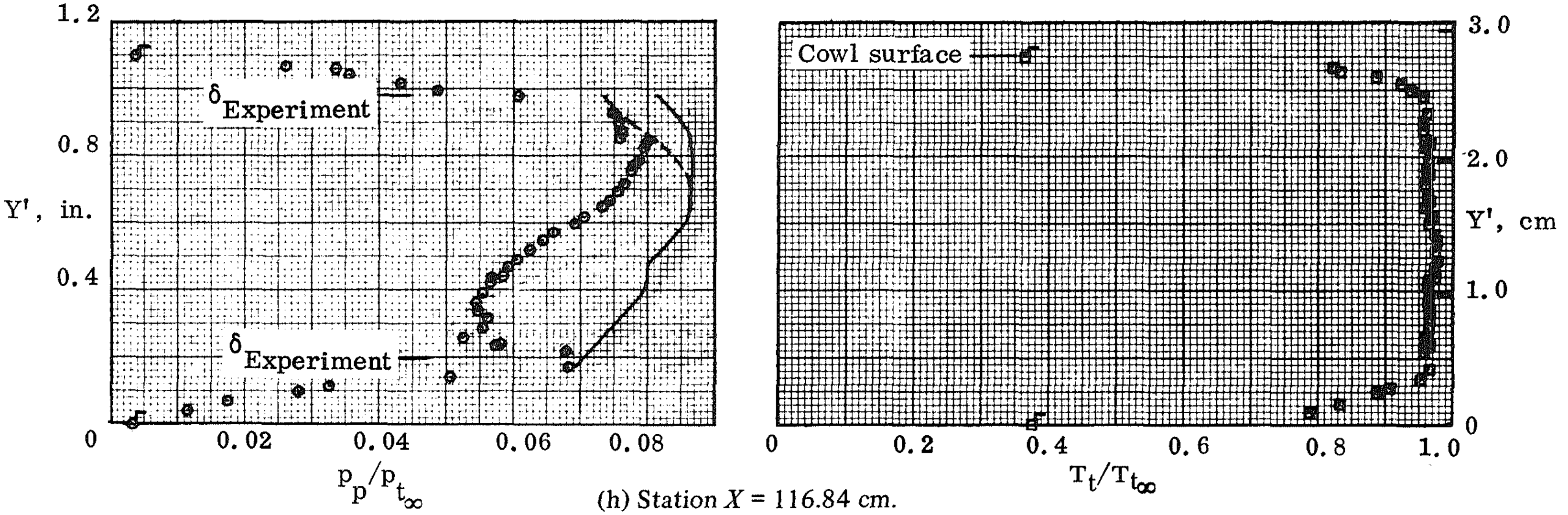

(h) Station X = 116.84 cm.

Figure 44.– Continued.

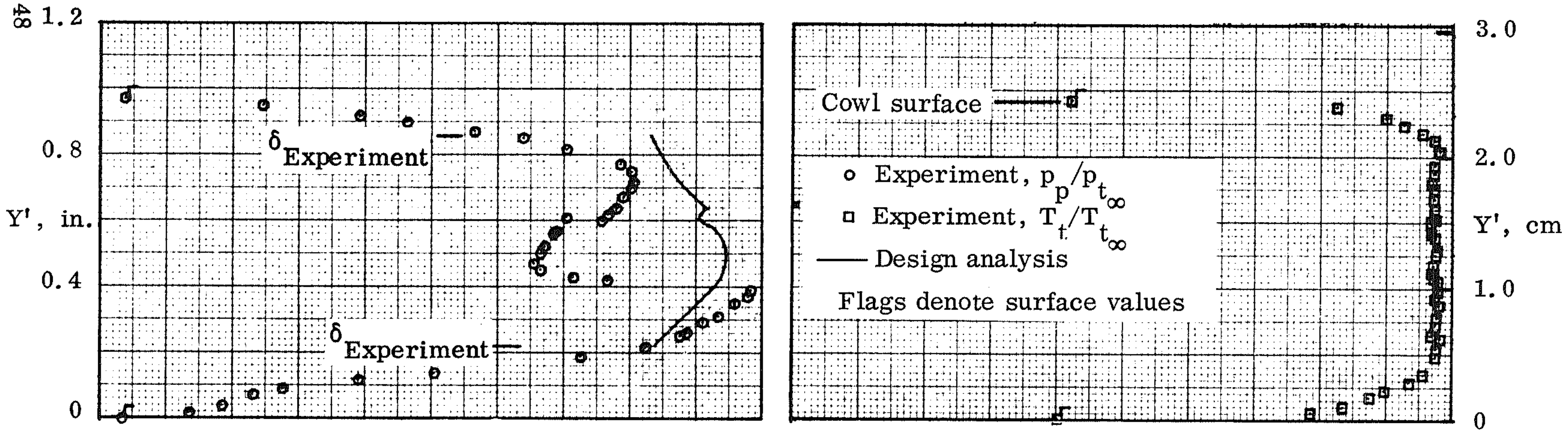

(i) Station *X* = 119.38 cm.

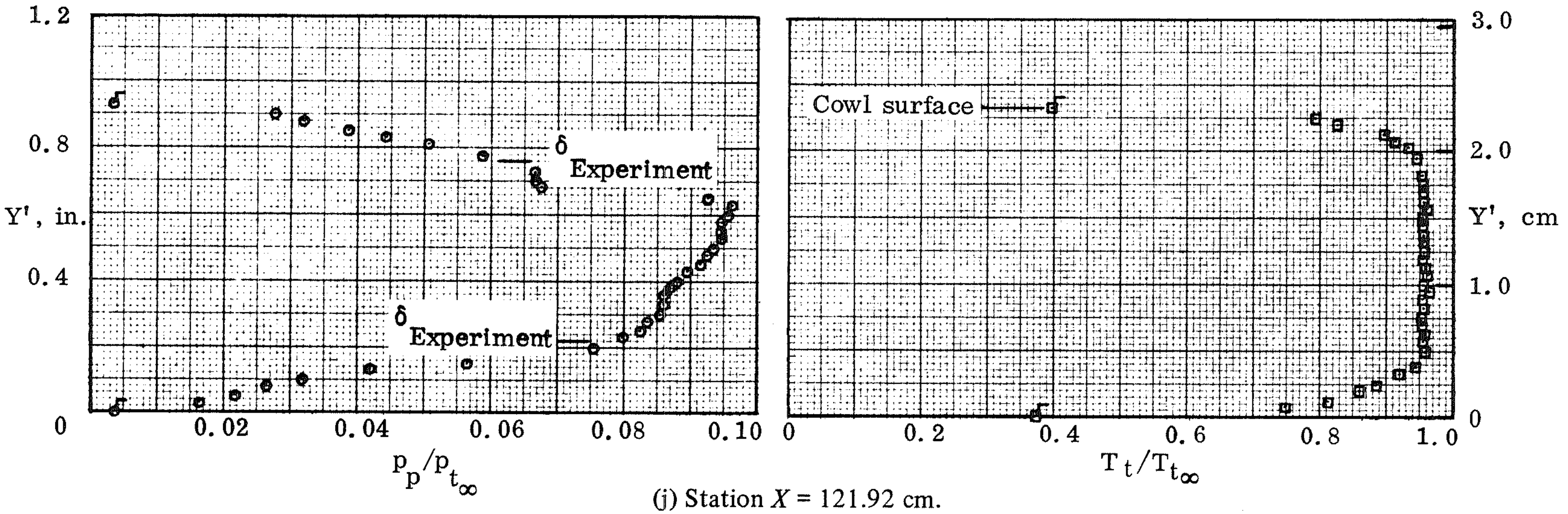

(j) Station *X* = 121.92 cm.

Figure 44.– Continued.

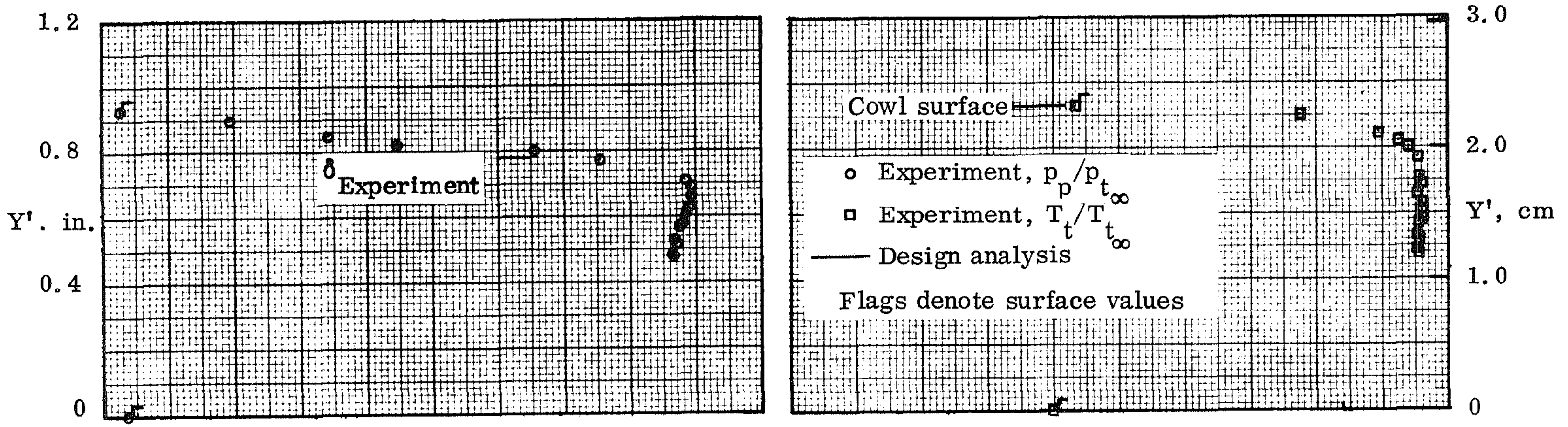

(k) Station X = 123.19 cm.

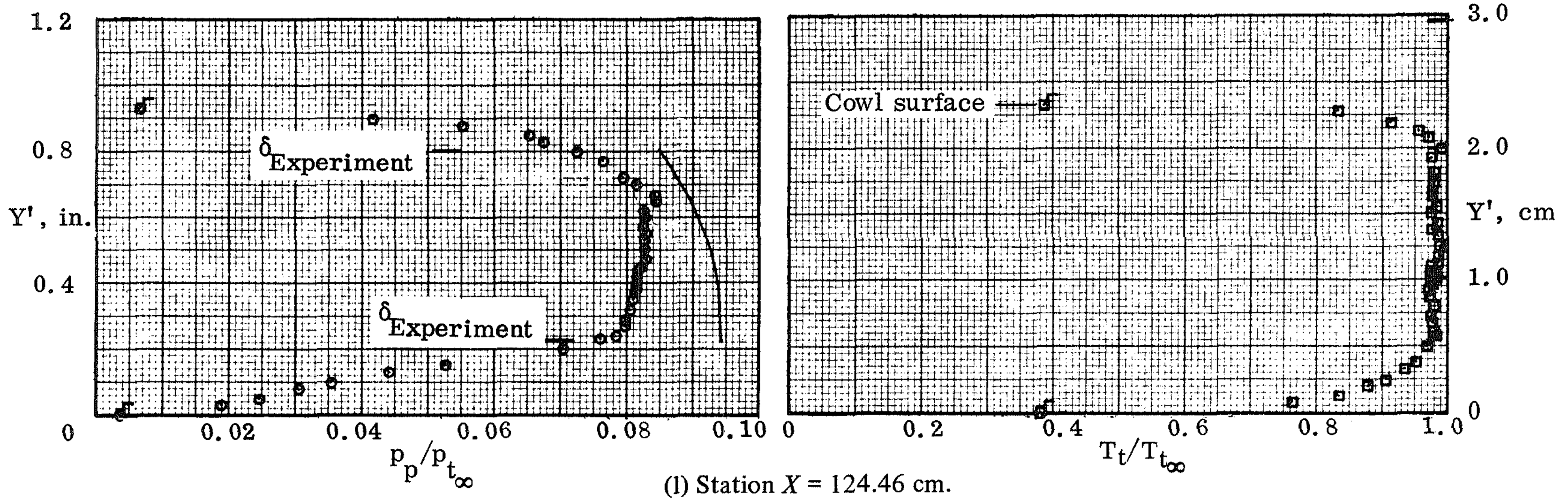

(l) Station X = 124.46 cm.

Figure 44.– Continued.

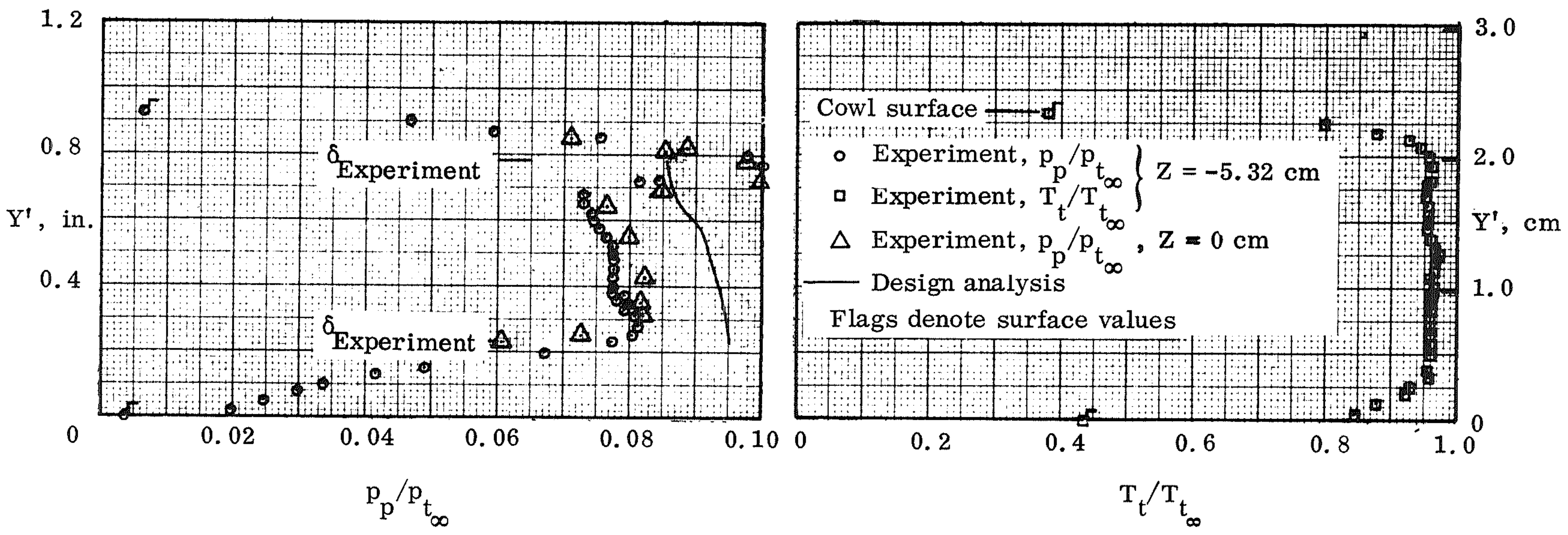

(m) Station X = 125.73 cm.

Figure 44.– Concluded.

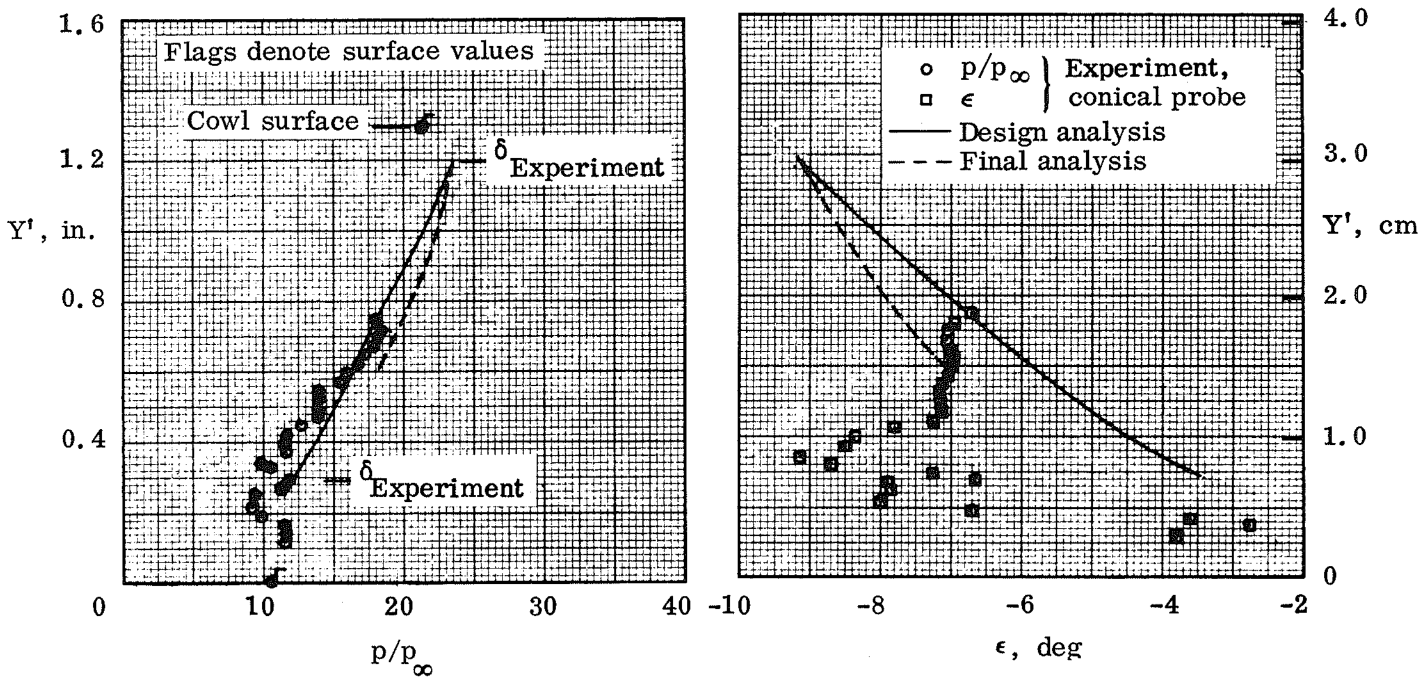

(a) Station $X = 114.3$ cm.

Figure 45.– Static pressure and flow angle distributions; $Z = -5.32$ cm, P8 inlet model.

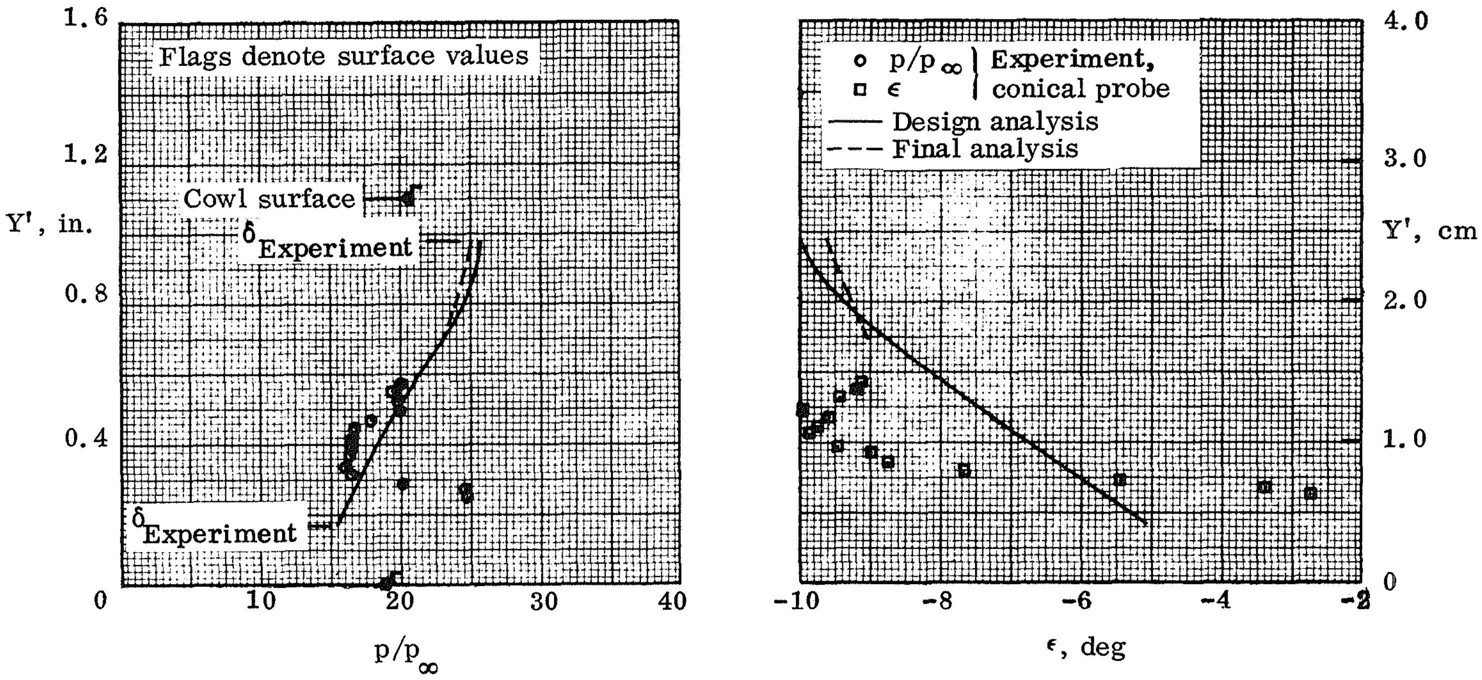

(b) Station $X = 116.84$ cm.

Figure 45.– Continued.

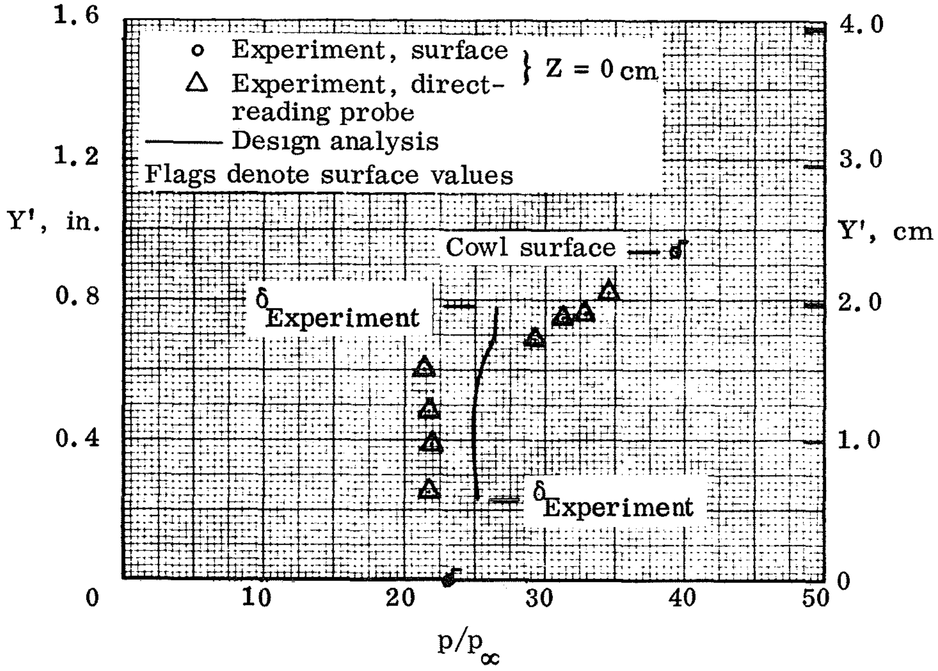

(c) Station X = 125.73 cm.

Figure 45.– Concluded.

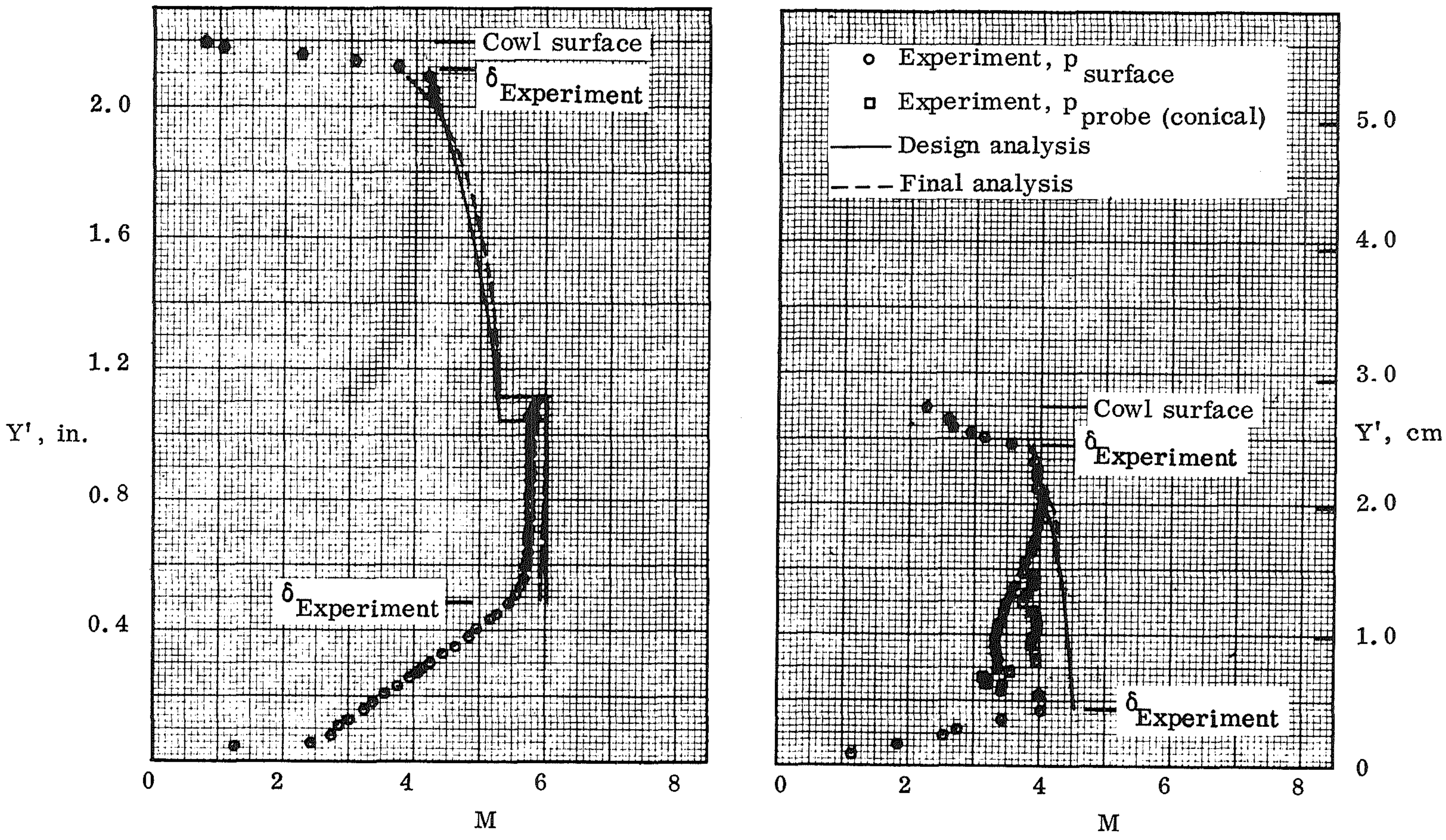

(a) Station X = 104.14 cm.

(b) Station X = 116.84 cm.

Figure 46.– Mach number distributions; Z = –5.32 cm, P8 inlet model.

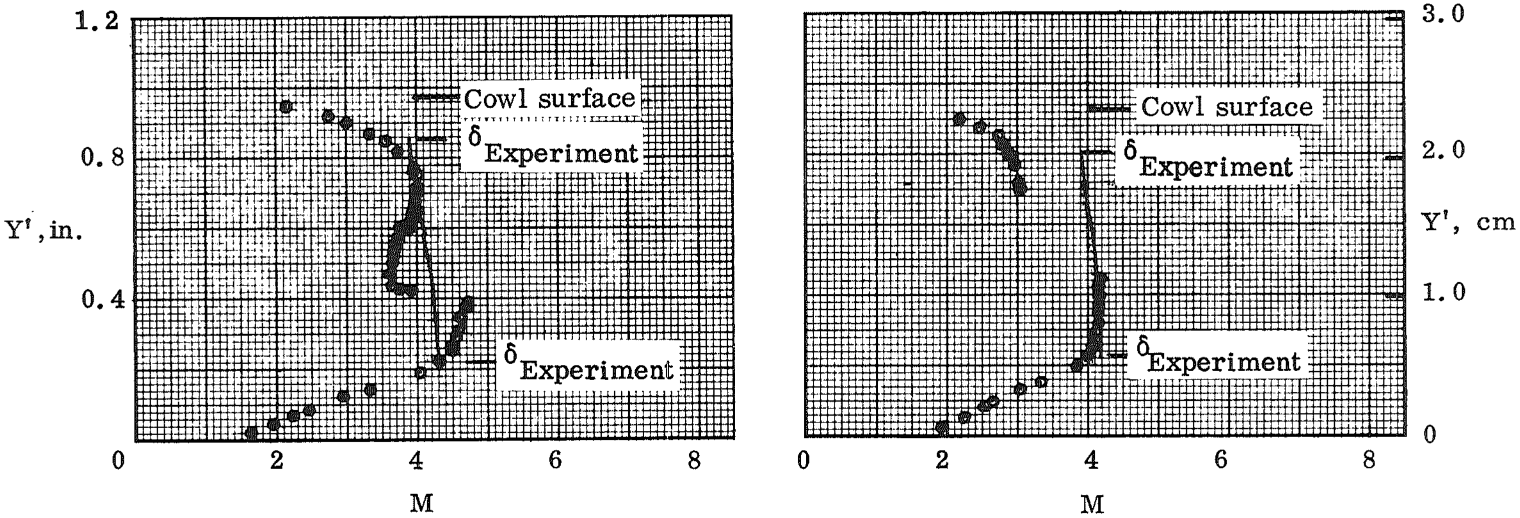

(c) Station X = 119.38 cm.

(d) Station X = 124.46 cm.

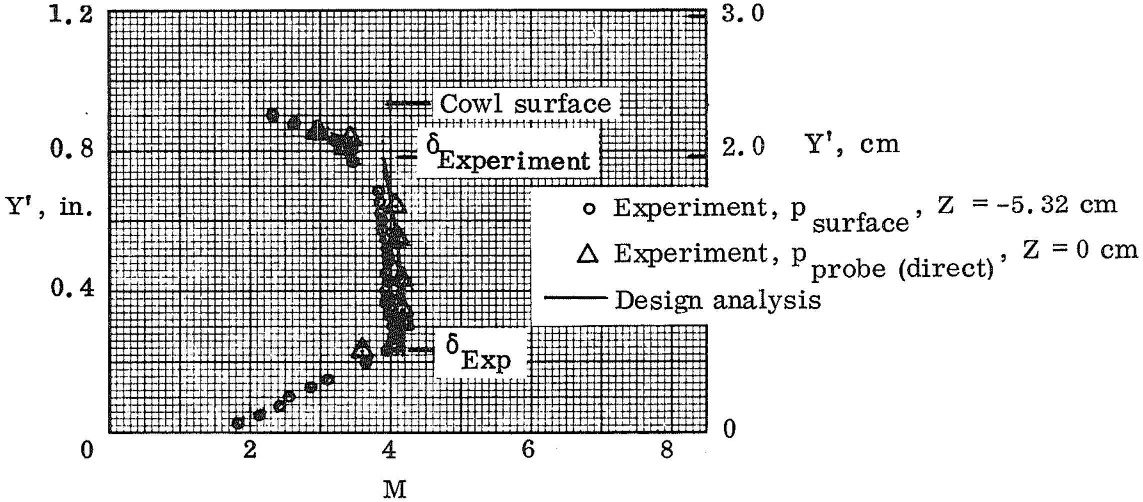

(e) Station X = 125.73 cm.

Figure 46.– Concluded.

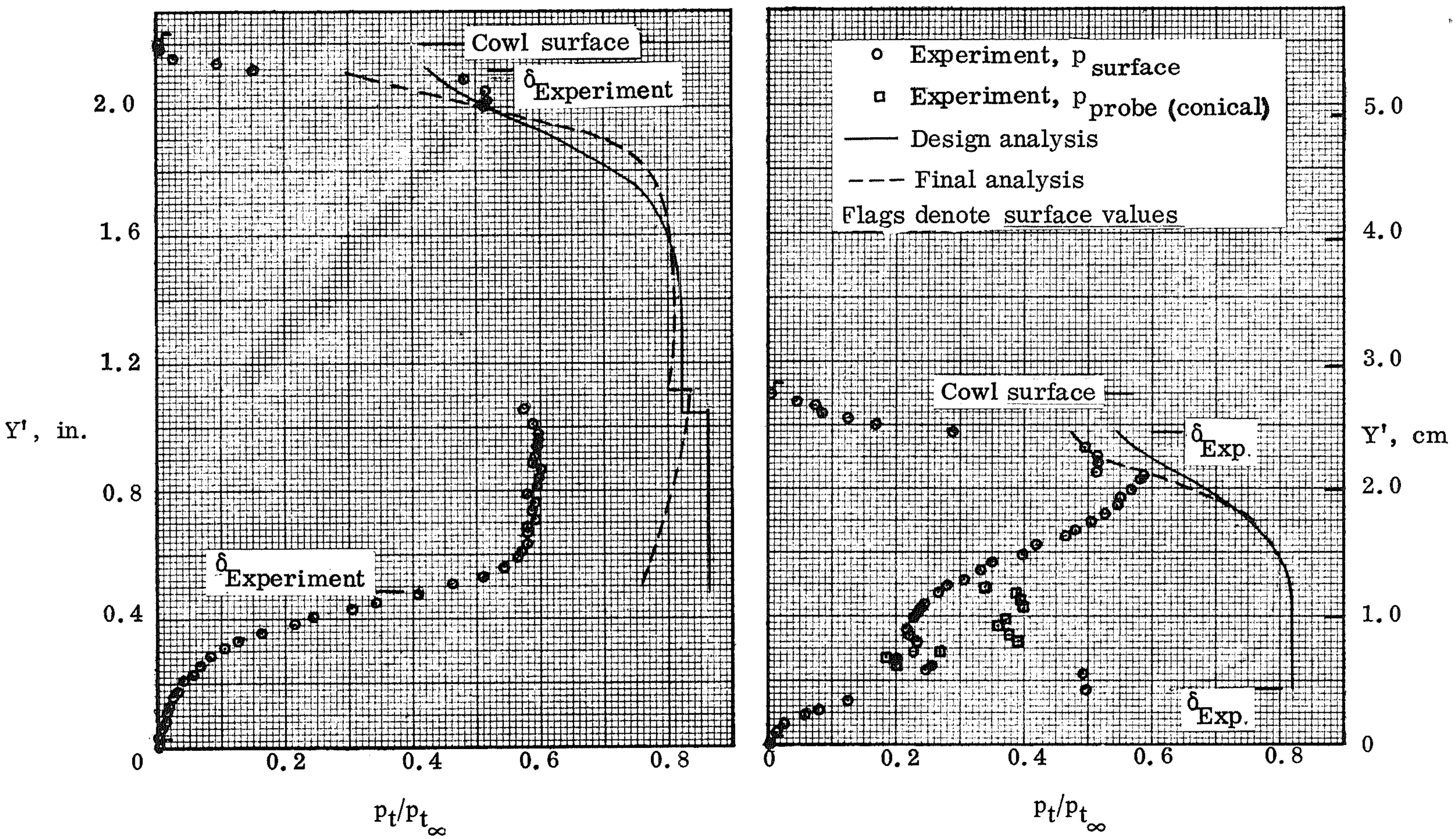

(a) Station $X = 104.14$ cm.

(b) Station $X = 116.84$ cm.

Figure 47.– Total-pressure recovery distributions; $Z = -5.32$ cm, P8 inlet model.

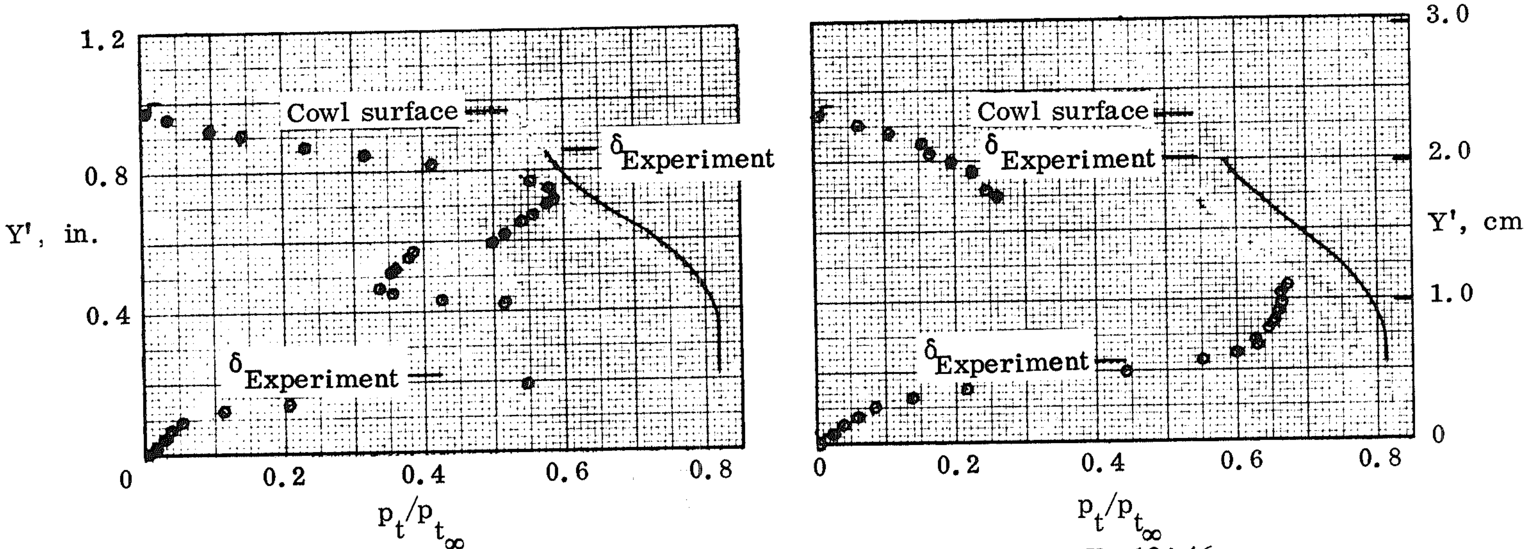

(c) Station X = 119.38 cm.

(d) Station X = 124.46 cm.

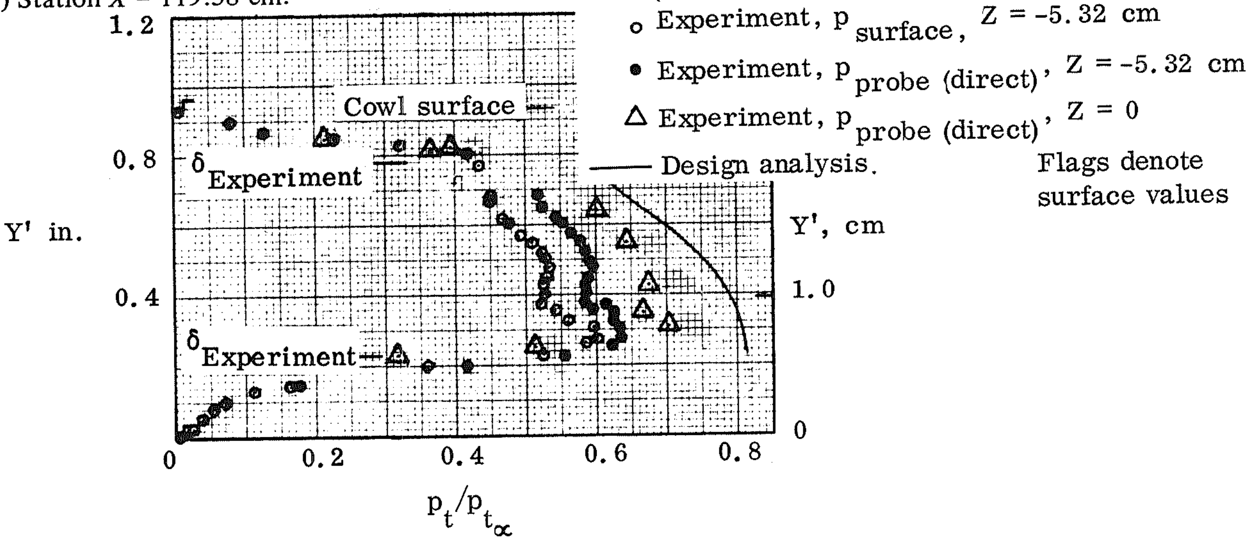

(e) Station X = 125.73 cm.

Figure 47.– Concluded.

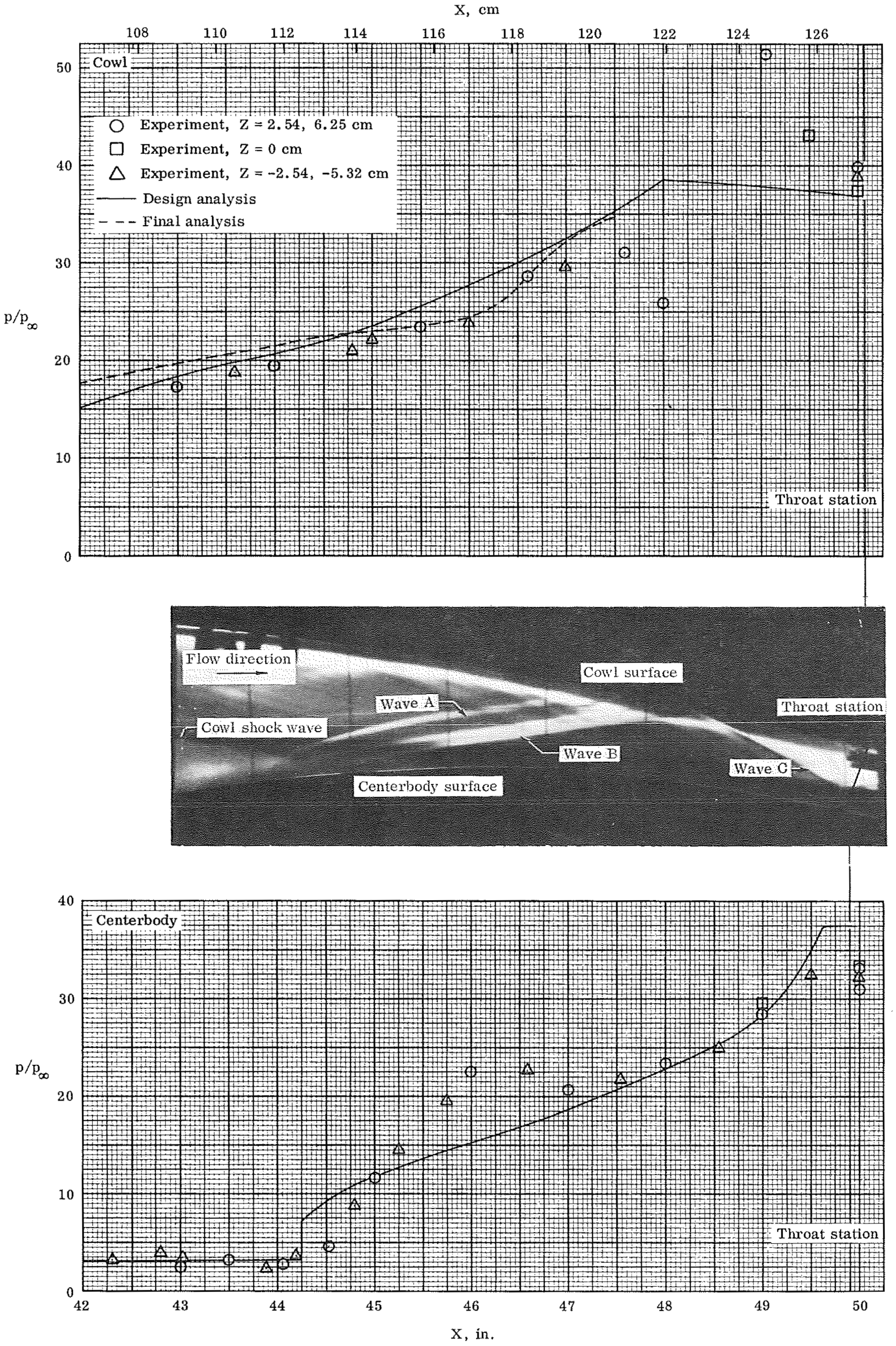

Figure 48.— Surface pressure distributions and shock-wave pattern; P12 inlet model.

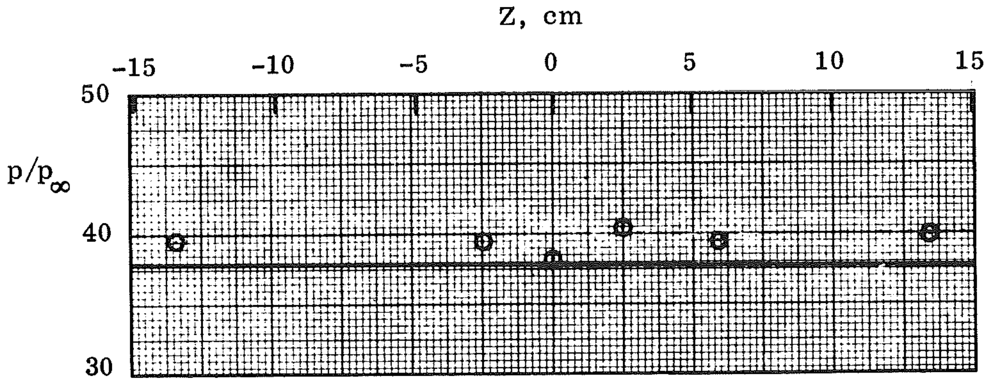

(a) Cowl; X = 127.2 cm.

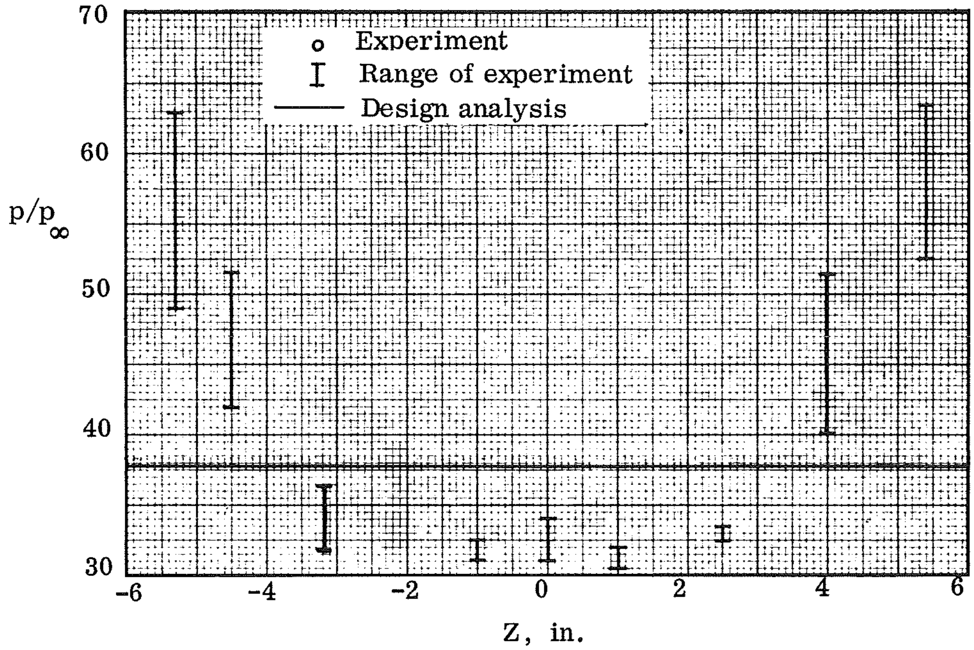

(b) Centerbody; X = 126.75 cm.

Figure 49.– Lateral distributions of surface pressure at throat station; P12 inlet model.

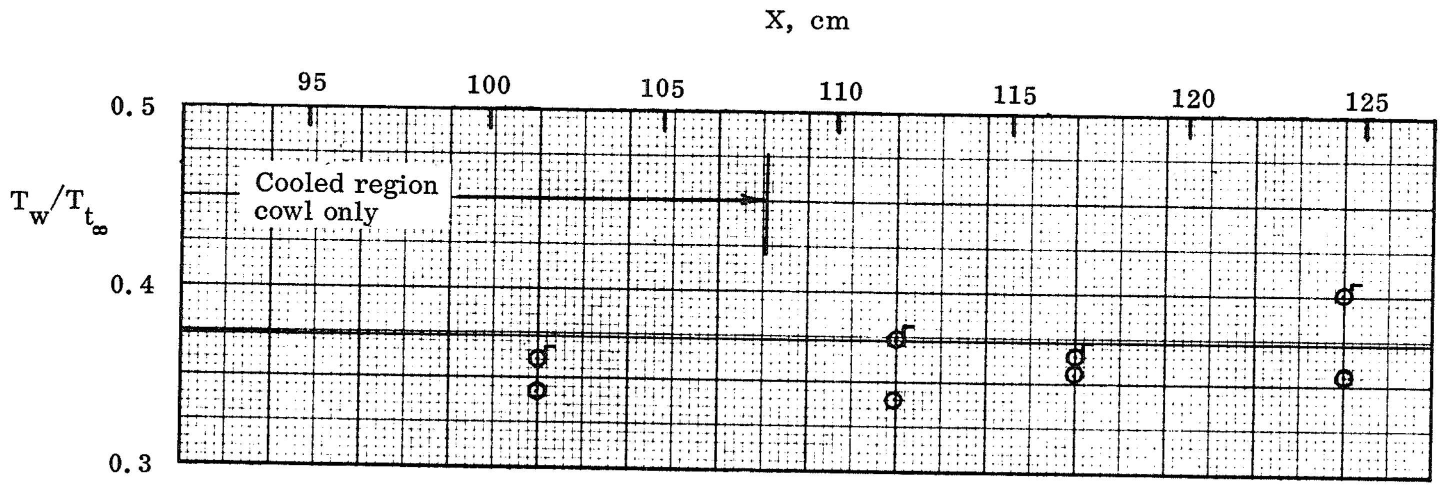

(a) Cowl.

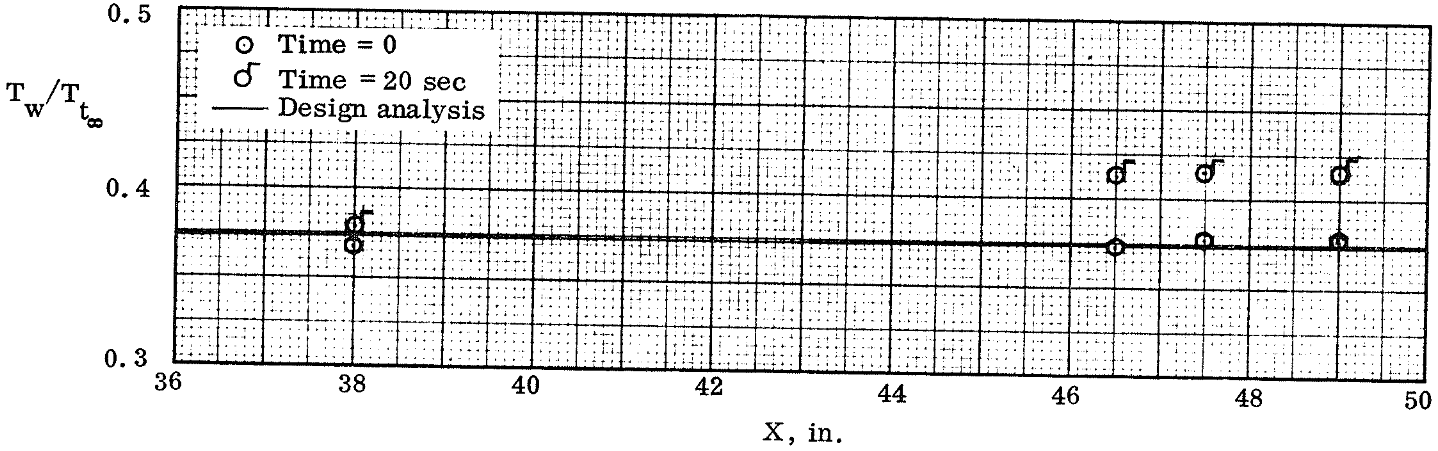

(b) Centerbody.

Figure 50.– Surface temperature distributions; P12 inlet model.

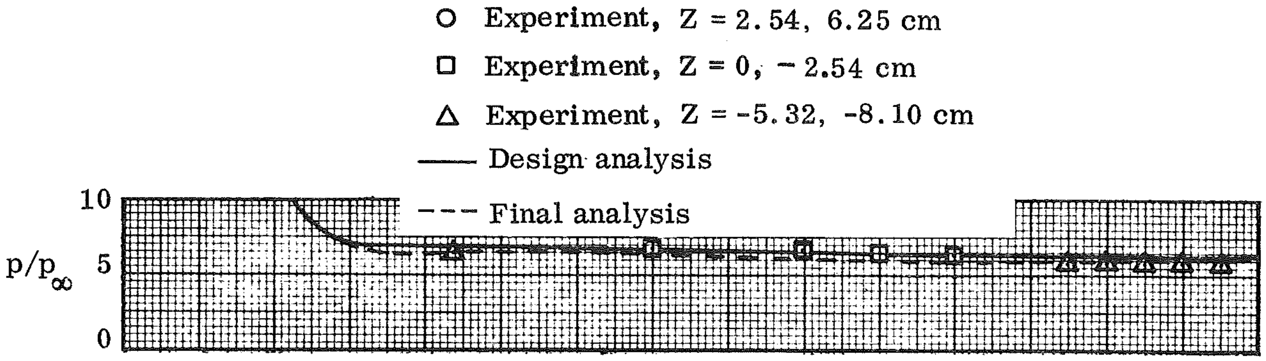

(a) P2 inlet model.

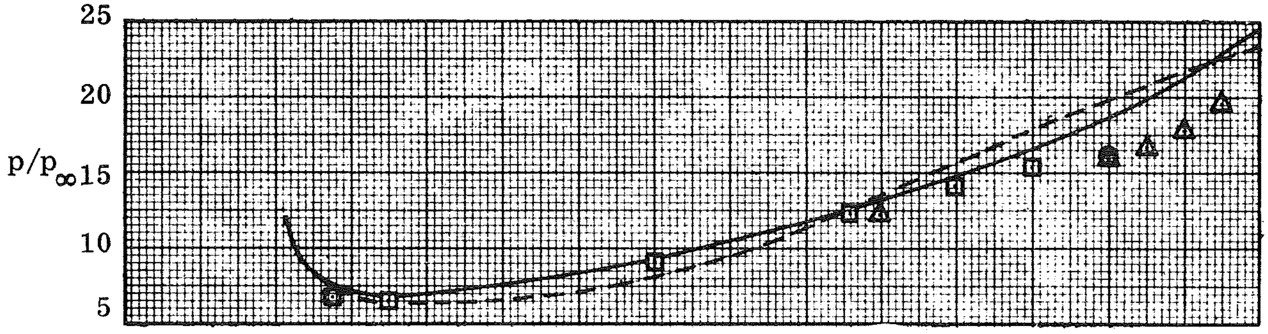

(b) P8 inlet model.

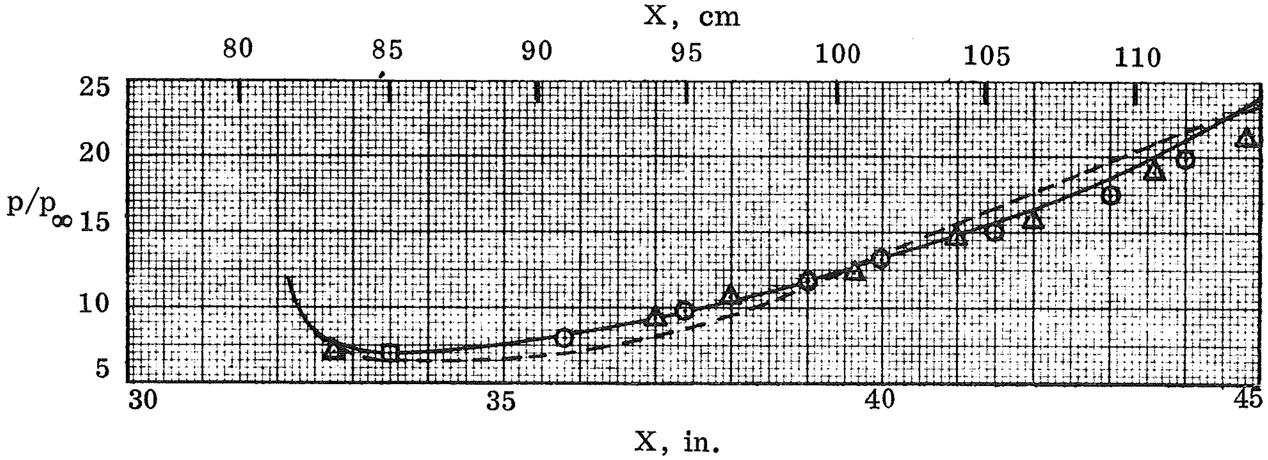

(c) P12 inlet model.

Figure 51.– Cowl surface pressure distributions.

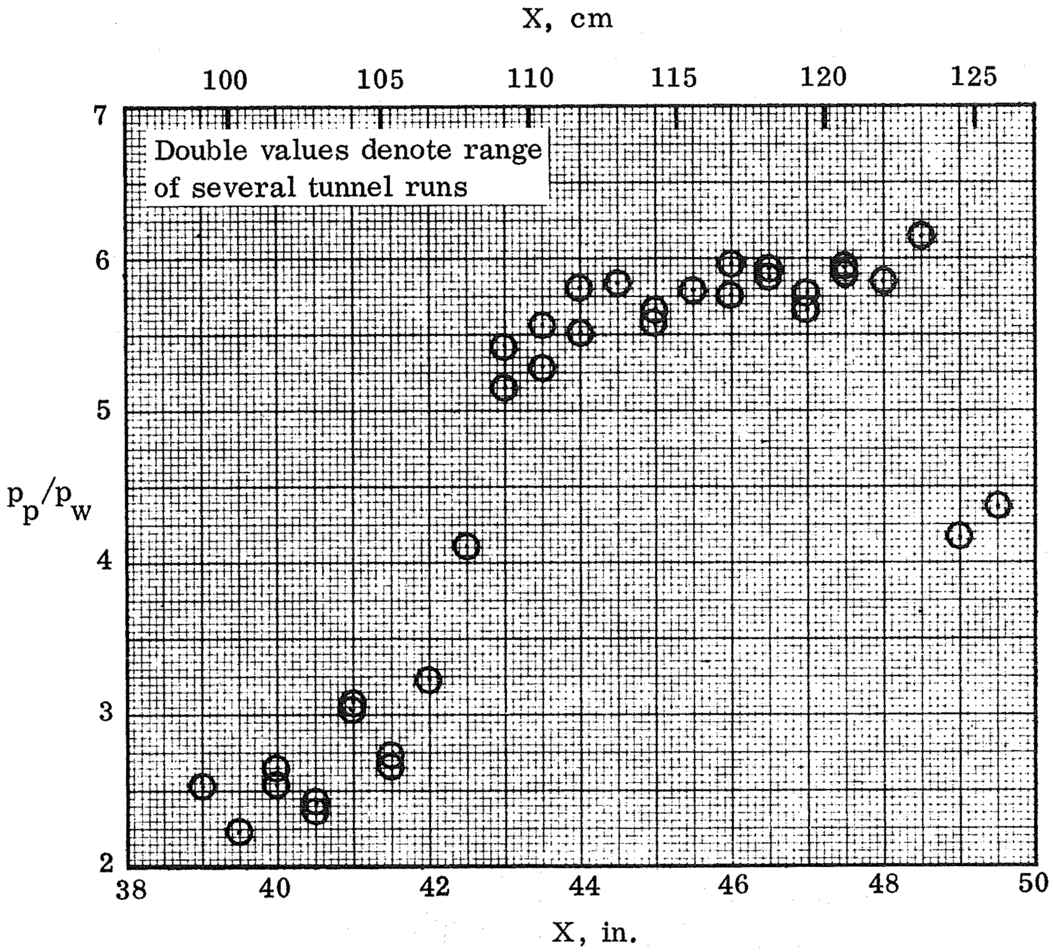

Figure 52.– Surface pitot-pressure distribution; Z = 3.27 cm, P8 inlet model cowl.

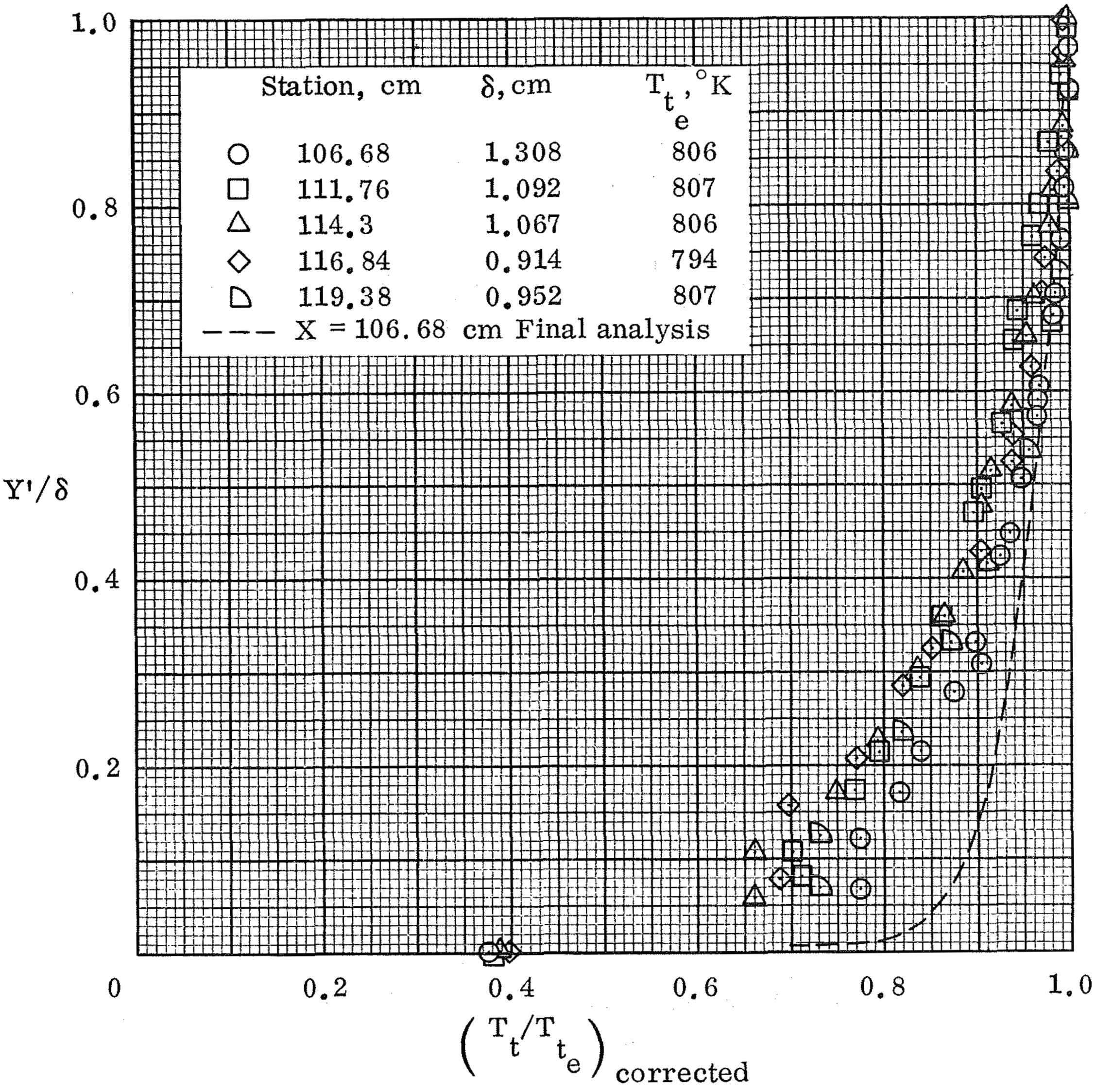

Figure 53.– Boundary layer total-temperature profiles; Z = –5.32 cm; P2 inlet model centerbody.

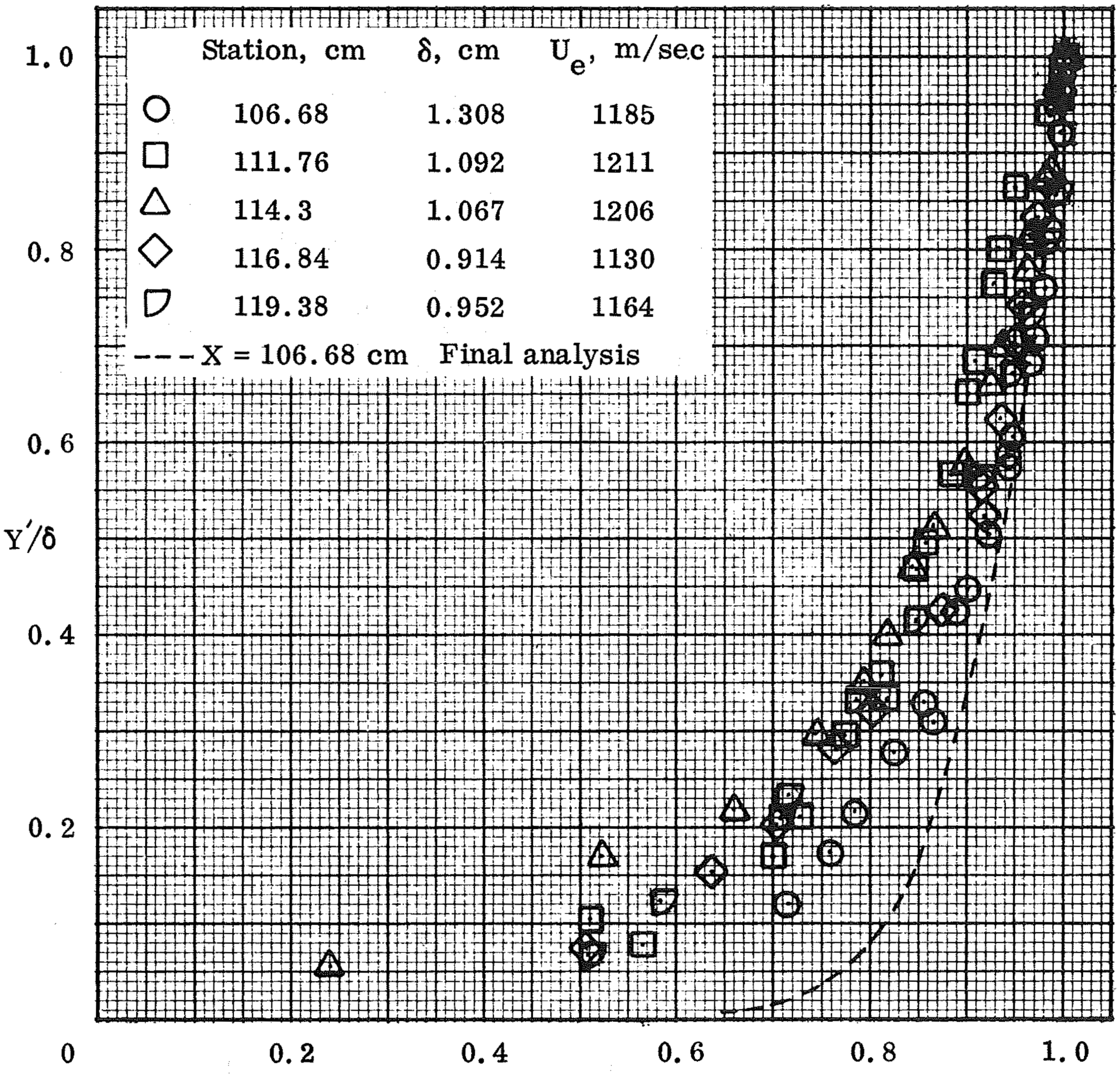

Figure 54.– Boundary layer velocity profiles; $Z = -5.32$ cm, P2 inlet model centerbody.

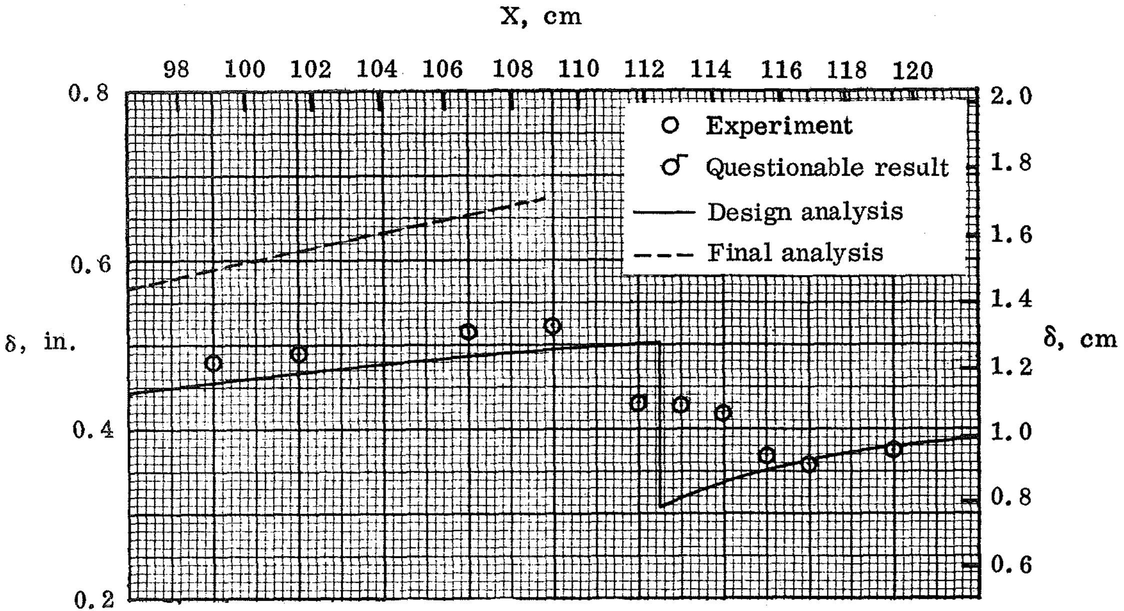

(a) Boundary-layer thickness.

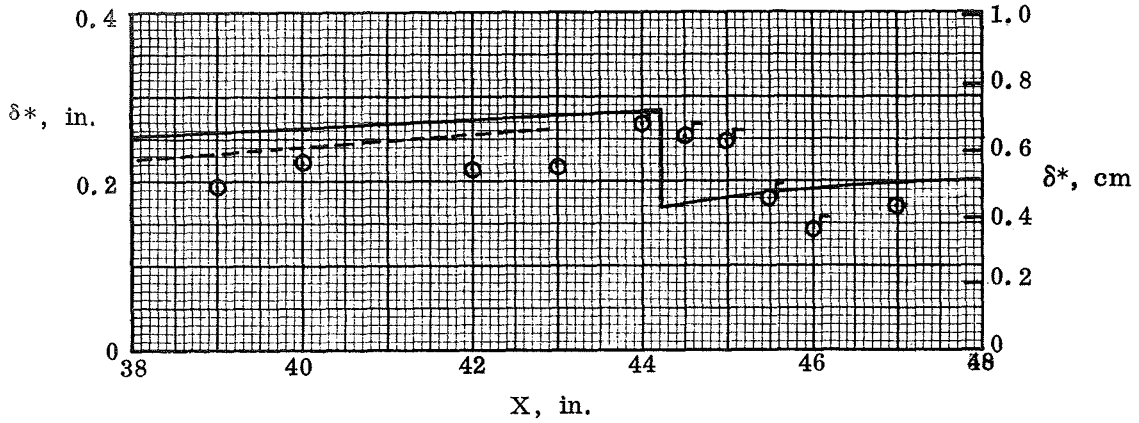

(b) Displacement thickness.

Figure 55.— Boundary-layer properties; $Z = -5.32$ cm, P2 inlet model centerbody.

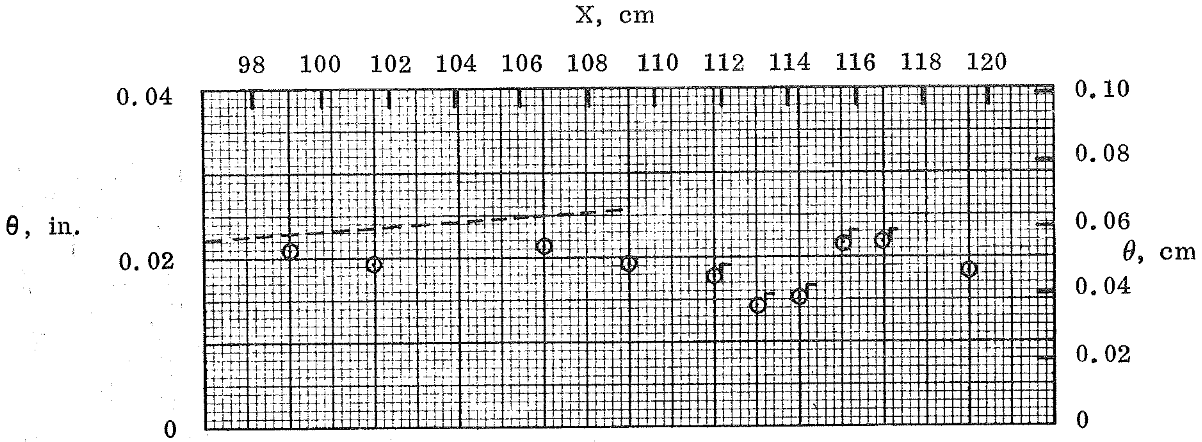

(c) Momentum thickness.

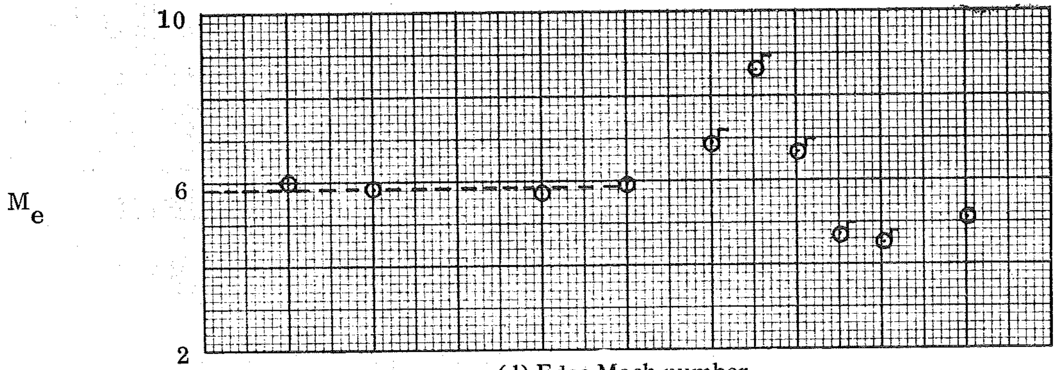

(d) Edge Mach number.

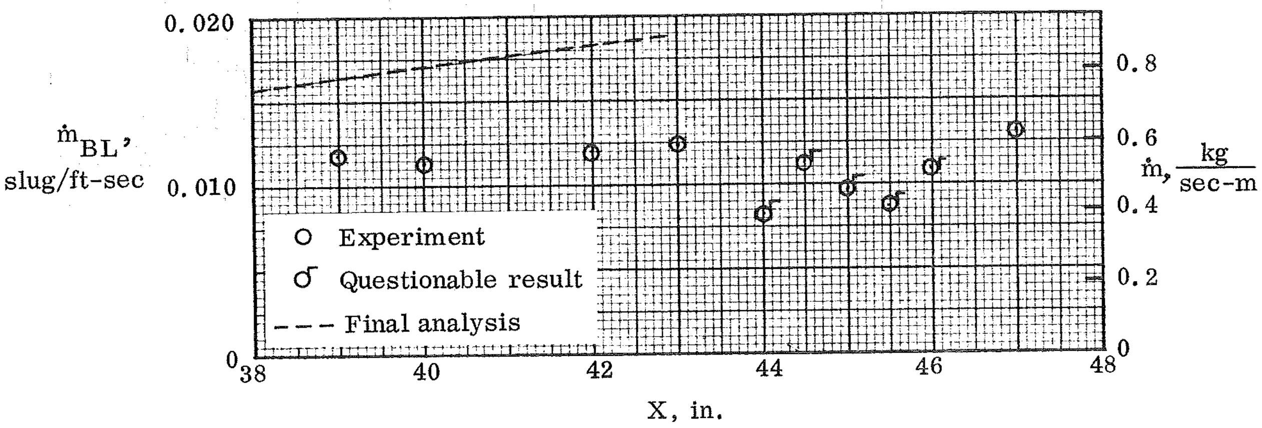

(e) Mass flow.

Figure 55.— Concluded.

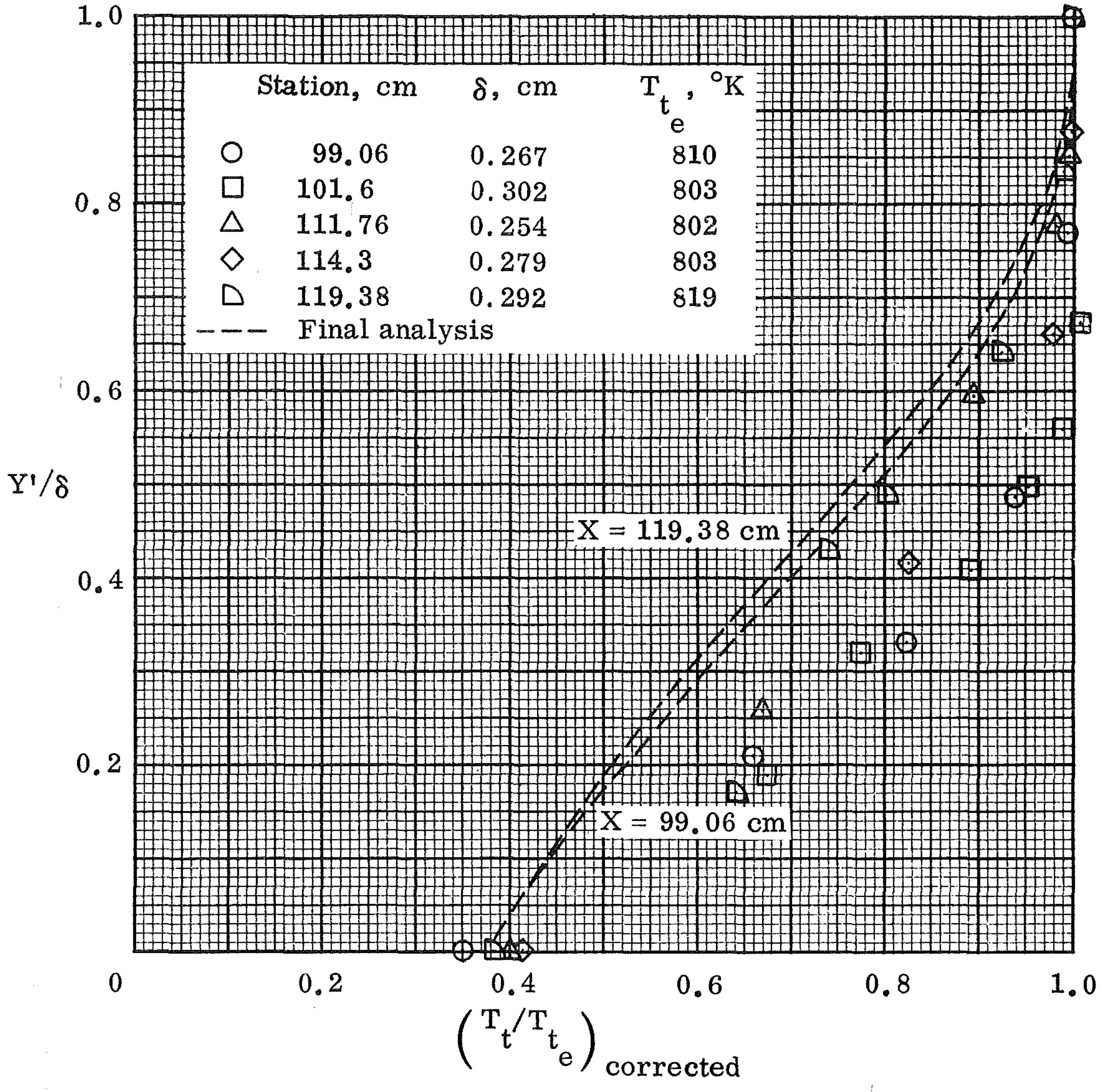

Figure 56.– Boundary-layer total-temperature profiles; $Z = -5.32$ cm,

P2 inlet model cowl.

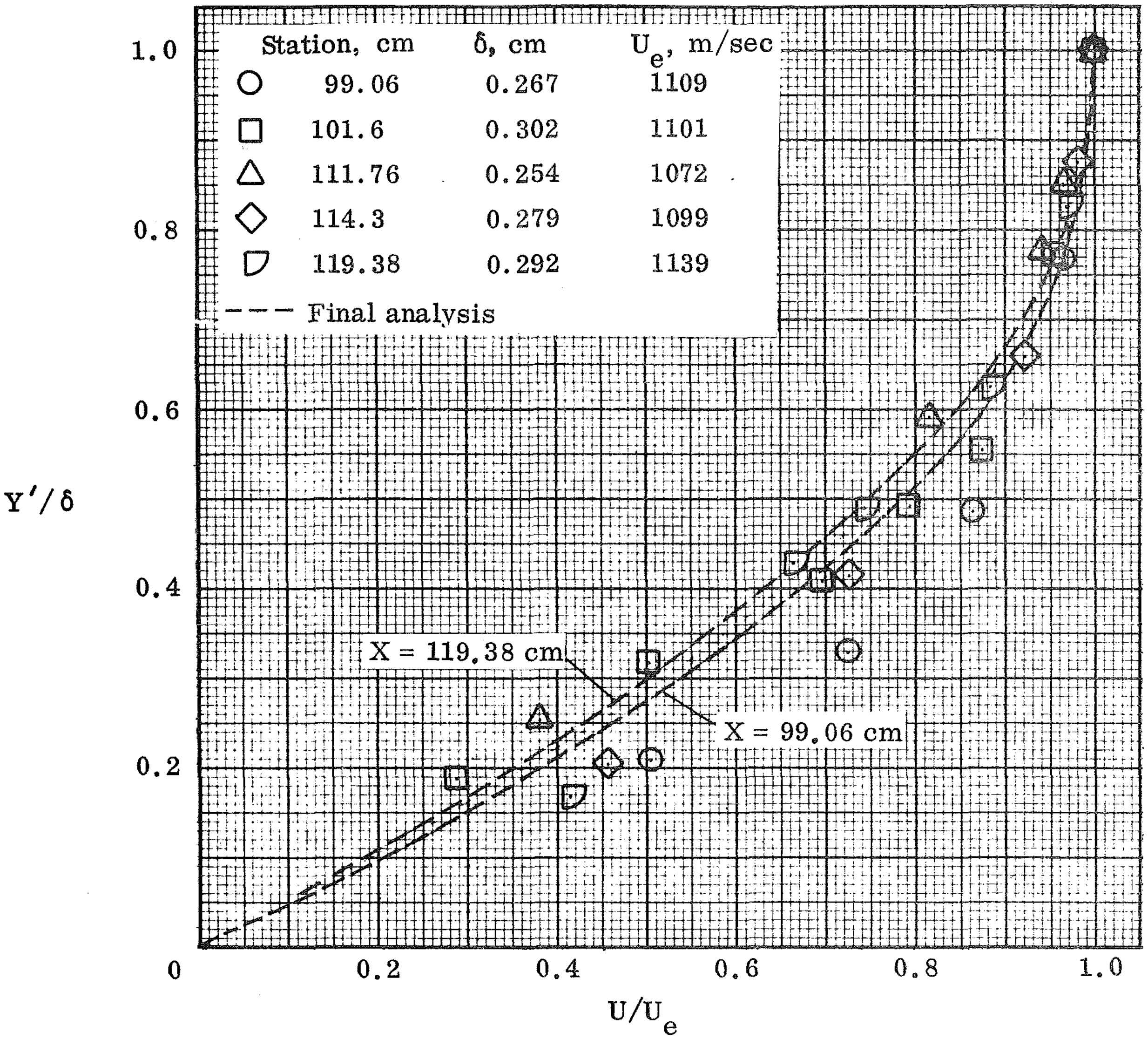

Figure 57.– Boundary layer velocity profiles; Z = –5.32 cm, P2 inlet model cowl.

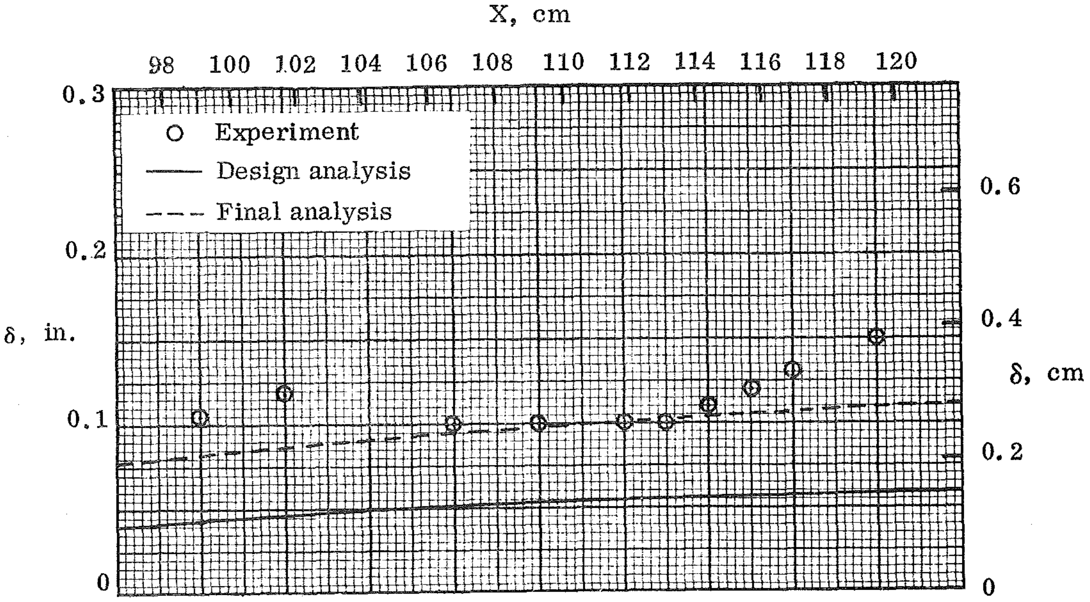

(a) Boundary-layer thickness.

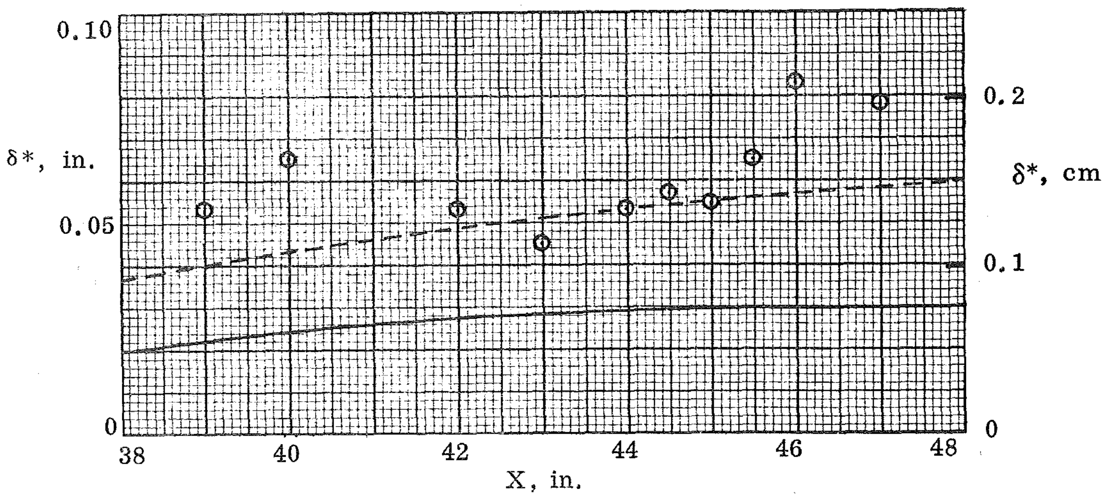

(b) Displacement thickness.

Figure 58.– Boundary-layer properties; $Z = -5.32$ cm, P2 inlet model cowl.

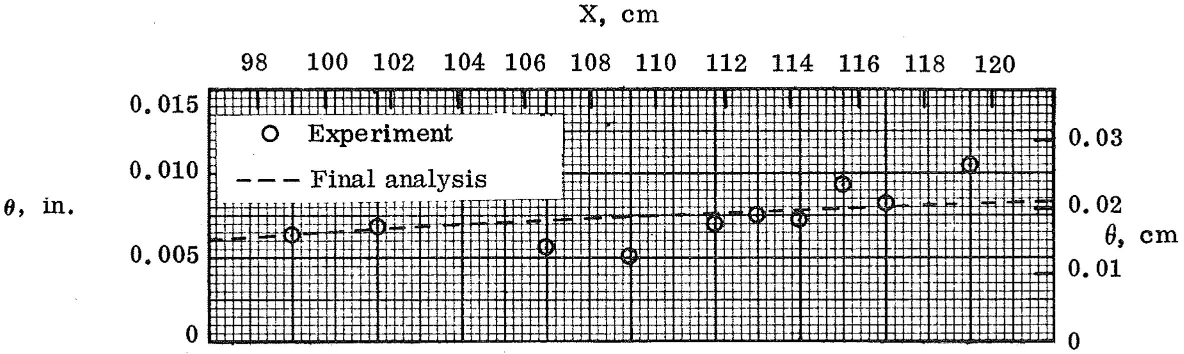

(c) Momentum thickness.

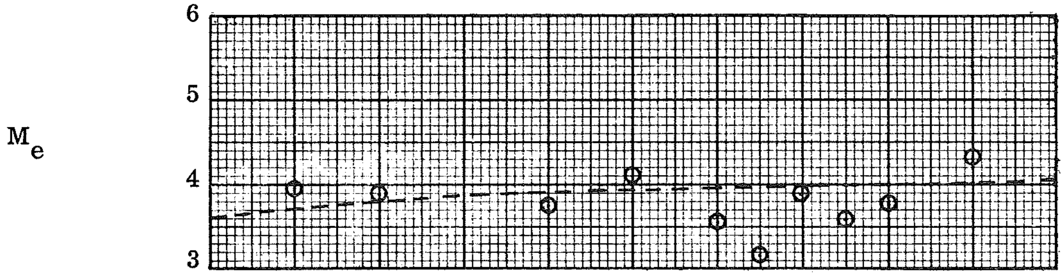

(d) Edge Mach number.

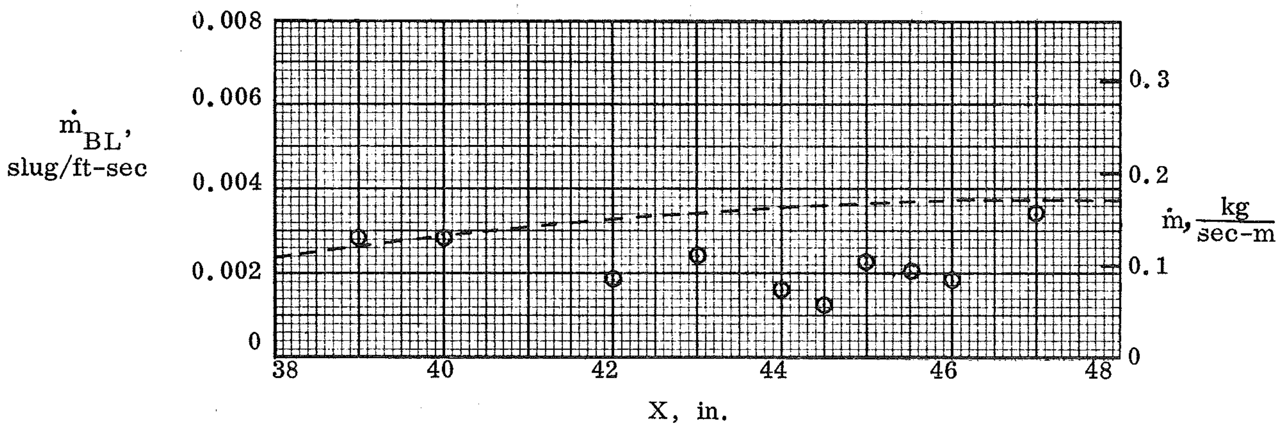

(e) Mass flow.

Figure 58.– Concluded.

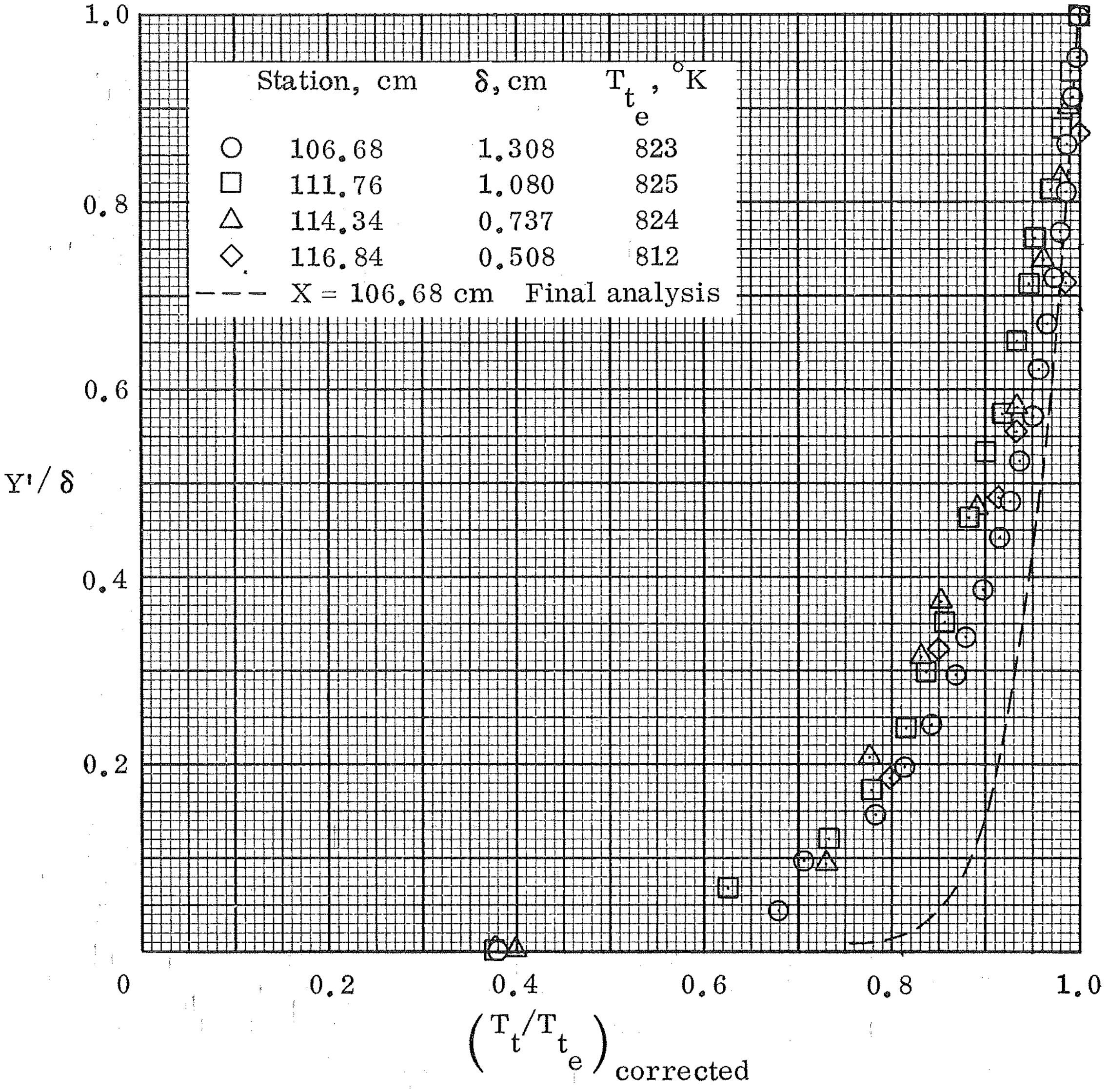

(a) Stations upstream and within interaction region.

Figure 59.– Boundary layer total-temperature profiles; $Z = -5.32$ cm, P8 inlet model centerbody.

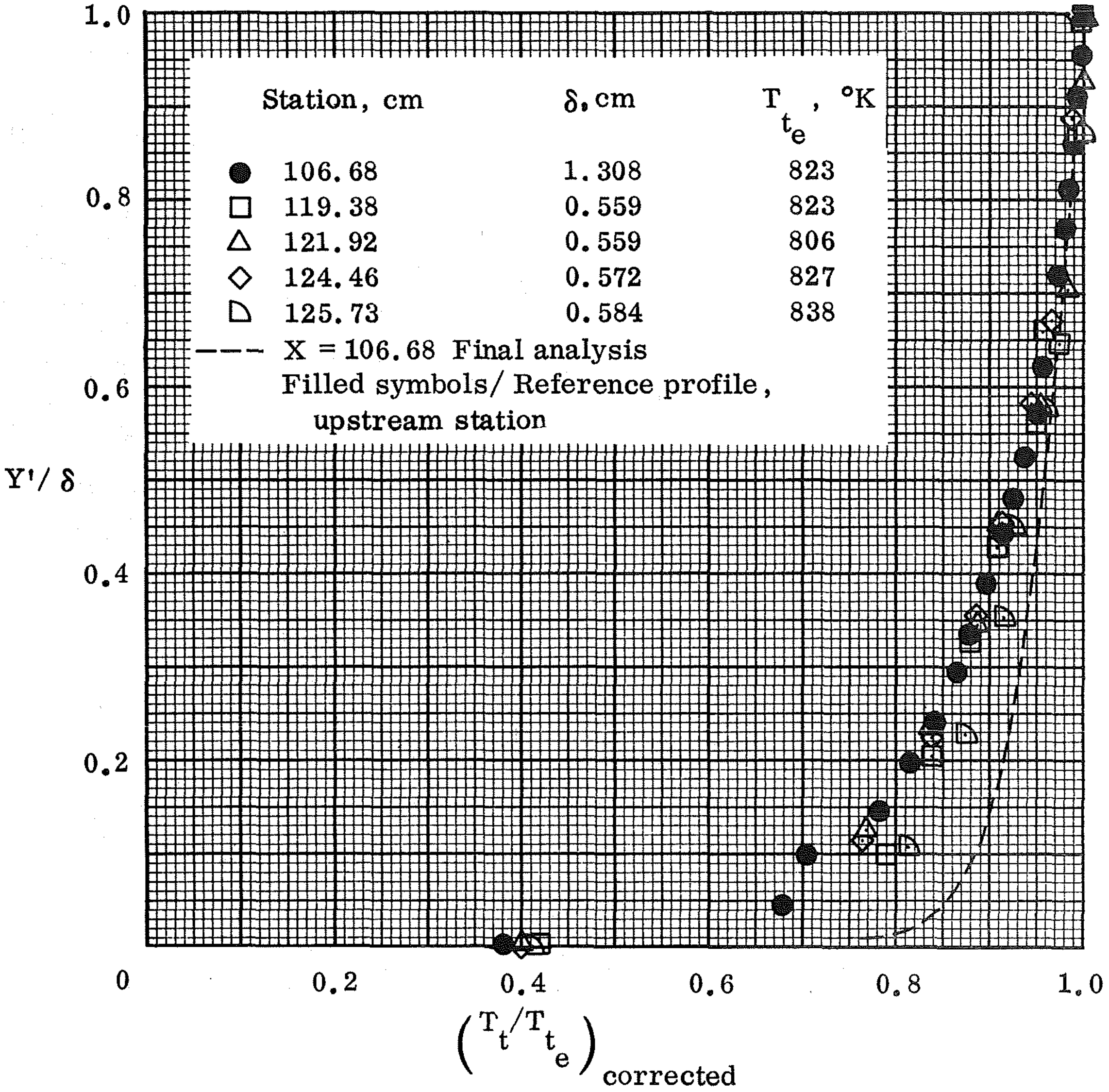

(b) Stations downstream of interaction region.

Figure 59.– Concluded.

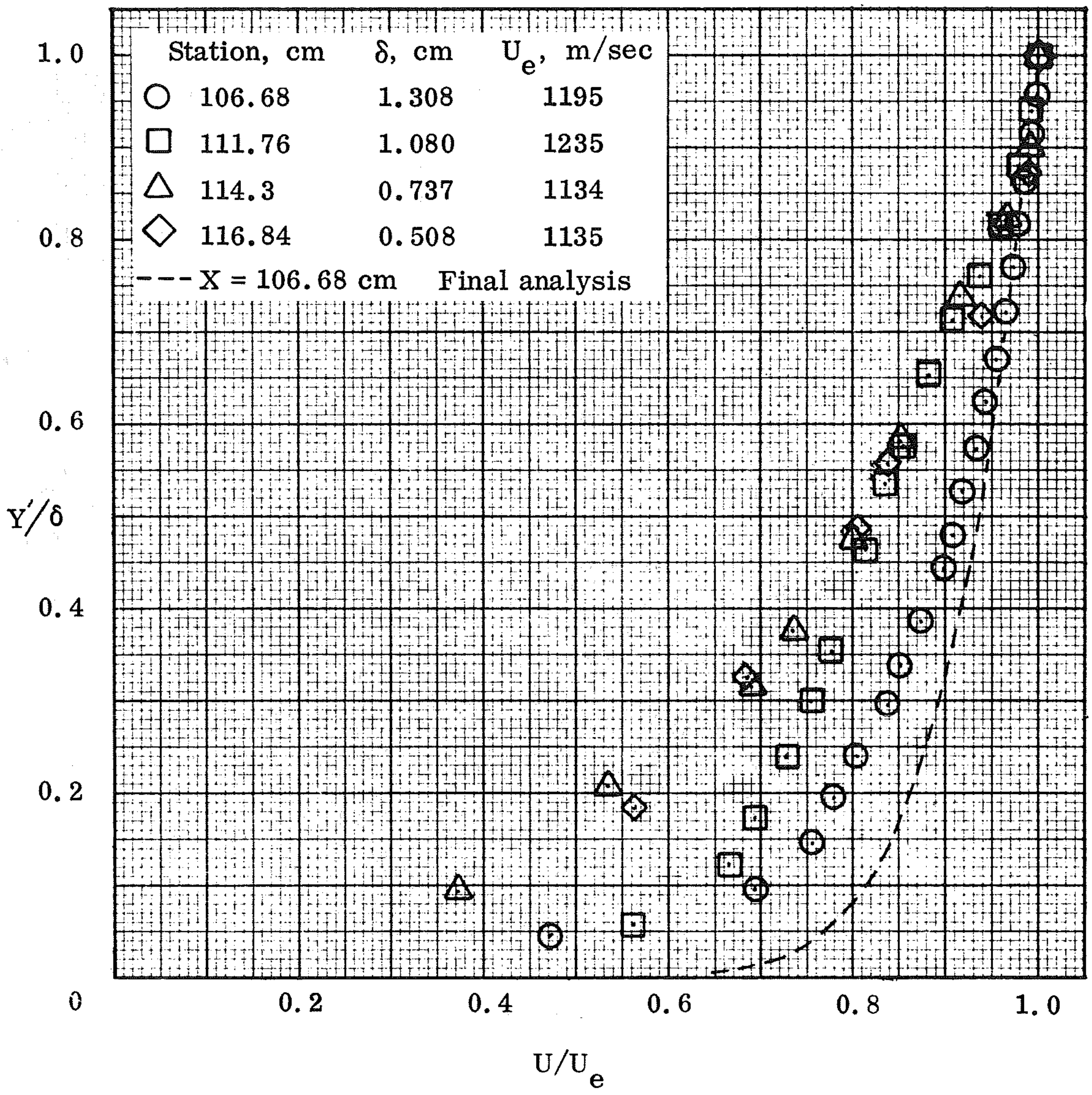

(a) Stations upstream and within interaction region.

Figure 60.– Boundary layer velocity profiles; $Z = -5.32$ cm, P8 inlet model centerbody.

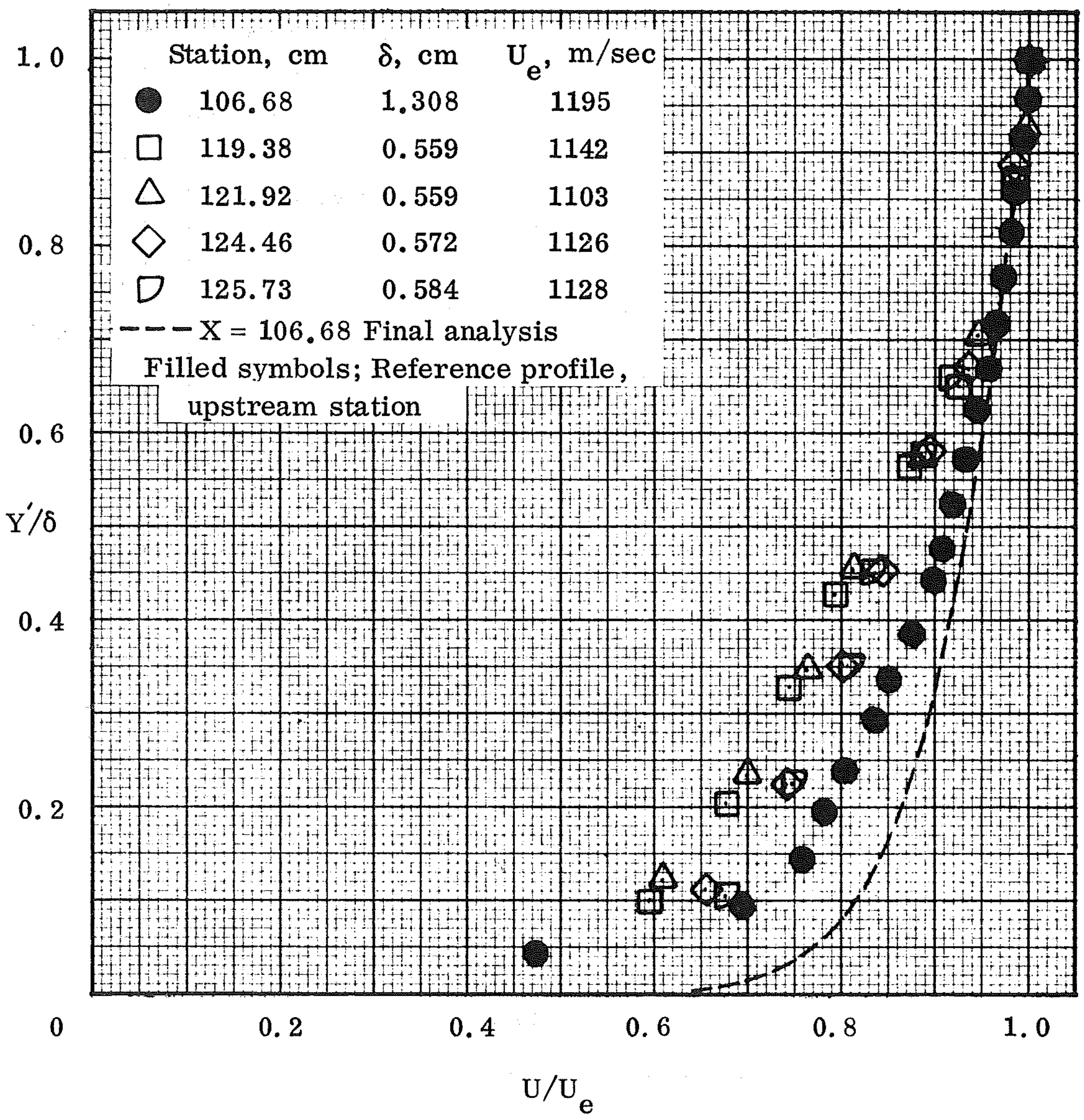

(b) Stations downstream of interaction region.

Figure 60.– Concluded.

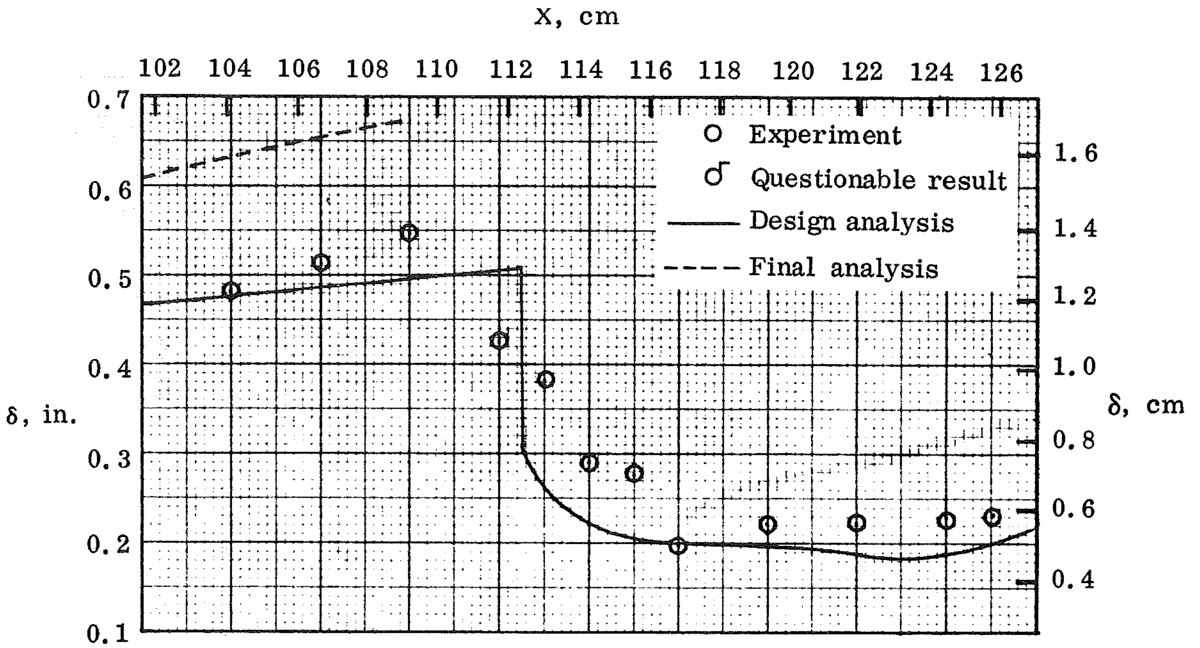

(a) Boundary–layer thickness.

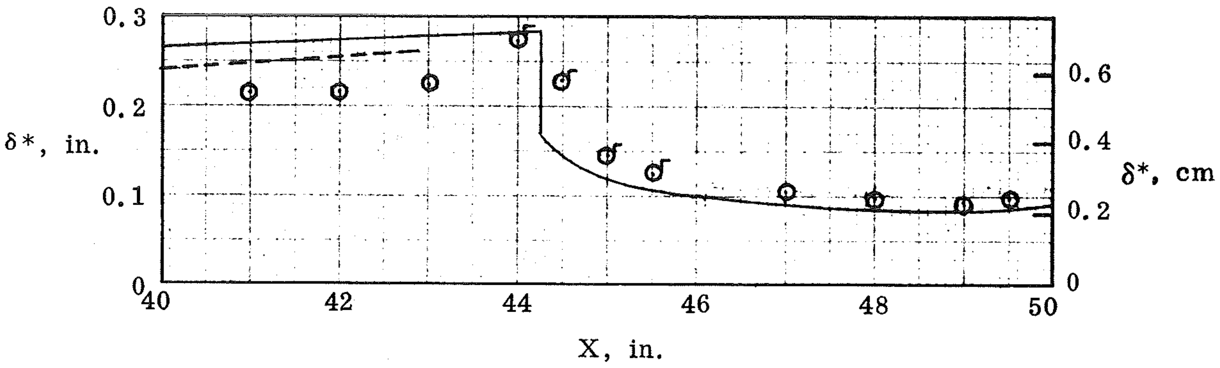

(b) Displacement thickness.

Figure 61.– Boundary–layer properties; Z = –5.32 cm, P8 inlet model centerbody.

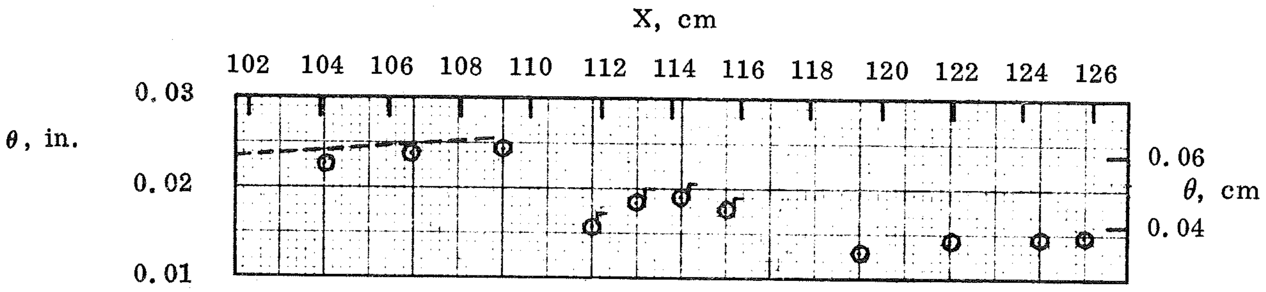

(c) Momentum thickness.

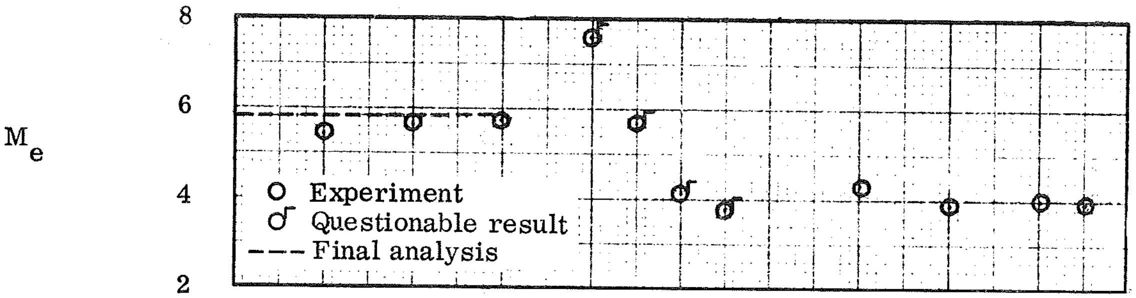

(d) Edge Mach number.

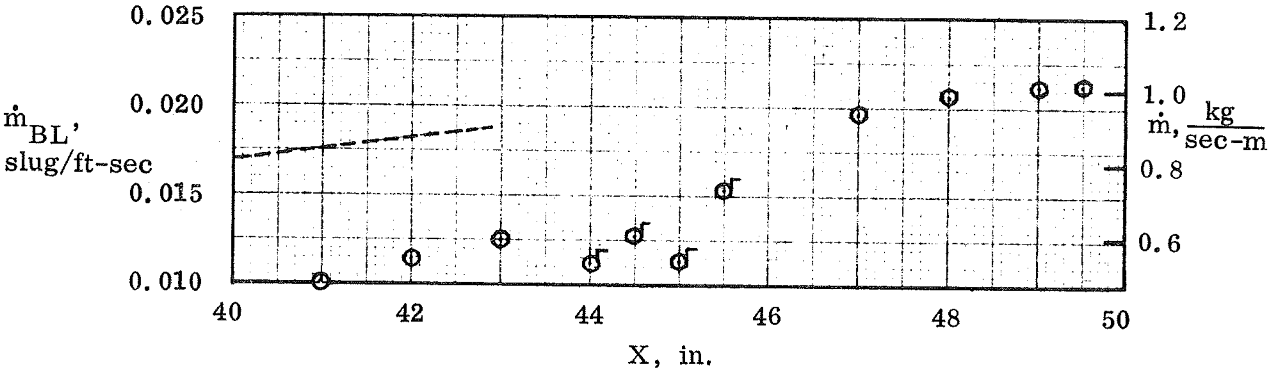

(e) Mass flow.

Figure 61.– Concluded.

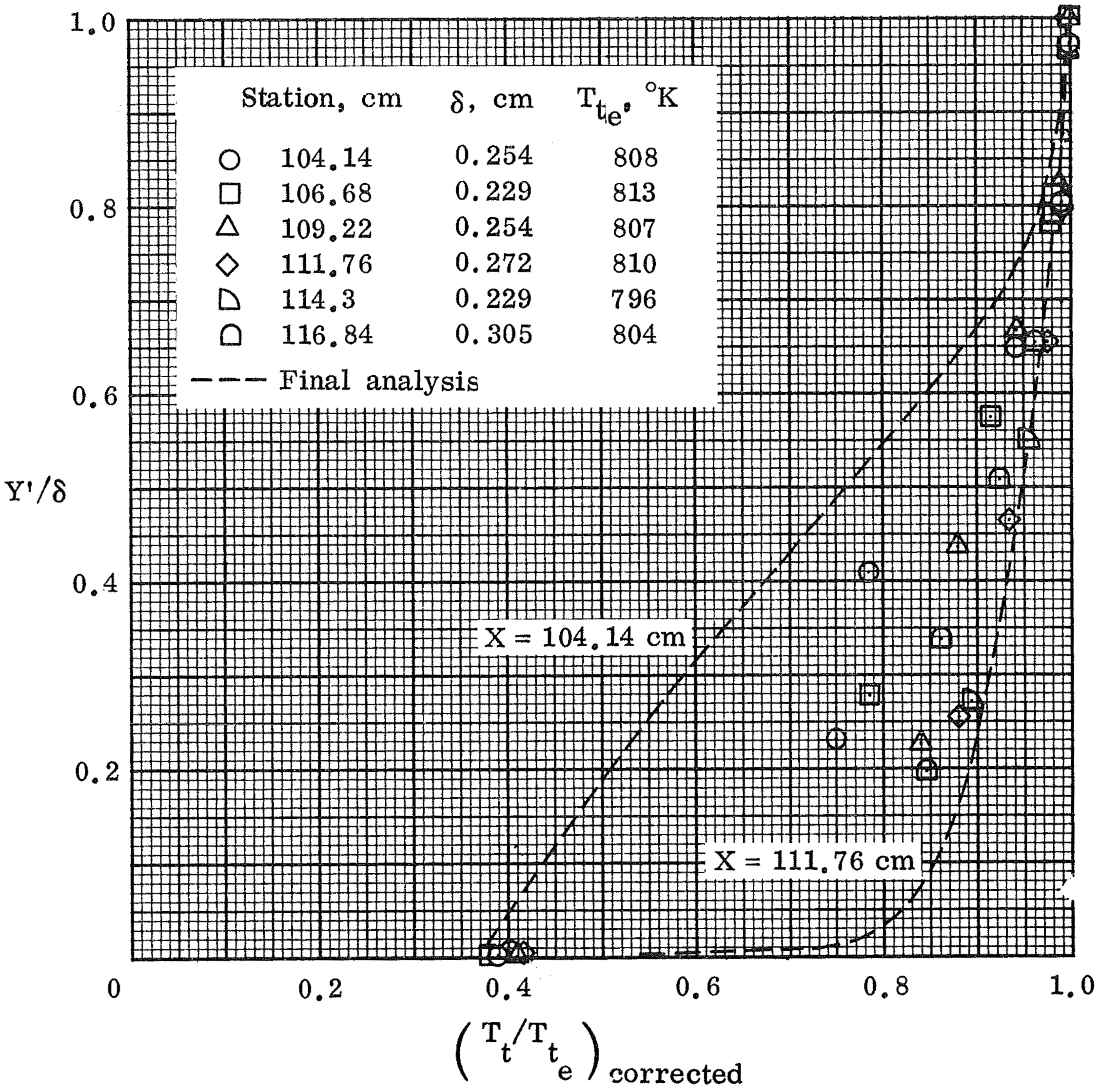

(a) Stations X = 104.14 to 116.84 cm.

Figure 62.– Boundary layer total-temperature profiles; Z = -5.32 cm, P8 inlet model cowl.

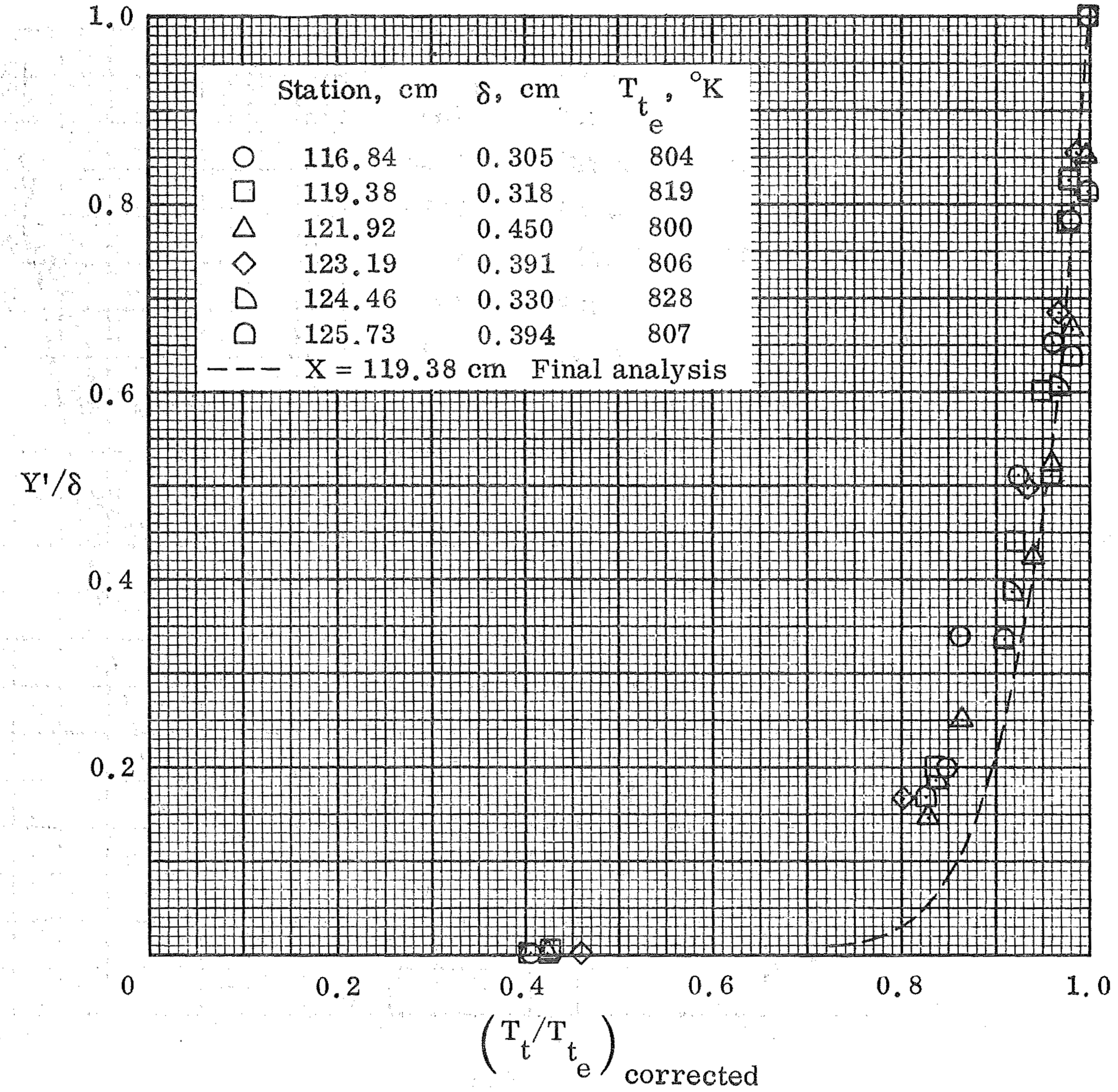

(b) Stations *X* = 116.84 to 125.73 cm.

Figure 62.– Concluded.

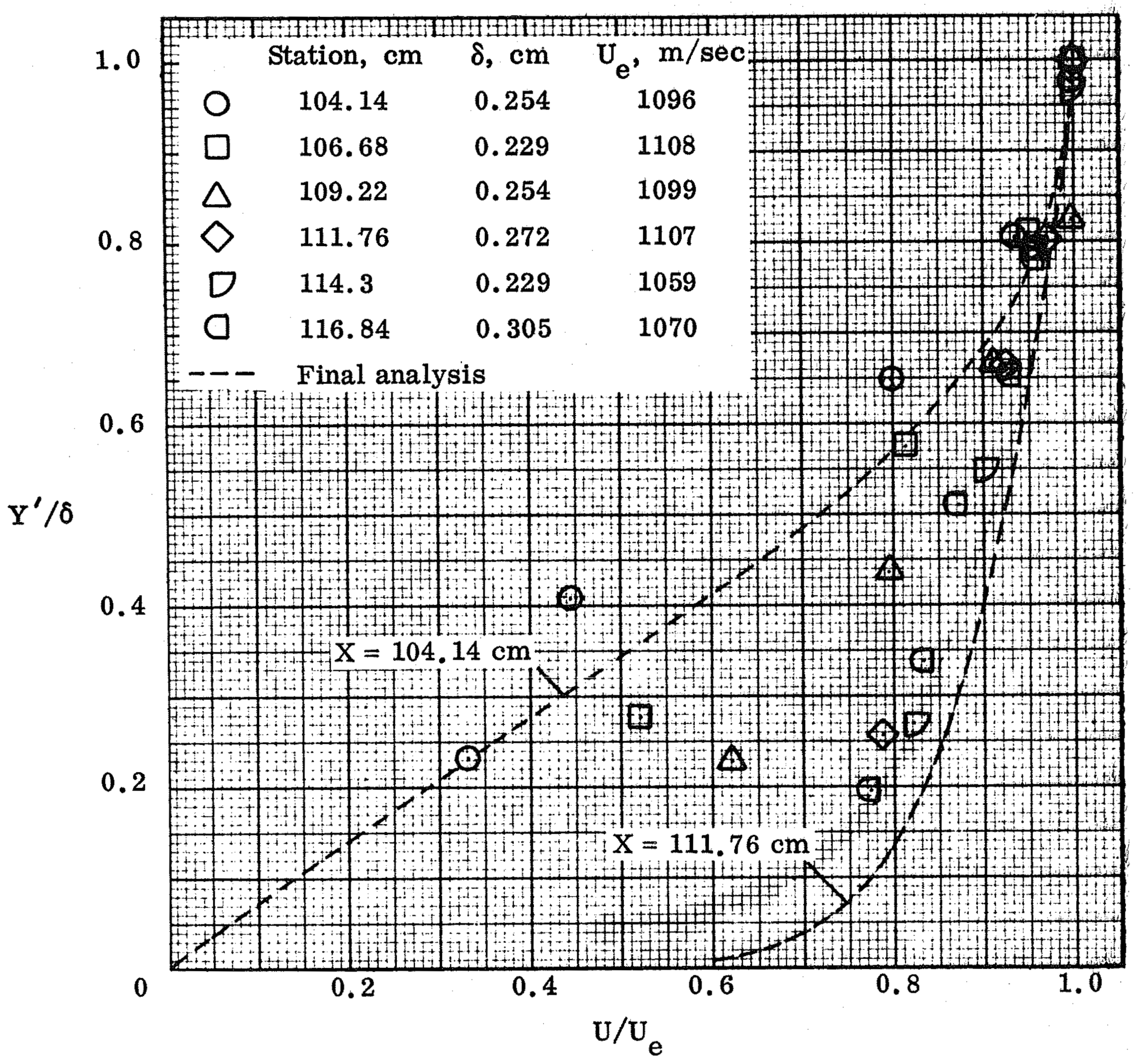

(a) Stations X = 104.14 to 116.84 cm.

Figure 63.– Boundary layer velocity profiles; Z = –5.32 cm, P8 inlet model cowl.

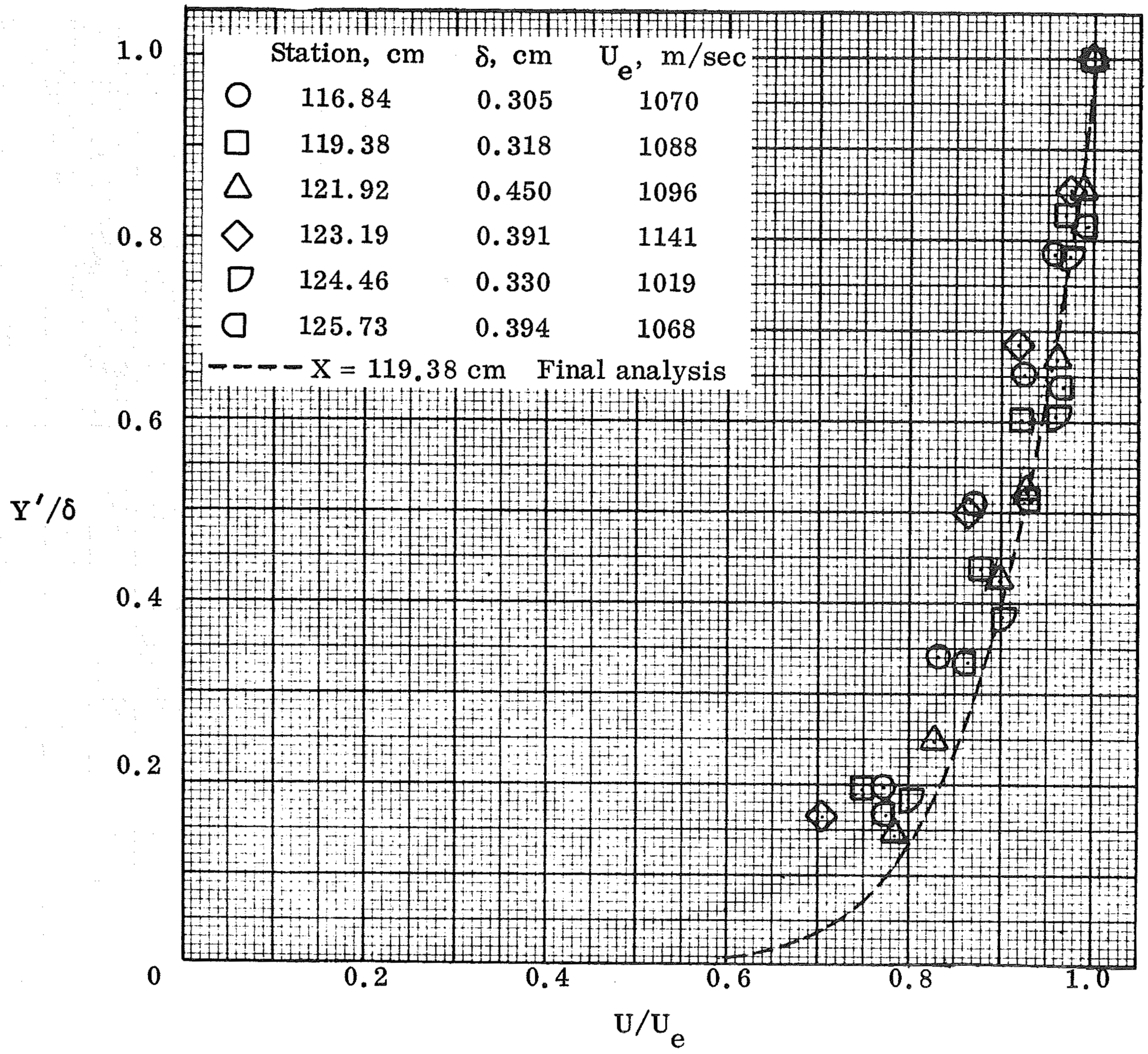

(b) Stations X = 116.84 to 125.73 cm.

Figure 63.– Concluded.

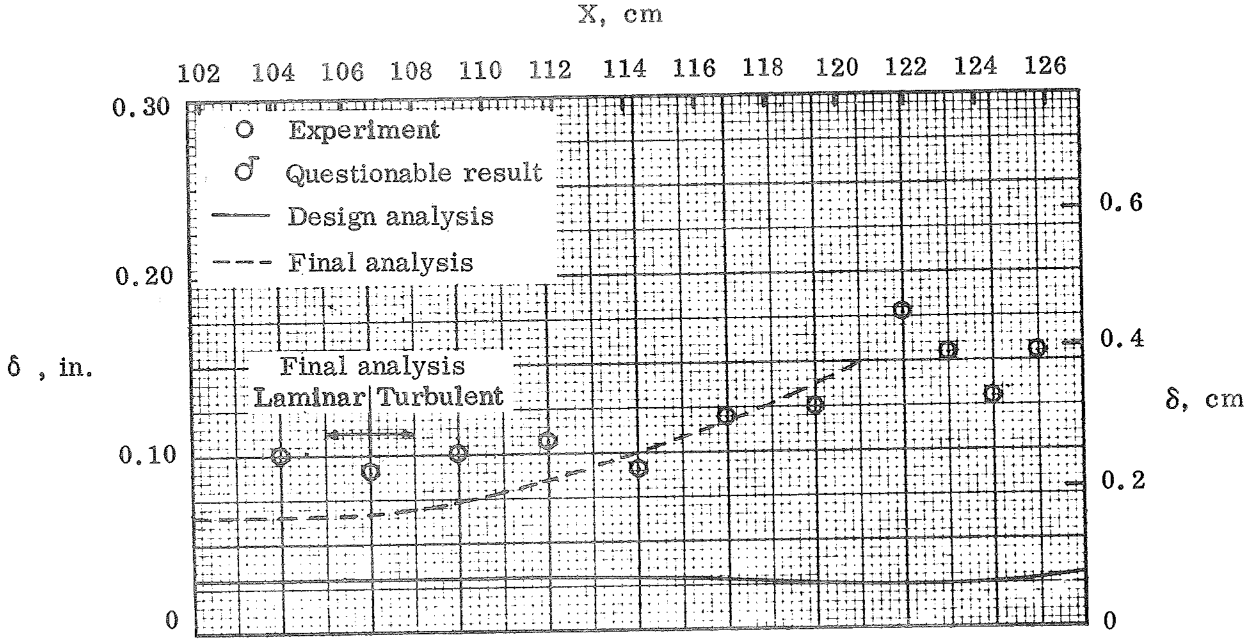

(a) Boundary-layer thickness.

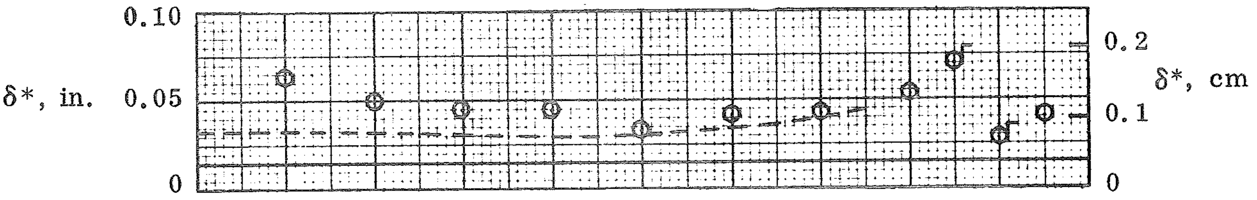

(b) Displacement thickness.

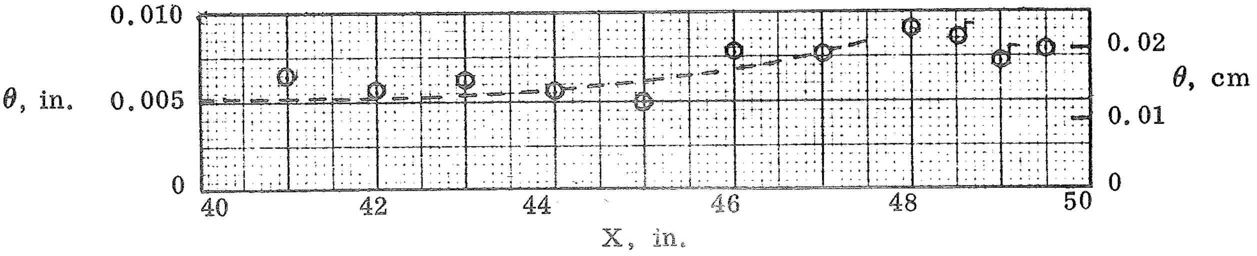

(c) Momentum thickness.

Figure 64.– Boundary-layer properties; $Z = -5.32$ cm, P8 inlet model cowl.

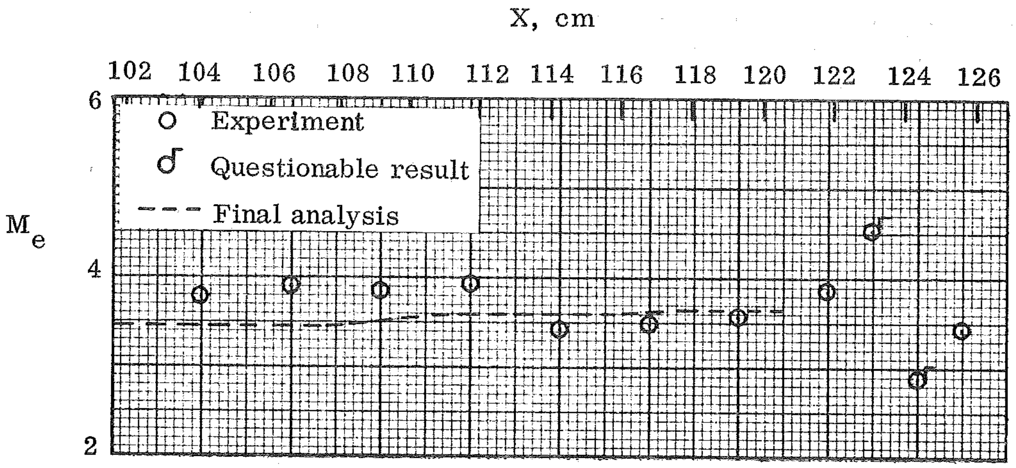

(d) Edge Mach number.

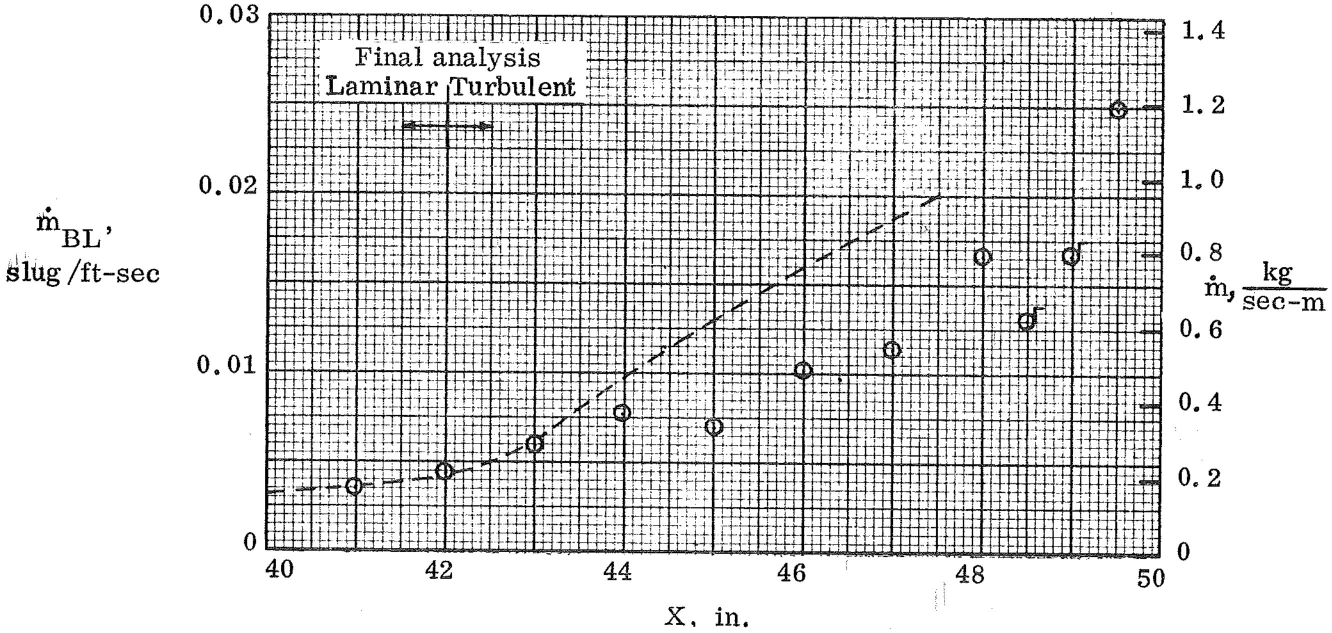

(e) Mass flow.

Figure 64.– Concluded.

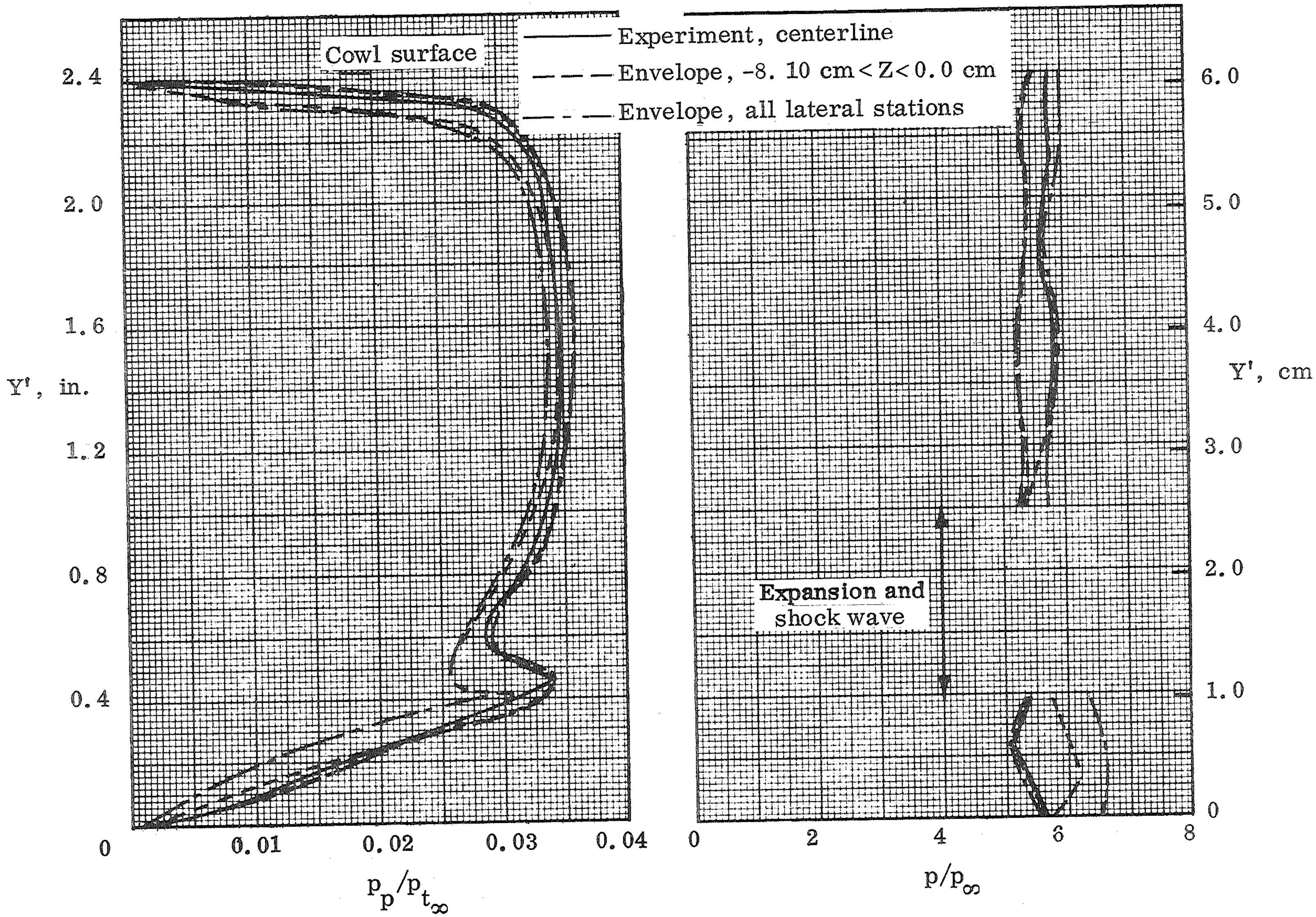

(a) Pitot pressure.

(b) Static pressure.

Figure 65.– Experimental flow-field properties at throat station X = 119.38 cm, P2 inlet model.

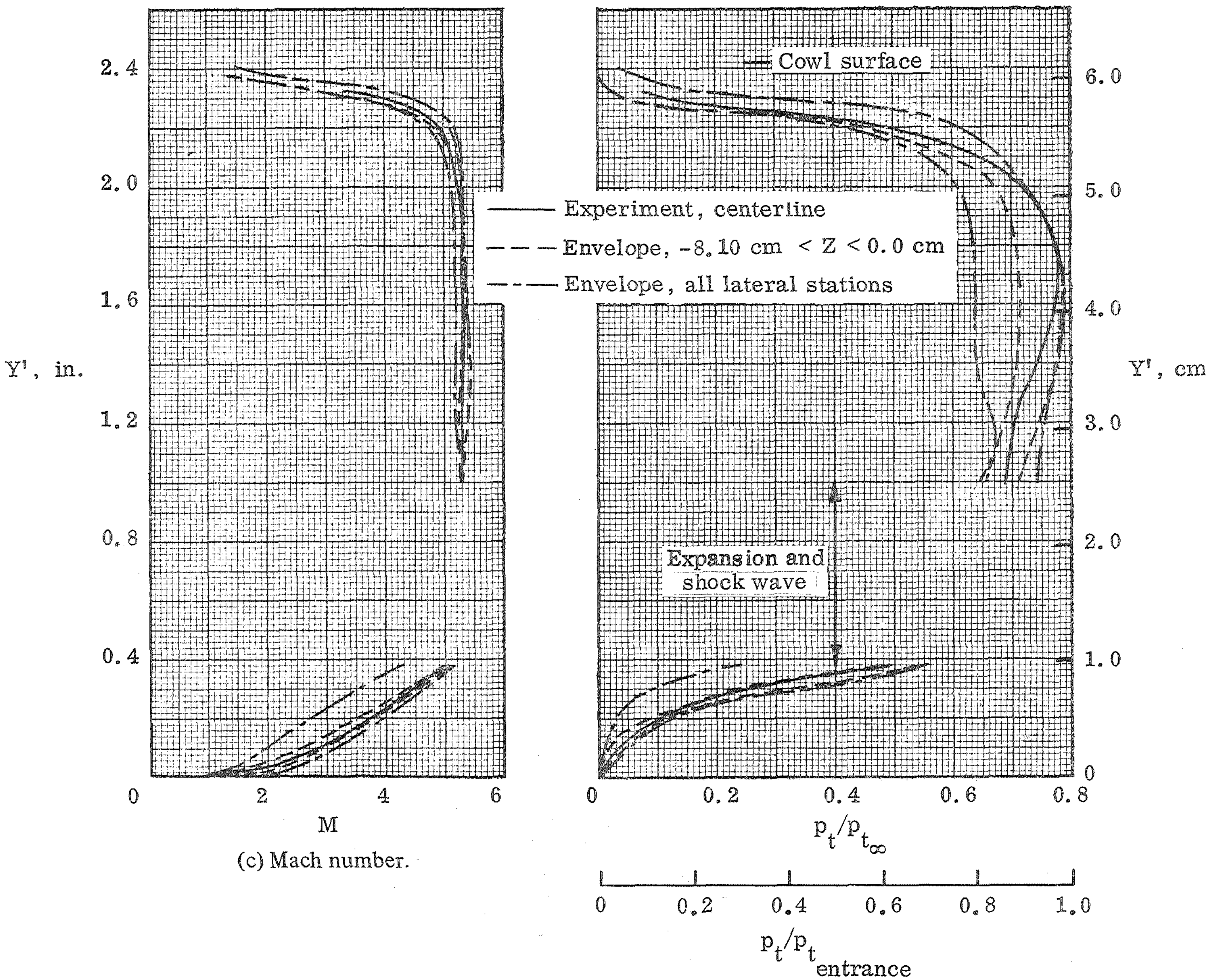

(c) Mach number.

(d) Total pressure recovery.

Figure 65.– Concluded.

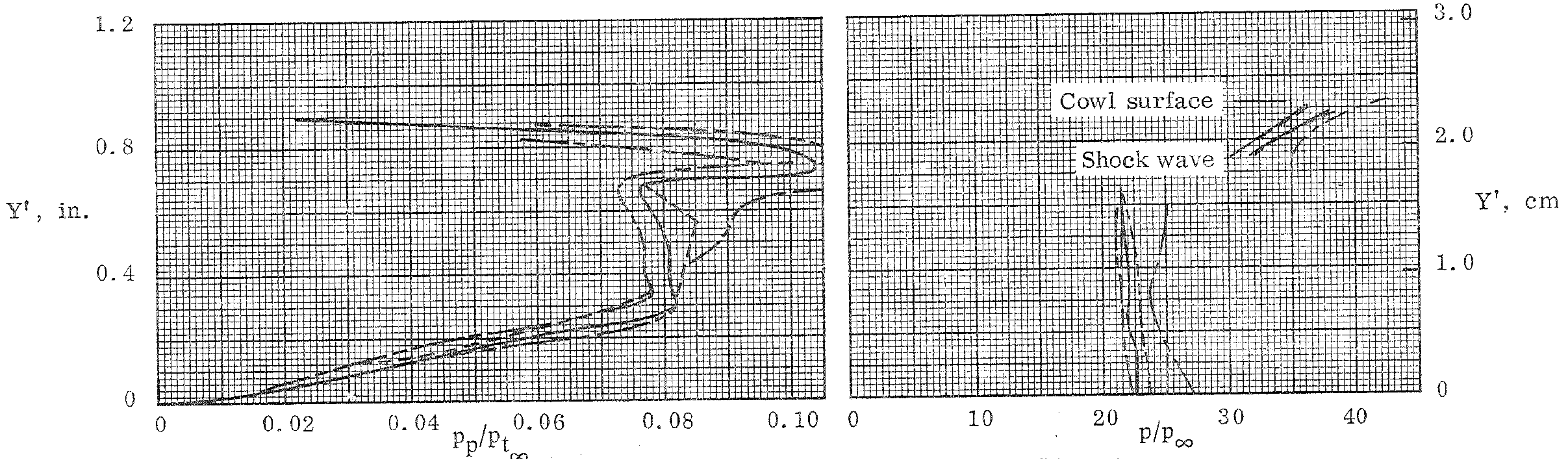

(a) Pitot pressure.

(b) Static pressure.

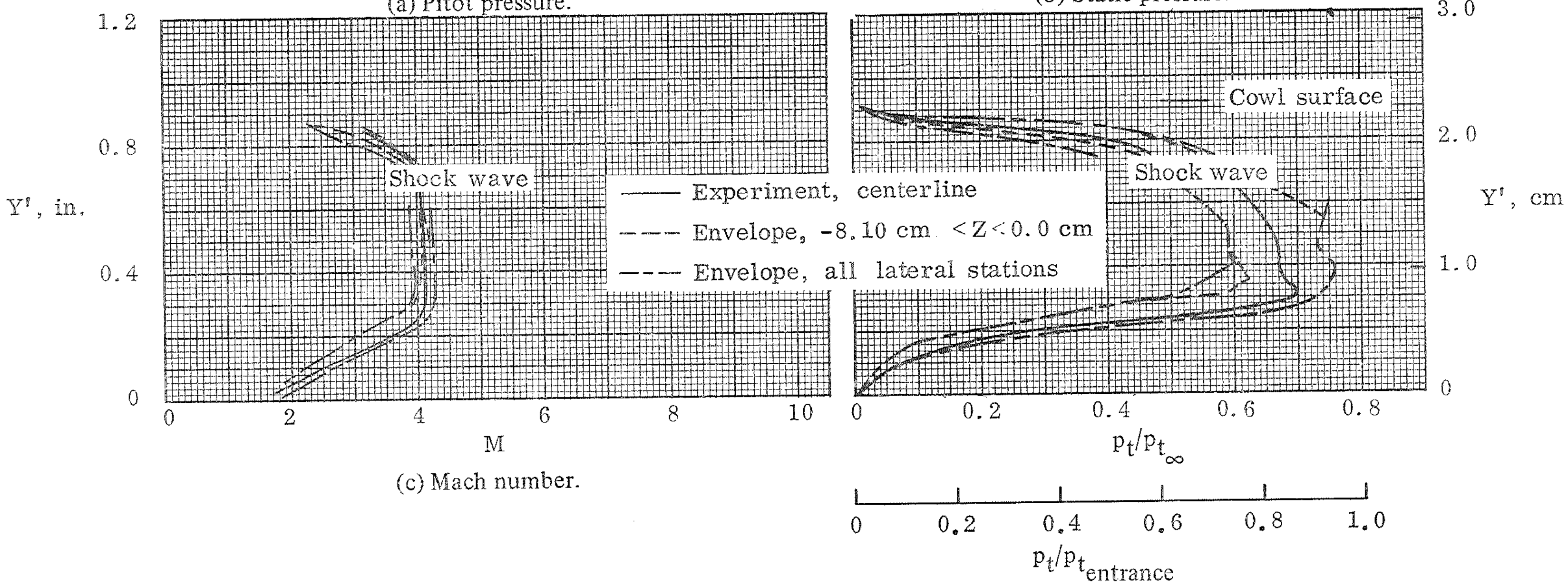

(c) Mach number.

(d) Total pressure recovery.

Figure 66.– Experimental flow-field properties at throat station $X = 125.73$ cm, P8 inlet model.

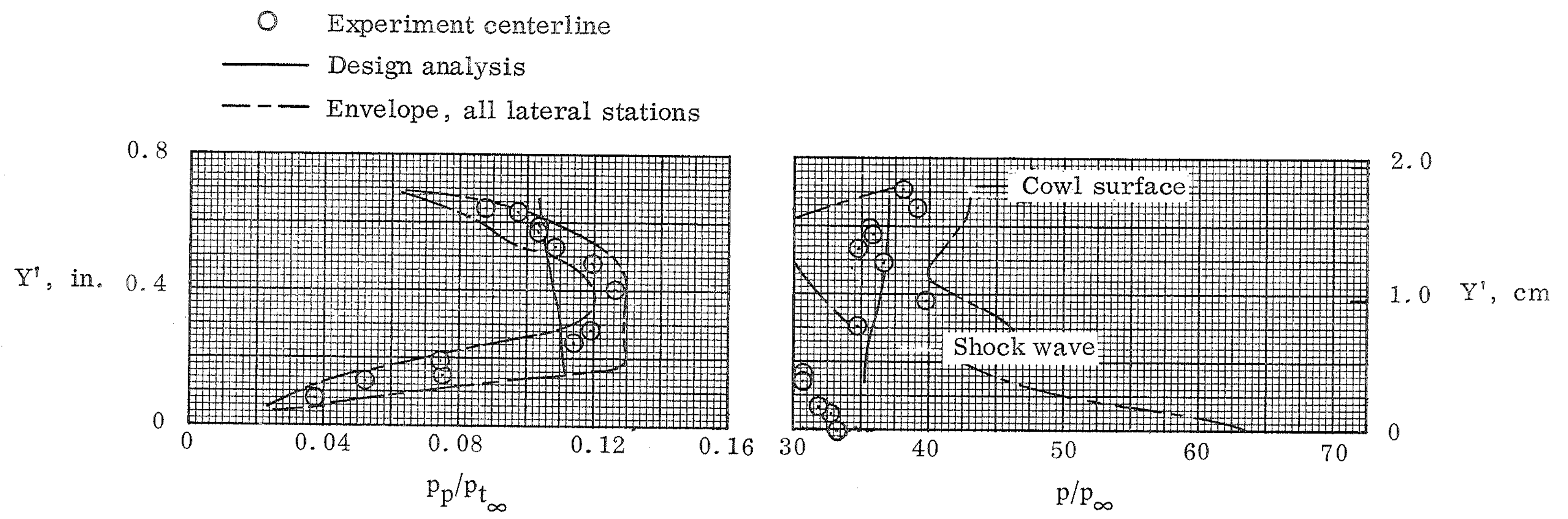

(a) Pitot pressure.

(b) Static pressure.

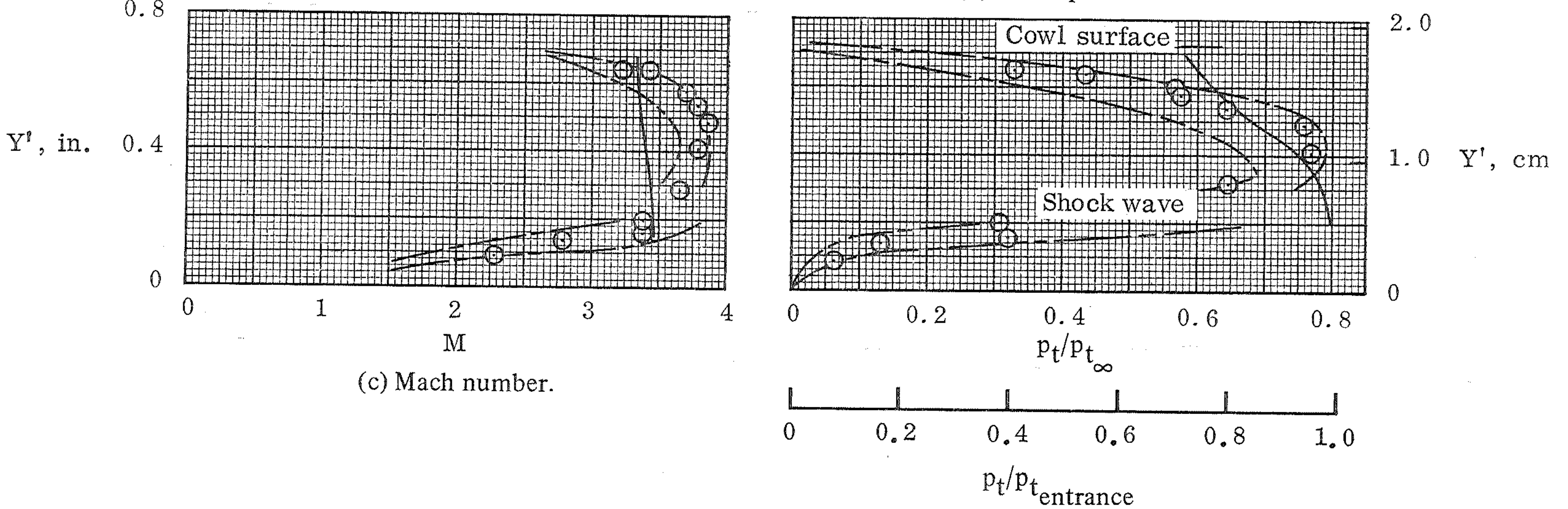

(c) Mach number.

(d) Total pressure recovery.

Figure 67.– Flow-field properties at throat station X = 126.75 cm, P12 inlet model.

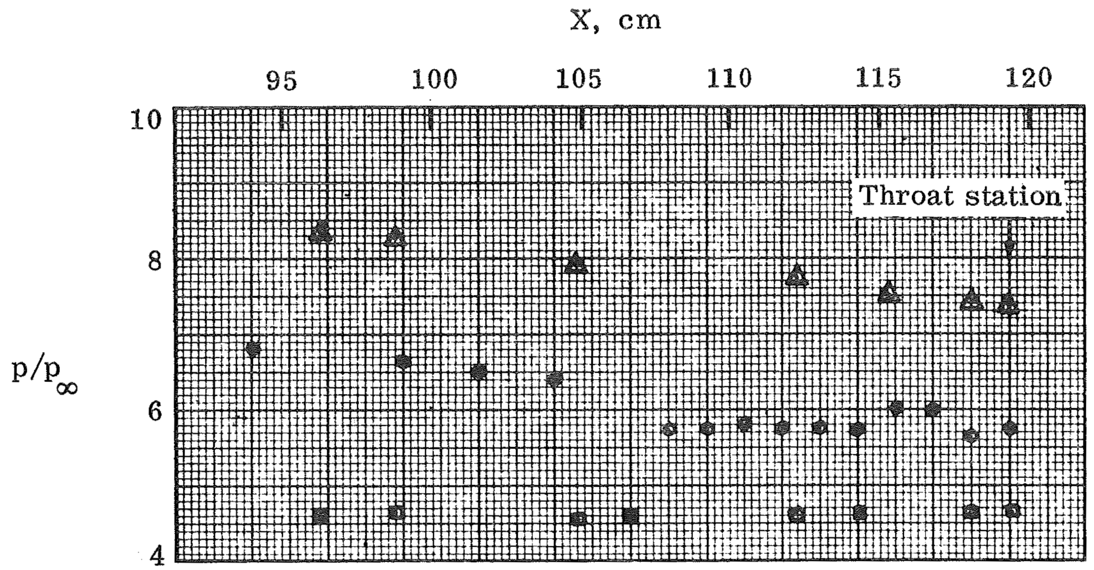

(a) Cowl.

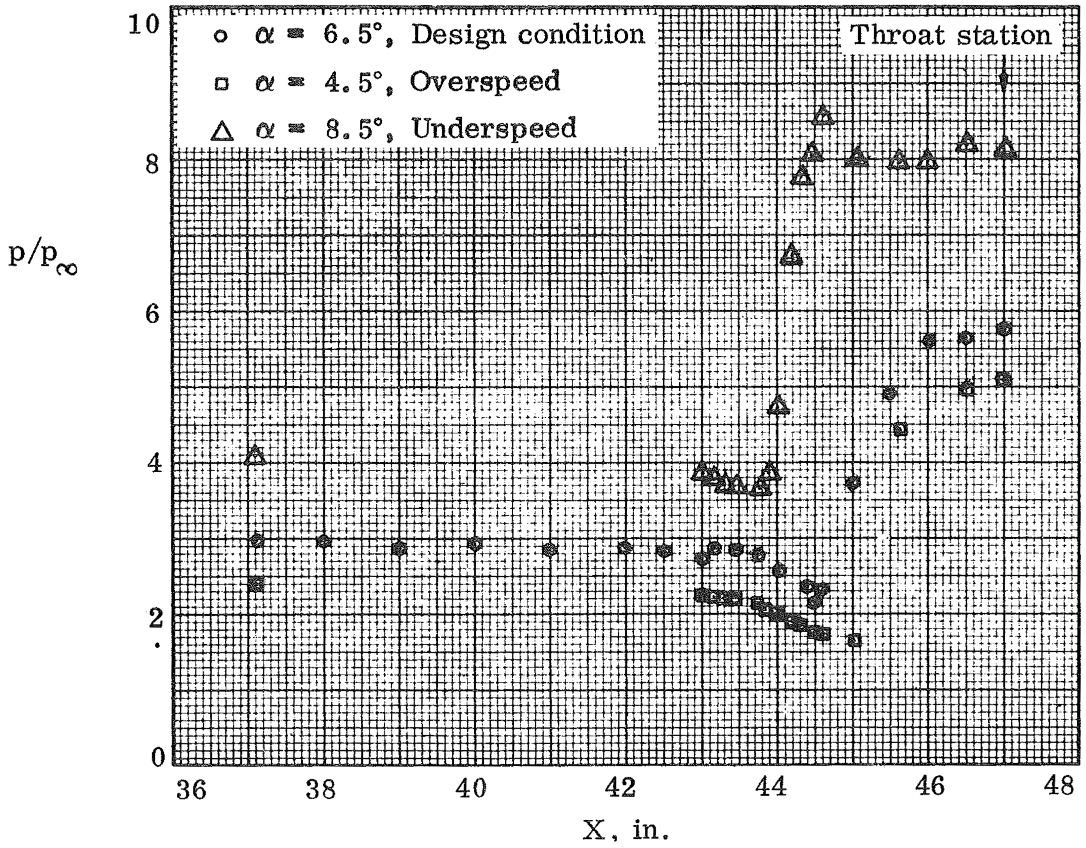

(b) Centerbody.

Figure 68.– Surface pressure distributions for off-design conditions; P2 inlet model.

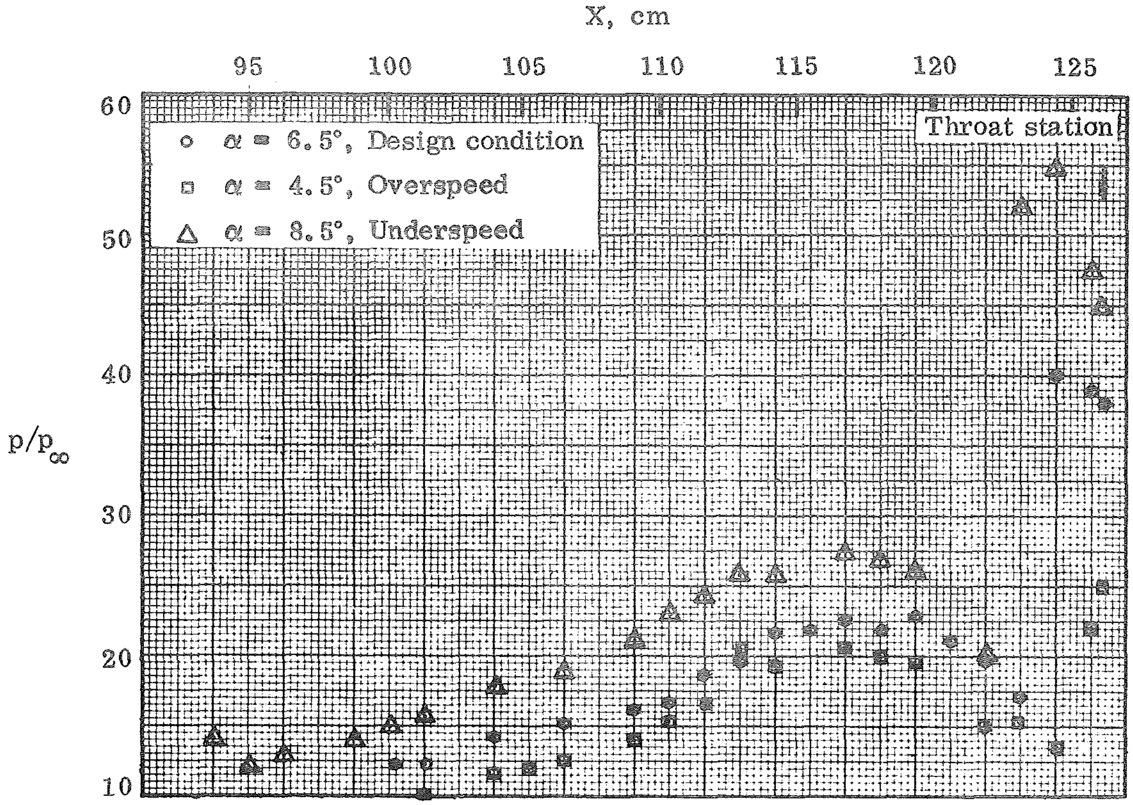

(a) Cowl.

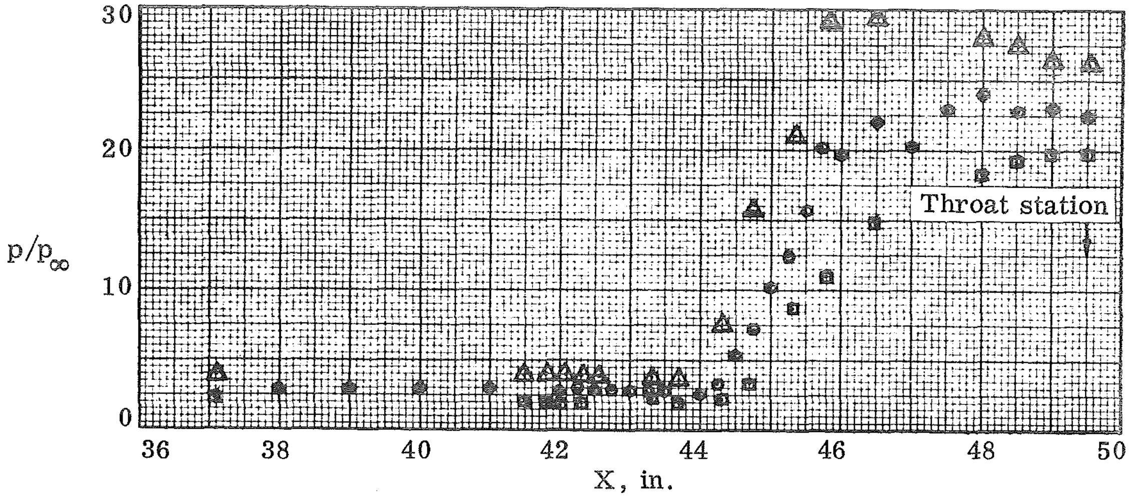

(b) Centerbody.

Figure 69.– Surface pressure distributions for off-design conditions; P8 inlet model.

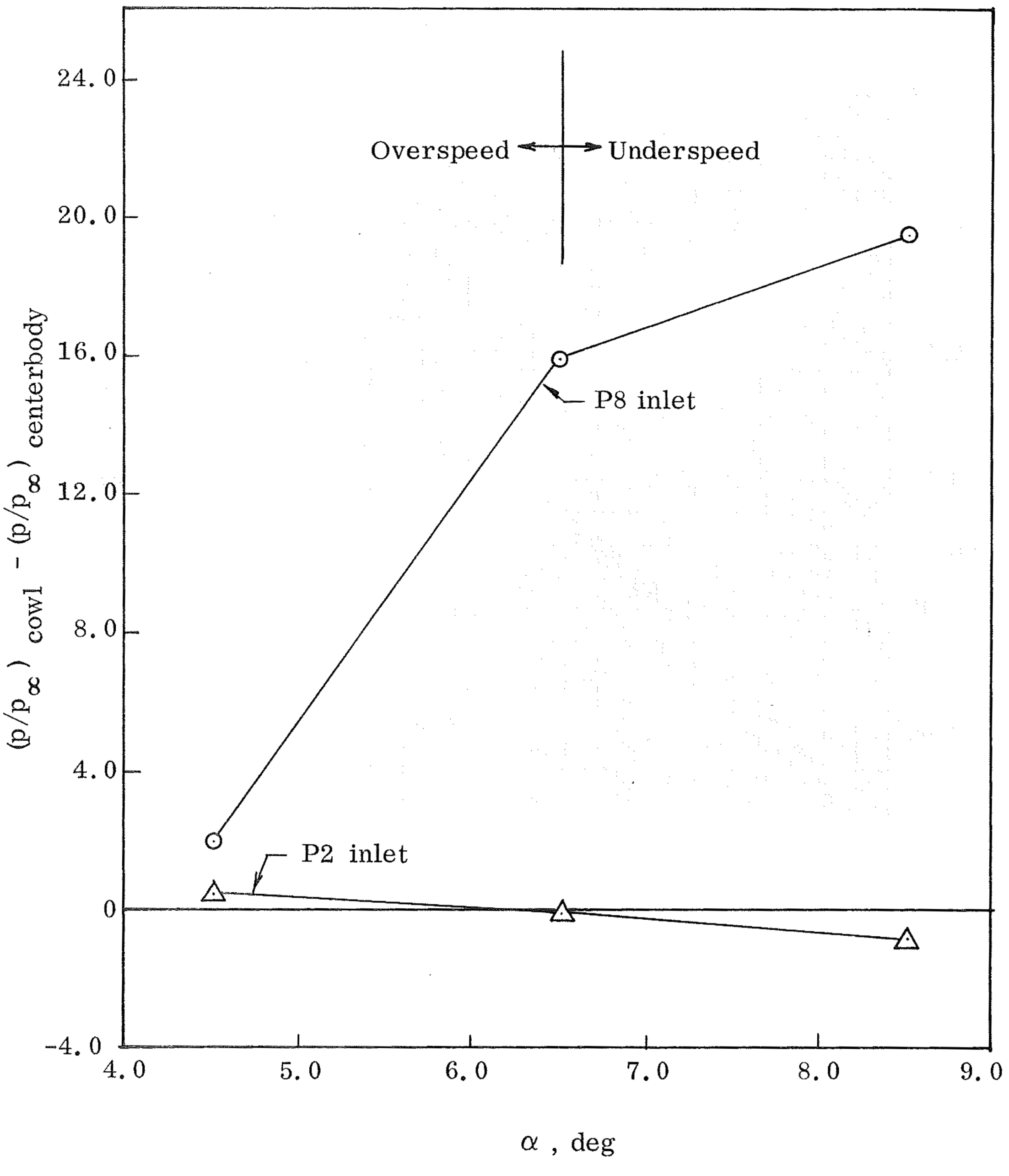

Figure 70.– Effect of off-design operation on inlet throat pressure differential.

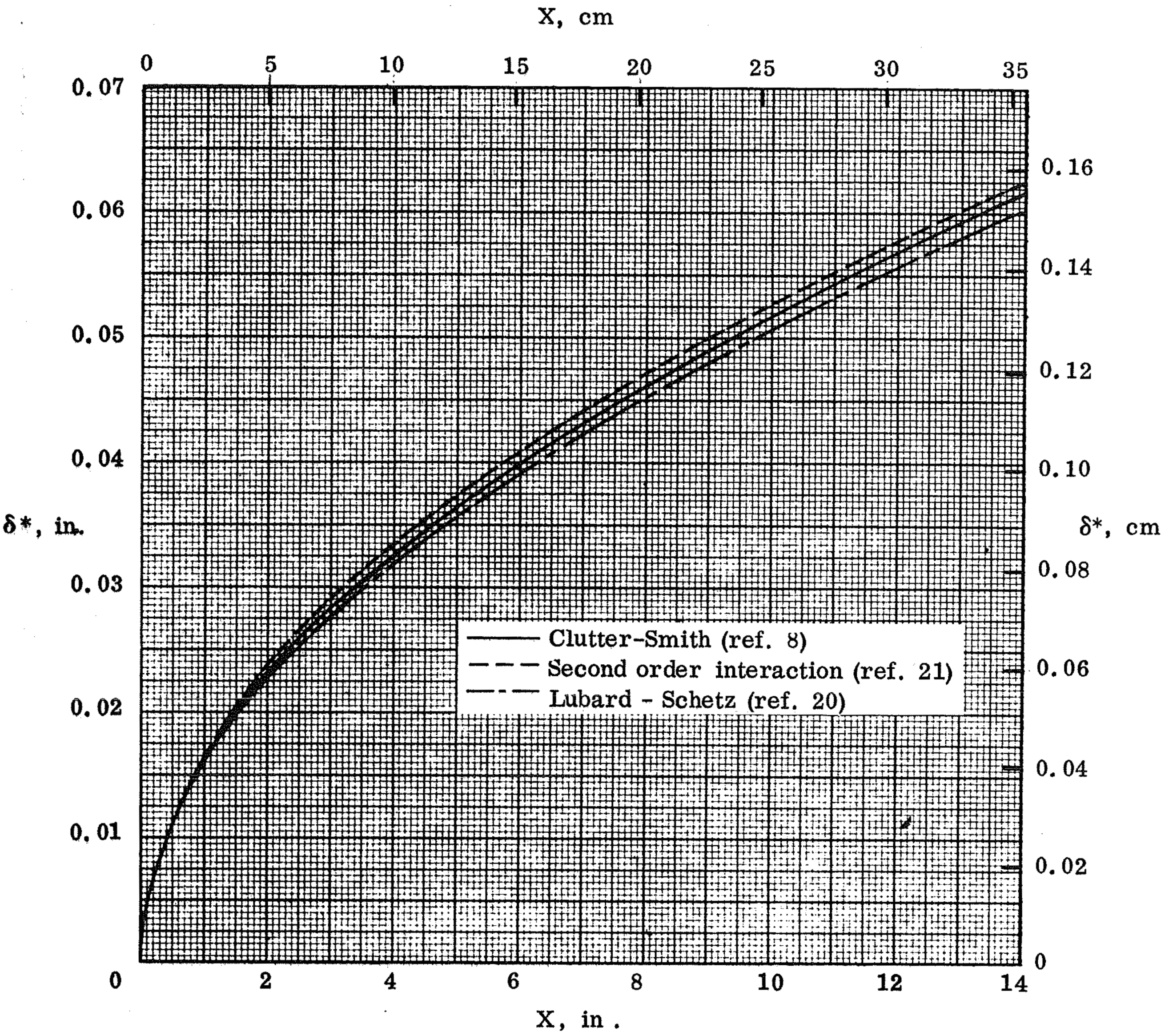

(a) Laminar boundary layer.

Figure 71.– Wedge-forebody boundary-layer development.

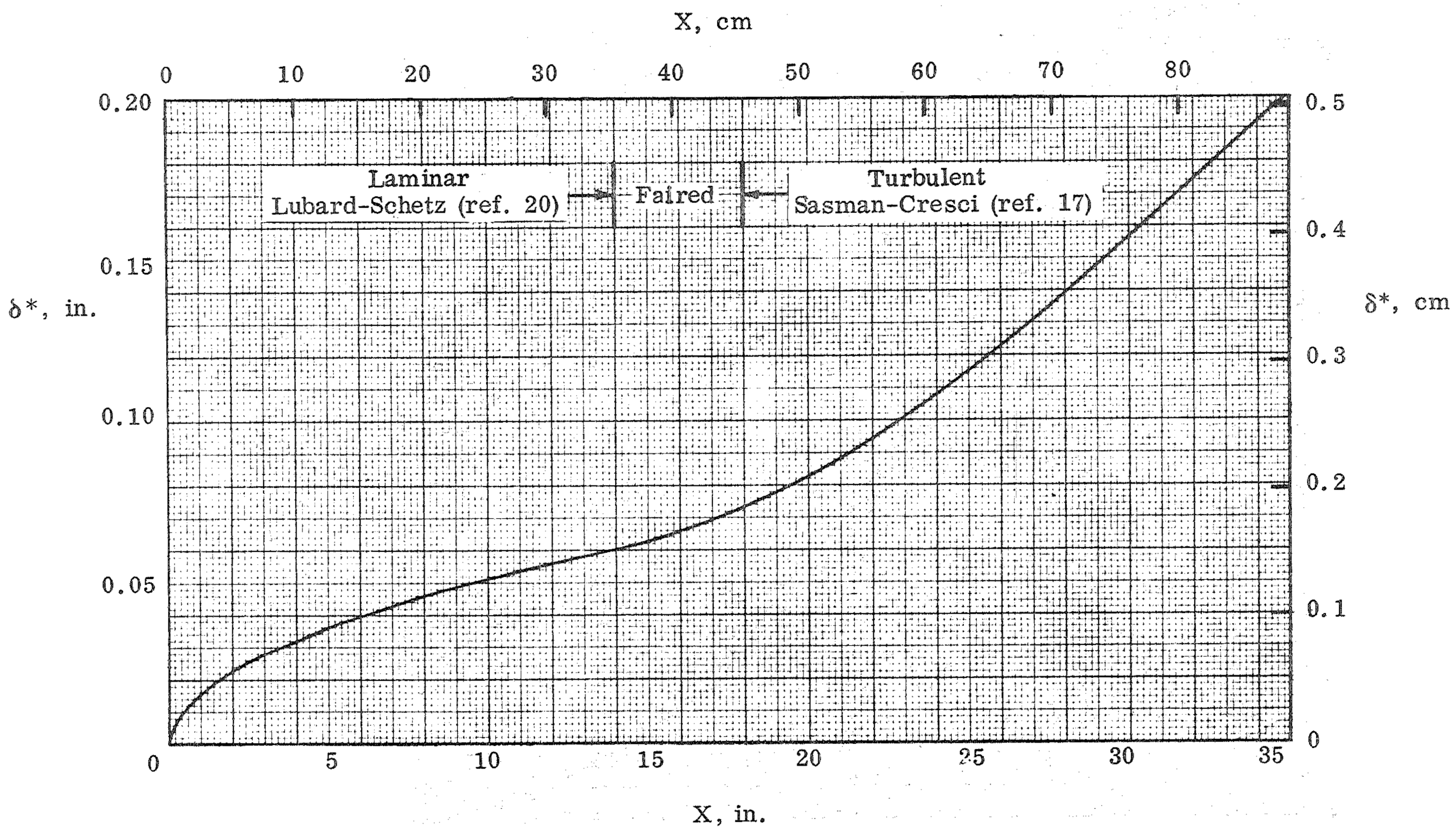

(b) Laminar and turbulent boundary layers.

Figure 71.– Concluded.

☆U.S. GOVERNMENT PRINTING OFFICE: 1973-739-026/8

NATIONAL AERONAUTICS AND SPACE ADMINISTRATION
WASHINGTON, D.C. 20546

OFFICIAL BUSINESS
PENALTY FOR PRIVATE USE $300

SPECIAL FOURTH-CLASS RATE
BOOK

POSTAGE AND FEES PAID
NATIONAL AERONAUTICS AND
SPACE ADMINISTRATION
451

U.S.MAIL

333 001 C1 U 01 730309 S00120BS
PHILCO FORD CORP
AERONUTRONIC DIV
ATTN: TECHNICAL INFO SERVICES
FORD RD
NEWPORT BEACH CA 92663

POSTMASTER: If Undeliverable (Section 158 Postal Manual) Do Not Return

---

"The aeronautical and space activities of the United States shall be conducted so as to contribute . . . to the expansion of human knowledge of phenomena in the atmosphere and space. The Administration shall provide for the widest practicable and appropriate dissemination of information concerning its activities and the results thereof."

—NATIONAL AERONAUTICS AND SPACE ACT OF 1958

NASA SCIENTIFIC AND TECHNICAL PUBLICATIONS

TECHNICAL REPORTS: Scientific and technical information considered important, complete, and a lasting contribution to existing knowledge.

TECHNICAL NOTES: Information less broad in scope but nevertheless of importance as a contribution to existing knowledge.

TECHNICAL MEMORANDUMS: Information receiving limited distribution because of preliminary data, security classification, or other reasons. Also includes conference proceedings with either limited or unlimited distribution.

CONTRACTOR REPORTS: Scientific and technical information generated under a NASA contract or grant and considered an important contribution to existing knowledge.

TECHNICAL TRANSLATIONS: Information published in a foreign language considered to merit NASA distribution in English.

SPECIAL PUBLICATIONS: Information derived from or of value to NASA activities. Publications include final reports of major projects, monographs, data compilations, handbooks, sourcebooks, and special bibliographies.

TECHNOLOGY UTILIZATION PUBLICATIONS: Information on technology used by NASA that may be of particular interest in commercial and other non-aerospace applications. Publications include Tech Briefs, Technology Utilization Reports and Technology Surveys.

Details on the availability of these publications may be obtained from:

SCIENTIFIC AND TECHNICAL INFORMATION OFFICE

NATIONAL AERONAUTICS AND SPACE ADMINISTRATION

Washington, D.C. 20546